RARE BOOKS LIB

Sykes, Stephen James
Ph.D. 1997

The University of Sydney

Copyright in relation to this thesis*

Under the Copyright Act 1968 (several provision of which are referred to below), this thesis must be used only under the normal conditions of scholarly fair dealing for the purposes of research, criticism or review. In particular no results or conclusions should be extracted from it, nor should it be copied or closely paraphrased in whole or in part without the written consent of the author. Proper written acknowledgement should be made for any assistance obtained from this thesis.

Under Section 35(2) of the Copyright Act 1968 'the author of a literary, dramatic, musical or artistic work is the owner of any copyright subsisting in the work'. By virtue of Section 32(1) copyright 'subsists in an original literary, dramatic, musical or artistic work that is unpublished' and of which the author was an Australian citizen, an Australian protected person or a person resident in Australia.

The Act, by Section 36(1) provides: 'Subject to this Act, the copyright in a literary, dramatic, musical or artistic work is infringed by a person who, not being the owner of the copyright and without the licence of the owner of the copyright, does in Australia, or authorises the doing in Australia of, any act comprised in the copyright'.

Section 31(1)(a)(i) provides that copyright includes the exclusive right to 'reproduce the work in a material form'. Thus, copyright is infringed by a person who, not being the owner of the copyright, reproduces or authorises the reproduction of a work, or of more than a reasonable part of the work, in a material form, unless the reproduction is a 'fair dealing' with the work 'for the purpose of research or study' as further defined in Sections 40 and 41 of the Act.

Section 51(2) provides that "Where a manuscript, or a copy, of a thesis or other similar literary work that has not been published is kept in a library of a university or other similar institution or in an archives, the copyright in the thesis or other work is not infringed by the making of a copy of the thesis or other work by or on behalf of the officer in charge of the library or archives if the copy is supplied to a person who satisfies an authorized officer of the library or archives that he requires the copy for the purpose of research or study'.

*'Thesis' includes 'treatise', dissertation' and other similar productions.

OPERATING CHARACTERISTICS OF THE SPINNING CONE COLUMN

A THESIS SUBMITTED FOR THE DEGREE OF

DOCTOR OF PHILOSOPHY

BY

STEPHEN J. SYKES BE, MEngSc

Department of Chemical Engineering

University of Sydney

October 1995

PREFACE

Chapter XIXD, Section 12(1) of the University of Sydney by-laws states that a candidate for the degree of Doctor of Philosophy "shall state, generally in the preface, and specifically in the notes, the sources from which his information is derived, the extent to which he has availed himself of the work of others, and the portion of work he claims to be original."

The work described in this thesis was carried out at the CSIRO Division of Food Science and Technology between March 1990 and June 1993. It is believed to be the original and independent work of the author, except where specifically acknowledged in the text. Neither this thesis, nor any part of it, has been submitted for a degree at this or any other university.

All experimental data presented in this thesis were collected by the author, or by persons acting under the author's direct supervision: Messrs J. Sywak and A. Dorigo, and Ms I. el-Mahmoud, undergraduate students on vacation placement from the Department of Chemical Engineering of this university, assisted in the collection of small- and medium-column flooding data, as indicated in the text. All experimental data were analysed by the author.

Department of Chemical Engineering
University of Sydney

October, 1995

ACKNOWLEDGEMENTS

I wish to express my gratitude to all those who provided assistance during the course of this work. In particular I should like to thank:

Professor Rolf Prince, for his support, guidance and invaluable advice;

Mr Andrew Craig, founder and Technical Director of Flavourtech Pty Ltd, for his support and forbearance;

Dr Don Casimir, father of modern spinning cone column technology, for the inspiration to undertake this work.

SUMMARY

The published literature concerning the spinning cone column (SCC) has been reviewed. In it the SCC was claimed to offer substantial advantages with regard to mass transfer performance. Superior performance in areas of pressure drop, liquid hold-up and residence time was also observed. The published literature, however, lacked generalized engineering data which could be used in the systematic design of SCCs. The increasing number of commercial applications of this technology in food processing have made the need for such engineering design data more acute.

In order to address this lack of design data, established methods for the design of conventional distillation columns, plate and packed columns, were studied; in such methods theoretical considerations and experimental data concerning the gas and liquid flows obtaining in the column and how these flows interact are combined to yield generalized information on flooding and entrainment, pressure drop, hold-up and residence time, and mass transfer. A key component of such design procedures is a generalized correlation of physical capacity, such as Fair's modification of the Souders-Brown correlation for entrainment flooding in plate columns, and the Sherwood-Leva-Eckert relationship for prediction of gas-induced flooding in packed columns. In this thesis a similar approach is taken to the design of SCCs.

The principal area of investigation reported in this thesis was the prediction of flooding in the SCC. Experimental data are presented, these data having been obtained on three SCCs which between them encompass the full range of sizes of all SCCs currently in service. On the basis of the conceptual similarities between packed columns and the SCC, the approach underlying the Sherwood-Leva-Eckert (SLE) correlation for flooding in packed columns is taken to the correlation of flooding in the SCC; the experimental flooding data are expressed as capacity parameters of the same form as that in the SLE correlation, requiring terms corresponding to characteristic flow area and packing factor. A number of options for these terms are evaluated; definitions most closely corresponding to the SLE correlation best correlate the SCC flooding data; i.e.

(a) the critical flow area within the cone set, at which the vapour velocity is evaluated, is the minimum flow area.
(b) the packing factor equivalent is wetted area per unit gas volume.

The correlation so obtained is similar in form and magnitude to the SLE packed column curve, and predicts gas rate at flooding to within ±25% across the range of sizes of the SCCs for which flooding data have been obtained. Flooding mechanisms in the SCC, and how these might relate to an overall flooding correlation, are discussed.

The work on the prediction of flooding was supported by studies on pressure drop. Pressure drop in the absence of liquid flow, firstly with the rotor fixed, and secondly with the rotor in motion, is considered. Experimental data are presented and compared with estimates of pressure drop obtained using published pressure loss coeffiicients for the flow of air in ducts. A quantitative representation of dry column pressure drop is developed; it is based on:

(a) the fixed-rotor dry-column pressure drop, including allowance for the effects of changes to the internal geometry of the cone set
(b) the modification of the fixed-rotor dry-column pressure drop response by the motion of the rotor. The effect of rotor motion was described and quantified in terms of the SCC's fan-like behaviour; i.e. the SCC was considered, for these purposes, to be a kind of multi-stage centrifugal fan.

Pressure drop in the presence of liquid flow is also considered; it is described as an extension of the dry-column pressure drop behaviour.

Subsidiary investigations were conducted on liquid flow and mass transfer.

Liquid flow in the SCC, specifically the flow of liquid films on rotating conical surfaces, was investigated. Theoretical descriptions of such a liquid flow regime, the Nusselt and the Bruin models, are presented. Experimental data on liquid film velocities for a range of liquid flows and rotational speeds typically encountered in operating (pilot-scale and commercial) SCCs are presented and analysed, and compared to the predictions of the theoretical models. The experimental results broadly confirmed the validity of the Bruin model. Neither the Bruin nor the Nusselt model, however, can be applied without modification to conditions which would typically obtain in a commercial SCC since the assumptions on which both models are based cease to be valid at radiuses and liquid flows well within the typical operating range.

Finally, mass transfer in the SCC is discussed. In particular, we compare the results of trials on two different SCCs with two different systems: total reflux trials using acetic acid/water in a small SCC, and ethanol stripping trials in a medium-sized SCC.

Comparison of predicted and observed mass transfer coefficients suggests that the resistance to mass transfer in the vapour phase is substantially lower than that predicted by the Sherwood-Gilliland correlation, from which estimates of the vapour mass transfer coefficients were obtained.

Stated in brief terms, the main outcomes of the work reported in this thesis are:

(a) a general correlation for flooding in the SCC of the same form as the SLE correlation for flooding in packed columns
(b) an understanding of gas flow in the SCC based on pressure drop studies
(c) a basic analysis of liquid flow in the SCC supported by experimental data
(d) some preliminary results and interpretation of mass transfer in the SCC.

CONTENTS

CHAPTER 1

THE HISTORY OF THE SPINNING CONE COLUMN

CHAPTER 2

PHYSICAL CAPACITY AND LIMITS OF OPERATION OF CONVENTIONAL DISTILLATION COLUMNS

CHAPTER 3

PRESSURE DROP IN THE SPINNING CONE COLUMN IN THE ABSENCE OF LIQUID FLOW

CHAPTER 4

PHYSICAL CAPACITY AND LIMITS OF OPERATION OF THE SPINNING CONE COLUMN

CHAPTER 5

FLOW OF A LIQUID FILM ON A ROTATING CONICAL SURFACE

CHAPTER 6

MASS TRANSFER IN THE SPINNING CONE COLUMN

CHAPTER 7

THE OPERATING CHARACTERISTICS OF THE SPINNING CONE COLUMN: GENERAL CONCLUSIONS

LIST OF FIGURES

LIST OF TABLES

CHAPTER 1

THE HISTORY OF THE SPINNING CONE COLUMN

1.1 Introduction

Although conceived in the 1930s, the spinning cone column has only recently begun to find industrial applications, these being distillation operations in food processing, where it is used for flavour recovery, alcohol removal, de-odourization of fats and oils, removal of taints, and other gas-liquid contacting operations.

The main advantages of the spinning cone column are:

(a) low liquid hold-up, short residence time
(b) low pressure drop
(c) high separation efficiency
(d) ability to handle liquids containing a high proportion of suspended solids.

The volatile components of foods are characterized by the following attributes:

(a) a broad range of relative volatilities with respect to water, varying by two orders of magnitude from 1 to 100 or more.
(b) heat-lability: many thermal components of foods are degraded at even moderately elevated temperatures.

Separation of food volatiles by distillation therefore requires a distillation column which offers a high separation efficiency so that acceptable recovery of less volatile components can be achieved. At the same time, the exposure to heat must be minimized; hence we require low product hold-up and short residence time; furthermore, low pressure drop is required to limit the temperature difference between bottom and top of column.

Finally, liquid food streams often contain a high proportion of suspended solids, which must be removed if the liquid is to be processed in a conventional distillation column. Such a separation of solids constitutes an additional and costly unit process; moreover, the volatile extracts obtained from liquids from which the solids have been removed are usually much inferior with respect to both concentration and sensory quality. The capability to process liquids containing solids is therefore a highly desirable attribute for any distillation system in which food volatiles are to be separated.

By possessing the capabilities and characteristics listed above the spinning cone column is particularly well suited for the separation of food volatiles and other gas-liquid contacting operations in food processing.

In this thesis the spinning cone column is considered from an engineering viewpoint. The increasing number of commercial applications has made the need for generalized engineering data which could be used in the design of SCCs more acute. The purpose of this chapter is to introduce the spinning cone column by presenting the history of the technology and the major research findings; in it we find that engineering data of the type now required to support the burgeoning commercial applications of the SCC are not available in the published literature.

The purpose of this thesis is to address this lack of generalized design data; in particular, we seek to devise correlations of physical capacity like those used in the design of plate and packed columns.

1.2 Description of the SCC: internal layout and dimensions of various units

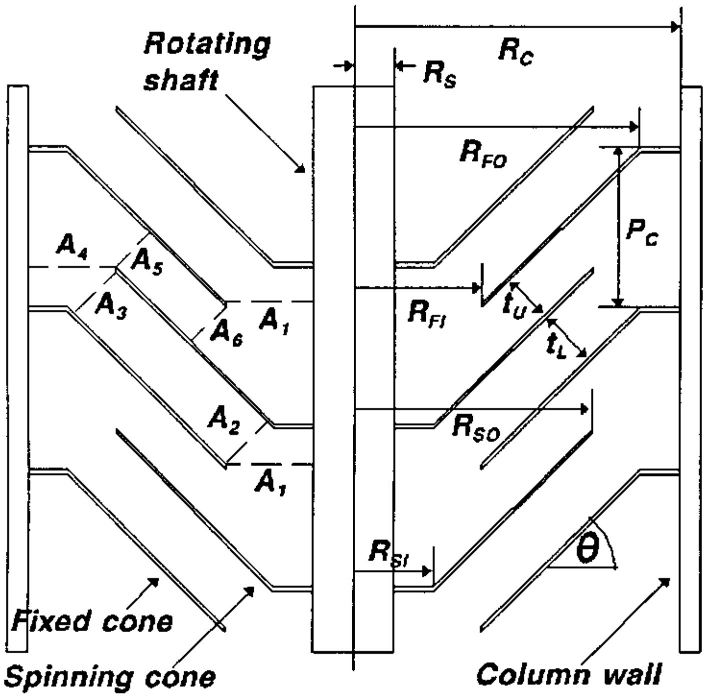

Figure 1.1
Schematic diagram of portion of a spinning cone column.
The symbols are defined in table 1.1; values of these dimensions for the columns discussed in this chapter are given in table 1.2.

The spinning cone column (SCC) is a gas-liquid contacting device consisting of a vertical countercurrent flow system which contains a succession of alternate rotating and stationary metal cones whose upper surfaces are wetted with a thin film of liquid. Liquid flows down the upper surfaces of the stationary cones under the influence of gravity and moves up the upper surfaces of the rotating cones in a thin film by the action of the applied centrifugal force. Vapour flows up the column, traversing the spaces between the successive fixed and rotating cones.

Table 1.1
Definitions of symbols used in fig. 1.1

Symbol	Definition
R_S	radius of shaft/spacing sleeve
R_C	inner radius of column shell
R_{FI}	inner radius of fixed cone
R_{FO}	outer radius of fixed cone
R_{SI}	inner radius of spinning cone
R_{SO}	outer radius of spinning cone
P_C	cone pitch; i.e. vertical distance between the upper surfaces of adjacent fixed (or spinning) cones
θ	cone angle
t_U	upper gap
t_L	lower gap
B	spacing parameter, the vertical distance between the upper surfaces of the fixed cone and the spinning cone immediately below divided by the cone pitch

The six gas/vapour flow areas A_1 to A_6 shown in fig. 1.1 are given by

$$\begin{aligned}
A_1 &= \pi\,(R_{FI}^2 - R_S^2) \\
A_2 &= \pi\, t_L\,(2R_{FI} - t_L \sin\theta) \\
A_3 &= \pi\, t_L\,(2R_{SO} + t_L \sin\theta) \\
A_4 &= \pi\,(R_C^2 - R_{SO}^2) \\
A_5 &= \pi\, t_U\,(2R_{SO} - t_U \sin\theta) \\
A_6 &= \pi\, t_U\,(2R_{FI} + t_U \sin\theta)
\end{aligned} \tag{4.1}$$

Table 1.2
Dimensions of SCCs discussed in Chapter 1

SCC designation	PUH	MW	Z	C	M
R_C (mm)	75	24	71	74	100
R_S (mm)	14	6	15	21	32
R_{FI} (mm)	22	12	27	30	38
R_{FO} (mm)	75	24	71	74	100
R_{SI} (mm)	20	6	15	25	38
R_{SO} (mm)	71	16	65	64	90
θ	40°	30°	45°	50°	50°
P_C (mm)	17	7	16	21	23
B	0.5	0.5	0.5	0.4	0.4
t_U (mm)	5.4	2.5	5.2	5.0	5.5
t_L (mm)	5.4	2.5	5.2	7.5	8.5
N_{CS}	610	77	25	40	30
A_1 (m^2)	0.0009	0.0004	0.0017	0.0013	0.0016
A_2 (m^2)	0.0007	0.0002	0.0008	0.0013	0.0020
A_3 (m^2)	0.0025	0.0003	0.0022	0.0032	0.0052
A_4 (m^2)	0.0016	0.0009	0.0024	0.0041	0.0060
A_5 (m^2)	0.0024	0.0003	0.0021	0.0019	0.0029
A_6 (m^2)	0.0008	0.0002	0.0010	0.0010	0.0013

The SCC designations used in table 1.2 are as follows:

PUH	the large SCC of Pegram, Urey and Huffman
MW	the SCC of Mair and Willingham
Z	the SCC of Ziolkowski *et al.*
C	the SCC of Casimir
M	the SCC of Menzi

N_{CS} is the number of cone sets in the SCC.

1.3 American beginnings

1.3.1 The work of Pegram, Urey and Huffman

The first published reference to a spinning cone column appeared in 1936 (Pegram, Urey and Huffman, 1936a, 1936b). Huffman and Urey (1937) gave the first detailed description of a spinning cone column, and presented the results of trials on the separation of isotopes of oxygen in water; the object was to produce "sufficiently large quantities of the heavier isotopes of this element for future physical, chemical and biological researches."

It had been shown a few years before this that heavy oxygen water (H_2O^{18}), is about 0.3% less volatile than normal water (H_2O^{16}). Efforts were made to exploit this difference in vapour pressure to separate the two materials by distillation. It was recognized, however, that existing designs of distillation column did not offer the performance required for such a demanding separation, hence the attention paid to alternative configurations.

The original conception of the spinning cone column was attributed jointly to G.B. Pegram, and to Manske of the Canadian Research Council (Huffman and Urey, 1937). The layout of the SCC cone set was compared to the "Feld-type washer": this refers to the use of a rotating cone, or set of coaxial cones, as an atomizer/spray head.

The work reported by Huffman and Urey was actually carried out on three SCCs, which had, with the exception of an initial set of trials on the second column, the same internal geometry and differed only in overall height and number of cone sets (throughout this thesis the term "cone set" is used to signify a pair of cones, one stationary and one rotating). The first of these columns had 15 cone sets, the third 610; the second, intermediate column was initially fitted with 105 cone sets with successive stationary cones spaced 12.7 mm apart but this layout was revised to 87 cone sets with a spacing of 15.9 mm, the same as that of the small and large units.

The smallest of the Pegram-Urey-Huffman columns was tested with 5% deuterium oxide in normal water. When run as a batch still at atmospheric pressure its separation efficiency varied with reflux ratio, from 13.8 theoretical stages at a reflux ratio of 0.96 to 4.1 theoretical stages at a reflux ratio of 0.74; these data correspond to cone set efficiencies of 92% and 27%. In these trials, heat input to the reboiler and rotor speed were varied as well as reflux ratio but only reflux ratio was found to have any influence on mass transfer efficiency.

The intermediate-sized column was run under total reflux at atmospheric pressure with 0.3% D_2O. The separation achieved was equivalent to 74 theoretical stages; i.e. a cone set efficiency of 85%.

Two series of trials were conducted on the largest of the three SCCs investigated by Urey and Huffman. The first was a set of two total reflux runs at atmospheric pressure; separations equivalent to 192 and 197 theoretical plates were achieved with throughputs of 95 and 92 ml/min. respectively, corresponding to cone set efficiencies of 31% and 32%.

The mode of operation was changed for the second series of trials on the large column. Rather than running the system under total reflux, liquid was continuously fed to the top of the column and fully evaporated in the reboiler at the bottom. Also, this second series was undertaken at reduced pressures, 0.2 and 0.27 bar respectively, to take advantage of the higher relative volatility (of H_2O^{16} with respect to that of H_2O^{18}) at these pressures. Throughputs of only 33 and 45 ml/min. were possible under these circumstances; this reduction in achievable throughput may have been due to the reduced gas density necessitating higher gas velocities for a given throughput. No separation figures (no. of theoretical stages) are given by Huffman and Urey for these last two runs because the system appeared not to have reached steady state, even after 300 hours of continuous running.

1.3.2 The work of Mair and Willingham

The next major investigation of the SCC was reported by Mair and Willingham (1939), who were concerned with high-efficiency laboratory distillation columns: "Though many improvements have been made in packed and bubble-cap laboratory distillation columns in the past few years, columns of still greater efficiency are needed for separating hydrocarbons of eight or more carbon atoms per molecule from the gasoline and kerosene fractions of petroleum."

The dimensions of the SCC used by Mair and Willingham are given in table 1.2. The test solution used in their experiments was n-heptane and methyl cyclohexane (relative volatility $\alpha = 1.07$).

In addition to the cone set geometry described in table 1.2, Mair and Willingham tested two other internal configurations:

(a) rotating cones were replaced by baskets having a flat disc base with a cylindrical perforated wall; the purpose of using such a rotating element was to promote the formation of a spray of fine liquid droplets; Mair and Willingham considered that "a considerable portion of the efficiency of this type of column is attributable to the contact between spray and vapour rather than to the contact between the film of liquid on the metal surfaces and the vapour." The stationary elements in this configuration were cones having an angle of 20°.

(b) rotating cones replaced by flat discs, stationary cones having an angle of 20°.

The column was run under total reflux for all trials. The results obtained were:

(a) rotating baskets, 20° stationary cones, spacing 9.5 mm: stage efficiency 56 to 70%, HETP 18.2 to 14.6 mm.

(b) rotating discs, 20° stationary cones, spacing 9.5 mm: stage efficiency 54%, HETP 18.8 mm.

(c) 30° rotating cones, 30° stationary cones, spacing 6.4 mm: stage efficiency 54 to 84%, HETP 13.5 to 8.7 mm.

Mair and Willingham found that neither rotor speed nor throughput (heat input to reboiler) had any discernible effect on mass transfer efficiency/HETP; throughput was varied only between 1 and 10 ml/min.

1.3.3 Discussion

The work of Pegram, Urey and Huffman was not a systematic study of the SCC; rather it was simply a reporting of what was done in pursuit of quite particular ends: the production of isotope-enriched water. This work was concerned with mass transfer in the SCC (a direct consequence of the application); other aspects of SCC performance, such as physical capacity and flow characteristics, were not considered.

Pegram, Urey and Huffman observed a wide variation in mass transfer performance (stage efficiencies between 25 and 100%) but did not propose, or attempt to devise by experiment, any explanations for such variations. Even so, their contribution was seminal; the concept of the SCC (internal layout and principle of operation) was described and, most importantly, the device was demonstrated to function in the manner envisaged by its originators.

The main contribution made by Mair and Willingham was to look at the effects on performance of different types of rotating element and internal geometry and, as a result, to establish that the basic (two-cone) configuration gave the best performance, at least with respect to mass transfer (stage efficiencies between 50 and 80%). An important implication of this aspect of their work was that the contact between gas and liquid droplets, maximized in the case where perforated baskets were used as rotating elements, did not appear to be the pre-eminent mode of mass transfer between the phases.

1.4 The work of Ziolkowski *et al.*

1.4.1 Summary of results

The publication of research findings on the SCC lapsed after the early (pre-war) American work until Ziolkowski *et al.* (1963) reported studies on the operational characteristics of a spinning cone column used for the separation of a benzene-carbon tetrachloride mixture. The dimensions of the column used in this work are given in table 1.2.

The experiments of Ziolkowski *et al.* were conducted in three series, all under total reflux. Each series was conducted at a single rotor speed, the values being 265, 610 and 1140 RPM. Within each series the only independent variable was heat input to the reboiler, which directly determined liquid and vapour loadings (throughput) in the column. For each run, measurements were made of pressure drop across the column, liquid hold-up and separation efficiency.

Fig. 1.2 shows the variation of pressure drop ΔP (upstream pressure minus downstream pressure) across the column with throughput. At the lower rotor speeds there is little change in ΔP with throughput until, at 610 RPM, it begins to rise sharply at throughputs above 12 litres/hour. The value of throughput at which this sudden increase in ΔP occurs is somewhat higher, about 15 litres/hour, at 265 RPM. With a rotor speed of 1140 RPM the pressure drop is substantially higher at all throughputs, although the general pattern is similar, ΔP rising slowly until throughput reaches 12 litres/hour, after which it rises sharply as was the case with the two lower rotor speeds. This pattern is similar to that observed in packed columns; the sharp rise in ΔP at high throughputs marking the onset of loading and flooding.

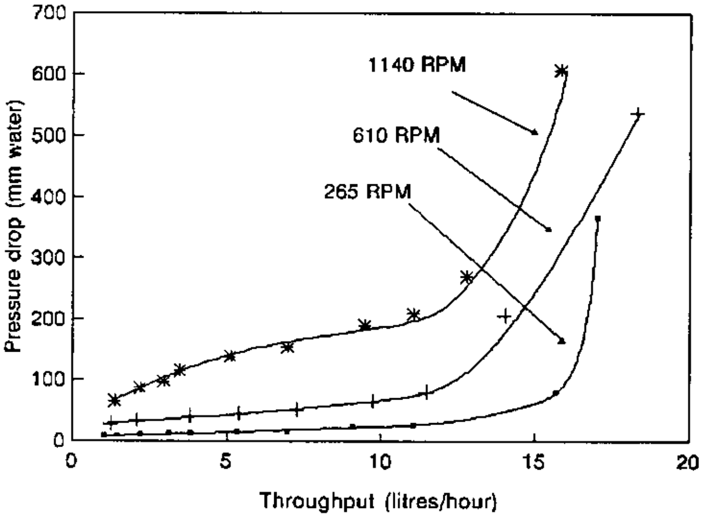

Figure 1.2
Variation of pressure drop with throughput (results of Ziolkowski *et al.*)

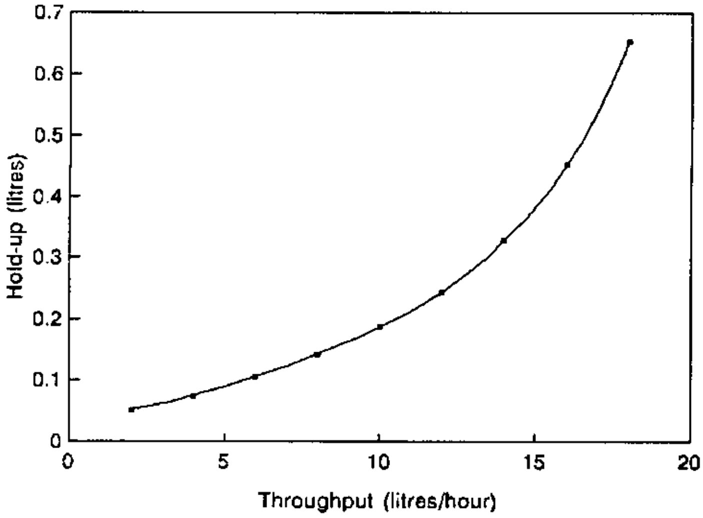

Figure 1.3
Variation of hold-up with throughput (results of Ziolkowski *et al.*)

Fig. 1.3 shows the variation of liquid hold-up with throughput observed by Ziolkowski *et al.* Liquid hold-up rises at an increasing rate as throughput increases, and, according to these results, is unaffected by rotor speed.

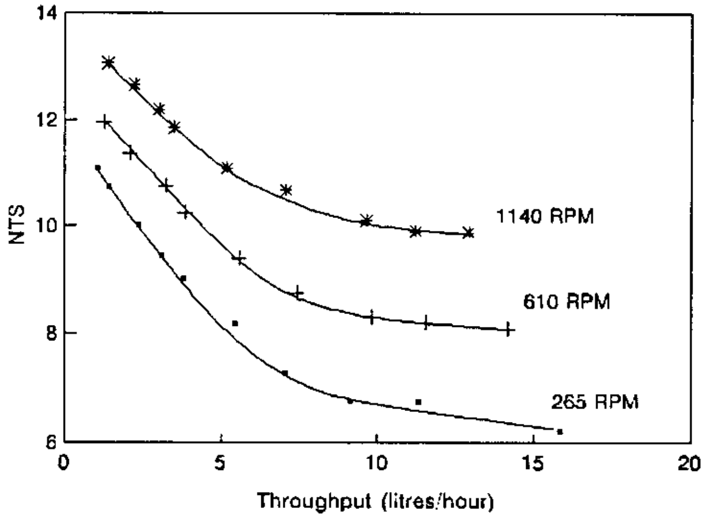

Figure 1.4
Variation of separation capacity (*NTS*) with throughput (results of Ziolkowski *et al.*)

Fig. 1.4 shows the variation of separation capacity (*NTS*) with throughput. *NTS* is highest at low throughputs, falling steadily as throughput rises until flattening out as throughput reaches about 10 litres/hour. Rotor speed has pronounced effect, more so at higher throughputs. *NTS* values range between 11 and 13 (corresponding to stage efficiencies of 44 and 52%) at the lowest loadings and 6.5 and 10 (corresponding to stage efficiencies of 26 and 40%) as the loading point is approached, at which point increasing the speed from 265 to 1140 RPM increases *NTS* by more than 50%.

1.4.2 Discussion

The work of Ziolkowski *et al.* was similar to the pre-war American work in that all results were obtained (with the SCC running) under total reflux. It was the first study in which gas pressure drop data were presented and in which the influence of rotor speed, on both mass transfer performance and gas pressure drop, was considered. Separation efficiency increased with rotor speed at all throughputs; at a given rotor speed separation efficiency tended to fall as throughput was increased (in a similar manner to that observed in packed columns).

The pressure drop data given by Ziolkowski *et al.* showed the behaviour of the column under conditions of increasing load, the locations of capacity limits and what happens when these limits are approached.

The relationships between rotor speed, throughput, pressure drop and mass transfer efficiency observed by Ziolkowski *et al.* are in accord with the experimental observations reported in this thesis; see Chapters 3, 4 and 6.

1.5 The application of the SCC to separation of food volatiles: the work of Casimir

1.5.1 Background

In the 1960s, D.J. Casimir of the CSIRO Division of Food Research was engaged in work on the processing of fruit juices, particularly products derived from passionfruit. He was particularly concerned to find ways of producing concentrated (evaporated) passionfruit juice which retained the distinctive and highly desirable aroma and flavour of the raw material.

The basis of the problem that Casimir addressed was as follows: fruit juices are almost always evaporated (reduced volume reduces packaging and transport costs, and lower moisture content enhances microbiological stability through lower water activity) and in the course of the removal of up to 85% of the original water content, a significant fraction of the juice's volatile components will be removed as well, the size of that fraction depending on the relative volatilities of the components. These volatile components are critical to the sensory character and perceived quality of the juice, and so must somehow be separated from the water and restored to the concentrate or to the reconstituted juice if the flavour and aroma of the final product is not to be substantially degraded.

Various systems have been developed for the separation and recovery of volatile components from fruit juices, typically comprising either a specific stripping process (single-stage flash evaporation with 10 - 30% evaporation) prior to the main evaporation step, or a system for the rectification of condensate from one or more effects of the evaporator, or a combination of the two.

Casimir's work on the evaporation of passionfruit juice led him to conclude that such systems would never provide an entirely satisfactory solution to the problem of volatile degradation and loss; simple systems inevitably gave crude results, and the more refined systems rapidly became highly complex and expensive. Instead, he took the view that the separation of volatiles was best effected prior to the evaporation step and that this would require a counter-current gas-liquid contacting device which offered a high mass transfer capacity, so allowing acceptable recovery of even the least volatile components, but which did not require operating conditions which would bring about damage to the product. On this basis the requirements for a device to be used for separation of heat labile volatile materials by distillation were (Casimir, 1974):

(a) countercurrent gas and liquid flows
(b) large interfacial gas-liquid contacting area
(c) high turbulence within gas and liquid phases

(d) little or no entrainment
(e) low hold-up volume, i.e. low retention time
(f) low pressure drop

1.5.2 Adoption of the SCC for volatile recovery

Having reviewed the available types of distillation column, Casimir determined that of all the possible configurations the SCC best met his stated criteria. He then designed a pilot-scale essence recovery system based around an SCC. His particular requirements for the pilot-scale column were:

(a) low HETP, at least 10 plates per metre
(b) low thermal inertia for rapid attainment of thermal equilibrium
(c) low hold-up volume
(d) low pressure drop across column
(e) adaptability to enable changing of number of theoretical plates in stripping and rectification sections
(f) non-absorbent and readily cleanable interior surfaces
(g) choice of feed points
(h) facility for removal of side-stream from any point
(i) capability for operation at reduced pressures
(j) uniform vapour and reflux distribution at any section at right angles to bulk flow

1.5.3 "A variable pressure drop countercurrent gas-liquid contacting device"

With the exception of size and geometry, the SCCs used by Mair and Willingham, and by Ziolkowski *et al.*, were essentially the same as the devices used by Huffman and Urey. Casimir's principal change to this basic design was the addition of radial fins to the undersides of the rotating cones. The following advantages were claimed:

(a) each spinning cone becomes a centrifugal impeller, and the whole column a multi-stage centrifugal fan; this fan action could be used to control pressure drop across the column; depending on operating conditions of fans and flows within column the pressure drop across the column could be negative, zero or positive.
(b) the rotatory motion imparted to vapour brought about a centrifugal de-entrainment any liquid droplets in vapour stream.
(c) the radial fins promoted a high degree of agitation in the vapour phase, thereby enhancing mass transfer within it.

The dimensions of Casimir's pilot-scale SCC are given in table 1.2.

Each spinning cone had three radial fins attached to its lower (conical) surface, running the full length of this surface from the base to the lip. The depth of the fin perpendicular to the cone surface was 7 mm.

Casimir (1974) proposed the first quantitative (*semi-theoretical*) analysis of the flow processes in the SCC; his model is presented in the following sections, 1.5.3.1 and

1.5.3.2, because it forms the basis of his explanation of the SCC's mass transfer performance.

1.5.3.1 Vapour flow in the variable pressure drop column

Casimir dealt first with vapour flow in space between the upper surface of the rotating cone and the lower surface of the stationary cone; he compared it to the flow pattern obtaining in a cyclone: at entry its velocity is (largely) tangential due to the rotatory motion imparted by the fins on the underside of the rotating cone. "This rotatory motion is continued as the vapour passes between the upper surfaces of the rotating cone and the lower surface of the stationary cone. Frictional drag occurs mainly between the rotating vapour and the stationary cone as the rotating cone is moving with the vapour."

1.5.3.1.1 Distance travelled by a particle in the vapour phase

Assuming that the perpendicular gap between adjacent cone surfaces is constant, the radial vapour velocity is inversely proportional to radius r. The tangential velocity increases with r due to the action of fins and other rotating surfaces. Hence, a vapour particle describes a spiral path, the distance between successive spirals decreasing as r increases.

1.5.3.1.2 Residence time of vapour particles between cones

The average radial vapour velocity at radius r is

$$\frac{dr}{dt} = \frac{Q\cos\theta}{2\pi r D} \tag{1.1}$$

where θ is the cone angle,
Q is the volumetric vapour flow rate, and
D is the perpendicular distance between adjacent cones.

Therefore the time taken for a vapour particle to move from r_1 to r_2 is

$$t = \int_{r_1}^{r_2} \frac{2\pi D}{Q\cos\theta} r\,dr$$

$$= \frac{\pi D}{Q\cos\theta}(r_2^2 - r_1^2) \tag{1.2}$$

1.5.3.1.3 Path length of vapour particle

The distance travelled by a vapour particle in time dt is:

$$ds = \sqrt{\frac{dr^2}{\cos^2\theta} + r^2 d\phi^2} \tag{1.3}$$

where dr and $d\phi$ are the radial and angular displacements in time dt.

We assume that $d\phi/dt = \omega$, the angular velocity of the column rotor. Therefore, from eq. (1.1)

$$d\phi = \frac{2\pi D\omega}{Q\cos\theta} rdr$$

and substituting into eq. (1.3) we obtain

$$ds = \sqrt{\frac{dr^2}{\cos^2\theta} + r^4 \left[\frac{2\pi D\omega}{Q\cos\theta}\right]^2 dr^2} \tag{1.4}$$

Therefore, the total distance travelled by a vapour particle between r_1 and r_2 is

$$s = \int_{r_1}^{r_2} \sqrt{\frac{1}{\cos^2\theta} + \left[\frac{2\pi D\omega}{Q\cos\theta}\right]^2 r^4}\ dr \tag{1.5}$$

The average velocity of the vapour particles can be calculated by dividing the path length by the residence time.

1.5.3.2 Liquid flow in the variable pressure drop column

1.5.3.2.1 Liquid flow on the upper surface of the rotating cones

Casimir states that the path described by liquid particle on the upper surface of the spinning cone is a straight line in the radial direction when viewed from a reference frame rotating at same speed as cone (in other words, the angular velocity of the liquid particle is the same as that of the rotor); "this is substantiated by "burn-on" pattern produced on conical heat transfer surface of centrifugal evaporators."

Viewed from a stationary reference frame the path of a liquid particle is spiral. Casimir cited Hickman (1944) and Heinze and Milborn (1950), in proposing that the spacing between successive windings is independent of radius (Archimedean spiral), and inferred from this that plug flow is approximated in the film.

1.5.3.2.2 Distance travelled by a liquid particle on the upper surface of the rotating cone

Projected on to a plane perpendicular to the axis of rotation the equation for the spiral path of a liquid particle is

$$r = r_0 + \frac{A'\phi}{2\pi} \tag{1.6}$$

Here $A' = A\cos\theta$ where A is the distance along the cone surface between successive windings of the spiral and r_0 is the initial radial position of the particle. Casimir uses an expression proposed by Hinze and Milborn (1950) to evaluate A:

$$A = 0.95 \left[\frac{\rho Q^2}{\mu \omega} \right]^{1/4}$$

Note that eq. (1.6) is the equation of an Archimedean spiral; this flow path implies a constant radial velocity and is therefore inconsistent with the Nusselt model of film flow, discussed in Chapter 5.

Therefore

$$d\phi = \frac{2\pi dr}{A'}$$

and the distance s travelled by liquid particle on the surface of the cone between r_1 and r_2 is

$$s = \int_{r_1}^{r_2} \sqrt{dr^2 + r^2 d\phi^2}$$

$$= \int_{r_1}^{r_2} \sqrt{1 + \frac{4\pi^2}{(A')^2}\, r^2 dr}$$

$$= \left[\frac{r}{2} \sqrt{1 + \frac{4\pi^2}{(A')^2} r^2} + \frac{A'}{4\pi} \ln \left(\frac{2\pi r}{A'} + \sqrt{1 + \frac{4\pi^2}{(A')^2} r^2} \right) \right]_{r_1}^{r_2}$$

Since the spacing between successive windings of the spiral is independent of cone angle we can substitute A for A' and integrate between the limits L_1 and L_2 where L_1 and L_2 are the distances up the cone from the apex.

Hence the distance travelled is

$$s = \left[\frac{r}{2} \sqrt{1 + \frac{4\pi^2}{A^2} r^2} + \frac{A}{4\pi} \ln \left(\frac{2\pi r}{A} + \sqrt{1 + \frac{4\pi^2}{A^2} r^2} \right) \right]_{L_1}^{L_2}$$

where $L_1 = r_1 / \cos\theta$ and $L_2 = r_2 / \cos\theta$.

1.5.3.2.3 Residence time of a liquid particle on the upper surface of the rotating cone

The residence time t of a liquid particle on the upper surface of the rotating cone is obtained by dividing the radial length of cone by the distance between adjacent spirals of the particle path and multiplying by the time for one revolution:

$$t = \frac{r_2 - r_1}{A} \times \frac{2\pi}{\omega}$$

The mean velocity of a liquid particle on the upper surface of the rotating cone is the path length s divided by residence time t.

1.5.3.2.4 Photographic studies of liquid flow on the upper surfaces of rotating cones

Casimir undertook photographic studies of liquid flow on the upper surface of a rotating cone to ascertain degree of wetting on conical surface and thereby area available for mass transfer. These tests were conducted on a single rotating cone mounted on vertical shaft and driven by variable speed motor. Water at 20°C was delivered (from above as a stream of droplets) to the centre of cone at 4.17 x 10-3 kg/s. Cone speed varied between 200 and 1200 rpm.

His findings were as follows: at low speeds, 200 to 500 rpm, the centrifugal force was insufficient to counteract gravitational effects, resulting in excessive pooling of liquid at the base of the cone; liquid moved over the cone surface in rivulets rather than as a film. Complete coverage of the upper surface of the rotating cone, where rivulets spread and completely wet cone surface, occurred at about 800 rpm.

1.5.3.2.5 Liquid retention times within the column

Liquid residence time in the column was studied by running water at 22°C through the column, with no countercurrent gas flow, for 120s, then halting the flow; flow decay curves were obtained by measuring flows from the bottom of the column every 10 s. These results were converted to dimensionless coordinates using the method of Danckwerts (1953); the resulting plot indicated a high percentage of "dead water" in the system, suggesting that some of the liquid was held up in eddies and pockets while most of the flow passes through a well defined passage. The shape of the curve suggested that the "well defined flow" approximated plug flow.

1.5.3.2.6 Liquid hold-up and flood point

Casimir stated that liquid hold-up is determined for any specified operating temperature and pressure by: liquid flow; vapour flow or pressure drop; rate of rotation; and cone geometry, dimensions and spacing.

He concluded that for constant liquid flow and rate of rotation the hold-up of liquid remained constant until the flood point was reached. Hold-up decreased as rate of rotation was increased, and the pressure drop at which flooding commenced decreased as the liquid flow was increased (see fig. 1.5). Note that the variation of liquid hold-up with rotor speed was not observed by Ziolkowski *et al.* (see fig. 1.3).

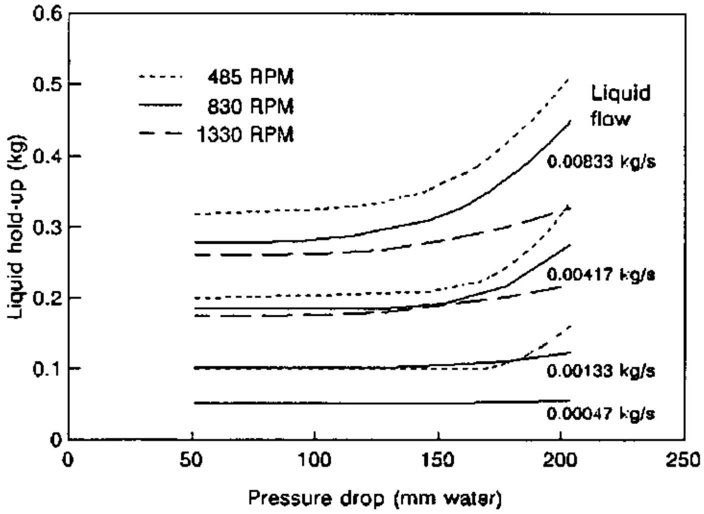

Figure 1.5
Variation of liquid hold-up with pressure drop across the column
for various liquid flows and rotor speeds (data of Casimir)

Fig. 1.6 shows the variation of liquid hold-up with air flow for various liquid flows at a rotor speed of 1480 RPM. The pattern is similar to that shown in fig. 1.5; at the lowest liquid flow hold-up is little affected by air flow but at the two higher liquid flows an air flow is reached at which hold-up begins to rise more rapidly. Casimir called this point at which liquid hold-up begins to increase at a much higher rate the flood point, although it corresponds more closely to the loading point as defined in relation to the performance of packed columns. Flooding in the SCC is the subject of Chapter 4 of this thesis.

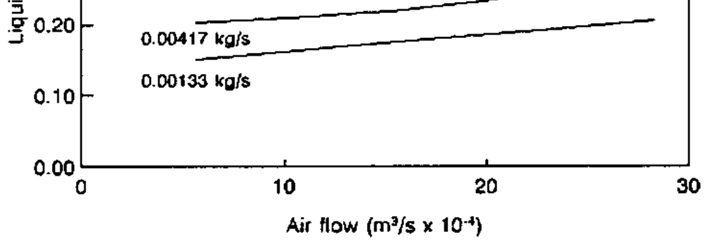

Figure 1.6
Variation of liquid hold-up with air flow

1.5.3.3 Pressure drop in the variable pressure drop column

Casimir studied pressure drop in the SCC (see fig. 1.7) and developed an empirical correlation which predicts pressure drop as function of gas flow and rotor speed; the form of the equation is

$$\Delta P = C_1 + C_2 \log Q + C_3 n^2 \log Q + C_4 n^2$$

where ΔP is the pressure drop (Pa),

Q is the air flow ($m^3/s \times 10^4$), and

n is the rotor speed ($RPM \times 10^{-2}$),

The values of the fitted constants are: C_1 = -219.7, C_2 = 560.6, C_3 = 12.8 and C_4 = -13.95.

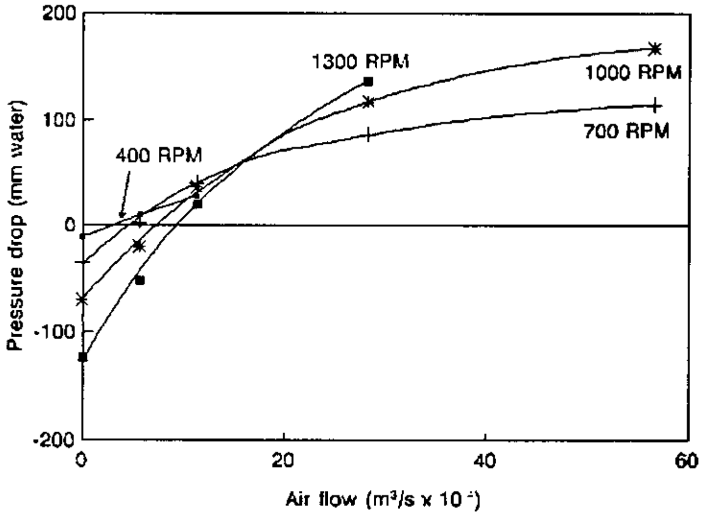

Figure 1.7
Variation of pressure drop with air flow in the absence of liquid flow for various rotor speeds (data of Casimir)

This empirical (fitted) relationship applies only for a liquid flow of 100 ml/min. and does not extend far towards the flooding region, where, as discussed earlier, increased liquid hold-up causes the pressure drop to rise much more quickly than this equation would predict. Note that pressure drop has been expressed as a function of the square of rotor speed, as well as gas flow, an instance of the SCC's fan-like behaviour, which is discussed at greater length in Chapter 3 of this thesis.

1.5.3.4 Mass transfer considerations in the variable pressure drop column

Casimir cites the work of Bakowski (1954, 1972) in proposing that the rate limiting resistance to mass transfer in the SCC is in the vapour phase and, consequently, that the rate of mass transfer between the phases is related to the differential velocity between the phases; i.e. "the velocity of the gas stream with respect to the liquid surface directly influences the mass transfer rate."

Casimir then states that the differential velocity is proportional to the difference between the path lengths of liquid and vapour particles and postulates that the mass transfer between the phases is highest when the difference between the particle path lengths is greatest. In other words, path length is proportional to, or a measure of, average velocity and therefore that difference in path length of vapour and liquid particles is a measure of average differential velocity.

Casimir conducted studies of mass transfer in the SCC in which an aqueous solution of methyl anthranilate (5×10^{-7} M) was fed to a point five cone sets above the bottom of the column at a rate of 4.17×10^{-3} kg/s. The column was run at atmospheric pressure; rotor speed was varied from 300 to 1200 RPM and the vapour flow was adjusted for each trial to hold the pressure drop across the five cone sets at 9.5 mm water.

Casimir's experimental mass transfer data are shown in figs 1.8, 1.9 and 1.10.

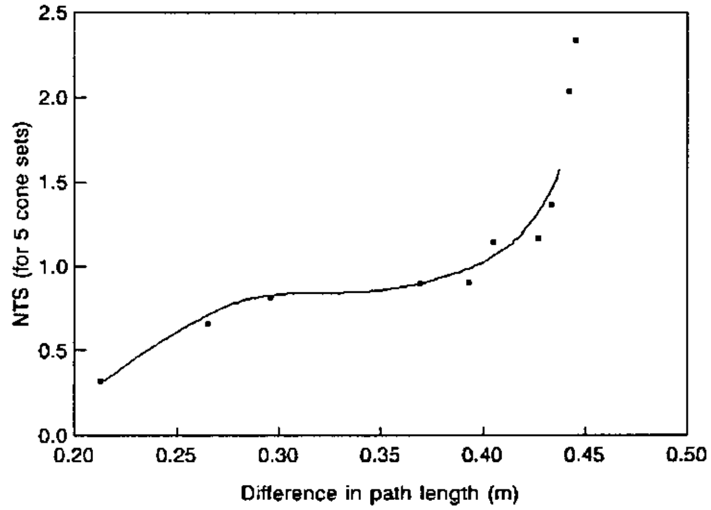

Figure 1.8
Number of theoretical stages vs calculated difference in path length of liquid and vapour particles (data of Casimir)

Fig. 1.8 shows the variation of mass transfer efficiency, *NTS*, with the calculated difference between path lengths of vapour and liquid particles. The increase in *NTS* with path length difference supports Casimir's proposition that mass transfer efficiency increases with differential velocity between the phases. The very sharp rise in *NTS* at the highest path length differences is not accounted for by this simple model; indeed, figs 1.9 and 1.10, plots of *NTS* and path length difference against rotor speed and against vapour flow respectively, suggest that the two highest observed values of *NTS* may be in error, and that a more realistic estimate of highest mass transfer efficiency would put *NTS* at about 1.3 theoretical stages for 5 cone sets, corresponding to a stage (cone set) efficiency of 26%.

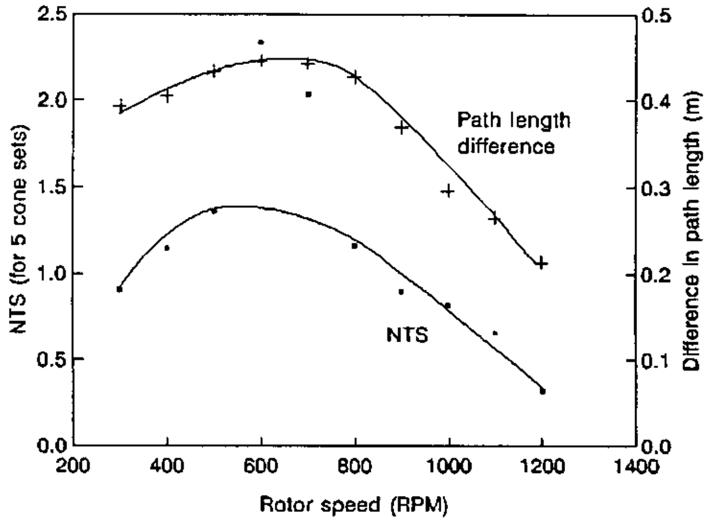

Figure 1.9
Number of theoretical stages and calculated path length difference vs rotor speed (data of Casimir)

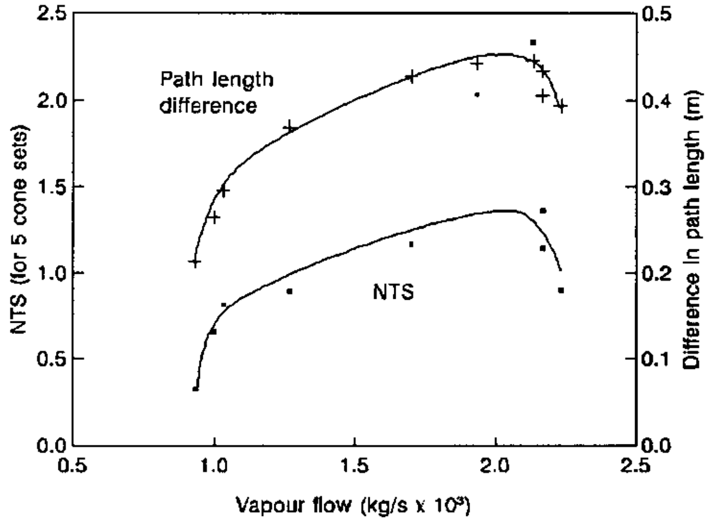

Figure 1.10
Number of theoretical stages and calculated path length difference vs vapour flow (data of Casimir)

1.5.4 Discussion

The scope of Casimir's work on the SCC was substantially greater than that of previous workers in this area; moreover, the somewhat novel application, separation of volatile components from liquid food streams, necessitated a difference in emphasis.

Whereas the bulk of earlier work on the SCC was concerned almost entirely with mass transfer performance, Casimir cited a number of characteristics, in addition to high mass transfer efficiency, which made the SCC likely to perform well in food applications: low pressure drop, low liquid hold-up and short residence time. These aspects of SCC performance were important in food applications because of the typically acute heat lability of volatile components of foods.

Casimir was the first to propose a quantitative description of the flow processes obtaining in the SCC, a necessary precursor of any theoretical or semi-theoretical treatment of the prediction of physical capacity or mass transfer efficiency. This model drew on a range of empirical and theoretical sources; it was ultimately used to support Casimir's conclusion that mass transfer efficiency is highest when the differential velocity between the phases is greatest. Casimir's model was reasonable although it could have been formulated in simpler terms without degrading its descriptive power. The relationship between flow processes and mass transfer in the SCC is the subject of Chapter 6 of this thesis.

Casimir proposes an equation for predicting pressure drop; it applies, however, only to the column on which his results were obtained and is based on a linear regression analysis of a relatively small data set. It does not extend into the region where the SCC's capacity limits are approached and in general has little to say about the underlying flow processes other than to recognize (implicitly) that pressure drop in the SCC is a function of, among other things, the square of rotor speed.

1.6 The work of Menzi

Menzi (1988, 1989) compared various aspects of the performance of a spinning cone column with those of a similarly sized bubble cap column. The dimensions of Menzi's SCC are given in table 1.2. Menzi's SCC had, like Casimir's, radial fins attached to the undersides of the spinning cones; each spinning cone had two radial fins attached to its lower (conical) surface, running the full length of this surface from the base to the lip. The depth of the fin perpendicular to the cone surface was 5 mm.

1.6.1 Liquid residence time

Menzi studied liquid residence time distribution in both the SCC and a similarly sized bubble cap column (BCC). The flow characteristics of both columns were obtained by injecting a small volume of potassium chloride into the liquid entering the column at the feed point. A conductivity cell detected the change in conductivity of the liquid leaving the column; the flow characteristics were obtained by plotting the output from the conductivity cell against time. Such characteristics for various liquid flows are shown in fig. 1.11.

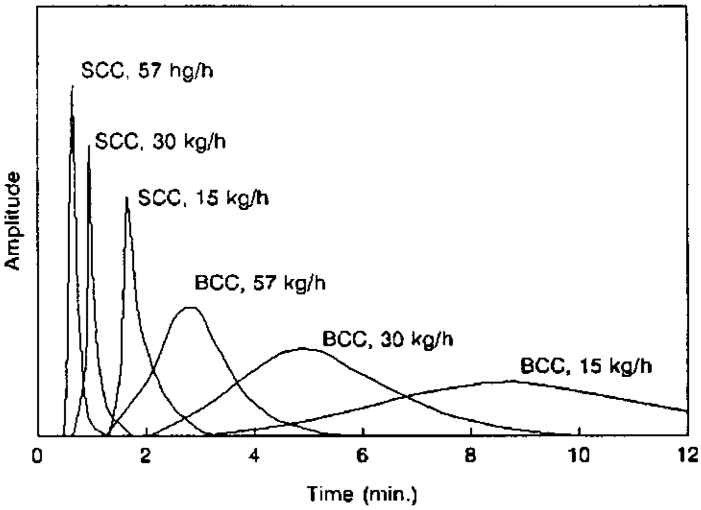

Figure 1.11
Liquid residence time distributions for SCC and BCC (data of Menzi)

Mean residence times decreased as liquid flow increased for both the SCC and the BCC. The width of the retention time distribution (RTD) increased as liquid flow decreased for both SCC and BCC. For all flows the mean residence time (MRT) in the SCC was significantly less than that obtained in the BCC, the difference increasing as flow rate decreased. These results were obtained with the SCC running at 600 rpm.

Menzi also looked at the effect of rotor speed on liquid residence time distribution in the SCC. The mean residence time decreased as shaft speed increased, falling from 2 min. at 300 rpm to 1.1 min. at 500 rpm thence to 1.0 min. at 1200 rpm; i.e., the mean residence time was nearly constant from 500 rpm upwards. The width of the RTD decreased rapidly from 300 to 350 rpm, stayed roughly constant from 350 to 800 rpm and then increased again, although in this region it was the tail of the RTD (difference between MRT and 98%-of-pulse time, the time at which the signal from the detector had decayed to 2% of its maximum value) which increased, the time between the start of the pulse and the MRT staying constant. These results were obtained with a liquid flow of 30 kg/h.

Both MRT and 98%-of-pulse times were much less for the SCC than for the BCC, although the values for the BCC decreased more rapidly as liquid flow increased. The difference between MRT and 98%-of-pulse time decreased as liquid flow increased for both SCC and BCC.

1.6.2 Liquid hold-up

For both the SCC and BCC liquid hold-up increased gently with liquid flow; the "indirect" SCC hold-up, calculated from the MRT, was about 17% of the corresponding BCC value.

Liquid hold-up in the SCC, running at a constant rotor speed of 600 RPM, increased with vapour flow in a similar manner to that observed by Ziolkowski *et al.* (1963); the difference between hold-ups for a given vapour flow increased with increase in liquid flow.

Unlike Ziolkowski *et al.* (1963), Menzi observed a strong interaction between rotor speed and liquid hold-up at rotor speeds below 500 RPM; hold-up decreased rapidly as shaft speed rose from 300 to 500 rpm then flattened out to be nearly constant from 500 to 1200 rpm (see fig. 1.12).

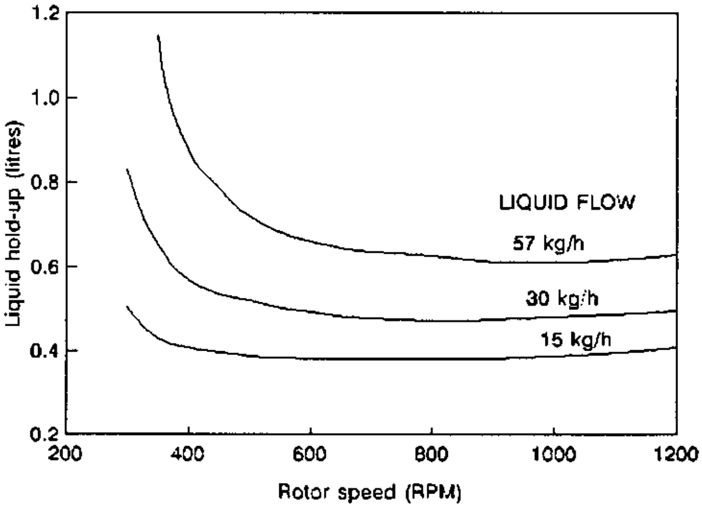

Figure 1.12
Variation of liquid hold-up with rotor speed for various liquid flows (data of Menzi)

1.6.3 Pressure drop and flooding

Fig. 1.13 shows the variation of pressure drop across the SCC with rotor speed in the absence of liquid flow. When both liquid and vapour flows are zero the pressure drop across the SCC falls from zero at zero shaft speed to -90 mm water at 1200 RPM, the shape of the curve being typical of fan characteristics. For all non-zero vapour flows tested, 2.8 m^3/h and above, the pressure drop increases with shaft speed, the rate of increase rising with gas flow. This behaviour is similar to that observed by Casimir. Fig. 1.14 is a plot of the same data as shown in fig. 1.13, but in this case showing variation of pressure drop with gas flow for various rotor speeds. The variation of pressure drop with vapour flow at zero shaft speed is as would be expected: monotonic and gently convex upwards. As shaft speed is increased the shape of the curve changes until at 1000 rpm its average slope is greater but is convex downwards.

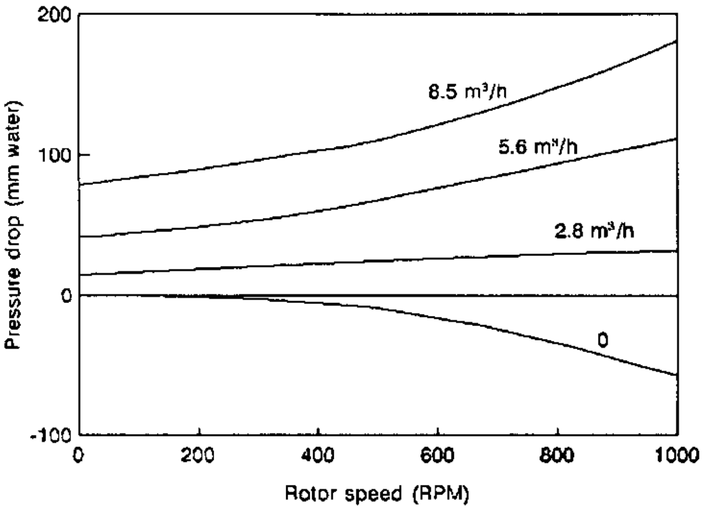

Figure 1.13
Variation of pressure drop with rotor speed in absence of liquid flow (data of Menzi)

These aspects of SCC performance are discussed at greater length in Chapter 3 of this thesis; suffice it to say at this stage that with the rotor stationary pressure drop across the column varies in a typically parabolic manner with gas flow; in the absence of gas flow pressure rise across the column increases with rotor speed, again in a parabolic manner; when we have both non-zero gas flow and rotor motion the behaviour of pressure drop is not inconsistent with the predictions of fan theory.

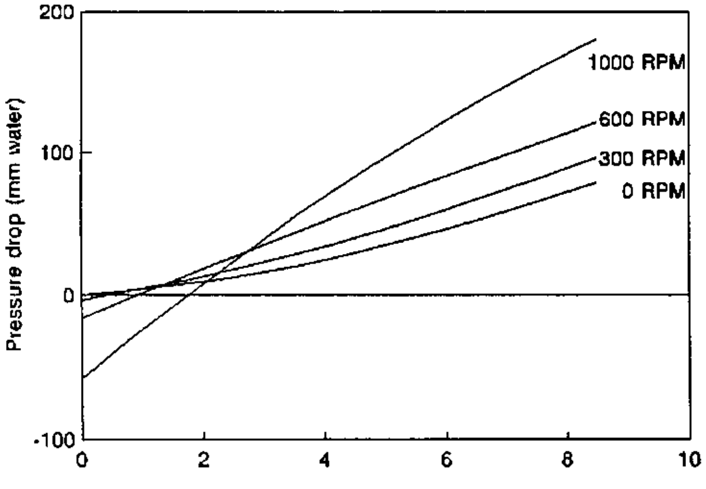

Figure 1.14
Variation of pressure drop with gas flow in absence of liquid flow (data of Menzi)

Fig. 1.15 shows the variation of pressure drop with gas flow in the presence of liquid flow at rotor speeds of 600 and 1000 RPM. In all cases pressure drop increases linearly with vapour flow, the slope of the curves increasing with liquid flow. The effect on slope of the liquid flow was less pronounced at 1000 rpm than at 600 rpm. These data bear little obvious similarity to those of Ziolkowski et al. (see fig. 1.2); there is no evidence of the region in which pressure drop is roughly constant with gas flow, nor of any transition to loading and flooding. This is most probably due to Menzi's not having measured pressure drop at substantially higher gas flows than those shown in these figures.

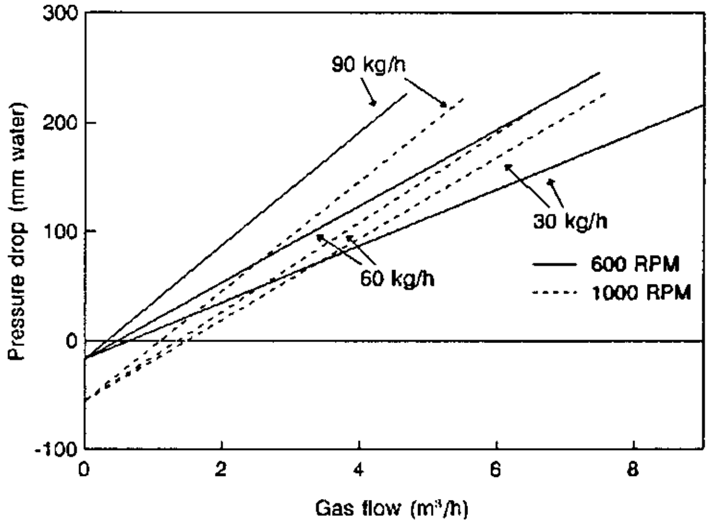

Figure 1.15
Variation of pressure drop with gas flow in presence of liquid flow (data of Menzi)

This lack of data at high gas flows seems to have led Menzi to draw a somewhat curious conclusion about flooding in the SCC. Fig. 1.16 shows the variation of pressure drop with rotor speed for various gas flows and a liquid flow of 60 kg/h. The sharp increase in pressure drop as rotor speed falls below 600 RPM is identified by Menzi as the onset of flooding in the SCC. Notice that this behaviour corresponds closely to that depicted in fig. 1.12, where liquid hold-up in the SCC rises sharply at these lower rotor speeds. That this is a form of flooding is not in question; it is not, however, gas-induced flooding but a result of the accumulation of liquid at the bases of the spinning cones brought about low centrifugal forces. The more conventional, and operationally important, form of flooding, in which stable liquid flow is prevented by interaction with a high velocity gas stream is not discussed by Menzi; indeed it appears not to have been observed at all.

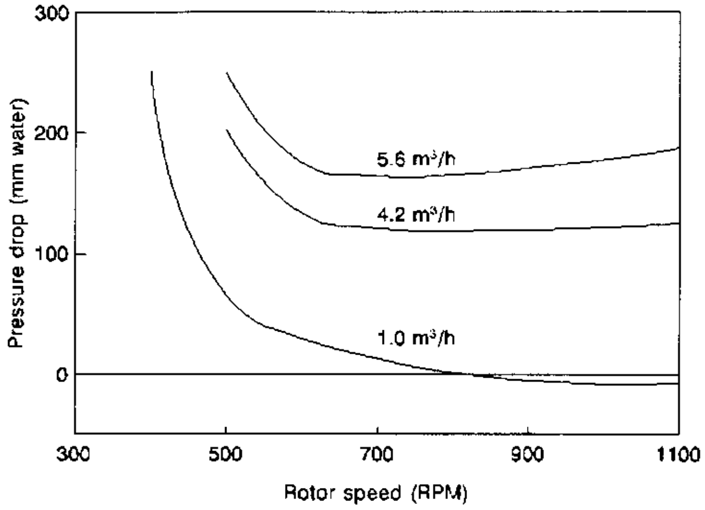

Figure 1.16
Variation of pressure drop with rotor speed in presence of liquid flow (data of Menzi)

1.6.4 Mass transfer

Menzi investigated mass transfer in the SCC by running the system under total reflux with a test solution of *n*-heptane and methyl cyclohexane. Two series of runs were conducted, one at atmospheric pressure, the other at 0.6 bar. The results are shown in table 1.3.

Table 1.3
Menzi's mass transfer data

Pressure	Throughput	F-factor (Pa^{½})	NTS	Stage efficiency (%)
Atmospheric	1.5 kg/h	1.8×10^{-3}	34.2	114
Atmospheric	0.5 kg/h	0.6×10^{-3}	37.8	126
Atmospheric	0.1 kg/h	0.1×10^{-3}	47.2	157
0.6 bar	1.0 kg/h	1.6×10^{-3}	32.9	109
0.6 bar	0.4 kg/h	0.6×10^{-3}	33.8	113

The F-factor (i.e. $\rho^{½}U$ where ρ is gas density, and U is average gas velocity) used by Menzi was based on the cross-sectional area of the column shell rather than any of the actual flow areas within the cone set. The reason for using this definition of F-factor was to allow comparison of these mass transfer data with those of a packed column having similar overall dimensions. Menzi quotes mass transfer performance for SULZER packing

BX as 8 to 4 theoretical stages per metre for F-factors between 0.5 and 5 $Pa^{1/2}$, whereas the F-factors in table 1.2 are about 3 orders of magnitude lower.

The stage efficiencies obtained by Menzi are the highest of any quoted in the literature reviewed here. It should be noted that these results were obtained at very low throughputs; recall that the data of Ziolkowski *et al.* (fig. 1.4) showed that at very low throughputs mass transfer efficiency is relatively high, and increases as throughput is reduced; Menzi's data show a similar tendency.

1.6.5 Discussion

Menzi presented data on liquid residence time distributions which showed the pronounced difference between the SCC and a similarly sized bubble-cap column in this aspect of their performance. These data confirm Casimir's findings with respect to residence time and support his view that the SCC offers significant advantages in this regard in the processing of heat-labile materials.

Menzi's work on throughputs and physical capacity was limited in scope; it was for the most part consistent with earlier work but was not used to support any general conclusions.

Menzi reported higher mass transfer efficiencies than any of the previous workers (stage efficiencies between 110 and 160%); these very high values may be a consequence of their having been obtained at very low throughputs.

1.7 Summary

The key results of the work reviewed in this chapter concerning mass transfer performance and physical capacity limits are set out in table 1.4. The estimated F-factors are obtained from the gas flows at the capacity limits given in the same table.

Table 1.4
Summary of results from work reviewed in Chapter 1

	Stage efficiency	Physical capacity	Estimated F-factor (Pa$^{1/2}$)
Pegram, Urey and Huffman:			
SCC 1 (15 stages)	27 - 92%	72 ml/min	2.3
SCC 2 (87 stages)	85%	120 to 140 ml/min	3.8 - 4.4
SCC 3 (610 stages)	32%	92 ml/min @ atm. pressure 33 ml/min @ 0.2 bar 45 ml/min @ 0.27 bar	2.9 2.2 2.6
Mair and Willingham:			
Baskets	56 - 70%		
Discs	54%		
Cones	54 - 82%		
Ziolkowski *et al.*	44 - 52% @ 1 l/h 26 - 40% @ 15 l/h	14 - 16 l/h (benzene/CCl_4)	2.9 - 3.3
Casimir	6 - 46%	20 × 10^{-4} m^3/s of air with 0.0833 kg/s of water flow	2.3
Menzi	109 - 157%		

The material reviewed in this chapter may be summarized as follows:

(a) Mass transfer
The bulk of the reported stage efficiencies were between 30 and 80%; mass transfer efficiency was found to be highly dependent on material throughputs and, to a lesser extent, on rotor speed.

(b) Physical capacity
The limited data on capacity limits suggest that these limits are approached when the F-factor of the gas flow is in the range of 2 to 4 Pa$^{1/2}$. The influence of liquid flow on capacity limits was largely ignored; only Casimir presented data which suggest a relationship between liquid flow and capacity limits (fig. 1.6).

(c) Operating characteristics

Pressure drop in the SCC was shown to be lower than in comparable packed columns; it was found to be influenced by rotor speed (fan-like behaviour) as well as material flows and internal layout and dimensions.

Liquid hold-up and residence time in the SCC were demonstrated to be substantially lower than in a similarly-sized bubble-cap column. Liquid hold-up was found to be influenced by rotor speed, falling as rotor speed rises.

1.8 The aims of this thesis

A significant shortfall in the knowledge of the SCC, constituted by the various contributions reviewed in this chapter, was a lack of generalized data which could be used for design; in particular there was no correlation of physical capacity limits with material flows and operating and configurational parameters, like the Souders-Brown correlation for plate columns or the Sherwood-Leva-Eckert correlation for packed columns, both discussed in Chapter 2 of this thesis; nor was any general quantitative description of mass transfer in the SCC proposed.

The purpose of this thesis is to address this deficiency by developing generalized descriptions of SCC operation which could form the basis of a systematic design procedure.

We start, in Chapter 2, by considering conventional distillation columns and the available numerical representations of their operation, particularly with regard to their physical capacity and limits of operation; we seek to devise models of SCC operation analogous to those established for conventional distillation columns.

In Chapters 3 and 4 flow processes in and capacity limits of the SCC are considered in detail; generalized correlations are proposed.

In Chapter 5 we consider the nature of liquid flow in the column, in particular the theoretical models available for description of it, and their applicability to the SCC in the light of experimental data.

In Chapter 6 aspects of the SCC's mass transfer performance are discussed; experimental data are compared with predictions based on standard representations of mass transfer processes; divergences between predictions and experimental results are discussed, particularly with regard to what they tell us about the actual flow and mass transfer processes obtaining in the SCC.

CHAPTER 2

PHYSICAL CAPACITY AND LIMITS OF OPERATION OF CONVENTIONAL DISTILLATION COLUMNS

2.1 Introduction

Essential for the design of any kind of distillation column is a method for estimating the column's limits of operation. The nature and the magnitude of these limits vary with the type of column in question. In this chapter the two most important classes of conventional distillation column, plate columns and packed columns, will be briefly described, with particular reference to their limits of operation and the available methods for predicting those limits. This chapter will serve as a basis for the discussion of the limits of operation of the spinning cone column in chapters 3 and 4. (Except where otherwise indicated, the material presented in sections 2.2 and 2.3 of this chapter is based on more detailed treatments of these topics by Treybal (1981), Coulson *et al.* (1978), and Fair *et al.* (1973))

Both plate columns and packed columns have been employed for gas-liquid contacting applications in food processing, although the latter are the more common.

Plate columns have been used for the removal of sulphur dioxide from fruit juices. Sulphur dioxide is used as a preservative, allowing extended storage without refrigeration; it must be removed prior to packaging and sale of the juice. The spinning cone column has begun to supplant the more traditional bubble cap columns for this application.

Packed columns are the most commonly used type of distillation column in food processing. A typical application is in the concentration of fruit juices by evaporation. In this operation the vapour which is removed from the juice carries the bulk of the flavour/aroma volatiles with it. This vapour stream is sometimes fed to a packed column in which it is rectified; the overhead product is a concentrated flavour/aroma fraction which can be added back to the fruit juice when it is re-constituted prior to sale to the consumer.

2.2 Plate columns

Plate columns are vertical vessels, normally cylindrical, in which liquid and gas are brought into contact in a stagewise manner on trays or plates (see fig. 2.1). The most common type of plate column uses cross-flow plates in which liquid enters the column at the top and flows downwards under gravity, during its passage flowing across each tray and through a downcomer to the tray below. The gas passes upward through openings in the tray, then bubbles through the liquid to form a froth, disengages from the froth, and flows upward to the next tray. In an overall sense the process constitutes a multiple countercurrent contact of gas and liquid, although the flow pattern on each tray is cross-flow, gas moving vertically and liquid horizontally.

2.2.1 Design of plate columns

The number of theoretical stages required to effect a particular separation, and the corresponding rates for the liquid and vapour phases, are determined from material balances and equilibrium considerations. To produce an actual design based on these quantities entails the choice of column dimensions and arrangements which will represent the best compromise between between several opposing tendencies; in general, conditions leading to high mass transfer efficiencies will ultimately lead to operational difficulties.

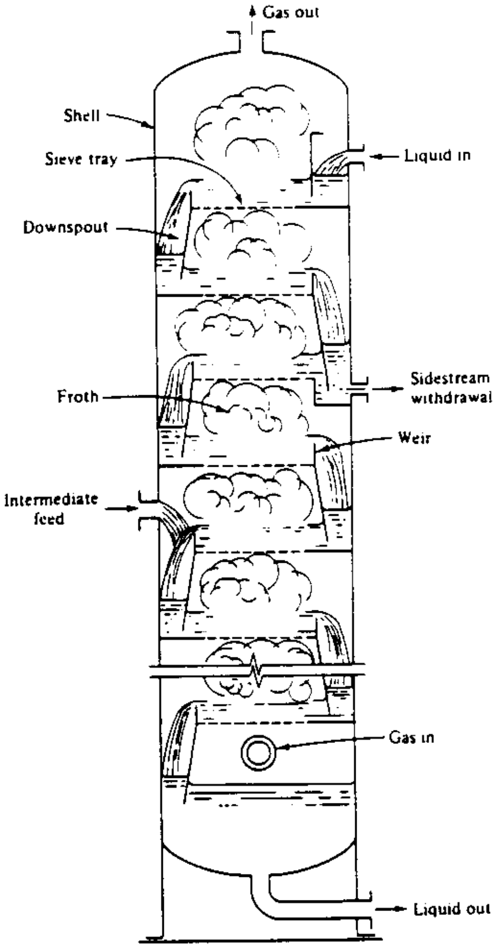

Figure 2.1
Schematic diagram of a plate column (after Treybal (1981))

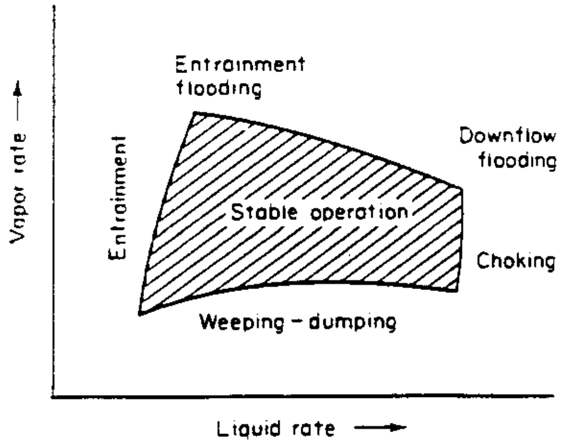

Figure 2.2
Stable operating regions for plate columns (after Fair et al. (1984))

A high degree of mass transfer is achieved on an individual plate by:

(a) long contact time between the phases,
(b) a large interfacial area between the phases, and
(c) a high degree of turbulence in the gas-liquid mixture on the plate.

A long contact time requires that the liquid body on each tray should be deep, so maximizing the path length of the gas bubble as it rises through the liquid. Large interfacial area and turbulence are achieved by high gas velocities; firstly, they promote the formation of smaller bubbles, which have a higher interfacial area per unit volume, and secondly, they provide greater agitation of the liquid and dispersion of the gas into the liquid. High plate efficiencies, therefore, require deep pools of liquid and relatively high gas velocities.

In creating these conditions, however, a number of operational problems are likely to be encountered. At high gas velocities, as the gas disengages from the froth, small droplets of liquid will be carried by the gas to the plate above. This phenomenon is called *entrainment*. The resultant back-mixing of the liquid stream reduces the concentration change brought about by the mass transfer and, thereby, the plate efficiency. Gas velocity may, therefore, be limited by the reduction in plate efficiency due to liquid entrainment.

In addition, high liquid levels on the plate and high gas velocities result in high pressure drop in the gas phase as it flows through the plate. In the case of distillation, high pressure at the bottom of the column results in high boiling temperatures, which in turn may lead to heating difficulties and damage to heat-sensitive compounds; this characteristic militates against the use of plate columns in food applications where the volatile components are typically strongly prone to heat damage. Also, high pressure drop translates to high operating cost, whether it be in fan power consumption (in absorbers and humidifiers) or heat input to the reboiler (in distillation columns).

As pressure drop continues to rise a point is reached where the pressure drop across the plate equals the liquid head in the downcomer. If the pressure difference is further increased by increasing the flow rate of either gas or liquid, the liquid level in the downcomer will rise further to permit the liquid to enter the lower plate, ultimately reaching that on the tray above. Further increase in either flow rate then aggravates the condition rapidly, and the liquid will fill the entire space between the plates. This condition is termed *downflow flooding;* the plate efficiency falls to a low value, the flow of gas becomes erratic, and liquid may be forced out of the exit pipe at the top of the column.

There are also limitations on the operation of plate columns associated with low material flows. If liquid rates are too low, the gas rising through the openings of the plate may push the liquid away (*coning*) and pass through as a continuous stream, with a consequent loss in contacting efficiency. If the gas rate is too low, much of the liquid may drain down through the openings of the plate (*weeping*), thus failing to obtain the benefit of complete flow over the plates; The extreme manifestation of this phenomenon, in which none of the liquid reaches the downspouts, is termed *dumping*.

A qualitative representation of the relations between these conditions is shown in fig. 2.2; all types of plate are are subject to these difficulties in some form.

2.2.2 Types of plate

Plates can be classified according to the flow pattern obtaining thereon and by the means by which the gas is dispersed in the liquid.

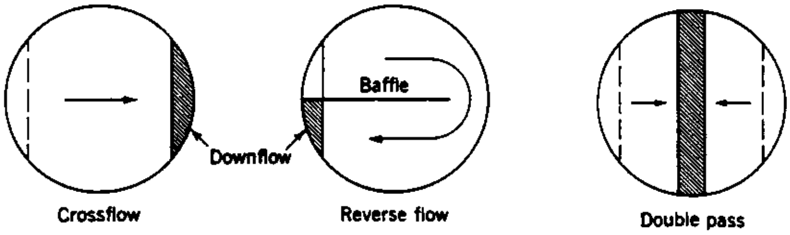

Figure 2.3
Flow patterns on cross-flow plates (after Fair et al. (1984))

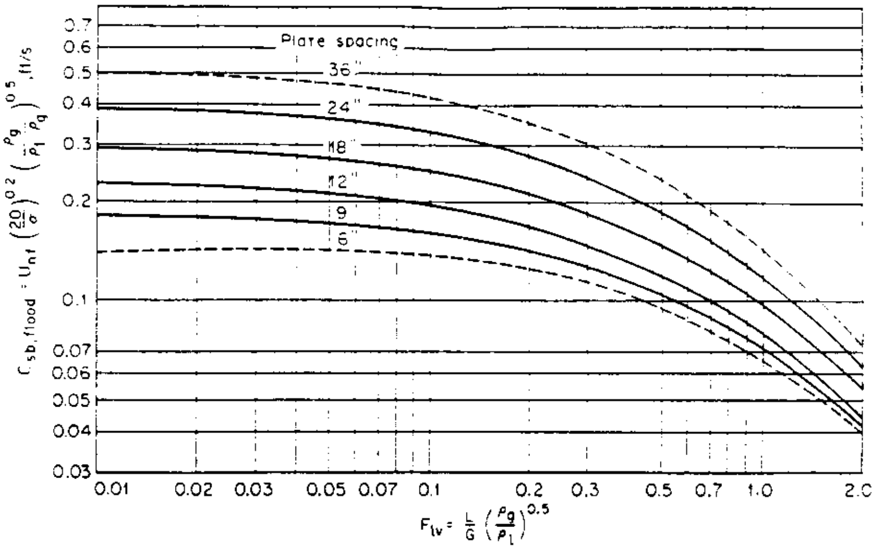

Figure 2.4
Entrainment flooding limits for bubble-cap and perforated plates (after Fair et al. (1984))

The flow pattern of the two phases brought into contact on a plate may be cross-flow or counterflow. Cross-flow plates are the more common. The cross-flow plate uses at least one downcomer to control the liquid flow pattern across the plate. Optimum design of the plate requires a balance between liquid flow accommodation and effective use of cross section for gas flow. This category can be further divided into three variants: simple cross-flow, reverse flow and double-pass. These are represented diagrammatically in fig. 2.3.

The reverse flow plate offers a long liquid path at the cost of reduced downcomer area, and is thereby suitable for low liquid-vapour ratios. On the double-pass plate the liquid flow is split, and offers large downcomer area but with a short liquid path; it is suitable for high liquid-vapour ratios.

In counterflow, or downcomerless, plates the liquid and vapour use the same openings for flow; gas and liquid flow in a pulsating fashion with a particular opening passing both liquid and gas intermittently. The hydrodynamic behaviour of counterflow plate columns bears similarities to that obtaining in packed columns; counterflow plates are more properly considered a type of structured packing (see section 2.3.3.2).

The various forms of gas disperser on cross-flow plates range from bubble caps and valves to simple round orifices.

2.2.3 Capacity and flooding in plate columns

The following discussion pertains to the design of sieve tray columns; the procedure used for bubble-cap columns is essentially the same, but as these have been superseded by sieve-plate configurations they will not be dealt with in detail.

2.2.3.1 Entrainment flooding

The vapour flow which will induce entrainment flooding in a plate column can be found by reference to a generalized correlation of flooding on sieve trays; Coulson *et al.* (1978), Fair *et al.* (1973) and Treybal (1981) all recommend use of Fair's modification of the Souders-Brown relationship, which is an empirically-based correlation between a capacity parameter, $C_{sb,\,flood}$, and a flow parameter, F_{lv}, defined as follows:

$$C_{sb,flood} = U_{nf} \left[\frac{20}{\sigma} \right]^{0.2} \sqrt{\frac{\rho_g}{\rho_l - \rho_g}} \quad . \tag{2.1}$$

$$F_{lv} = \frac{L}{G} \sqrt{\frac{\rho_g}{\rho_l}} \tag{2.2}$$

where U_{nf} is the linear gas velocity at flooding based on net flow area (the total cross-sectional area of the column minus the area taken up by one downcomer), ρ_L and ρ_G are the liquid and gas densities, and σ is the liquid surface tension. The relationship between $C_{sb,\,flood}$ and F_{lv} is represented graphically in fig. 2.4.

The Souders-Brown relationship is based on a force balance on a (notionally) average suspended droplet of liquid; it can be used to predict gas velocities at flooding to within ±10% (Fair *et al.*, 1973).

2.2.3.2 Downflow flooding

Plate columns may flood because of excessive liquid flow which causes the level of liquid in the downcomer to rise to the plate above. The height of liquid in the downcomer can be calculated from a pressure balance involving the total pressure drop across the plate, the height of the weir at the plate outlet, the height of the crest over the weir, the head loss due to the liquid flow under the downcomer apron, and the liquid gradient across the plate.

2.2.4 Plate columns: summary of key characteristics

The key characteristics of plate columns, in the context of the present discussion, can be summarized as follows:

(a) In distillation operations overall plate efficiency, E_0 (the ratio of theoretical to physical plates), typically varies between 0.9 for $\alpha_{av}\mu_L = 10^{-4}$ and 0.3 for $\alpha_{av}\mu_L = 6 \times 10^{-4}$, where α_{av} is the relative volatility at the average column temperature and μ_L is the liquid viscosity (O'Connell, 1946). Given that food systems would generally have a viscosity greater than that of water at the same temperature and that volatile food components would often have relative volatilities well in excess of 10, we should expect plate efficiencies for these applications to be towards the lower end of the range quoted.

Plate spacings in columns of up to 1 metre in diameter (encompassing the range of sizes normally encounterd in food applications) vary between 0.15 and 0.5 m. The corresponding HETP values (for $E_0 = 0.3$) are therefore between 0.5 and 1.7 m.

(b) Liquid loads are typically no more than 0.015 m^3/s per metre column diameter.

(c) Physical capacity of plate columns can be correlated by a curve of type shown in fig. 2.4; if entrainment is the factor determining capacity limits, eqs 2.1 and 2.2 appropriately measure vapour load and ratio of liquid to vapour loads respectively.

(d) Pressure drop per plate is typically up to 40 mm water at an operating pressure of 5 kPa (abs.) and between 50 and 80 mm water at atmospheric pressure. If the pressure at the top of the column is required to be 5 kPa, a column having 10 actual plates will have only 3 theoretical plates (assuming $E_0 = 0.3$); moreover the total pressure drop will be 400 mm water requiring the pressure at the bottom of the column to be roughly 4 kPa higher, corresponding to a temperature difference of more than 10°C in a water-based system.

2.3 Packed columns

Packed columns have been used in the chemical and process industries since before the turn of the century, although in the first half of this century the designs tended to be crude, and the applications limited to corrosive systems or to columns of relatively small diameter, such as pilot plant installations where flexibility was an important requirement (Fair and Bravo, 1990).

2.3.1 General description of packed columns

Packed columns are vertical columns which have been filled with either randomly oriented packing material (random packings) or carefully positioned devices of large surface area (structured packings). Liquid is distributed over, and trickles down through, the packed bed, exposing a large surface to contact the gas. Flow of the phases can be either counter- or co-current although counter-current flow is more usual.

A typical packed column consists of a cylindrical shell containing a support plate for the packing material and a liquid-distributing device designed to provide effective irrigation of the packing. Devices may be added to the packed bed to provide redistribution of liquid that might channel down the wall. A schematic diagram of a packed column is shown in fig. 2.5.

2.3.2 Comparison of packed columns with plate columns

Factors favouring the use of packed column rather than plate columns include the following:

(a) Packed columns can be designed to give substantially lower gas-phase pressure drop than that obtained in plate columns, so favouring their use in critical vacuum distillations.
(b) Hold-up of liquid is lower in packed columns than in plate columns, making them more suitable for use with thermally sensitive materials.
(c) Modern packed columns may have a lower capital cost than equivalent plate columns, particularly for units of less than 300 mm diameter.
(d) Since the degree of agitation of the liquid phase is lower in packed columns they are more suitable for handling liquids which tend to foam.
(e) Use of packings made of ceramics, carbon or other resistant materials allows acids and other corrosive streams to be handled more easily than in plate columns.

Of these factors, the first three have the most bearing on food applications, particularly (a) and (b) because of the heat sensitivity of food volatiles.

2.3.3 Types of packing

The packing material used in a packed column is required to offer the following main characteristics:

(a) It should provide a large interfacial area between the liquid and gas.
(b) It should possess desirable fluid flow characteristics. In general this means that the fractional void volume ϵ in the packed bed should be large.

Packings are of two major types, random and structured.

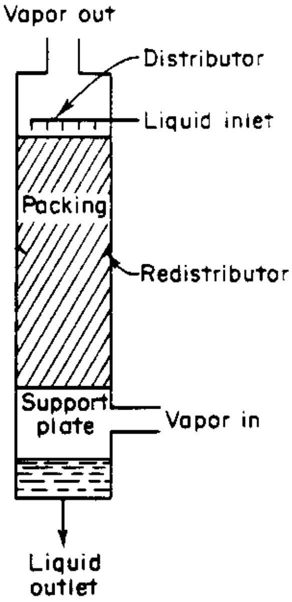

Figure 2.5
Schematic diagram of packed column (after Fair et al. (1984))

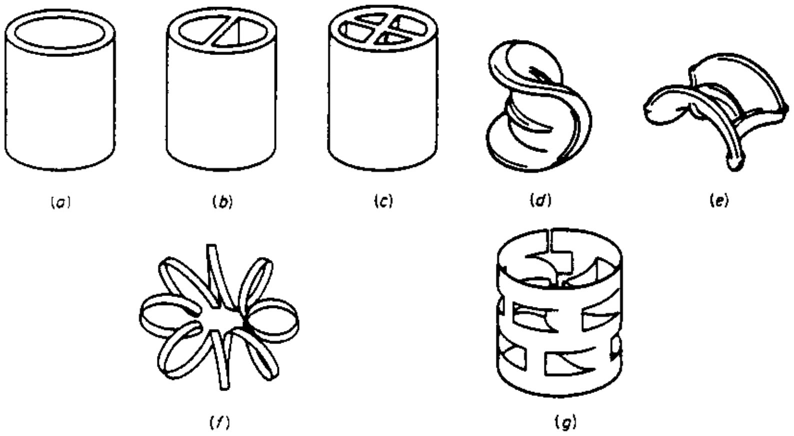

Figure 2.6
Common types of random packing element: (a) Raschig rings, (b) Lessing ring, (c) partition ring, (d) Berl saddle, (e) Intalox saddle, (f) Tellerette, and (g) Pall ring (after Treybal (1981))

2.3.3.1 Random packings

The simplest and oldest of the manufactured random packings are Raschig rings. These are hollow cylinders having diameters ranging from 6 to 100 mm or more. They may be made of chemical stoneware or porcelain, carbon, metals or plastics. Lessing rings and others with internal partitions are less frequently used.

Another important category of manufactured random packing is the saddle-shaped packings, such as Berl, Intalox and Super Intalox saddles. These are available in sizes from 6 to 75 mm, made of chemical stoneware or plastic.

The development, in the 1940s, of "flow-through" packings, such as Pall rings, enabled packed columns to compete more directly with cross-flow plate columns for use in large commercial distillation applications. Flow-through packings eliminated much of the form drag associated with traditional dumped packings, allowing low pressure drop without loss of efficiency or capacity. Variants of this type of packing include Flexirings, Cascade rings, and Hy-Pak; they are available in metal and plastic. Because of their high performance characteristics and low pressure drop, these packings now account for a large share of the market.

Generally the smaller sized random packings offer larger specific surface (and larger gas pressure drop), but the larger sized elements cost less per unit volume. Typically, packing sizes of 25 mm or larger are used for gas rates of 0.25 m^3/s, 50 mm or larger for gas rates of 1 m^3/s. The voidage obtainable with these packings varies from about 0.45 to 0.95. Common types of random packing element are shown in fig. 2.6.

2.3.3.2 Structured packings

There are numerous types of structured packing. The counterflow trays already considered in section 2.2 are a form of structured packing, as are the arrangements of fig. 2.7. Structured packings offer the advantages of low pressure drop for the gas and greater possible fluid flow rates, usually at the expense of higher capital and/or installation costs than random packings.

The development of modern structured packings arose from the extension of the flow-through concept which produced random packings such as the Pall ring; the first structured packing employing modern geometry was developed by Sulzer Brothers in Switzerland. It was first made in metal gauze but later from metal sheet. There are several designs, known under proprietary names such as Intalox, Gempak, Flexipac, Mellapak, Sulzer and Montz. In general they consist of layers of vertically-oriented corrugated metal sheet, the corrugations typically at 45° to the vertical. Fluid flowing through such packings tends to be repeatedly split into left- and righthand streams, each stream breaking into increasingly smaller streams. The sheets may also be perforated to promote inter-phase contact and reduce resistance to gas flow.

The adoption of these modern structured packings was initially slow due to their relatively high cost. As their superior performance characteristics (high efficiency, high capacity and low pressure drop) came to be recognized, more applications followed. It is now generally accepted that for many vacuum and moderate-pressure distillations, structured packings compete well with cross-flow plates and other types of packing on the basis of cost. Indeed, many existing vacuum columns in the chemical and process industries have been converted from valve or sieve plates to structured packings (Humphrey and Seibert, 1992).

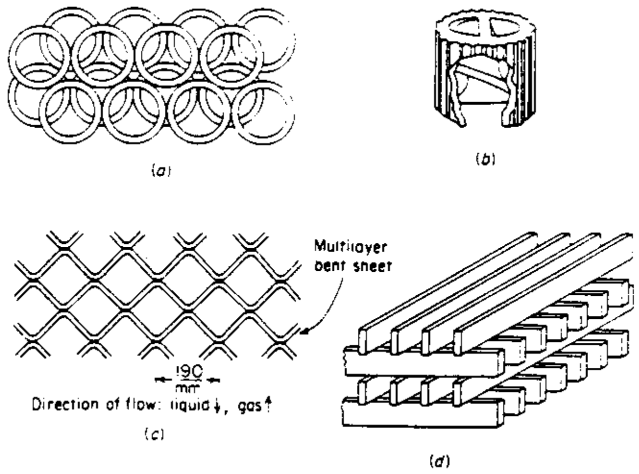

Figure 2.7
Some types of structured packing: (a) stacked, staggered Raschig rings (plan view), (b) double spiral ring, (c) section through expanded-metal grid packing, (d) wood grid (after Treybal (1981))

2.3.4 Hydrodynamics of packed columns

The material in this section, on the hydrodynamics of packed columns, is presented because we shall be using an understanding of packed column behaviour, particularly numerical capacity correlations, in characterizing the SCC.

2.3.4.1 A qualitative description of fluid flow in packed columns

The pressure drop experienced by a gas stream flowing upward through a packing, in the presence of a downward liquid flow, is represented graphically in fig. 2.8. At very low liquid rates, the effective open cross section of the packing is only marginally reduced from that of dry packing, and pressure drop is due to flow through a series of randomly sized and located openings in the bed. The pressure drop is therefore roughly proportional to the square of the gas velocity, as indicated in the region AB, implying that flow is turbulent for most practical gas velocities.

At higher liquid rates the presence of liquid significantly decreases the effective cross section, and a portion of the energy of the gas stream is used to support an increasing quantity of liquid in the column (region A'B').

For all liquid rates, a gas flow is reached above which pressure drop rises very much more quickly, proportional to a gas-flow rate power distinctly higher than 2; this range of gas velocities is called the *loading zone.* In this range the liquid flow is interfering with the gas flow and the hold-up of liquid is progressively increasing. The increased resistance to gas flow, and the corresponding accelerated increase in pressure drop with gas flow, is due to depletion of the free packing-void volume by the rapid accumulation of liquid. At increased liquid rates the loading point is reached at a lower gas velocity but at a similar (marginally higher) pressure drop.

As the gas rate is increased to C, at a fixed liquid rate, one of a number of changes occurs: (1) a layer of liquid, through which the gas bubbles, may form at the top of the packing; (2) liquid may fill the tower, starting at the bottom or at any intermediate restriction such as packing support, so that there is a change from gas-continuous liquid-dispersed to liquid-continuous gas-dispersed (inversion); or (3) slugs of foam may rise rapidly upward through the packing. At the same time, entrainment of liquid by the effluent gas increases rapidly, and the tower is *flooded.* The gas pressure drop then increases very rapidly. The change in conditions in the region B to C of fig. 2.8 is gradual, and initial loading and flooding are frequently determined by the change in slope of the pressure-drop curves rather than through any visible effect.

Whilst it is desirable to operate a packed column with a reasonable liquid hold-up, since this promotes good interphase contact, it is not normally possible to maintain stable, satisfactory operation under flooding conditions, and columns are best operated in the loading region (BCC'B'). Since the transition from loading to flooding occurs over a narrow range of gas flow, the safe practice is to design for operation at or just below the loading point.

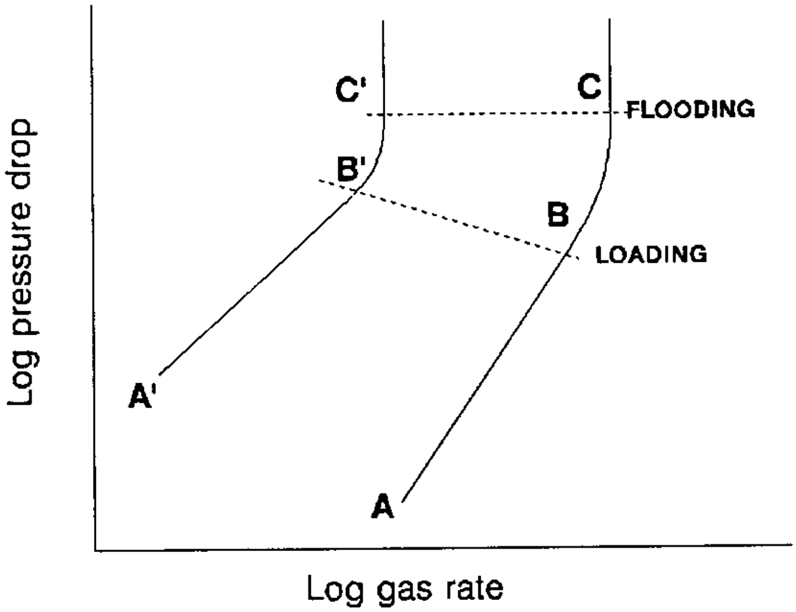

Figure 2.8
Pressure drop characteristics of packed columns

2.3.4.2 Prediction of flooding in packed columns

The first generalized correlation of packed-column flood points was developed by Sherwood, Shipley and Holloway (1938). It was derived from laboratory experiments primarily on the air-water system. The relationship can be expressed as

$$\frac{U_t^2 a_p}{g\epsilon^3}\frac{\rho_g}{\rho_l}\mu_l^{0.2} = f\left[\frac{L}{G}\sqrt{\frac{\rho_g}{\rho_l}}\right]$$

where U_t is the superficial gas velocity
a_p is the total (specific) area of packing
ϵ is the fractional voids in the dry packing
g is the gravitational acceleration
ρ_g is the gas density
ρ_l is the liquid density
L is the liquid-mass rate
G is the gas-mass rate
μ_l is the liquid viscosity

and is shown graphically in fig. 2.9. Leva (1954) and Eckert (1970) modified and extended the Sherwood correlation on the basis of studies on air and liquids other than water. Eckert's modification is shown in fig. 2.10. In this form of the correlation the ordinate group in fig. 2.10, the capacity parameter, includes ψ, the ratio of the density of water to the density of the liquid; also, the ratio a_p/ϵ^3, characteristic of a particular packing material, has been replaced by the *packing factor* F_p, also characteristic of a given packing but obtained experimentally rather than of calculated from packing geometry.

It has become conventional practice to retain the correlating parameters of fig. 2.10 and vary the values of the packing factor as more experimental data become available. Although in recent years the Sherwood-Leva-Eckert (SLE) correlation has been criticized on various grounds (Bolles and Fair, 1979, McNulty and Hsieh, 1982), and its limitations have been subject to considerable attention, it has not fallen into disuse. On the contrary, it continues to be used widely as the basis for correlations of flooding, loading and pressure drop in packed columns (Kister and Gill, 1991a, 1991b; York et al., 1992).

The objections raised to the SLE correlation and its variants tend to stress the empirical nature of the packing factor, and also that operating conditions influence the performance of the packing in ways which are not allowed for in the basic model. More elaborate correlations have been proposed, particularly for application to structured packings (Bravo et al., 1986; Stichlmair et al., 1989) but all rely heavily on empirical data and could legitimately be considered to be extensions and/or refinements of the basic pressure drop model, of which the Sherwood correlation is an early, simple form.

Fair *et al.* (1973) recommend that in general the design throughput for a packed column should allow for a ±30% error in the predicted flood point.

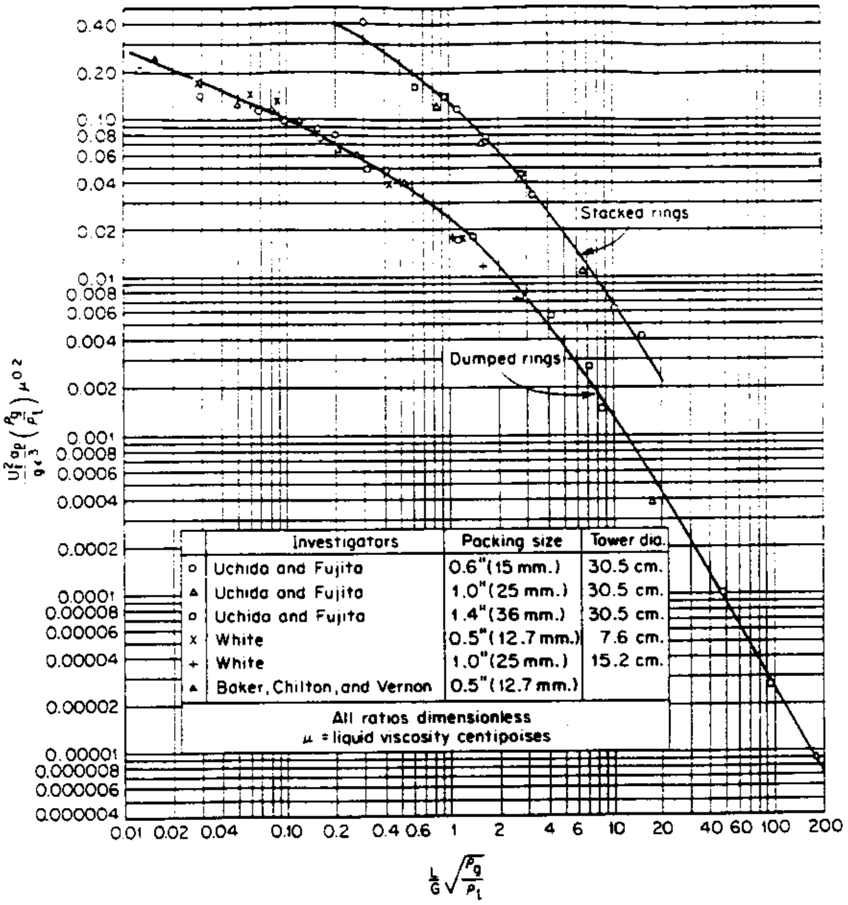

Figure 2.9
Flooding correlation of Sherwood, Shipley and Holloway (after Fair *et al.* (1984))

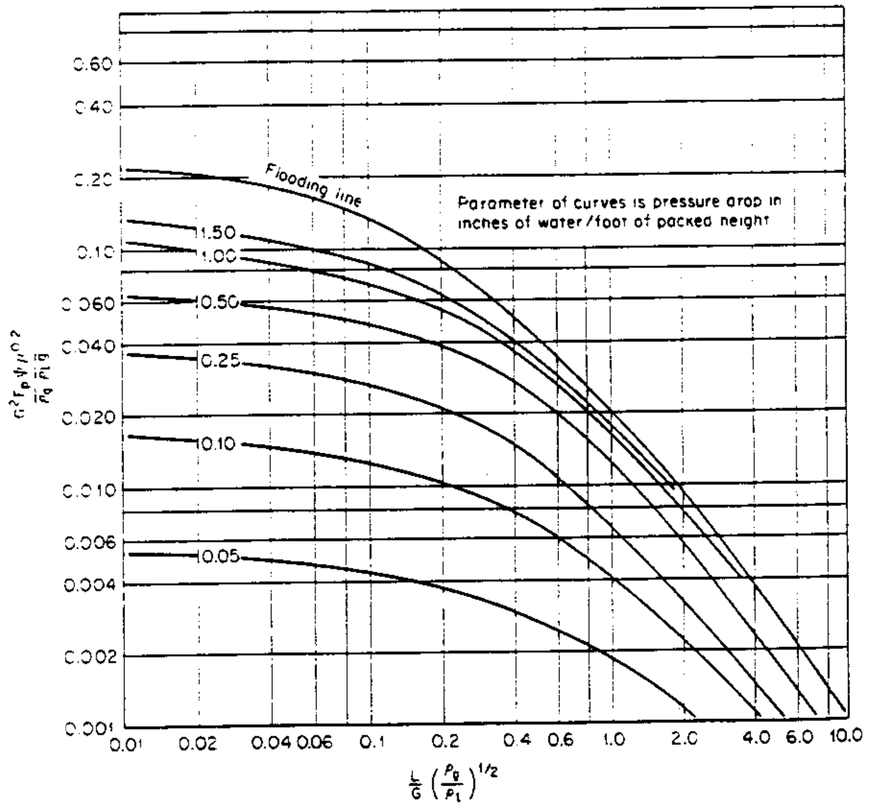

Figure 2.10
Generalized flooding and pressure drop correlation for packings (after Fair *et al.* (1984))

2.3.4.3 The origin and form of the Sherwood capacity parameter: the Carman-Kozeny equations

Since the flooding and loading behaviour of the spinning cone column will be described in analogous terms to those conventionally used to correlate flooding in packed columns, the basis for the parameters used in the Sherwood correlation and its variants is examined in this section.

The capacity parameter used in the Sherwood correlation arises from consideration of pressure drop in packed beds.

The pressure drop experienced by a fluid flowing in a conduit of constant cross section can be expressed as

$$\frac{\Delta P}{L} = f \frac{1}{4r_h} \frac{1}{2} \rho u_0^2 \tag{2.3}$$

where ΔP is the pressure drop,
f is the Fanning friction factor,
L is the length of the conduit,
r_h is the hydraulic radius of the conduit,
ρ is the density of the fluid, and
u_0 is the average velocity of the fluid.

The friction factor is in general a function of Reynolds number; it is defined as

$$f = \frac{\tau_0}{\frac{1}{2}\rho u_0^2}$$

where τ_0 is the wall shear stress.

In the laminar flow region, the wall shear stress τ_0 is proportional to the average velocity u_0. When the flow is fully turbulent, τ_0 is roughly proportional to u_0^2 . That is

$$\frac{\Delta P}{L} \propto \frac{1}{r_h} \frac{1}{2} \rho u_0^2 \, \mathrm{Re}^{n-2} \tag{2.4}$$

where the Reynolds number Re is defined as

$$\mathrm{Re} = \frac{4r_h u_0 \rho}{\mu} \tag{2.5}$$

and n is called the state-of-flow factor. For laminar flow $n = 1$, whereas as the flow becomes fully turbulent, $n \rightarrow 2$. Substituting for Re in the expression (2.4) above gives, for laminar flow

$$\frac{\Delta P}{L} \propto \frac{\mu u_0}{8 r_h^2} \tag{2.6}$$

and for turbulent flow

$$\frac{\Delta P}{L} \propto \frac{1}{r_h} \frac{1}{2} \rho u_0^2 \tag{2.7}$$

If the free space in in a packed bed is assumed to consist of a series of tortuous channels equation (2.7) can be re-cast to describe turbulent flow through the packed bed as follows:

$$\frac{\Delta P}{L'} = K' \frac{1}{d_h'} \frac{1}{2} \rho u_1^2 \tag{2.8}$$

where d_m' is some equivalent diameter of the pore channels,
K' is a dimensionless constant whose value depends on the structure of the bed,
L' is the length of the channel, and
u_1 is the average through the pore channels.

We assume that the length of the fluid flow path L' is proportional to the bed height L, and also that the average linear velocity u_1 can be expressed as

$$u_1 = \frac{u_0}{\epsilon} \tag{2.9}$$

(although equation (2.9) is reasonably accurate for random packings it does not apply to all structured packings; with a bed of spheres arranged in a cubic packing, $\epsilon = 0.476$ but the fractional free area varies continuosly from 0.215 in a plane across the diameters to unity between successive layers.)

Kozeny proposed the following expression for the equivalent pore diameter (Coulson *et al.*, 1978):

$$d_m' = \frac{\epsilon}{a_p}$$

$$= \frac{\text{volume of voids filled with fluid}}{\text{wetted surface area of the bed}} \tag{2.10}$$

$$= \frac{\text{cross-sectional area normal to flow}}{\text{wetted perimeter}}$$

$$= \frac{1}{4} \times \text{hydraulic mean diameter}$$

where a_p is the specific surface area of the packing.

Substituting these values into equation (9) gives

$$\frac{\Delta P}{L} = K'' \frac{a_p}{\epsilon} \frac{1}{2} \rho \frac{u_0^2}{\epsilon^2}$$

$$= K'' \frac{a_p}{\epsilon^3} \frac{1}{2} \rho u_0^2 \tag{2.11}$$

where K'' is a dimensionless constant.

Equation (2.11) can be re-written to give head loss experienced by a gas flowing through a packed bed in metres of liquid per metre of bed height:

$$\frac{\Delta h}{L} = \frac{K''}{2g} \frac{a_p}{\epsilon^3} \frac{\rho_g}{\rho_l} u_0^2 \tag{2.12}$$

where ρ_g is the gas density, and
ρ_l is the liquid density.

It can be seen that the right hand side of equation (2.12) is in fact the capacity parameter used in the Sherwood correlation multiplied by $K''/2$. That is, the capacity parameter used in the Sherwood correlation is, in effect, a pressure drop per unit height of the packed bed.

2.3.5 Packed columns: summary of key characteristics

The key operating characteristics of packed columns, in the context of the present discussion, can be summarized as follows:

(a) HETP values for packed columns vary with type and size of packing, column height and diameter, gas velocity, density and viscosity, relative volatility and other material properties. Yang and Chuang (1995) give HETP values for 1" Pall rings between 0.3 and 0.8m, and for 2" Pall rings, between 0.5 and 1.3m. In general terms, packing efficiency is mainly influenced by internal design whereas plate efficiency is determined largely by physical properties and is less sensitive to plate design.

(b) Liquid loads typically vary between 0.5 and 50 kg/m^2s.

(c) Physical capacity of packed columns can be correlated by a relationship such as the Sherwood-Holloway curve shown in fig. 2.9, which is based on consideration of gas pressure drop in a packed bed. Numerous variations and refinements of this basic approach to capacity prediction in packed columns have been proposed.

(d) Pressure drop in packed columns varies between 5 and 120 mm water per metre of bed height; flooding occurs typically when gas pressure drop reached 125 to 150 mm water per metre of bed height.

2.4 Conclusions

In this chapter the two most important classes of conventional distillation column, plate columns and packed columns, have been described. In particular, it has been shown that for both types, the prediction of physical capacity for design is normally based on a semi-empirical correlation of gas velocity at flooding with reflux ratio: the Souders-Brown correlation for plate columns, and the Sherwood-Leva-Eckert correlation for packed columns. Such models are considered semi-empirical in the sense that their general form is based on a theoretical analysis of the fluid flow pattern (assumed to be) prevailing at the limits of capacity; this theoretical model is then adapted, modified and enhanced in the light of experimental data.

In Chapter 4 this approach to the prediction of physical capacity is applied to the spinning cone column.

CHAPTER 3

PRESSURE DROP IN THE SPINNING CONE COLUMN IN THE ABSENCE OF LIQUID FLOW

3.1 Introduction

This chapter consists of a discussion of pressure drop in the SCC in the absence of liquid flow. The subject is treated in two stages:

(a) Pressure drop with rotor fixed

(b) Pressure drop with the rotor in motion

The reason for this approach is to allow a general description of pressure drop in the SCC to be assembled in discrete stages, the first serving as the basis for the second; pressure drop in the presence of liquid flow is discussed in Chapter 4, in the light of its differences from, and similarities to, the behaviour of the column in the absence of liquid flow.

3.2 Materials and methods

3.2.1 Description of test column

The experiments described in this section (3.2) were carried out on the CSIRO Mk II SCC; this column was the same unit as used by Casimir (see dimensions in table 1.1) but modified in the following ways: (i) the inner radius of the stationary cone was increased to 35 mm and (ii) the depth of the radial fins perpendicular to the cone surface varied linearly between 4 mm at the base of the cone and 7 mm at the lip. These fins limited the amount by which the rotor could be displaced downwards with respect to the stationary elements, and thereby imposed an upper bound on the value of the spacing parameter *B* attainable on this column. That is, the smallest possible lower gap was 7 mm, corresponding to a spacing parameter *B* of 0.42.

3.2.2 Experimental procedure

The following parameters were varied in the dry-column pressure drop trials:

(a) Rotor speed
Trials were run with the rotor stationary and at three rotor speeds: 500, 1000 and 1500 RPM. A variable frequency motor speed controller was used to vary the rotor speed.

(b) Spacing parameter *B*
Measurements of pressure drop in the absence of liquid flow were obtained at four values of spacing parameter *B*: 0.21, 0.30, 0.33 and 0.40. The spacing parameter

3.3 Pressure drop with fixed rotor in the absence of liquid flow

3.3.1 Estimation of pressure drop in the cone set

Pressure drop in the SCC cone set will be considered to be made up of wall friction and dynamic losses, these last being energy losses arising from changes in flow area and direction.

3.3.1.1 Friction losses

In order to estimate friction losses we adapt the well known pipe-flow model, Darcy's equation, to the flow within the cone set. In any conduit which has constant cross sectional area the pressure drop per unit length is

$$\frac{\Delta P}{L} = f \frac{1}{D_h} \frac{1}{2} \rho U_{av}^2 \tag{3.1}$$

where ΔP is the pressure drop,
L is the length of the conduit,
D_h is the hydraulic diameter of the conduit,
U_{av} is the average fluid velocity,
ρ is the density of the fluid, and
f is the friction factor.

In our case the flow area is not constant but changes with position in the cone set. We allow for this by re-writing eq. (3.1) in differential form:

$$dP = f \frac{1}{D_h} \frac{1}{2} \rho \frac{Q^2}{A^2}\, dL \tag{3.2}$$

where Q is the volumetric flow rate of the fluid and
A is the area of the cross section.

If the hydraulic diameter is constant over the length of the flow passage being considered eq. (3.2) can be integrated to give

$$\Delta P = f \frac{1}{D_h} \frac{1}{2} \rho Q^2 \int_{L_0}^{L_1} \frac{dL}{A^2} \tag{3.3}$$

If we consider the two conical flow passages, those between sections 2 to 3 and 5 to 6 (see fig. 1.1), the hydraulic diameter at any radius R is

$$\begin{aligned} D_h &= \frac{4\times \textit{flow area}}{\textit{wetted perimeter}} \\ &= \frac{4\pi t(2R + t\sin\theta)}{2\pi R + 2\pi(R + t\sin\theta)} \\ &= 2t \end{aligned} \tag{3.4}$$

In other words, the hydraulic diameter in these flow passages is indeed constant (or at least independent of radius R) and therefore eq. (3.3) can be used to estimate pressure drop due to wall friction. The integral term on the right hand side of eq. (3.3) in effect defines a characteristic flow area, A_{char} , for the conical gap:

$$A_{char} = \frac{1}{L_1 - L_0}\left[\int_{L_0}^{L_1} \frac{dL}{A^2}\right]^{-\frac{1}{2}} \tag{3.5}$$

We can express L_1 , L_0 , dL and A as functions of distance R from the axis and substitute these expressions into eq. (3.5); i.e.

$$\begin{aligned} L_0 &= R_0 \;/\; \cos\theta \\ L_1 &= R_1 \;/\; \cos\theta \\ dL &= dR \;/\; \cos\theta \\ A &= \pi\; t\; (2R + t\; \sin\theta) \end{aligned} \tag{3.6}$$

so that

$$
\begin{aligned}
A_{char} &= \left[\frac{\cos\theta}{R_1 - R_0} \int_{R_0}^{R_1} \frac{dR}{A^2 \cos\theta} \right]^{-\frac{1}{2}} \\
&= \left[\frac{1}{R_1 - R_0} \int_{R_0}^{R_1} \frac{dR}{\pi^2 t^2 (2R + t \sin\theta)^2} \right]^{-\frac{1}{2}} \qquad (3.7) \\
&= \left[\frac{1}{\pi^2 t^2 (2R_0 + t \sin\theta)(2R_1 + t \sin\theta)} \right]^{-\frac{1}{2}} \\
&= \left[\frac{1}{A_0 A_1} \right]^{-\frac{1}{2}} = [A_0 A_1]^{\frac{1}{2}}
\end{aligned}
$$

and the characteristic flow area is simply the geometric mean of the entry and exit areas of the frustro-conical flow passage. This value can be substituted directly into the more usual form of Darcy's equation, eq. (3.1).

The friction factor f is in general a function of the surface roughness of the conduit and of the Reynolds number, Re, given by

$$
\mathrm{Re} = \frac{\rho U_{av} D_h}{\mu} \qquad (3.8)
$$

The relationship between f and Re is represented graphically in the well-known Moody chart. In estimating friction losses in the test column f was taken to be 16/Re for values of Re less than 1000 and 0.015 for values above 1000. This represents a simplification of the relationship between f and Re as represented in the Moody chart; the effects of this simplification are discussed in section 3.3.1.4.

We will not attempt to estimate friction losses in the flow passages other than the two frustro-conical gaps (sections 2 to 3 and 5 to 6 in fig. 1.1). There are two reasons for this: firstly, in a typically configured cone set they constitute a minor fraction of the total length of the notional mean flow path and so we expect their contribution to overall friction loss to be correspondingly small; secondly, the flow geometry in these zones does not allow even the much simplified analysis used for the frustro-conical passages. The question whether neglecting friction losses in these zones is a legitimate simplification can only be addressed by consideration of experimental results; these will be discussed later in this chapter (section 3.3.2.2).

3.3.1.2 Estimation of dynamic losses

The gas/vapour flow pattern in the SCC cone set is characterized by rapid, even abrupt, changes in flow area and direction. Referring to fig. 1.1 we see that from section 3 to section 5, and from section 6 to section 2 in the cone set above, the direction of flow is reversed. We expect such radical changes in flow direction to occasion substantial energy losses by the formation of eddies, zones of highly agitated recirculating flow. Also, the geometry of the cone set may be such that there are abrupt changes in flow area: if the spinning cone is located close to the fixed cone either above or below - in other words, if the position parameter *B* is significantly less than or greater than 0.5 - the areas at sections 3 and 5, and at sections 2 and 6, will be substantially different. Abrupt expansions and contractions in a flow passage will normally cause some loss of flow energy, the degree of loss being related to the severity of the change in area.

We can identify six potential sources of dynamic pressure loss in the SCC cone set:

(a) reversal of flow direction around the lip of the stationary cone
(b) abrupt change in flow area, A_6 to A_2, around the lip of the stationary cone
(c) rapid expansion, A_2 to A_3
(d) reversal of flow direction around the lip of the spinning cone
(e) abrupt change in flow area, A_3 to A_5, around the lip of the spinning cone
(f) rapid contraction, A_5 to A_6

Estimates of dynamic losses in the cone set will be obtained using correlations pertaining to the flow of air in ducts (Croome and Roberts, 1981). These methods are described in the following sections 3.3.1.2.1, 3.3.1.2.2 and 3.3.1.2.3. The applicability of such correlations to the flow in the SCC cone set can be assessed only by comparing the predictions of pressure drop derived from them to experimental data.

3.3.1.2.1 Abrupt contraction

The pressure drop caused by an abrupt contraction in a flow passage can be expressed as

$$\begin{aligned}\Delta P &= P_1 - P_2 + \frac{1}{2}\rho u_1^2 - \frac{1}{2}\rho u_2^2 \\ &= k \times \frac{1}{2}\rho u_1^2\end{aligned} \tag{3.9}$$

where *P* is the pressure, *u* is the average velocity, ρ is the fluid density and *k* is called the loss coefficient (Croome and Roberts, 1981). Subscripts 1 and 2 refer to flow sections upstream and downstream of the contraction respectively. The results of tests on air flow in ducts have been used to relate the value of the loss coefficient *k* to the ratio of the inlet to exit velocities, u_1/u_2 (see table 3.1).

Table 3.1
Abrupt contraction: values of loss coefficient k as a function of ratio of inlet to exit velocity u_1/u_2 (Croome and Roberts, 1981)

u_1/u_2	0.25	0.30	0.35	0.40	0.45	0.50	0.55	0.60	0.65	0.70
k	0.37	0.34	0.32	0.28	0.25	0.23	0.19	0.16	0.12	0.09

3.3.1.2.2 Abrupt expansion

We can use a similar formulation of the Bernoulli (energy) equation to express pressure drop caused by an abrupt expansion in the flow passage to that used for the abrupt contraction. The definition of the loss coefficient is different, however (Croome and Roberts, 1981):

$$\Delta P = k \times (\frac{1}{2}\rho u_1^2 - \frac{1}{2}\rho u_2^2) \tag{3.10}$$

The quantity (1-k) is called the static regain coefficient and is used as a measure of the efficiency of a diffuser/diverging passage; a value close to unity implies nearly complete conversion of velocity pressure upstream of the expansion to static pressure downstream.

Table 3.2
Abrupt expansion: values of loss coefficient k as a function of ratio of exit to inlet velocity u_2/u_1 (Croome and Roberts, 1981)

u_2/u_1	0.20	0.25	0.30	0.35	0.40	0.45	0.50	0.55	0.65	0.75
k	0.67	0.60	0.54	0.48	0.43	0.38	0.33	0.29	0.21	0.14

3.3.1.2.3 Reversal of flow direction - 180° bend

The case of a complete reversal in flow direction is not specifically treated in the correlations for air flow in ducts used here. The loss coefficient for a 90° bend, however, is given as 1.25 where there are no turning vanes or other flow control devices (Croome and Roberts, 1981). We shall therefore assume, in the absence of more directly applicable data, that the loss coefficient for a 180° bend is simply double the value given for a 90° bend: i.e. $k = 2.5$. We shall further assume that, in the case where the entry and exit sections of the bend are of unequal area, the velocity pressure to which the coefficient applies is that at the smaller of the two sections.

3.3.1.3 Dynamic loss estimations for test column

Dynamic pressure loss within the cone set due to the six sources identified earlier (section 3.3.1.2) can be expressed in terms of the maximum velocity in the cone set, in this case the velocity at section A_6 (see fig. 1.1 and table 3.3), using the equations given in sections 3.3.1.2.1, 3.3.1.2.2 and 3.3.1.2.3. That is:

$$\Delta P_i = K_i \times \frac{1}{2}\rho u_{A_6}^2 \tag{3.11}$$

where

$$K_1 = k_1$$

$$K_2 = k_2[1 - (u_{A_2}/u_{A_6})^2] = k_2[1 - (A_6/A_2)^2]$$

$$K_3 = k_3[(u_{A_2}/u_{A_6})^2 - (u_{A_3}/u_{A_6})^2] = k_3[(A_6/A_2)^2 - (A_6/A_3)^2]$$

$$K_4 = k_4(u_{A_5}/u_{A_6})^2 = k_4(A_6/A_5)^2$$

$$K_5 = k_5(u_{A_5}/u_{A_6})^2 = k_5(A_6/A_5)^2$$

$$K_6 = k_6$$

Experimental data were obtained for four different values of the spacing parameter ***B***. Values of the flow areas, A_1 to A_6, along with the pressure loss coefficients k_1 to k_6 and K_1 to K_6 corresponding to each value of B are shown in table 3.3.

Table 3.3
Details of the four shaft positions and corresponding geometrical parameters and pressure loss coefficients

Shaft position	1	2	3	4
B (spacing parameter)	0.40	0.33	0.30	0.21
A_1 (m^2)	0.00244	0.00244	0.00244	0.00244
A_2 (m^2)	0.00149	0.00164	0.00172	0.00193
A_3 (m^2)	0.00311	0.00347	0.00365	0.00419
A_4 (m^2)	0.00409	0.00409	0.00409	0.00409
A_5 (m^2)	0.00175	0.00144	0.00128	0.00081
A_6 (m^2)	0.00103	0.00084	0.00074	0.00046
t_U (mm)	4.5	3.7	3.3	2.0
t_L (mm)	7.4	8.2	8.6	9.9
k_1	2.50	2.50	2.50	2.50
k_2	0.18	0.32	0.40	0.62
k_3	0.35	0.36	0.36	0.37
k_4	2.50	2.50	2.50	2.50
k_5	0.19	0.27	0.31	0.40
k_6	0.17	0.18	0.18	0.19
K_1	2.50	2.50	2.50	2.50
K_2	0.09	0.24	0.33	0.59
K_3	0.13	0.07	0.05	0.02
K_4	0.87	0.84	0.83	0.80
K_5	0.07	0.09	0.10	0.13
K_6	0.17	0.18	0.18	0.19
ΣK_i	3.83	3.92	3.99	4.22

3.3.1.4 Implications of pressure drop estimation

The relative contributions of wall friction and dynamic losses to the estimates of total pressure drop can be assessed by expressing them in terms of the maximum velocity in the cone set. The total dynamic loss can be written as

$$\Delta P_d = K_d \times \frac{1}{2}\rho u_{A_6}^2 \tag{3.12}$$

where K_d = ΣK_i (see table 3.3).

A similar expression for friction losses can also be written:

$$\Delta P_f = K_f \times \frac{1}{2}\rho u_{A_6}^2 \tag{3.13}$$

Because the Fanning friction factor f in eq. (3.1) is a function of Reynolds number, K_f varies with flow, unlike K_d, which is assumed to be constant with respect to flow.

Table 3.4
Comparison of estimated friction and dynamic loss coefficients, K_f and K_d

	B	0.40	0.33	0.30	0.21
	K_d	3.83	3.92	3.99	4.22
	K_f				
Q (l/min)	0	0.25	0.28	0.29	0.40
	40	0.17	0.18	0.20	0.27
	60	0.13	0.14	0.15	0.20
	80	0.10	0.11	0.12	0.16
	100	0.07	0.07	0.08	0.11
	160	0.06	0.07	0.08	0.11
	180	0.06	0.07	0.07	0.10
	200	0.06	0.07	0.07	0.10

Values of K_f for the four shaft positions and air flows between zero and 200 l/min. are set out in table 3.4, along with the corresponding dynamic loss coefficients, K_d.

These estimates of pressure loss coefficient suggest that wall friction makes only a minor contribution to overall pressure drop; with the rotor in its lowest position (B = 0.40) estimated friction losses vary between 6% of the total at 40 l/min to 1.5% at air flows above 220 l/min. With the rotor in its highest position the corresponding contributions are 8.7% to 2.4% over the same flow range. The reduction in the predicted friction loss with flow is a consequence of the fall in the value of the friction factor *f* as *Re* increases in the laminar flow region (see section 3.3.1.1). It can be seen that a more precise determination of *f* than that described in section 3.3.1.1 would have a negligible effect on the total pressure drop estimate.

The values of *K* given in table 3.3 shows that the bulk of the estimated pressure drop is due to the two reversals in flow direction, the 180° turn at the (inner) throat accounting for about 60-65% of the total for all shaft positions and the 180° turn at the lip of the spinning cone accounting for a further 20%. These estimates of pressure drop resulting from the reversal of flow direction are of course directly dependent on our choice of loss coefficient ($k_1 = k_4 = 2.5$). Whilst the true value is unlikely to be exactly 2.5, and may indeed vary to some extent with both flow and position parameter *B*, there is no striking feature of this flow system which would lead us to expect a substantially lower value.

3.3.2 Measurements of pressure drop with stationary rotor in the absence of liquid flow

Fig. 3.2 shows the experimentally observed variation of pressure drop across the test column with air flow for the four values of the spacing parameter *B*.

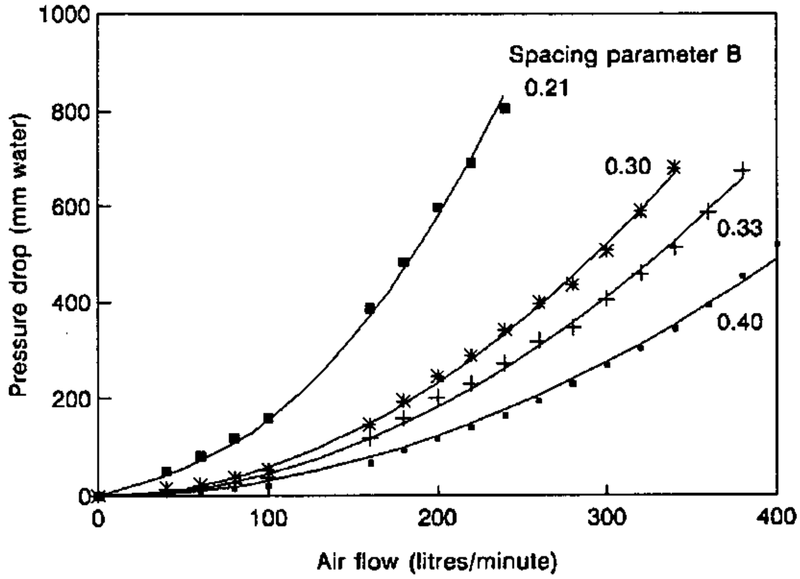

Figure 3.2
Experimentally observed variation of pressure drop across test column with air flow for various values of spacing parameter *B*; rotor stationary and in absence of liquid flow

We see that in all cases pressure drop increases in parabolic fashion with air flow. The effect of spacing parameter *B* is as expected: as *B* is reduced so is the minimum flow area within the cone set, and therefore at a given air flow the maximum gas velocity in the cone set is increased, resulting in increased pressure drop.

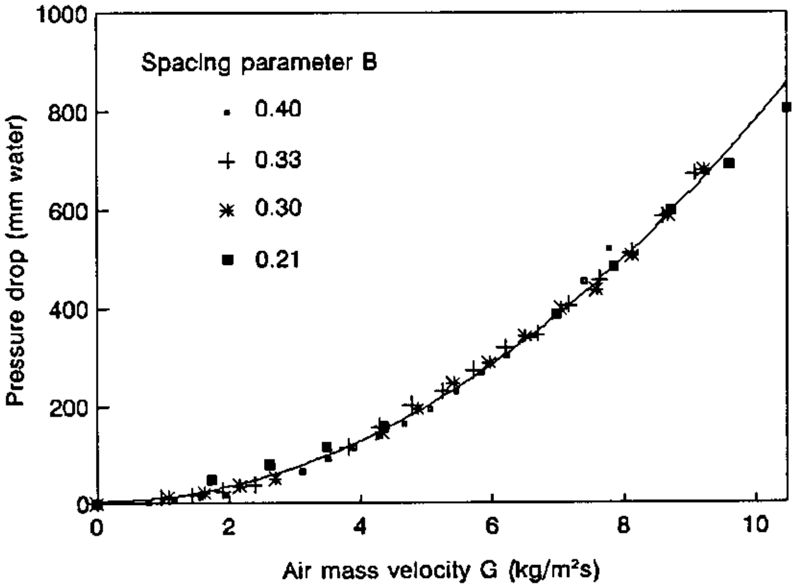

Figure 3.3
Variation of pressure drop across the test column with air mass velocity *G* based on minimum flow area (rotor stationary, no liquid flow)

We can examine the effect of minimum flow area on pressure drop by transforming air volume flow to mass velocity *G*:

$$G = \frac{\rho_{air} Q}{A_{min}} \tag{3.14}$$

where Q is the air volume flow (m^3/s)
ρ_{air} is the air density, and
A_{min} is the minimum flow area within the cone set.

Fig. 3.3 is a plot of the same pressure drop data as shown in fig. 3.2 but plotted against mass velocity *G* defined above.

The observed values of pressure drop here lie on or close to a single curve, suggesting that pressure drop in the SCC is a function of gas velocity through the smallest flow area within the cone set.

3.3.2.1 Regression analysis of experimental data

3.3.2.1.1 Power curve model: results of linear regression

A power curve relationship, of the form

$$\Delta P = b_0 G^{b_1} \tag{3.15}$$

was fitted to the data.

Table 3.5
Results of power curve regression (including 95% confidence limits)

B	0.40	0.33	0.30	0.21	Pooled data
$\ln(b_0)$	1.76 ± 0.09	2.21 ± 0.18	2.24 ± 0.15	2.86 ± 0.23	2.12 ± 0.11
b_1	2.17 ± 0.06	1.92 ± 0.11	1.90 ± 0.09	1.61 ± 0.13	1.97 ± 0.07
r^2	0.997	0.989	0.993	0.991	0.982

In the regression analysis we have four groups of data, each corresponding to a single value of the position parameter *B*. As stated above, the data depicted in fig. 3.3 are closely grouped around a single curve (the curve drawn in fig. 3.3 is that obtained from regression of the pooled data). We can check whether the differences between the coefficients obtained from the regression analysis are statistically significant. There are four possible models to evaluate:

(1) the least restrictive model, in which b_0 and b_1 are (possibly) different for each value of *B*
(2) parallel regressions; curves have the same slope b_1 but differing intercepts b_0
(3) concurrent regressions; curves have the same intercept b_0 but differing slopes b_1
(4) coincident regressions; curves have the same slope and intercept.

We use the method of comparing regression lines described by Weisberg (1985). Our analysis of each model yields a residual sum of squares, *RSS*, and an associated number of degrees of freedom, *df*. These data are given in table 3.6.

Table 3.6
Residual sums of squares and associated degrees of freedom
for comparing regression lines

	Model 1	Model 2	Model 3	Model 4
RSS	0.55	1.30	1.62	1.67
df	48	51	51	54

We compare model (4), the most restrictive, to model (1), the least restrictive, by conducting an F-test as follows:

$$F_{4,1} = \frac{(RSS_4 - RSS_1)/(df_4 - df_1)}{RSS_1/df_1} \tag{3.16}$$

$$= \frac{(1.67 - 0.55)/(54 - 48)}{0.55/48}$$

$$= 16.3$$

The corresponding value from the F distribution at the 99% confidence level is $F(0.01, 6, 48) = 3.22$; we consequently reject the hypothesis that the most restrictive model describes the data as well as the least restrictive. Comparisons of model (3) and model (2) with model (1) yield similarly high F values (21.8 and 31.2 respectively). In other words, the differences between the values of b_0 and b_1 obtained for the different values of spacing parameter B are statistically significant; the least restrictive model provides a better description of the data set than any of the other three.

3.3.2.1.2 Discussion of regression analysis

If all four sets of data, corresponding to each value of B, were equally and unbiasedly correlated by the maximum velocity we would conclude that those resistances directly and constantly proportional to that velocity - corresponding to loss coefficients K_1 and K_4 - predominate; if, on the other hand, all four sets of data were not equally and unbiasedly correlated by the maximum velocity then, as B varied, the ratio of other resistances to the maximum resistance would also vary, thereby giving rise to changes in the values of the regression constants b_0 and b_1.

The regression analysis of the experimental data indicates that b_0 and b_1 vary with B to a statistically significant extent. The variations are not gross, however; all four fitted curves (model 1) have very similar form and magnitude, and a single curve, based on the pooled data, provides a good numerical description of the data set, evidenced by the values of r^2 given in table 3.7, which show that more than 98% of the variation of ΔP is accounted for by the most restrictive model, 4 (see table 3.7 and fig. 3.3).

We may interpret these results as follows: those resistances which are directly proportional to maximum velocity make the predominant contribution to overall pressure drop; the contribution of other resistances, which are not directly proportional to maximum velocity, is small but detectable. These finding are consistent with the estimates of pressure drop set out in table 3.3.

Note that error in the measurement of the smallest flow cross section, which is used to calculate G, could well give rise to statistically significant variation of the coefficient b_0 with B; such error, however, would not bring about statistically significant variation in the value of the exponent b_1 with B.

3.3.2.2 Comparison of predicted and observed pressure drop data

Recall that our estimates of pressure drop in the SCC cone set were expressed in the form

$$\Delta P = K \times \frac{1}{2}\rho u^2 = K \times \frac{G^2}{2\rho} \tag{3.17}$$

where ΔP is pressure drop per cone set expressed in Pa.

To compare our observed data to these estimates we must recast the fitted relationships in equivalent terms; we re-write eq. (3.15) as

$$\Delta P_{CS} = \frac{c}{N_{CS}} \times b_0'\left(\frac{G^{b_1}}{2\rho}\right) \tag{3.18}$$

where ΔP_{CS} is the pressure drop per cone set (Pa),
c is a conversion from mm water to Pa = 9.80665 Pa/mm water,
N_{CS} is the number of cone sets in the test column (40), and
b_0' $= b_0 \times \rho_{air} \times 2$.

After making these conversions we obtain

$$\begin{aligned}
&\text{For } B = 0.40,\ \Delta P_{CS} = 3.43\left(\frac{G^{2.12}}{2\rho}\right)\\
&\text{For } B = 0.33,\ \Delta P_{CS} = 4.92\left(\frac{G^{1.92}}{2\rho}\right)\\
&\text{For } B = 0.30,\ \Delta P_{CS} = 5.38\left(\frac{G^{1.90}}{2\rho}\right)\\
&\text{For } B = 0.21,\ \Delta P_{CS} = 5.55\left(\frac{G^{1.61}}{2\rho}\right)
\end{aligned} \tag{3.19}$$

The corresponding equations obtained from the pressure drop estimation procedure described in section 3.3.1.3 are

$$\begin{aligned}
&\text{For } B = 0.40,\ \Delta P_{CS} = 3.83\left(\frac{G^2}{2\rho}\right)\\
&\text{For } B = 0.33,\ \Delta P_{CS} = 3.92\left(\frac{G^2}{2\rho}\right)\\
&\text{For } B = 0.30,\ \Delta P_{CS} = 3.99\left(\frac{G^2}{2\rho}\right)\\
&\text{For } B = 0.21,\ \Delta P_{CS} = 4.22\left(\frac{G^2}{2\rho}\right)
\end{aligned} \qquad (3.20)$$

and the ratios of the values of ΔP_{CS} obtained from the curves fitted to the experimental data to those obtained from the estimation procedure are

$$\begin{aligned}
&\text{For } B = 0.40,\ \frac{\Delta P_{CS,fitted}}{\Delta P_{CS,estimated}} = 0.89\,G^{0.12}\\
&\text{For } B = 0.33,\ \frac{\Delta P_{CS,fitted}}{\Delta P_{CS,estimated}} = 1.26\,G^{-0.08}\\
&\text{For } B = 0.30,\ \frac{\Delta P_{CS,fitted}}{\Delta P_{CS,estimated}} = 1.35\,G^{-0.10}\\
&\text{For } B = 0.21,\ \frac{\Delta P_{CS,fitted}}{\Delta P_{CS,estimated}} = 1.32\,G^{-0.39}
\end{aligned} \qquad (3.21)$$

Note that these ratios are functions of G. This is a consequence of the regression procedure yielding exponents b_1 which are not equal to 2; it is explicitly assumed in the estimation procedure that pressure drop varies with the square of gas velocity.

There are well-established fluid mechanic arguments, and data, which indicate that the true value of the exponent b_1 is in fact less than 2. For example, Treybal (1981) suggests that pressure drop for gas flow through a dry packed bed varies with gas velocity raised to a power between 1.8 and 2.

The ratios defined in equations (3.21) are plotted against G in fig. 3.4.

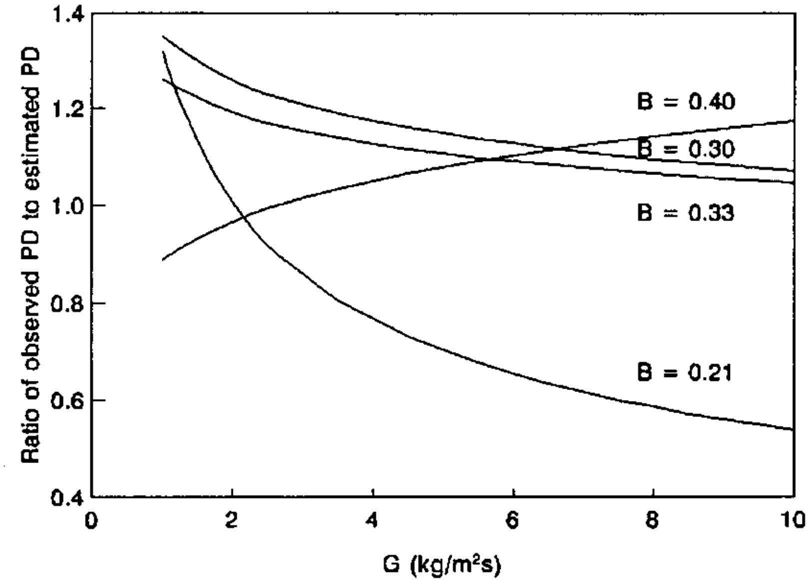

Figure 3.4
Plot of $\Delta P_{CS,fitted} / \Delta P_{CS,estimated}$ against gas mass velocity, G (see equations 3.21 above)

For $B = 0.30$, 0.33 and 0.40 the values of ΔP_{CS} obtained from the estimation procedure described in section 3.3.1 are within 20% of the values of ΔP_{CS} obtained from the power curve fit to the experimental data for all but the lowest values of G. The numerical similarity of the estimated and observed values broadly supports the validity of the estimation procedure, particularly the use of a pressure loss coefficient $k = 2.5$ for the two reversals of flow direction in the cone set; recall that it is this part of the estimation procedure which has by far the greatest bearing on the magnitude of the ΔP estimate (see table 3.3). In other words the observed pressure drop data support the proposition that the bulk of fixed-rotor dry-column pressure drop arises from the multiple reversals in flow direction in the SCC.

The observed data do not, however, allow firm conclusions to be drawn about the contributions to pressure drop from other sources; the estimates suggest they are small, and the observed data are consistent with this; whether their magnitudes correspond closely to the estimated values cannot be determined from the data reported here, since they are effectively swamped by the larger terms arising from the changes in flow direction.

There is appreciably greater divergence between the observed and estimated pressure drops for $B = 0.21$; much of this can be attributed to the difference between the exponents of G in the two models: 1.61 in the power curve fit as opposed to 2 in the estimation procedure.

3.4 Effect of rotor motion on pressure drop in the dry column

In this section the results of pressure drop trials with the rotor in motion and in the absence of liquid flow are presented and discussed. Our aim is to examine how the motion of the rotor changes the manner in which pressure drop varies with gas flow from *that observed with the rotor stationary (see section 3.3), and ultimately to develop a procedure by which pressure drop in the SCC, in the case where there is no liquid flow,* can be predicted as a function of both gas flow and rotor speed.

3.4.1 SCC fan performance

In section 3.2.1 the presence of radial fins on the underside of the spinning cone was mentioned. These were considered in the analysis of fixed-rotor pressure drop only with respect to their role in limiting the range of vertical positions that the rotor could assume. Their contribution to fixed-rotor dry-column (FRDC) pressure drop was neglected.

The addition of fins to the undersides of the spinning cones was one of the principal additions to the original SCC design made by Casimir (see section 1.5.3). This modification was made as a relatively easily incorporated enhancement to the efficiency of the column as a gas-liquid contactor. The purpose of the fins was to increase the amount of mechanical/kinetic energy imparted to the gas by the moving rotor, with the ultimate goals, firstly, of augmenting mass transfer by increased agitation of the gas/vapour stream, and, secondly, of reducing overall pressure drop across the column, thereby deriving operational benefits arising from the corresponding reduction in temperature difference between bottom and top of column.

The shape, size and number of fins attached to the spinning cone were chosen so that there would be no interference with the liquid flow pattern and that the fins could be easily fabricated and incorporated into the final assembly. There was no attempt to design the spinning cone/fin assembly as a centrifugal impeller. Even so, the influence of the moving rotor on gas flow through the column can be usefully described by considering the SCC as a multi-stage centrifugal fan.

3.4.1.1 The SCC fan characteristic

The performance of a fan is commonly represented by a graph of (static) pressure rise across the fan against volume flow through the fan. Such a graph is called the fan characteristic. A curve of the form shown in fig. 3.5 is typical.

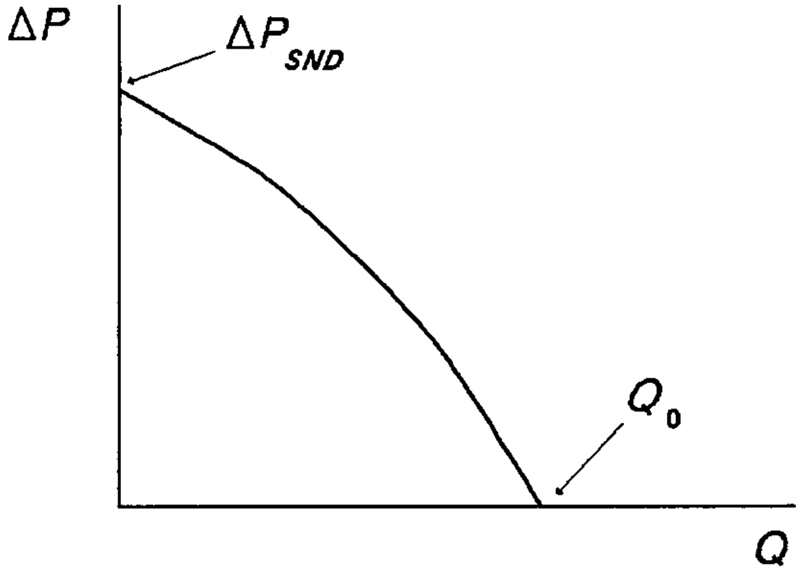

Figure 3.5
Typical fan characteristic

Two parameters which together define the limits of a particular fan's performance are the static no-discharge pressure, ΔP_{SND}, and the wide-open flow, Q_0. ΔP_{SND} is the static pressure developed by the fan at zero flow, and corresponds to the point at which the fan characteristic intercepts the vertical (pressure) axis. The wide-open flow Q_0 is the maximum flow which can be delivered by the fan and corresponds to the point at which the characteristic intercepts the horizontal (flow) axis.

At zero flow the theoretical rise in static pressure across a centrifugal impeller is

$$\Delta P_{th,\ SND} = \frac{1}{2}\rho u_{tip}^2 \tag{3.22}$$

where u_{tip} is the peripheral velocity of the impeller (Eck, 1973).

For the purposes of the present discussion the SCC is considered a multi-stage centrifugal fan, each cone set representing a stage. The theoretical static no-discharge pressure drop for the column is therefore

$$\Delta P_{th,\ SND} = -N_{CS} \times \frac{1}{2}\rho u_{tip}^2 \tag{3.23}$$

where N_{CS} is the number of cone sets.

Note that, in order to maintain consistency across the full range of experimental observations, we have defined $\Delta P_{th,SND}$ as a pressure drop rather than a pressure rise.

3.4.1.2 Fan laws

The so-called fan laws are derived from a dimensional analysis of the main parameters which influence the performance of the fan (Osborne, 1977). These include

(a) design and type of fan
(b) point of operation on the fan characteristic
(c) the size of the fan
(d) the impeller speed
(e) the physical properties of the gas being conveyed.

Stated in their simplest form the fan laws can be expressed as

$$\begin{aligned} Q &= k_q d^3 \omega \\ \Delta P &= k_p d^2 \omega^2 \rho \end{aligned} \tag{3.24}$$

where ω is the impeller speed,
d is the impeller diameter, and
ρ is the gas density.

The coefficients k_q and k_p are constant for a range of geometrically similar fans and for a particular point of operation on the fan characteristic.

The important implication of the fan laws for our present discussion is that volume flow Q is proportional to impeller speed whereas change in pressure ΔP is proportional to the square of impeller speed.

Since the fan laws are valid for any particular point on the fan pressure/volume characteristic, similar laws will be valid for every other point of operation, the only difference being the numerical values of the coefficients. Thus a plot of k_q against k_p will have the same form as the pressure/volume characteristic of each fan in a homologous series, and may be used to represent the performance of any fan in the series and also to compare the performance of the series design to that of another series design (Osborne, 1977).

Various dimensionless coefficients are used for this purpose; in the following discussion we shall use the static pressure coefficient ψ_{st} and the volume coefficient ϕ defined by

$$\psi_{st} = \frac{\text{fan static pressure}}{\frac{1}{2}\rho u_{tip}^2} \tag{3.25}$$

$$\phi = \frac{\text{volume flow}}{\frac{\pi d^2}{4} u_{tip}} \tag{3.26}$$

where u_{tip} is the impeller peripheral velocity, and
d is the impeller diameter.

There is no idealized representation of the flow in a centrifugal fan (comparable to that used to predict the static no-discharge pressure) which allows us to predict the wide-open flow Q_0. We can, however, look at the variation of Q_0 with rotor speed and compare the observed relationship with that predicted by the fan laws stated above. We can also compare the values of the static no-discharge pressure coefficient $\psi_{SND} = \Delta P_{SND} / \frac{1}{2}\rho u_{tip}^2$ and the wide-open flow coefficient $\phi_0 = 4Q_0 / \pi d^2 u_{tip}$ to those of geometrically similar impellers.

3.4.2 Rotor speed and pressure drop: experimental observations

The effect of rotor speed on pressure drop in the dry column is illustrated in figures 3.6 (a) to (d), which show the experimentally observed variation of pressure drop with air flow for rotor speeds of zero, 500, 1000 and 1500 RPM, each graph pertaining to a single value of spacing parameter *B*.

The motion of the rotor modifies the parabolic fixed-rotor dry-column pressure drop response by creating a pressure rise (i.e a negative pressure drop) at zero and low air flows and an additional pressure drop at air flows above 30 to 40 litres/min. The degree of this distortion of the fixed-rotor pressure drop response increases with rotor speed at all flows. The parabolic shape of the fixed rotor curve changes with rotor speed, becoming more sigmoid as rotor speed increases.

Pressure drop is effectively a loss of energy experienced by the gas stream on its passage through the column. In figs 3.6 (a) - (d) we see that at zero and low gas flows the motion of the rotor increases the energy of the gas stream; in this flow range the SCC is behaving like a multi-stage centrifugal fan.

At gas flows above 30 - 40 l/min., depending on spacing parameter *B*, the motion of the rotor reduces the energy of the gas stream. For instance, at $B = 0.40$ (fig. 3.6(a)), at an air flow of 160 litres/minute the pressure drop at 1500 RPM is more than three times the pressure drop with the rotor fixed for the same air flow and shaft position. Note that, as mentioned earlier, the intensity of this "bulging" increases with rotor speed. This behaviour implies that the movement of vapour through the column is impeded by the action of the rotor at moderate to high gas flows.

Although these data do not allow a precise explanation of this behaviour we can suggest two mechanisms by which the energy of the gas stream might be reduced by the motion of the rotor:

(a) the gas stream is expending energy as work on the rotor; in other words, the SCC is behaving like a turbine. Although it was not possible to assess this turbine effect in the experimental trials reported in this chapter, we would expect such an effect to be evidenced by a fall in the current drawn by the rotor drive motor. The possibility of turbine behaviour in the SCC warrants further investigation.

(b) the moving rotor is generating recirculating zones (eddies) in the gas stream. These eddies act to impede the flow by effectively entraining some of the energy of the gas stream, energy which is ultimately dissipated as heat. The rotor is not removing energy from the gas stream but rather is converting useful (flow) energy to heat; by agitating the gas stream it is increasing the entropy of the stream, and expending mechanical energy (electrical power to the drive motor) in the process. This behaviour can be likened to that occurring in stirred vessels.

The following discussion and quantitative analysis of the experimental data is arranged in two parts; we will firstly consider the behaviour of the column at low gas flows since it is in this region of operation that the SCC's fan-like performance is dominant; we will then consider the pressure drop in the SCC across the full range of gas flows for which experimental data have been obtained; in particular we will devise a quantitative description of pressure drop in the dry column which is based on both the fixed-rotor pressure drop performance, discussed in the first part of this chapter, and the SCC's fan-like behaviour. Methods for predicting dry-column pressure drop for design, based on this quantitative analysis, are proposed.

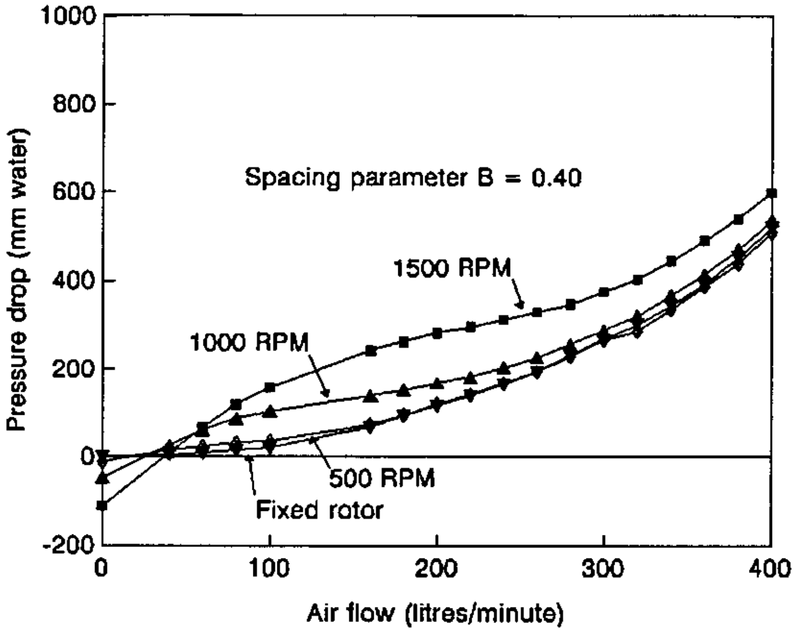

Figure 3.6 (a)
Variation of pressure drop across the SCC with air flow for various rotor speeds, *B* = 0.40

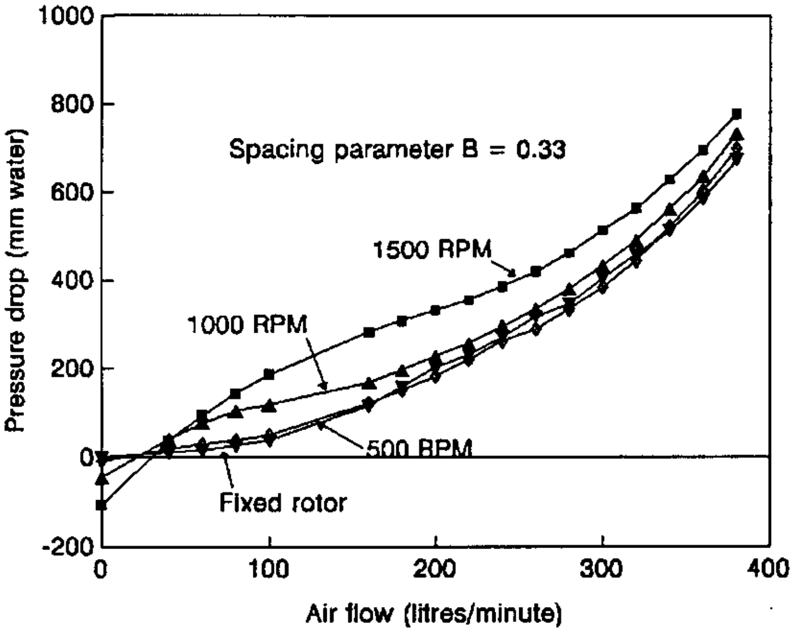

Figure 3.6 (b)
Variation of pressure drop across the SCC with air flow for various rotor speeds, *B* = 0.33

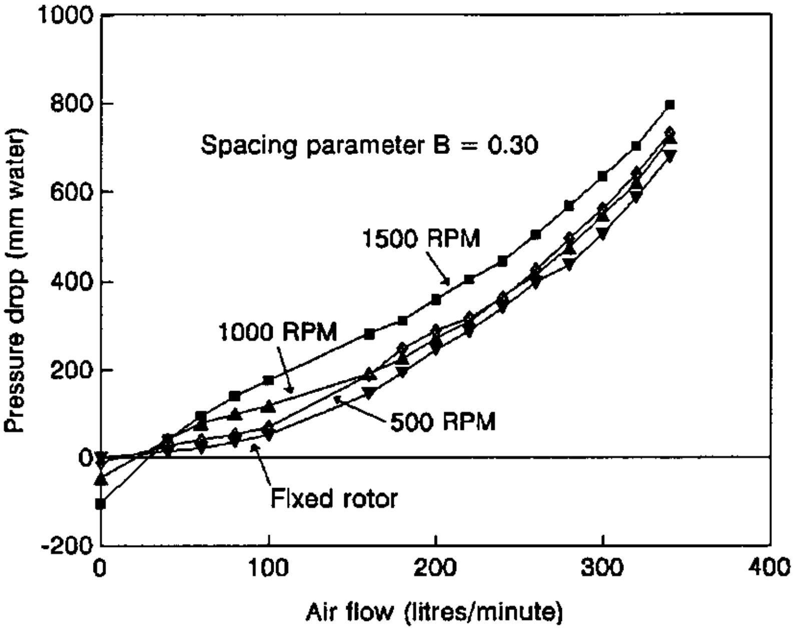

Figure 3.6 (c)
Variation of pressure drop across the SCC with air flow for various rotor speeds, B = 0.30

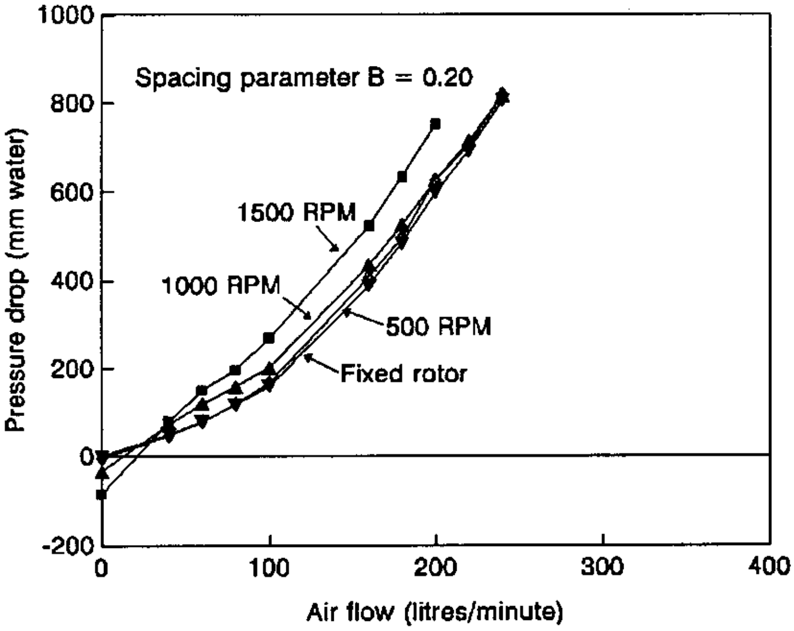

Figure 3.6 (d)
Variation of pressure drop across the SCC with air flow for various rotor speeds, B = 0.21

3.4.2.1 Estimates of experimental error

In order to obtain estimates of experimental error, repeated observations of pressure drop ΔP were made at shaft position 1 ($B = 0.40$) and at rotor speeds of 500, 1000 and 1500 RPM for various values of air flow Q. These results are shown in table 3.7.

Table 3.7
Repeated observations (ΔP and 95% confidence limits expressed in mm water)

Q (l/min)	500 RPM		1000 RPM		1500 RPM		s	95% conf. limits
	ΔP_1	ΔP_2	ΔP_1	ΔP_2	ΔP_1	ΔP_2		
0	-12	-12	-48	-47	-112	-106	2.5	±6.2
60	24	20	60	50	66	55	6.3	±15.6
200	120	116	168	164	282	275	3.7	±9.1
300	266	279	288	311	376	369	11.2	±27.7
400	510	517	538	576	600	562	22.1	±55.0

Values of the standard error s were obtained by assuming that the variance of the observed values of ΔP was the same at all rotor speeds; hence

$$s^2 = \frac{\frac{1}{2}(\Delta P_1 - \Delta P_2)^2_{500} + \frac{1}{2}(\Delta P_1 - \Delta P_2)^2_{1000} + \frac{1}{2}(\Delta P_1 - \Delta P_2)^2_{1500}}{3} \qquad (3.27)$$

The 95% confidence limits are $\pm\, t(n\text{-}1,\, 0.975)s/\sqrt{n}$ where $n = 3$.

In table 3.7 we see that the standard error of the observed pressure drop s tends to increase with air flow Q; in particular, the ratio of variance at $Q = 400$ l/min to that at Q = zero is $(22.1/2.5)^2 = 78.1$ whereas the corresponding F value is $F(0.99,3,3) = 29.5$. That is, the probability of observing a ratio of sample variances of this magnitude in samples from the same population is less than 0.01; we therefore reject the hypothesis that the variance of the observed pressure drop is constant with respect to air flow Q. This result suggests that there is a large proportional component in the overall error.

3.4.2.2 Pressure drop at low gas flows: fan performance

Figs 3.7 (a) - (c) are plots of pressure drop for gas flows up to 100 litres/minute; these graphs are effectively inverted fan (pressure/volume) characteristics, pressure rise shown as negative pressure drop.

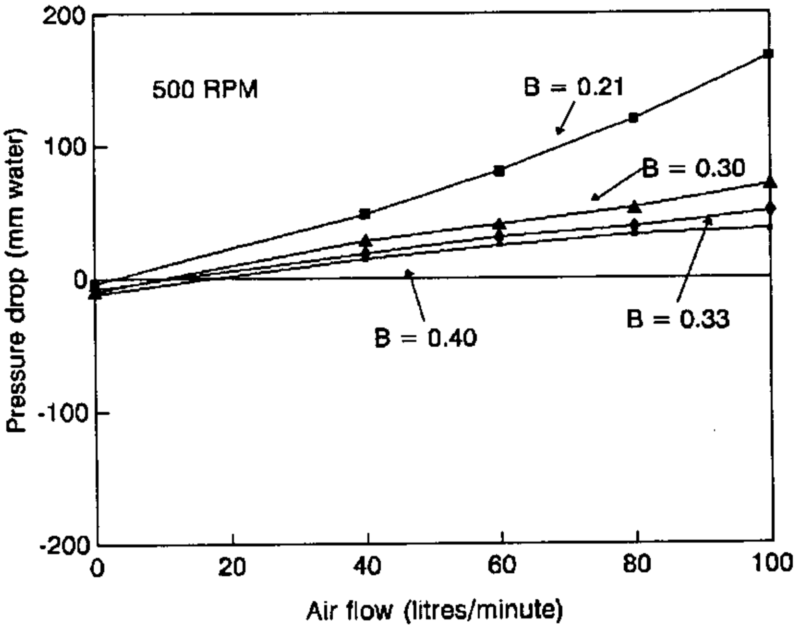

Figure 3.7 (a)
Pressure drop vs gas flow at low flows for various values of spacing parameter *B* at a rotor speed of 500 RPM.

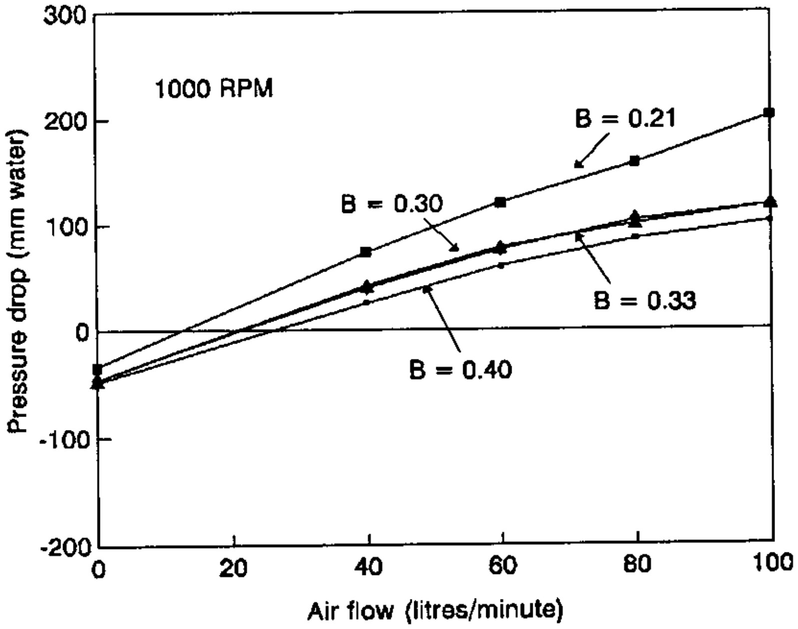

Figure 3.7 (b)
Pressure drop vs gas flow at low flows for various values of spacing parameter *B* at a rotor speed of 1000 RPM.

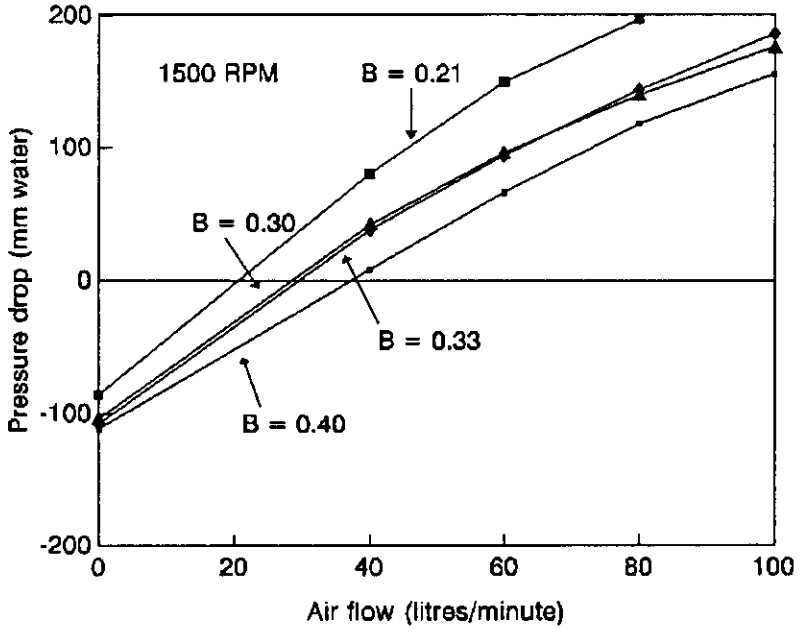

Figure 3.7 (c)
Pressure drop vs gas flow at low flows for various values of spacing parameter *B* at a rotor speed of 1500 RPM.

The points at which the pressure drop curves intersect the vertical (ΔP) and horizontal (Q) axes correspond to the static no-discharge pressure and wide-open flow defined in section 3.4.1.1.

Fig. 3.8 is a plot of the static no-discharge pressure ΔP_{SND} against the square of rotor speed.

Recall that the fan laws predict that ΔP_{SND} should be proportional to the square of rotor speed; the experimentally observed data shown in fig. 3.8 are consistent with this prediction. The effect of spacing parameter *B* is slight; only at $B = 0.21$, the lowest value covered by these data, are the values of ΔP_{SND} noticeably lower than at the other values of *B*. Values of the static no-discharge pressure coefficient ψ_{SND} corresponding to the various rotor speeds and spacing parameters are given in table 3.8.

The fan laws predict that ψ_{SND} should be constant for geometrically similar fans, in this case for a particular value of *B*. The data shown in table 3.8 are broadly consistent with this prediction, the largest deviations occurring at 500 RPM and the lower values of *B*.

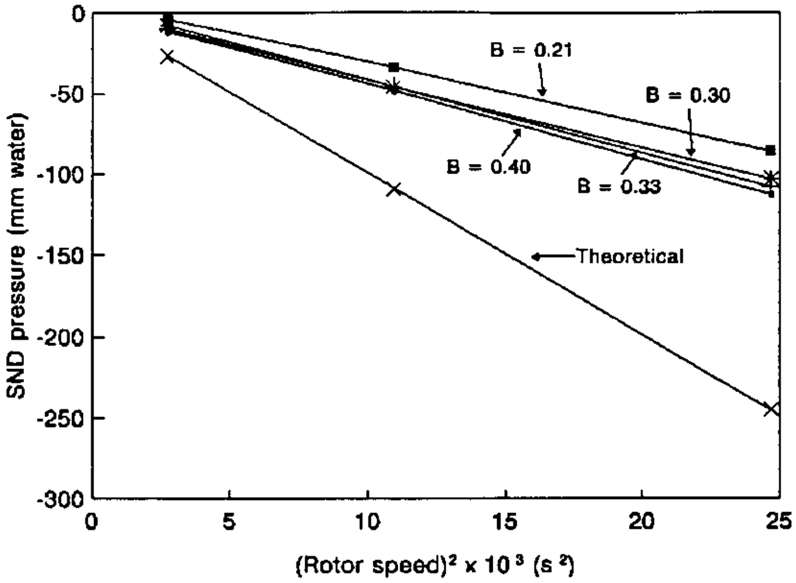

Figure 3.8
Variation of static no-discharge (negative) pressure drop ΔP_{SND} with the square of rotor speed.

Table 3.8
Static no-discharge pressure coefficient ψ_{SND}

Rotor speed (RPM)		500	1000	1500
Tip speed, u_{tip} (m/s)		3.3	6.7	10.0
$\Delta P_{th,\ SND} = -N_{CS}\ \frac{1}{2}\rho u_{tip}^2$ (mm water)		-27	-109	-245
ψ_{SND}	$B = 0.40$	0.44	0.44	0.46
	$B = 0.33$	0.37	0.42	0.44
	$B = 0.30$	0.29	0.42	0.42
	$B = 0.21$	0.15	0.31	0.35

Fig. 3.9 is a plot of wide-open flow Q_0 against rotor speed for the four values of B. The values of Q_0 were obtained from the intersection points of the ΔP vs Q graphs with the horizontal axes shown in figs 3.7(a) - (c). In the case where rotor speed was 500 RPM, the ΔP vs Q lines are nearly parallel to the horizontal (flow) axis, and so these values of Q_0 are subject to greater uncertainty that those corresponding to the higher rotor speeds.

The fan laws predict that Q_0 should be proportional to rotor speed; again, the data shown in fig. 3.9 are consistent with this prediction, the largest deviations from linearity occurring at the lowest rotor speed, at which the values of Q_0 are least well defined.

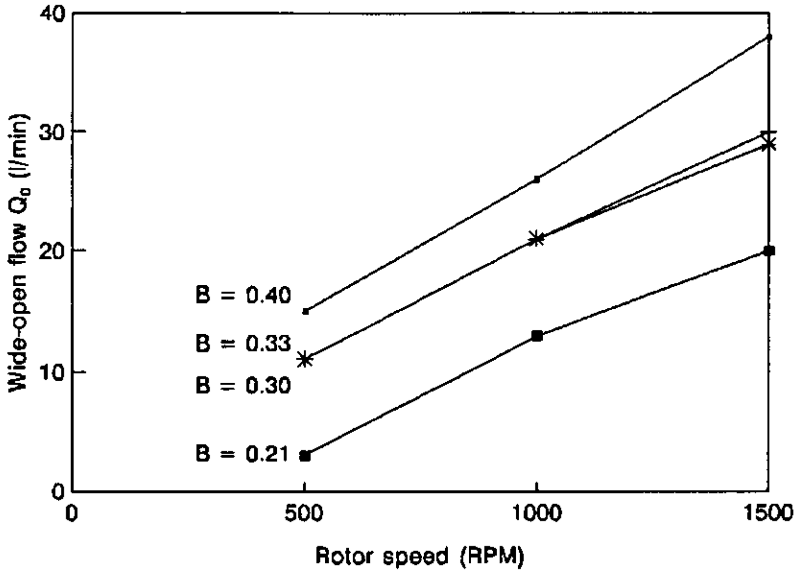

Figure 3.9
Variation of wide-open flow Q_0 with rotor speed for various values of spacing parameter B (Note that the plots for B = 0.33 and 0.30 are very nearly coincident)

Table 3.9
Values of wide-open flow coefficient, ϕ_0

	Rotor speed (RPM)	500	1000	1500
ϕ_0	B = 0.40	0.0058	0.0050	0.0049
	B = 0.33	0.0043	0.0041	0.0039
	B = 0.30	0.0043	0.0041	0.0037
	B = 0.21	0.0012	0.0025	0.0026

Eck (1973) gives typical values of ϕ for various common types of impeller design; in particular for centrifugal impellers in which the radial blade length is 70% of the impeller radius ϕ varies between 0 and 0.03; where the radial blade length is 85% of the impeller radius ϕ varies between 0 and 0.00185.

3.4.2.3 Fan performance of a full-size SCC

Pressure drop trials, using air, were conducted on a full-size SCC to assess its fan performance. This column had N_{CS} = 20 cone sets and a spinning cone outer diameter d = 720 mm. Data were obtained at rotor speeds of 380 and 560 RPM. The observed values of the static no-discharge pressure and wide-open flow, along with the corresponding non-dimensional coefficients are given in table 3.10.

Table 3.10
Fan performance parameters of a full-size SCC

Rotor speed (RPM)	u_{tip} (m/s)	ΔP_{SND} (mm water)	Q_0 (l/min)	ψ_{SND}	ϕ_0
380	14.3	-95	1440	0.38	0.004
560	21.1	-210	2060	0.38	0.004

The values of the pressure and flow coefficients ψ_{SND} and ϕ_0 agree well with those obtained on the (smaller) test column (see tables 3.8 and 3.9); this agreement suggests that for design purposes, values of $\psi_{SND} = 0.4$ and $\phi_0 = 0.004$ will give satisfactory predictions of SCC fan performance across a wide range of sizes of column.

3.4.3 Effect of rotor speed on pressure drop at flows in excess of Q_0

To study the effect of rotor motion on pressure drop across the full range of flows covered by the experimental data we define the change in pressure drop due to rotor motion, ΔP_r, as

$$\Delta P_r = \Delta P_{MRDC} - \Delta P_{FRDC} \tag{3.28}$$

where ΔP_{MRDC} is the observed moving-rotor dry-column pressure drop and
ΔP_{FRDC} is the observed fixed-rotor dry-column pressure drop at the same gas flow.

Fig. 3.10 is a plot of ΔP_r against air flow Q for a rotor speed of 1500 RPM. Fig. 3.11 is a plot of the same data but in this case plotted against air mass velocity G.

Consider first the variation of ΔP_r with Q (fig. 3.10); we see that the curves for all values of B, whilst not precisely coincident, lie close together (for the most part within the 95% confidence limits set out in table 3.10) and have the same general shape. This suggests that we might characterize the relationship between ΔP_r and Q by using five parameters: firstly, at $Q = 0$ ΔP_r is simply equal to ΔP_{SND}, the static no-discharge pressure discussed in the previous section; ΔP_r then rises rapidly with Q attaining a maximum value $\Delta P_{r,max}$ of about 180 mm water at a flow Q_1 of 160 l/min. As flow increases above Q_1, ΔP_r falls gradually, approaching a constant value $\Delta P_{r,final}$ of about 100 to 120 mm water at a flow Q_2 of about 300 to 400 l/min. Note that when these same ΔP_r data are plotted against air mass velocity G (see fig. 3.11), the resulting curves do not coincide as closely, suggesting that, unlike fixed-rotor dry-column pressure drop, rotor-induced pressure drop is a function of gas flow rather than of maximum gas velocity.

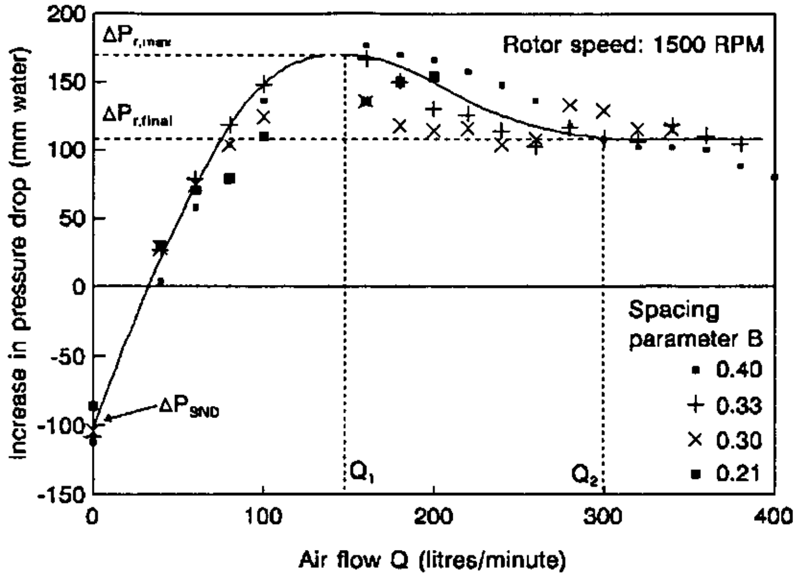

Figure 3.10
Increase in pressure drop due to rotor motion ΔP_r vs air flow Q for various values of spacing parameter B at a rotor speed of 1500 RPM

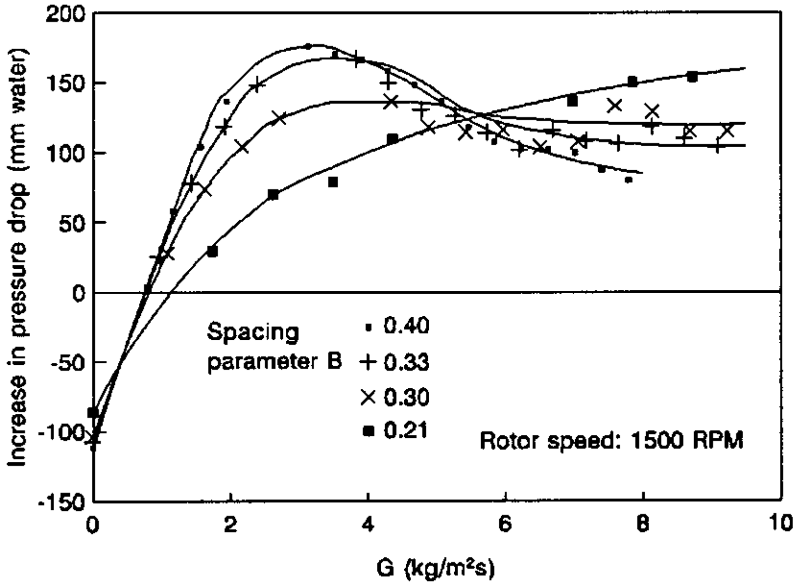

Figure 3.11
Increase in pressure drop due to rotor motion ΔP_r vs air mass velocity G for various values of spacing parameter B at a rotor speed of 1500 RPM

Figs 3.12 and 3.13 are similar plots to fig. 3.10, but for rotor speeds of 1000 and 500 RPM. Note that the curves for 500 RPM are not nearly so well defined; this is not altogether surprising, given that the effect of rotor speed at 500 RPM is slight (see figs 3.11(a) - (d)) and with the effects of experimental error (see table 3.7), small differences between the fixed- and moving-rotor pressure drops are likely to be quite scattered, especially at higher air flows where the experimental error is largest. Notwithstanding the inherent imprecision of these data, estimates of the five characteristic parameters are given in table 3.11. Note that no differentiation has been made between values of spacing parameter *B*; inspection of figs 3.10, 3.12 and 3.13 shows that *B* does appear to influence the relationship between ΔP_r and Q. For the purposes of devising an approximate numerical description, however, these differences will be ignored.

Table 3.11

Estimates of the five parameters defining relationship between ΔP_r and Q

Rotor speed (RPM)	ΔP_{SND} (mm water)	$\Delta P_{r,max}$ (mm water)	$\Delta P_{r,final}$ (mm water)	Q_1 (l/min)	Q_2 (l/min)
500	-10	14 - 18		60 - 80	
1000	-50	60 - 80	20 - 40	100	200 - 300
1500	-110	130 - 180	100 -120	160	300 - 400

We can express these parameters in non-dimensional form using the pressure and volume coefficients defined in section 3.4.1.2; see table 3.12.

Table 3.12

Non-dimensional parameters defining relationship between ΔP_r and Q

Rotor speed (RPM)	ψ_{SND}	Φ_0	$\psi_{r,max}/\psi_{SND}$	$\psi_{r,final}/\psi_{SND}$	Φ_1/Φ_0	Φ_2/Φ_0
500	0.35	0.005	-1.4 to -1.8		4 to 5	
1000	0.40	0.005	-1.2 to -1.6	-0.4 to -0.8	4.5	9 to 14
1500	0.40	0.005	-1.2 to -1.6	-0.9 to -1.1	4 to 5	9 to 14

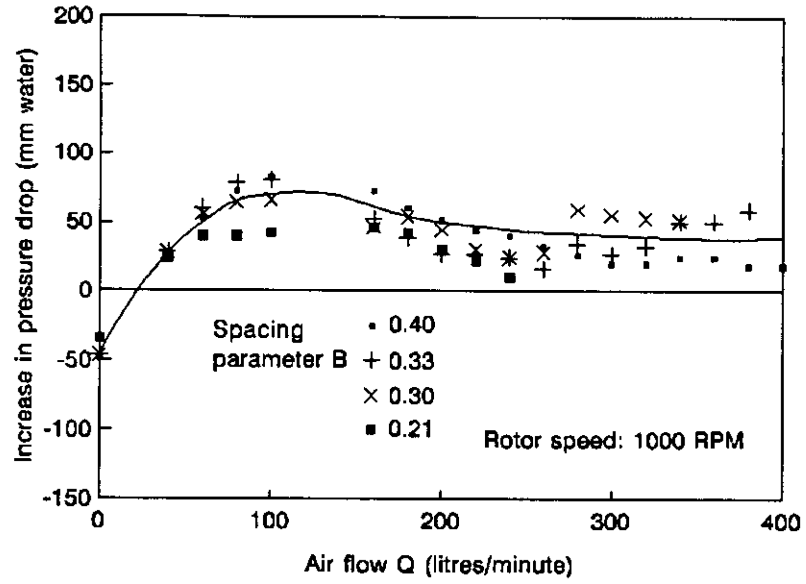

Figure 3.12
Increase in pressure drop due to rotor motion ΔP_r vs air flow *Q* for various values of spacing parameter *B* at a rotor speed of 1000 RPM

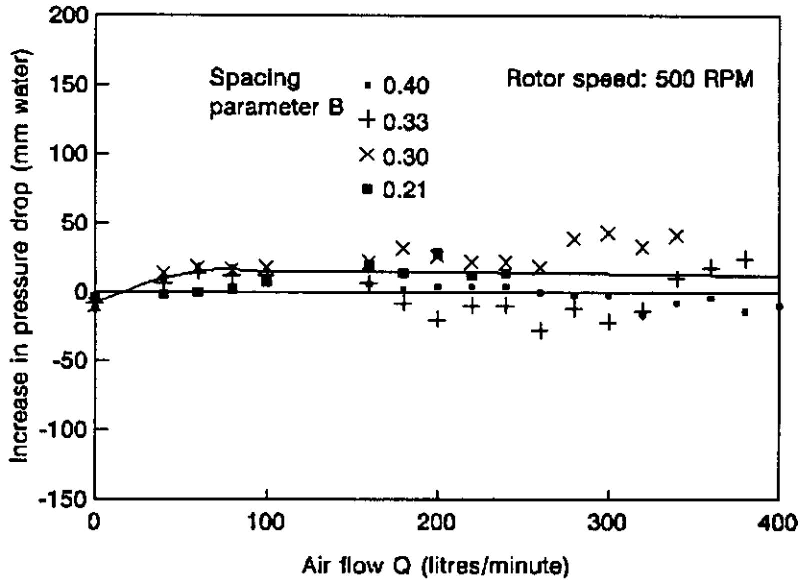

Figure 3.13
Increase in pressure drop due to rotor motion ΔP_r vs air flow *Q* for various values of spacing parameter *B* at a rotor speed of 1000 RPM

3.5 Prediction of dry-column pressure drop for design

We can use the non-dimensional parameters in table 3.12, along with known values of rotor speed and diameter of the spinning cone, to predict the relationship between the moving-rotor dry-column pressure drop ΔP_{MRDC} and gas flow Q for design; a conservative estimate would be based on the higher values from the ranges given.

In order to illustrate this proposed procedure for prediction of dry-column pressure drop we use the data listed in table 3.13.

Table 3.13
Data for illustration of procedure for design estimation of ΔP_{MRDC}

Spinning cone diameter, *d*	0.128 m
Rotor speed, ω	1000 RPM = 105 s^{-1}
Spacing parameter, *B*	0.40
Minimum flow area, A_{min}	0.00103 m^2
Gas density, ρ	1.204 kg/m^3
Number of cone sets, N_{CS}	40

(a) we obtain the fixed-rotor dry-column pressure drop (in mm water) from eq. (3.19) with $B = 0.40$; i.e.

$$\Delta P_{FRDC} = \frac{N_{CS}}{9.81} \times 3.43 \times \frac{G^{2.12}}{2\rho}$$

(b) we use the non-dimensional parameters in table 3.12 and the data in table 3.13 to estimate the pressure drop due to rotor motion ΔP_r; i.e.

$$\begin{aligned} u_{tip} &= 6.70 \text{ m/s} \\ \Delta P_{th,SND} &= -N_{CS} \times \tfrac{1}{2}\rho u_{tip}^2 \\ &= -110 \text{ mm water} \end{aligned}$$

We assume the following dimensionless relationships (based on discussion in section 3.4.3):

$$\begin{aligned} \phi_0 &= 0.005 & \psi_{SND} &= 0.4 \\ \phi_1/\phi_0 &= 5 & \psi_{r,max}/\psi_{SND} &= -1.6 \\ \phi_2/\phi_0 &= 14 & \psi_{r,final}/\psi_{SND} &= -0.8 \end{aligned}$$

(i) Static no-discharge pressure $\Delta P_{SND} = \psi_{SND} \times \Delta P_{th,SND}$
$= 0.4 \times -110$
$= -44$ mm water

(ii) For $Q = 0$ $\quad \Delta P_r = \Delta P_{SND}$
$= -44$ mm water

(iii) Wide-open flow $\quad Q_0 = \phi_0 \times \tfrac{1}{4}\pi d^2 u_{tip}$
$= 0.005 \times 0.0862$
$= 4.31 \times 10^{-4}\ \mathrm{m^3/s}$
$= 26$ l/min

(iv) For $Q = Q_0$ $\quad \Delta P_r = -\Delta P_{FRDC}$
i.e. $\quad \Delta P_{MRDC} = \Delta P_{FRDC} + \Delta P_r$
$= 0$

(v) $\quad Q_1 = \phi_1/\phi_0 \times Q_0$
$= 5 \times 26$
$= 130$ l/min

(vi) For $Q = Q_1$ $\quad \Delta P_r = \Delta P_{r,max}$
$= \psi_{r,max} / \psi_{SND} \times \Delta P_{SND}$
$= -1.6 \times -44$
$= 71$ mm water

(vii) $\quad Q_2 = \phi_2/\phi_0 \times Q_0$
$= 14 \times 26$
$= 360$ l/min

(viii) For $Q = Q_2$ $\quad \Delta P_r = \Delta P_{r,final}$
$= \psi_{r,final} / \psi_{SND} \times \Delta P_{SND}$
$= -0.8 \times -44$
$= 35$ mm water

(c) we obtain the total moving-rotor dry-column pressure drop from

$$\Delta P_{MRDC} = \Delta P_{FRDC} + \Delta P_r$$

Fig. 3.14 is a plot of the total moving-rotor dry-column pressure drop calculated using this procedure against air flow; also shown is the experimentally observed relationship between ΔP_{MRDC} and air flow in the test column at a rotor speed of 1000 RPM and $B = 0.40$. Note that the predicted relationship between ΔP_{MRDC} and Q is based on the location of only four points; the procedure is predicated on the assumption that these four points adequately characterize the relationship when used in conjunction with the predicted fixed-rotor dry-column pressure drop. There are not sufficient data reported in the present work to test the validity of this assumption; indeed, establishing more firmly the relationship between ΔP_{MRDC} and Q is an appropriate area for further study, particularly with regard to the influence of cone set geometry and fin design.

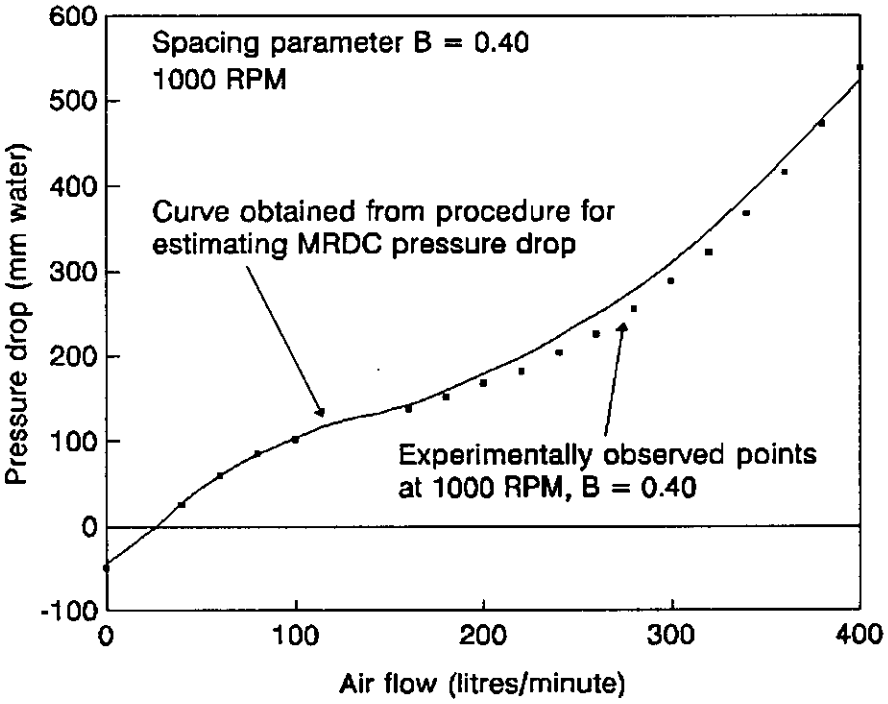

Figure 3.14
Variation of pressure drop with air flow in test (small) column: experimentally observed points and curve obtained from estimation procedure described above

3.6 Pressure drop in the dry column: summary

The purpose of this chapter has been to consider pressure drop in the SCC in the absence of liquid flow, in particular to study the way pressure drop in the SCC responds to gas flow, rotor motion and cone set configuration, and ultimately to devise a numerical representation of the observed behaviour which could serve both as the basis for predicting dry-column pressure drop in the course of design and as the foundation for more comprehensive models of pressure drop in the SCC.

The task was approached in two stages: firstly the behaviour of pressure drop with the rotor stationary was studied, and its response to gas flow and cone set configuration quantified; secondly pressure drop with the rotor in motion was studied, and described in the context of its differences from the behaviour of the column with the rotor stationary.

3.6.1 Fixed-rotor dry-column pressure drop

Pressure drop in the SCC with rotor fixed and in the absence of liquid flow was found to be well correlated ($r^2 > 0.98$) by an equation of the form

$$\Delta P_{CS} = b_0 G^{b_1}$$

where ΔP_{CS} is the pressure drop per cone set (mm water),
G is the maximum gas mass velocity within the cone set (kg/m^{2}s),
$b_0 = 0.21 \pm 0.023$, and
$b_1 = 1.97 \pm 0.07$.

Although this equation was obtained from pooled data, for all values of position parameter B, the values of b_0 and b_1 in fact exhibited slight but statistically significant variation with B.

The regression analysis of experimental data, on which the above results were based, was broadly consistent with estimates of pressure drop obtained using published pressure loss coefficients for the flow of air in ducts; the most important aspect of this procedure was that it indicated that by far the greatest part of the fixed-rotor pressure drop is due to the multiple reversals in flow direction experienced by the gas stream on its passage through the column.

3.6.2 Moving-rotor dry-column pressure drop

Pressure drop in the SCC with the rotor in motion was represented as a modification of fixed-rotor behaviour, the nature and magnitude of the modification being related to rotor speed, gas flow and cone set configuration.

The numerical representation of the moving-rotor pressure drop behaviour was based on consideration of a pressure drop due to rotor motion

$$\Delta P_r = \Delta P_{MRDC} - \Delta P_{FRDC}$$

where ΔP_r is the pressure drop due to rotor motion,
ΔP_{MRDC} is the total pressure drop (with rotor moving), and
ΔP_{FRDC} is the fixed-rotor pressure drop at the same gas flow.

The basic form of the relationship between ΔP_r and Q was quantified by relating dimensionless coefficients obtained by considering the SCC as a multi-stage centrifugal fan to the experimentally observed variation of ΔP_r with Q.

This approach to the characterization of pressure drop in the SCC is based on a limited data set, and warrants more exhaustive validation.

CHAPTER 4

PHYSICAL CAPACITY AND LIMITS OF OPERATION OF THE SPINNING CONE COLUMN

4.1 Introduction

The subject of this chapter is the physical capacity of the SCC, and is approached from the point of view of design. That is, we address specifically the following question: given a particular column and set of operating conditions (liquid flow, pressure, temperature, rotor speed, cone set geometry etc.) what is the highest gas rate that can be achieved while maintaining stable operation and acceptable mass transfer performance? (Note that in general a designer/operator will also be concerned with the extent of the operating range ("turndown") and so requires knowledge of the minimum load at which acceptable performance can be maintained; this aspect of SCC operation is not considered in the present work).

In Chapter 2 it was shown that the prediction of physical capacity of packed columns is based on consideration of pressure drop of turbulent gas flow through a packed bed. Parallels can be drawn between the modes of operation of packed columns and the SCC: in both types the vapour and liquid phases are effectively continuous rather than one or other being the dispersed phase. In fact, both types of column could be considered to be particular classes of falling film contactor.

The conceptual similarity between the modes of operation of packed columns and the spinning cone column suggest that an approach to the prediction of physical capacity similar to those used for packed columns may be applied to the SCC.

In this chapter, the experimental determination of flood points on three different spinning cone columns is reported. The data so obtained are used to correlate flooding in the SCC with material flows and properties, and with geometrical and configurational parameters.

Descriptions of the three SCCs and the experimental procedures used are given in section 4.2.

The experimental results are discussed in section 4.3; we start by considering pressure drop in the SCC in the presence of liquid flow, which leads us directly to a discussion of flooding behaviour in the SCC, and thence to generalized correlation of SCC flooding behaviour and capacity limits.

4.2 Materials and methods

4.2.1 Equipment

Table 4.1
Dimensions of SCCs for which flooding data were obtained

	Small SCC	Medium SCC	Large SCC
Shaft radius, R_S (mm) Column inner radius, R_C (mm)	21 73	25 185	45 458
Spinning cone: Inner radius, R_{SI} (mm) Outer radius, R_{SO} (mm)	 25 64	 50 145	 125 360
Fixed cone: Inner radius, R_{FI} (mm) Outer radius, R_{FO} (mm)	 35 73	 50 145	 160 360
Cone angle, θ Cone pitch, P_C (mm)	50° 21	45° 40	45° 130
Number of cone sets, N_{CS}	40	30	21

Table 4.2
Flow areas, inter-cone gaps and wetted area per unit gas volume for the three SCCs for which flooding data were obtained

	Small SCC			Medium SCC	Large SCC
Spacing parameter B	0.40	0.33	0.30	0.70	0.50
A_1 (m^2)	0.00244	0.00244	0.00244	0.00589	0.07420
A_2 (m^2)	0.00149	0.00164	0.00172	0.00227	0.03990
A_3 (m^2)	0.00311	0.00347	0.00365	0.00617	0.09515
A_4 (m^2)	0.00409	0.00409	0.00409	0.04147	0.25184
A_5 (m^2)	0.00175	0.00144	0.00128	0.01584	0.09515
A_6 (m^2)	0.00103	0.00084	0.00074	0.00645	0.04849
t_U (mm)	4.5	3.7	3.3	18.2	44
t_L (mm)	7.4	8.2	8.6	6.9	44
a_p (m^2/m^3)	123			52.3	15.2

4.2.2 Experimental procedure

4.2.2.1 Pressure drop trials on the small column

The bulk of the experimental data referred to in this chapter were obtained from pressure drop trials on the small test column (see dimensions in tables 4.1 and 4.2). In these pressure drop trials the following operating parameters were varied:

(a) Liquid flow
Liquid flow was varied between zero and 0.025 kg/s in steps of 0.05 kg/s. In all trials on the small column liquid flow was measured using an electronic vibrating-tube mass flow meter.

(b) System
Trials were conducted with air and water at atmospheric pressure, steam and water at atmospheric pressure, and steam and water at reduced pressure.

(c) Rotor speed
Trials were run at three rotor speeds, 500, 1000 and 1500 RPM: a variable frequency motor speed controller was used to vary the rotor speed.

(d) Spacing parameter *B*
Measurements of pressure drop in the presence of liquid flow were obtained at three values of spacing parameter *B*: 0.30, 0.33 and 0.40. Stable flow of liquid through the column was not possible at *B* = 0.21. The spacing parameter *B* was varied in the manner described in section 3.2.2. Details of the three values of spacing parameter for which pressure drop and flooding data were obtained, and corresponding geometrical parameters, are given in table 4.2.

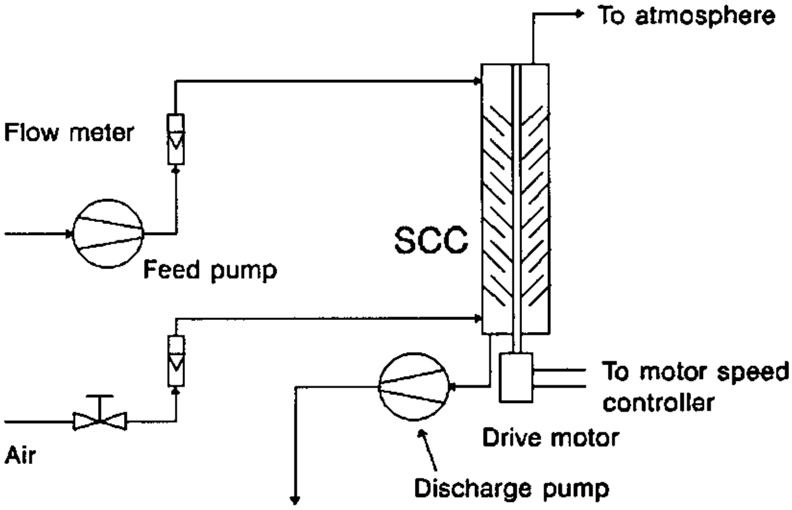

Figure 4.1
Schematic diagram of experimental set-up for air/water pressure drop trials on small column

Pressure tappings at the vapour inlet and outlet of the column were connected to a water manometer. In the air/water trials air from the high pressure mains was admitted to the column at its base. The air flow was measured by one of two rotameters, 150 l/min and 400 l/min capacity. The layout of the system used in the air/water trials on the small column is shown in fig. 4.1.

For steam/water trials the procedure was the same except that vapour flow was determined by measuring the flow of condensate from the overhead condenser. For the runs conducted at atmospheric pressure this flow was measured using a rotameter in the condensate discharge line (see fig. 4.2). For the runs conducted under vacuum this condensate flow was measured by allowing the condensate to drain into a collection vessel, also under vacuum, for a fixed time interval, then isolating the collection vessel from the system vacuum and draining the collected liquid from the vessel into a measuring cylinder (see fig. 4.3)

Vapour flow was controlled by a manual throttling valve on the steam line into the base of the column. The feed was brought up to the operating temperature of the column in a steam-heated pre-heater; the feed temperature was controlled by manual adjustment of a throttling valve on the steam supply to the pre-heater.

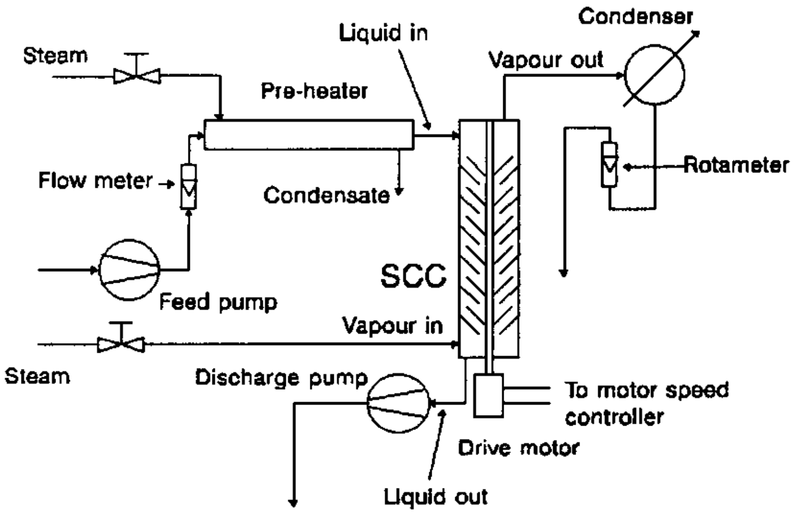

Figure 4.2
Schematic diagram of experimental set-up for steam/water pressure drop trials at atmospheric pressure on small column

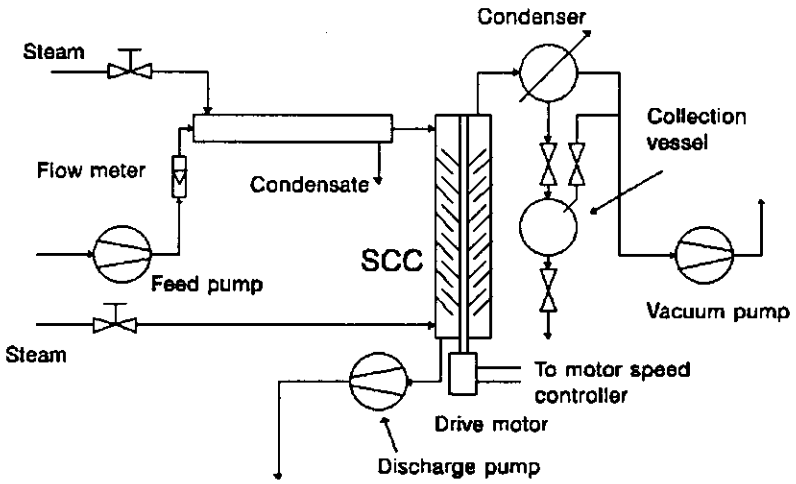

Figure 4.3
Schematic diagram of experimental set-up for steam/water pressure drop trials under vacuum on small column

(Some of the small column trials reported here were conducted, under the author's supervision, by Messrs J. Sywak and A. Dorigo, undergraduate students on vacation placement from the Dept of Chemical Engineering, University of Sydney.)

4.2.2.2 Flooding trials on medium column

Flooding data were obtained on the medium column (CSIRO Mk III SCC; see dimensions in tables 4.1 and 4.2) using steam and water both at atmospheric pressure and under vacuum. The rotor was 500 RPM in all cases. In the atmospheric pressure runs the liquid flow was varied between 2.8 and 10 kg/min. Vacuum runs were conducted at pressures ranging between 20 and 50 kPa abs.; the liquid flow varied between 2 and 4 kg/min.

The experimental procedure followed in the medium column runs differed from that used on the small column. Flood points were identified on the medium column by monitoring pressure drop, but also by checking the discharge flow; when the column was flooded the discharge flow fell sharply, indicating that liquid was accumulating inside the column. In general flooding was indicated by a steady rise in pressure drop and, at some point, a sharp fall in the discharge flow. Pressure drop data of the same form as obtained on the small column were not as indicative of column behaviour in this case; at atmospheric pressure the pressure drop was low and changed very little with vapour flow until flooding occurred, at which point stability was lost and pressure drop continued to rise even though the liquid and vapour flows remained unchanged.

(Some of the medium column trials reported here were conducted, under the author's supervision, by Ms I. el Mahmoud, an undergraduate student on vacation placement from the Dept of Chemical Engineering, University of Sydney.)

4.2.2.3 Flooding trials on large column

The large column flooding data were obtained in the course of commissioning and subsequent testing of a commercial 10000 litre/hour SCC. Steam and water were used in all cases; the system was operated under vacuum (20 kPa abs.). The liquid flow varied between 1500 and 9000 kg/hour (25 to 150 kg/min.).

The flood points were identified by direct observation of the column behaviour rather than by inspection of the response of pressure drop to gas flow; external indications of flooding include:

- a sudden fall in discharge flow
- an abrupt rise in current drawn by the rotor drive motor
- overflow of liquid into the condensing system

In general, flooding will be indicated by some, though not necessarily all, of these changes in column behaviour. Moreover, since large SCCs, including the one on which these data were obtained, have viewports installed in the shell of the column it is possible to see directly whether liquid is accumulating inside the column; this is the simplest and most positive indication of flooding.

4.3 Results and discussion

The results of the pressure drop trials on the small column are presented in full, in both graphic and tabular form, in Appendices 1 and 2 respectively. In the following discussion certain figures from Appendix 1 are reproduced, the purpose being to illustrate points made in the discussion.

The results of flooding trials on the medium and large columns are also presented in tabular form in Appendix 2.

4.3.1 Pressure drop in the presence of liquid flow

In this section we will discuss the following questions:

(a) how does the presence of liquid flow modify the dry-column pressure drop response?
(b) what is the effect of vapour density on pressure drop?
(c) what is the effect of rotor speed on pressure drop in the presence of liquid flow?
(d) what is the effect of cone set geometry (i.e. spacing parameter *B*) on pressure drop in the presence of liquid flow?

4.3.1.1 General observations on the effect of liquid flow on pressure drop in the SCC

The general effect of liquid flow on pressure drop in the SCC is illustrated in figs 4.4 and 4.5. Fig. 4.4 is a plot of pressure drop against air flow for liquid flows from zero to 0.025 kg/s at a rotor speed of 1000 RPM and a spacing parameter *B* of 0.40.

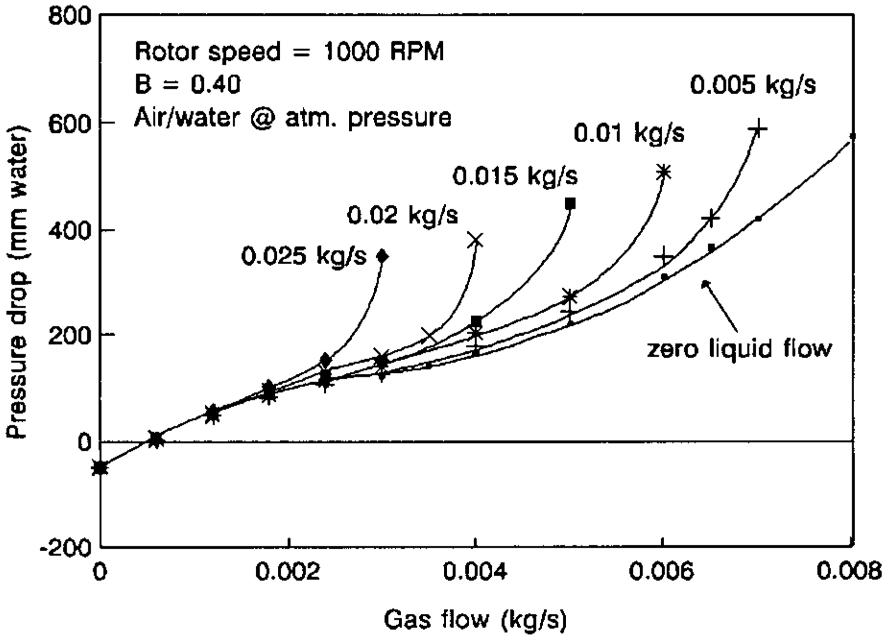

Figure 4.4
Variation of pressure drop in the small column with air flow for various liquid flows: rotor speed = 1000 RPM, B = 0.40.

In broad terms, the presence of liquid flow makes the following changes to the dry-column pressure drop response:

(a) at low gas rates the pressure drop is approximately equal to the dry-column pressure drop.

(b) as the gas rate rises the difference between wet- and dry-column pressure drops increases.

(c) at a fixed (low) gas rate, the difference between wet- and dry-column pressure drops increases as liquid flow increases; for the conditions represented in fig. 4.4 the wet-column pressure drop is at most 20% higher than the corresponding dry-column value for gas rates below the flood point (see (d) below).

(d) for all non-zero liquid flows, a gas rate is reached at which the pressure drop across the column begins to rise much more steeply than the corresponding dry-column pressure drop. The gas rate at which this sudden increase occurs falls as liquid flow rises. This deviation from dry-column behaviour marks the onset of flooding in the SCC, and the limits of physical capacity. Note the close correspondence between this behaviour and the loading and flooding behaviour typically observed in packed columns (see fig. 2.8).

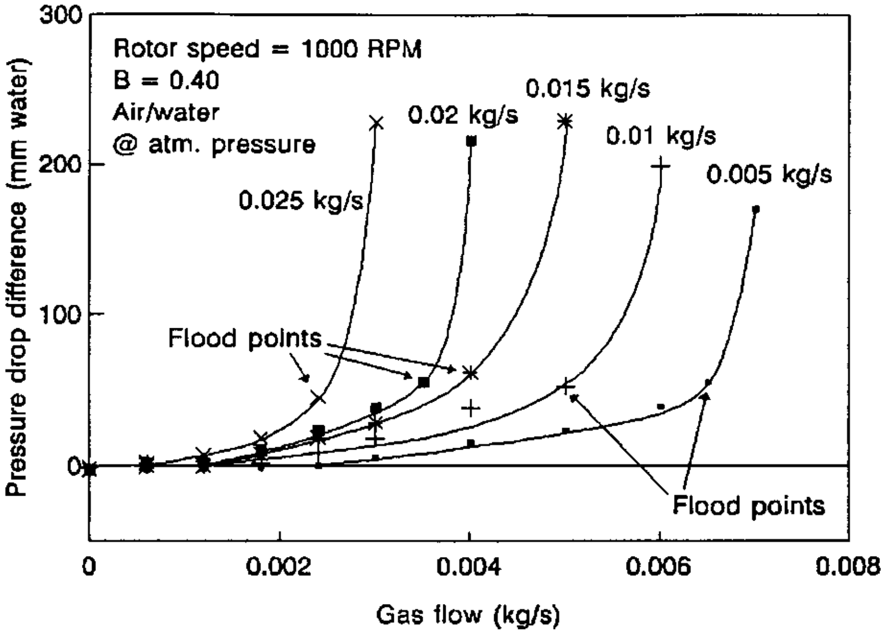

Figure 4.5
Difference between wet- and dry-column pressure drops, showing flood points: rotor speed = 1000 RPM, *B* = 0.40.

Fig. 4.5 is a plot of the difference between the wet-column pressure drop and the dry-column pressure drop at the same gas flow; in this graph the onset of flooding is clearly indicated by a sharp increase in the difference between the wet- and dry-column pressure drops. Graphs of this type are included in Appendix 1 along with the actual pressure drop profiles, because the flood points are more easily identified in plots of this type and because the effect of liquid flow on pressure drop is more clearly illustrated.

Throughout the discussion of capacity limits and flooding in the small column we will use this definition of the flood point: the gas rate at which the wet-column pressure drop increases sharply above the corresponding dry-column value.

It is important to recognize that the definition of flood point is somewhat arbitrary; we could for instance have defined it as the "break point" in the plot of wet-column pressure drop vs gas flow; our definition has been chosen, at least in part, because it is simple and relatively unambiguous; it is simply the value of *G* at the last observation before an abrupt increase in the difference between the wet- and dry-column pressure drops is observed.

Note that in defining the flood point in this way we are not distinguishing between flooding and loading behaviour as is conventionally done with respect to packed columns. The form of the pressure drop difference plots (fig. 4.5 and similar graphs in Appendix 1) suggests that the SCC does not exhibit distinct loading and flooding points.

4.3.1.2 Effect of vapour density on pressure drop

The effect of vapour density on pressure drop in the SCC is illustrated in figs 4.6 and 4.7.

Fig. 4.6 shows the variation of pressure drop with gas rate for air and water at atmospheric pressure, steam and water at atmospheric pressure and steam and water at 20 kPa abs. (liquid flow = 0.01 kg/s, spacing parameter B = 0.40 and rotor speed = 500 RPM). Under these conditions the gas densities are 1.20, 0.60 and 0.13 kg/m^3.

We see from fig. 4.6 that as gas density is reduced the gas rate which gives rise to a given pressure drop also falls. This result conforms with our expectations: we expect pressure drop ΔP to be proportional to G^2/ρ, where G is the gas mass velocity and ρ is the gas density. Hence as ρ is reduced the value of G which gives rise to a given pressure drop must also fall. We can check whether the effect of gas density is fully accounted for by normalizing the gas rates in the following way:

$$m_{GN} = m_G \times \sqrt{\rho_{ref}/\rho_G} \tag{4.1}$$

where m_G is the gas mass flow,
m_{GN} is the normalized gas mass flow,
ρ_G is the gas density, and
ρ_{ref} is an arbitrary reference density (in this case that of air at atmospheric pressure).

Fig. 4.7 shows the same data as in fig. 4.6 but in this case plotted against normalized gas rate. The coincidence of the three pressure drop curves indicates that the effect of gas density on pressure drop is fully accounted for by use of the normalized gas rate.

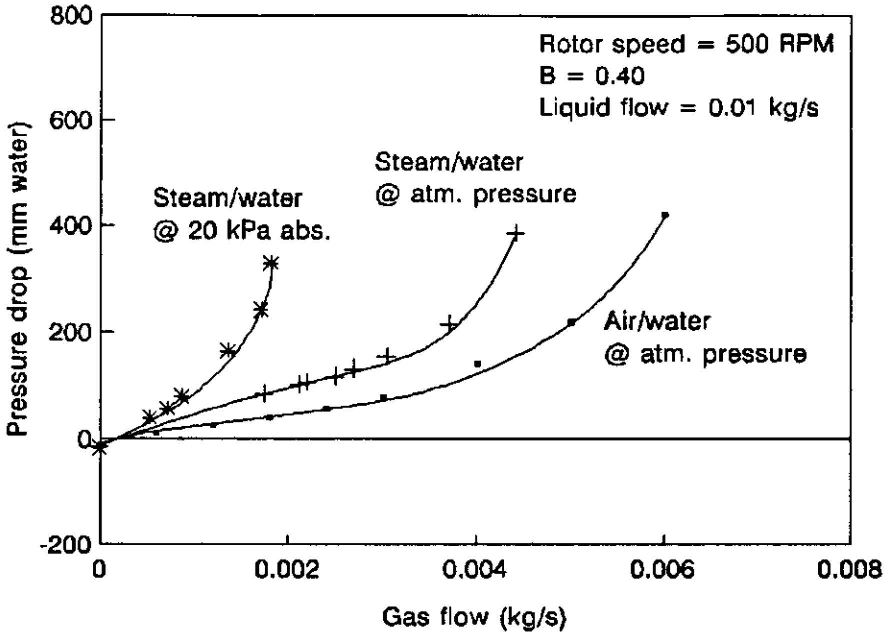

Figure 4.6
Variation of pressure drop with gas rate for air/water at atm. pressure, steam/water at atm. pressure and steam/water at 20 kPa abs.: liquid flow = 0.01 kg/s, $B = 0.40$, rotor speed = 500 RPM

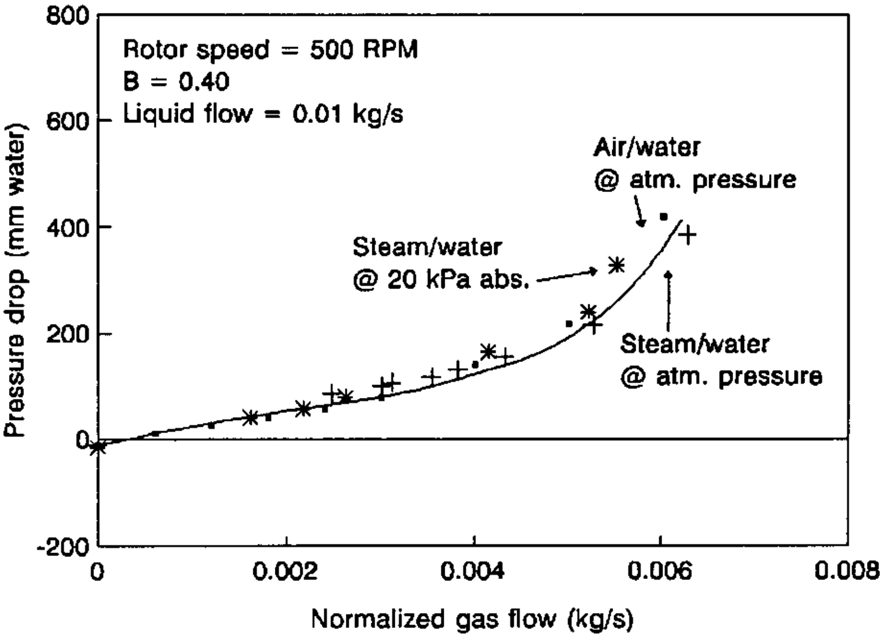

Figure 4.7
Variation of pressure drop with normalized gas rate for air/water at atm. pressure, steam/water at atm. pressure and steam/water at 20 kPa abs.: liquid flow = 0.01 kg/s, $B = 0.40$, rotor speed = 500 RPM

4.3.1.3 The effect of rotor speed and spacing parameter on pressure drop in the presence of liquid flow

The effects of rotor speed and spacing parameter on pressure drop in the presence of liquid flow are discussed jointly because there is evidence that they interact; specifically, the largest deviations from the general pattern of pressure drop variation in the presence of liquid flow occur when both rotor speed and spacing parameter are low.

Figs 4.8, 4.9 and 4.10 are plots of the difference between wet- and dry-column pressure drops, henceforth designated ΔP_L (the change in pressure drop across the column due to the presence of liquid flow), against gas rate for the three values of rotor speed and spacing parameter, and at a liquid flow of 0.01 kg/s. We can assess the effects of rotor speed and spacing parameter on pressure drop in the presence of liquid flow by considering these graphs in turn.

At 500 RPM and $B = 0.40$ (see fig. 4.8), the wet-column pressure drop is hardly changed from the corresponding dry-column value (i.e. $\Delta P_L \approx 0$) until the onset of flooding. With $B = 0.33$ the pattern is similar although ΔP_L is greater at all gas rates.

With the spacing parameter $B = 0.30$ a marked change is apparent; ΔP_L rises sharply as gas rate rises from zero to 0.002 kg/s, then falls between 0.002 and 0.004 kg/s, at which value it rises sharply again with the onset of flooding.

Fig. 4.9 shows data for identical conditions except at a rotor speed of 1000 RPM rather than 500 RPM. Again, at $B = 0.40$ ΔP_L is smallest, although there is a steady rise with gas rate until the onset of flooding. At the lower values of B this pattern is maintained but the value of ΔP_L increases as B is reduced. At 1500 RPM (see fig. 4.10) the variation of ΔP_L with gas rate, prior to the onset of flooding, is similar to that observed at 1000 RPM.

Note that the sharp rise and fall in ΔP_L at low gas rates observed at 500 RPM and $B = 0.30$ is not apparent at the higher rotor speeds. Inspection of the full set of pressure drop profiles in the Appendix 1 that this behaviour was consistently observed at 500 RPM and the two lower values of spacing parameter B. Fig. 4.11, which shows the variation of ΔP_L with gas rate at 500 RPM and $B = 0.33$, indicates that the intensity of this phenomenon, increases with liquid flow.

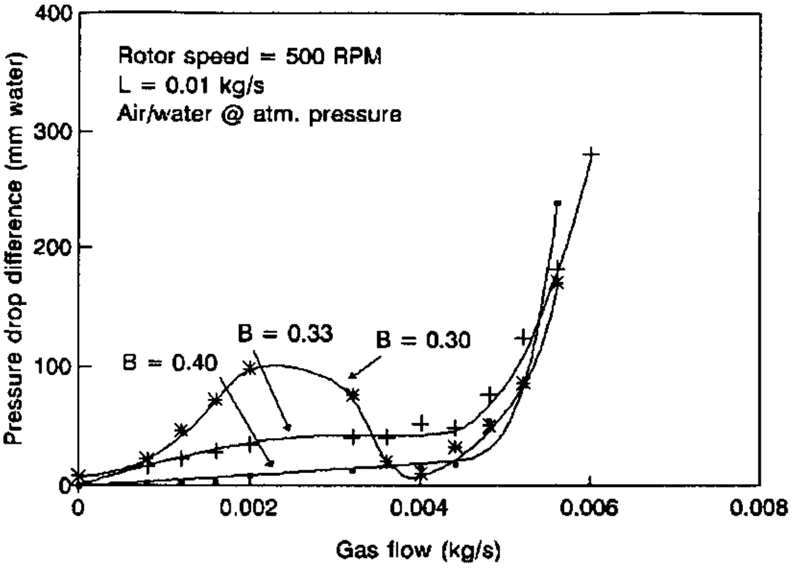

Figure 4.8
Variation of difference between wet- and dry-column pressure drops with gas rate for spacing parameter B = 0.40, 0.33 and 0.30; liquid flow = 0.01 kg/s, rotor speed = 500 RPM, air/water at atmospheric pressure

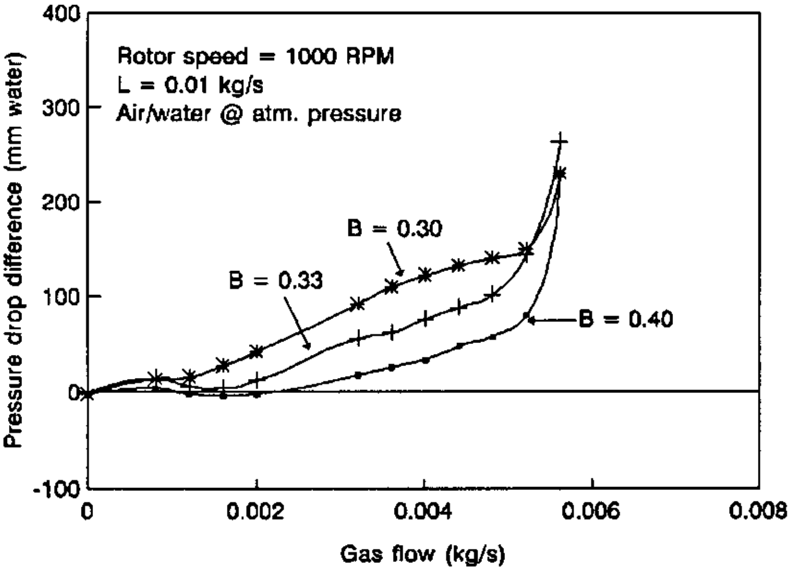

Figure 4.9
Variation of difference between wet- and dry-column pressure drops with gas rate for spacing parameter B = 0.40, 0.33 and 0.30; liquid flow = 0.01 kg/s, rotor speed = 1000 RPM, air/water at atmospheric pressure

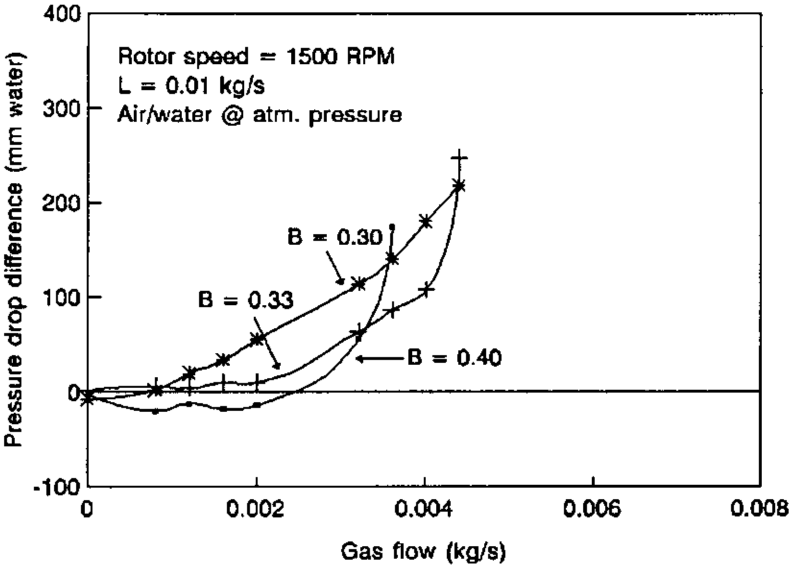

Figure 4.10
Variation of difference between wet- and dry-column pressure drops with gas rate for spacing parameter $B = 0.40$, 0.33 and 0.30; liquid flow = 0.01 kg/s, rotor speed = 1500 RPM, air/water at atmospheric pressure

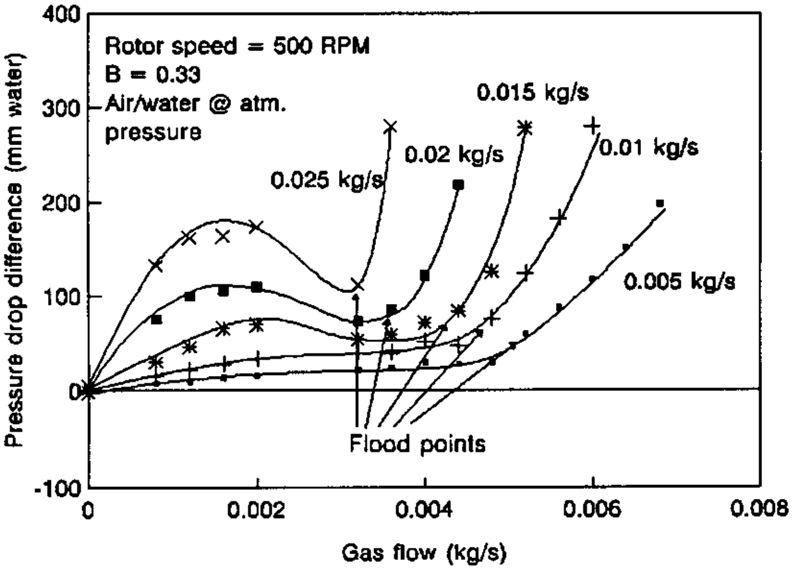

Figure 4.11
Variation of difference between wet- and dry-column pressure drops, ΔP_L, with gas rate; rotor speed = 500 RPM, $B = 0.33$, air/water at atmospheric pressure.

4.3.1.4 Pressure drop at low rotor speed

In general, the effect of liquid flow on pressure drop in the SCC is similar to that observed in packed columns. At low liquid rates the pressure drop is only marginally greater than the corresponding dry-column value until the onset of flooding, at which point it rises rapidly in response to the accumulation of liquid in the column. The data discussed in section 4.3.1.3 indicate, however, that in at least one respect the pressure drop behaviour of the SCC deviates significantly from that of packed columns: the sharp rise in pressure drop at low gas flows, low rotor speed and low values of spacing parameter *B*. This effect became more pronounced as spacing parameter was reduced from 0.40, but virtually disappeared at the higher rotor speeds. In other words, the intensity of this phenomenon, which we may term "pre-loading", is increased both as the liquid flow rises and as the gap between the base of the spinning cone and the lip of the stationary cone immediately above is reduced; it is decreased as the rotor speed rises.

This pattern suggests that pre-loading is brought about by interaction of the gas stream with liquid held up at the base of the spinning cone. We expect the volume of liquid retained in this region to rise with liquid flow and to fall as rotor speed is increased. The level of liquid in this region may be such that the area available for gas flow immediately below the lip of the stationary cone is significantly reduced; indeed, the sharp rise in pressure drop with the introduction of gas flow may be due to the necessity for the gas to force a path through this section by pushing some of the retained liquid away from the gap.

We may assume that the difference between wet- and dry-column pressure drops, ΔP_L, is a response to reduction in flow area and increased liquid hold-up. Flow area might be increased by forcing liquid away from the gap but this increase in area should be accompanied by an increased liquid hold-up term. Whether the reduction in ΔP_L due to increased flow area is necessarily be balanced by an increase in ΔP_L due to increased liquid hold-up cannot be determined from the data reported here; indeed they suggest that it is not.

Another possible explanation for the fall in ΔP_L is that the pressure drop due to the reversal in flow direction, which we believe to be the major component of dry column pressure drop, is in some way reduced by the presence of liquid flow.

4.3.2 Flooding in the SCC

In this section we discuss flooding in the SCC. The topic will be approached in the following way:

(a) the flooding data obtained on the small test column will be presented and analysed.

(b) a generalized correlation of these data, of the Sherwood-Leva-Eckert type discussed in Chapter 2, will be assessed, with particular reference to the choice of appropriate correlating parameters such as characteristic flow area and mean hydraulic radius.

(c) flooding data obtained on larger columns will be presented and discussed, with particular reference to their agreement with the generalized correlation set up using the small column flooding data.

4.3.2.1 Loading and flooding: identification of capacity limits

As foreshadowed in the discussion of pressure drop in the presence of liquid flow, there is no evidence of a distinct range of gas flow between loading and flooding. Therefore, we will speak only of flooding in the SCC, and we define the flood point as that gas rate at which the difference between wet- and dry-column pressure drops ΔP_L rises sharply (i.e. the break-point in the ΔP_L vs G curve).

4.3.2.2 Small column flooding data

The flood points obtained from pressure drop trials on the small column are tabulated in tables 4.3, 4.4 and 4.5, each table pertaining to a particular rotor speed. The abbreviations LP and AP refer to atmospheric pressure and low pressure (vacuum) respectively.

Table 4.3
Small column flood points, rotor speed = 500 RPM

Liquid flow	System	B	ρ_G	m_G	m_{GN}
kg/s			kg/m^3	kg/s	kg/s
0.005	LP steam/water	0.30	0.12	0.00158	0.00492
0.005	AP air/water	0.30	1.20	0.00562	0.00562
0.005	AP air/water	0.33	1.20	0.00522	0.00522
0.005	LP steam/water	0.40	0.13	0.00190	0.00578
0.005	AP steam/water	0.40	0.60	0.00394	0.00559
0.005	AP air/water	0.40	1.20	0.00562	0.00562
0.005	AP air/water	0.40	1.20	0.00652	0.00652
0.010	LP steam/water	0.30	0.12	0.00148	0.00459
0.010	AP steam/water	0.30	0.60	0.00351	0.00498
0.010	AP air/water	0.30	1.20	0.00522	0.00522
0.010	AP air/water	0.30	1.20	0.00482	0.00482
0.010	AP air/water	0.33	1.20	0.00482	0.00482
0.010	LP steam/water	0.40	0.13	0.00172	0.00522
0.010	AP steam/water	0.40	0.60	0.00371	0.00527
0.010	AP air/water	0.40	1.20	0.00522	0.00522
0.010	AP air/water	0.40	1.20	0.00552	0.00552
0.015	AP air/water	0.30	1.20	0.00401	0.00401
0.015	AP air/water	0.30	1.20	0.00401	0.00401
0.015	AP air/water	0.33	1.20	0.00441	0.00441
0.015	LP steam/water	0.40	0.13	0.00145	0.00441
0.015	AP steam/water	0.40	1.20	0.00502	0.00502
0.015	AP air/water	0.40	1.20	0.00452	0.00452
0.020	AP air/water	0.33	1.20	0.00361	0.00361
0.020	LP steam/water	0.40	0.13	0.00100	0.00304
0.020	AP steam/water	0.40	0.60	0.00220	0.00312
0.020	AP air/water	0.40	1.20	0.00401	0.00401
0.020	AP air/water	0.40	1.20	0.00401	0.00401
0.025	AP air/water	0.33	1.20	0.00321	0.00321
0.025	AP air/water	0.40	1.20	0.00271	0.00271
0.025	AP air/water	0.40	1.20	0.00321	0.00321

Table 4.4
Small column flood points, rotor speed = 1000 RPM

Liquid flow	System	B	ρ_G	m_G	m_{GN}
kg/s			kg/m^3	kg/s	kg/s
0.005	AP steam/water	0.30	0.60	0.00402	0.00570
0.005	AP steam/water	0.40	0.60	0.00423	0.00600
0.005	AP air/water	0.40	1.20	0.00652	0.00652
0.005	AP air/water	0.40	1.20	0.00642	0.00642
0.010	AP steam/water	0.30	0.60	0.00375	0.00532
0.010	AP air/water	0.30	1.20	0.00522	0.00522
0.010	AP air/water	0.33	1.20	0.00482	0.00482
0.010	AP steam/water	0.40	0.60	0.00353	0.00501
0.010	AP air/water	0.40	1.20	0.00502	0.00502
0.010	AP air/water	0.40	1.20	0.00522	0.00522
0.015	AP steam/water	0.30	0.60	0.00222	0.00315
0.015	AP air/water	0.30	1.20	0.00361	0.00361
0.015	AP air/water	0.30	1.20	0.00301	0.00301
0.015	AP air/water	0.33	1.20	0.00401	0.00401
0.015	AP steam/water	0.40	0.60	0.00207	0.00294
0.015	AP air/water	0.40	1.20	0.00401	0.00401
0.015	AP air/water	0.40	1.20	0.00401	0.00401
0.020	AP air/water	0.30	1.20	0.00281	0.00281
0.020	AP air/water	0.33	1.20	0.00281	0.00281
0.020	AP air/water	0.40	1.20	0.00351	0.00351
0.020	AP air/water	0.40	1.20	0.00261	0.00261
0.025	AP air/water	0.30	1.20	0.00241	0.00241
0.025	AP air/water	0.33	1.20	0.00201	0.00201
0.025	AP air/water	0.40	1.20	0.00241	0.00241

Table 4.5
Small column flood points, rotor speed = 1500 RPM

Liquid flow	System	B	ρ_G	m_G	m_{GN}
kg/s			kg/m^3	kg/s	kg/s
0.005	AP air/water	0.40	1.20	0.00602	0.00602
0.005	AP air/water	0.40	1.20	0.00562	0.00562
0.010	AP steam/water	0.30	0.60	0.00282	0.00400
0.010	AP air/water	0.30	1.20	0.00361	0.00361
0.010	AP air/water	0.33	1.20	0.00401	0.00401
0.010	AP air/water	0.40	1.20	0.00452	0.00452
0.010	AP air/water	0.40	1.20	0.00321	0.00321
0.015	AP air/water	0.30	1.20	0.00321	0.00321
0.015	AP air/water	0.33	1.20	0.00361	0.00361
0.015	AP air/water	0.40	1.20	0.00401	0.00401
0.020	AP air/water	0.30	1.20	0.00281	0.00281
0.020	AP air/water	0.33	1.20	0.00281	0.00281
0.020	AP air/water	0.40	1.20	0.00301	0.00301
0.025	AP air/water	0.30	1.20	0.00201	0.00201

4.3.2.3 Statistical analysis of small column flooding data

4.3.2.3.1 Description of data set

The flooding data obtained on the small column were organized, for the purposes of statistical analysis, as shown in table 4.6:

Table 4.6
Small column flooding data: independent variables

Level	Liquid flow (kg/s)	Spacing parameter *B*	Rotor speed (RPM)	Gas density (kg/m^3)
1	0.005	0.30	500	0.12
2	0.010	0.33	1000	0.13
3	0.015	0.40	1500	0.60
4	0.020			1.20
5	0.025			

The dependent variables were gas mass flow at flooding, m_G, and normalized gas mass flow at flooding, m_{GN}.

4.3.2.3.2 Results of statistical analysis

The statistical analysis of these data consists of three parts:

(a) an analysis of variance for m_G
(b) an analysis of variance for m_{GN}
(c) a multiple linear regression of m_{GN} on liquid flow, spacing parameter and rotor speed.

All three of these statistical analyses were carried out using the General Linear Model (GLM) in the statistical software package, MINITAB Release 7 (Anon., 1989). GLM allows analysis of variance and regression to be performed on unbalanced data sets, i.e. those in which there are not necessarily observations of the dependent variable/s for each combination of factors (independent variables). The small column flooding data set is, by this definition, unbalanced. Note that statistical analysis of the flooding behaviour of the small column was not specifically envisaged prior to the execution of the trial programme; no attempt was made to design a statistically optimal experimental procedure.

The results of the three statistical procedures are given in tables 4.7, 4.8 and 4.9.

The fourth column in tables 4.7, 4.8 and 4.9 lists the "adjusted" sums of squares for each of the factors; these terms correspond to the sequential sum of squares for the case where the factor is the last added to the model. The *F* test uses the corresponding adjusted mean squares. This feature of the GLM command in MINITAB obviates the necessity to repeat the analysis of variance with predictors entered in different sequence.

Table 4.7
Analysis of variance for gas mass flow at flooding, m_G

SOURCE	DF	Sequential SS (× 10^6)	Adjusted SS (× 10^6)	Adjusted MS (× 10^6)	F	p
Liquid flow	4	3.67	5.68	1.42	74.1	0.000
Spacing parameter	2	0.483	0.179	0.090	4.8	0.012
Rotor speed	2	0.031	0.555	0.277	14.7	0.000
Gas density	3	6.56	6.56	2.19	115.7	0.000
RESIDUALS	56	1.06	1.06	0.019		
TOTAL	67	11.80				

In table 4.7 we see that all the factors, liquid flow, spacing parameter, rotor speed and gas density, have a significant influence, at the 95% level, on the gas rate at flooding, m_G, in the small column.

In the earlier discussion of pressure drop in the presence of liquid flow we concluded that the effect of gas density was accounted for by normalizing the gas rate, a transformation analogous to use of the F-factor. We check this by conducting a second analysis of variance, this time replacing the gas rate m_G with the normalized gas rate m_{GN}. The results of this second analysis of variance are given in table 4.8.

Table 4.8
Analysis of variance for normalized gas mass flow at flooding, m_{GN}

SOURCE	DF	Sequential SS (× 10^6)	Adjusted SS (× 10^6)	Adjusted MS (× 10^6)	F	p
Liquid flow	4	7.32	6.68	1.67	88.3	0.000
Spacing parameter	2	0.279	0.156	0.078	4.1	0.021
Rotor speed	2	0.470	0.567	0.284	15.0	0.000
Gas density	3	0.130	0.130	0.043	2.3	0.088
RESIDUALS	56	1.06	1.06	0.019		
TOTAL	67	9.25				

We see here that effect of gas density on normalized gas rate at flooding m_{GN} is not significant at the 95% level ($p > 0.05$); this result supports our earlier conclusion that the effect of gas density is accounted for by scaling gas rate by a factor proportional to the square root of gas density.

The analysis of variance for m_{GN} shows that liquid flow, spacing parameter and rotor speed all have a significant influence on the normalized gas rate at flooding at the 95% level.

In the third and last of the statistical analyses we carry out a multiple linear regression of m_{GN} at flooding on liquid flow, spacing parameter and rotor speed. That is, we fit a relationship of the form

$$m_{GN} = b_0 + b_1 m_L + b_2 B + b_3 \omega \tag{4.2}$$

where m_L is the liquid mass flow (kg/s),
B is the spacing parameter,
ω is the rotor speed (RPM), and
b_i are regression constants (i = 0 to 3).

The multiple linear regression is also performed using GLM but here the independent variables are treated as covariates (i.e. continuous variables) rather than factors (discrete classes to which arbitrary integer values can be assigned). The results of the regression are given in table 4.9.

Table 4.9
Results of multiple linear regression of m_{GN} on m_L, B and ω

SOURCE	DF	Sequential SS (× 10^5)	Adjusted SS (× 10^5)	Adjusted MS (× 10^5)	F	p
Liquid flow, m_L	1	7.22	6.86	6.86	353.5	0.000
Spacing parameter, B	1	0.308	0.231	0.231	11.9	0.001
Rotor speed, ω	1	0.483	0.483	0.483	24.9	0.000
RESIDUALS	64	1.24	1.24	0.0194		
TOTAL	67	9.25				

TERM		Coefficient (× 10^3)	95% confidence limits (× 10^3)
Constant	b_0	5.60	±0.943 (±17%)
m_L	b_1	-161.4	±17.2 (±11%)
B	b_2	4.06	±2.36 (±58%)
ω	b_3	-0.0007	±0.00028 (±40%)

Note that the rationale underlying this linear fit to the data is not that we expect the true relationship between these quantities necessarily to be a simple linear one; rather, we use this approach because it gives some indication of the influence of the independent variables and assists in the graphical presentation of the small column flooding data.

The observed small column flood points are plotted, along with the fitted linear relationships described above, in figs 4.12, 4.13 and 4.14.

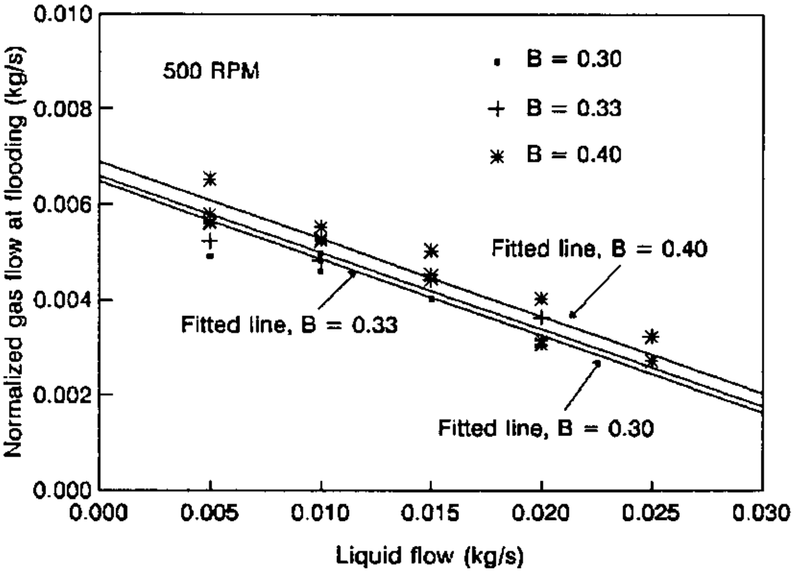

Figure 4.12
Small column flooding data: normalized gas rate at flooding vs liquid rate at 500 RPM.

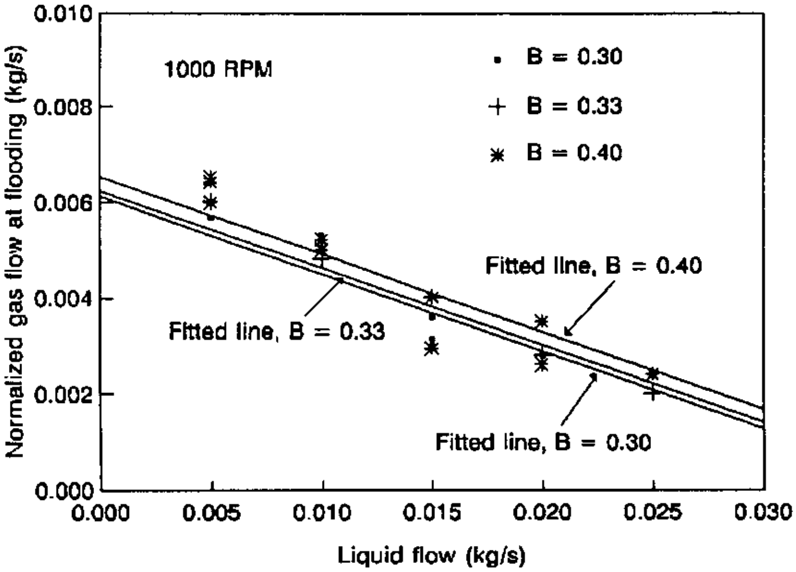

Figure 4.13
Small column flooding data: normalized gas rate at flooding vs liquid rate at 1000 RPM.

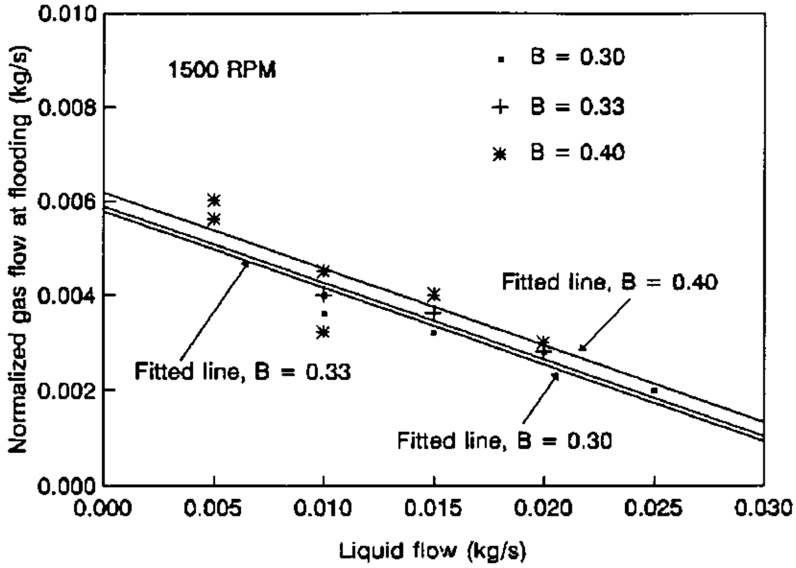

Figure 4.14
Small column flooding data: normalized gas rate at flooding vs liquid rate at 1500 RPM.

4.3.2.3.3 Discussion of statistical analysis

The main result of the statistical analysis is that gas rate at flooding falls as liquid flow increases, a result which is entirely consistent with both our expectations and the behaviour of plate and packed columns.

For example, where B = 0.40 and ω = 1000 RPM the gas rate at flooding m_{GN} changes from 0.0057 kg/s to 0.0025 kg/s (a 56% reduction) as the liquid flow m_L is increased from 0.005 kg/s to 0.025 kg/s.

4.3.2.3.3.1 The effect of rotor speed on gas rate at flooding

The quantitative effect of rotor speed on gas rate at flooding may be summarized as follows: where m_L = 0.005 kg/s and B = 0.40 the gas rate at flooding m_{GN} changes from 0.0061 kg/s to 0.0054 kg/s (an 11% reduction) as the rotor speed is increased from 500 RPM to 1500 RPM. Similarly, where m_L = 0.025 kg/s and B = 0.40 the gas rate at flooding m_{GN} changes from 0.0028 kg/s to 0.0021 kg/s (a 25% reduction) as the rotor speed is increased from 500 RPM to 1500 RPM.

The observed effect of rotor speed is less pronounced than that of liquid flow but significant nonetheless; it raises in particular the question why increasing rotor speed reduces the vapour flow required to flood the column at a given liquid flow? To find an explanation for the effect of rotor speed we must consider the manner in which the rotor and the liquid interact:

(a) Increasing rotor speed increases the angular momentum imparted to the liquid in the column. This swirl, or the centrifugal force associated with it, opposes the gravitational force acting on the liquid and so may be impeding the downward flow of liquid at all points on the stationary cone, including the liquid leaving the lip of the stationary cone. If the net force acting on the liquid film at the lip of the stationary cone is reduced, the film will thicken and its velocity will be reduced; consequently the available gas flow area will also be reduced.

(b) Flooding can be thought of as being due to gas pressure overcoming the weight of the liquid, and thereby pushing it upward. This is essentially what happens in flooding in plate columns. The reduction in net downward force acting on the liquid due to the swirl-induced centrifugal force is equivalent to a reduction in weight; the gas flow requires less energy to overcome the weight of the liquid and flooding is induced at a lower gas flow.

Implicit in these proposed explanations of the effect of rotor speed is the idea that flooding in the SCC, or at least in the small column, is associated with liquid flow on the stationary cone, in particular the liquid draining from the lip of the stationary cone on to the base of the spinning cone below.

4.3.2.3.3.2 The effect of spacing parameter on gas rate at flooding

The quantitative effect of spacing parameter on gas rate at flooding m_{GN} can be summarized as follows: where $m_L = 0.005$ kg/s and $\omega = 1000$ RPM, m_{GN} changes from 0.0057 kg/s to 0.0053 kg/s (a 7% reduction) as the spacing parameter B is reduced from 0.40 to 0.30. Similarly, where $m_L = 0.025$ kg/s and $\omega = 1000$ RPM, m_{GN} changes from 0.0025 kg/s to 0.0021 kg/s (a 16% reduction) as the spacing parameter B is reduced from 0.40 to 0.30.

The gas rate at flooding does not appear to vary as much as we would expect if flooding was directly related to maximum gas velocity in the cone set, since this will be inversely proportional to minimum flow area, which itself varies linearly with spacing parameter. That is, we would have expected the gas rate at flooding where $B = 0.30$ to be about 75 % of the corresponding value where $B = 0.40$. The observed effect of spacing parameter was, though statistically significant, not as large as this.

A check on the effect of changes in minimum flow area, brought about by changing the spacing parameter, was made by dividing the normalized gas mass flow m_{GN} by the minimum flow area to give a normalized gas mass velocity G_N, and repeating the analysis of variance. If flooding were simply a function of maximum gas velocity within the cone set we should expect that the influence of spacing parameter would be allowed for by use of G_N, and that the effect of spacing parameter on G_N, unlike the effect of spacing parameter on m_{GN}, would not be statistically significant. The results of the analysis of variance of G_N are shown in table 4.10.

Table 4.10
Analysis of variance for normalized gas mass velocity at flooding, G_N

SOURCE	DF	Sequential SS	Adjusted SS	Adjusted MS	F	p
Liquid flow	4	74.7	72.8	18.2	81.72	0.00
Spacing parameter	2	13.8	15.6	7.82	35.10	0.00
Rotor speed	2	7.02	7.02	3.51	15.76	0.00
RESIDUALS	59	13.1	13.1	0.223		
TOTAL	67	108.7				

We see from table 4.10 that the effect of spacing parameter on gas mass velocity G_N at flooding is in fact "more significant" that its effect on gas mass flow at flooding m_{GN} (see table 4.8). We conclude from this result that, on the basis of the small column flooding data, flooding in the SCC is not simply related to maximum gas velocity within the cone set.

4.3.2.4 Generalized correlation of small column flooding data

Before discussing the flooding data obtained on larger columns, we shall consider the options available for representing the flooding behaviour of the small column in a general (i.e. non-dimensional) form. As mentioned in the introduction to this chapter, the conceptual similarities between the operation of the packed column and the spinning cone column suggest that it may be possible to develop a generalized correlation of flooding in the spinning cone column similar to that used to predict flooding in packed columns, the Sherwood-Leva-Eckert (SLE) correlation.

The SLE correlation is a plot of a capacity parameter Y against a flow parameter X, which are defined in the following way:

$$X = \frac{L}{G}\sqrt{\frac{\rho_G}{\rho_L}} \tag{4.3}$$

$$Y = \frac{F_p \psi G^2}{\rho_G \rho_L g}\left[\frac{\mu_L}{\mu_w}\right]^{0.2} \tag{4.4}$$

where L is the liquid mass velocity,
G is the vapour mass velocity,
ρ_G is the vapour density,
ρ_L is the liquid density,
F_p is the packing factor,
ψ is the ratio of the density of water to that of the liquid,

μ_L is the dynamic viscosity of the liquid,
μ_W is the dynamic viscosity of water, and
g is the gravitational acceleration.

To apply the same correlation to flooding in the SCC (that is, to calculate a capacity parameter) we require:

(a) a vapour velocity term
(b) a term which is equivalent to the packing factor F_p

4.3.2.4.1 Characteristic vapour velocity

In the SLE correlation for packed columns the characteristic vapour velocity is taken to be the superficial or approach velocity, the volume flow of vapour divided by the cross-sectional area of the column, divided by the voids fraction: i.e.

$$u_1 = \frac{u_0}{\epsilon} = \frac{Q_V}{A_C\epsilon} = \frac{G}{\rho_G\epsilon} \tag{4.5}$$

where u_1 is the characteristic (or pore) velocity,
u_0 is the approach velocity,
Q_V is the vapour volume flow, and
A_C is the cross-sectional area of the column shell.

In the case of the SCC the geometry and dimensions of the vapour flow path are better defined than in packed columns, and so we can calculate average (radial) vapour velocities at any flow section within the cone set; the problem then becomes determining which of these velocities can be used to characterize flooding behaviour in the SCC.

We shall evaluate flooding correlations based on two characteristic flow areas:

- the minimum flow area (in the small column, the frustro-conical area bounded by the lip of the stationary cone and the spinning cone immediately below)
- the inner annular area, bounded by the lip of the stationary cone and the rotor shaft; this area has been chosen because it is unaffected by changes in shaft position, but is still representative of the available flow area in the most constricted region of the cone set.

4.3.2.4.2 Packing factor and hydraulic radius

The capacity parameter used in the SLE correlation includes a packing factor, F_p, which in the original formulation, was taken to be the specific area of the packing a_p per divided by the cube of the void fraction, ϵ. As was shown in Chapter 2, a_p/ϵ is the inverse of the hydraulic radius; this is multiplied by $1/\epsilon^2$ to convert the square of superficial velocity u_0^2

to the square of pore velocity u_1^2. The whole term is defined as the packing factor, and has come to be treated as a coefficient characterizing the packing, which is determined by experiment.

The question now arises whether this same approach can be usefully applied to the prediction of flooding in the spinning cone column. In other words, is there a linear dimension which can be used to correlate flooding in the SCC corresponding to a_p/ϵ in the basic form of the SLE correlation for packed columns?

The following definitions of packing factor/hydraulic radius will be considered:

- wetted area per unit unoccupied internal volume
- the hydraulic radius of the smallest flow cross-section
- hydraulic radius of annular flow section bounded by the lip of the stationary cone and the rotor shaft

The first definition is obtained by direct analogy with the packed column correlation. The second and third definitions arise from consideration of the geometry of the inner throat region. We assume from the outset that flooding is, under normal circumstances, most likely to occur in this region because the flow passages within it are more constricted than at any other location in the cone set. Moreover, there is potential for liquid to be held up at the base of the spinning cone, further reducing available flow area.

It was shown in Chapter 3 (eq. 3.4) that the hydraulic radius for gas flow through any frustro-conical flow section between two adjacent cones is simply half the perpendicular gap between the cones. Note that if we assume the flow passage throughout the SCC to consist of a series of narrow frustro-conical passages, the surface area per unit volume is in fact equal to the perpendicular gap between the cone surfaces; in other words, the first two definitions of hydraulic radius differ by a factor of two in the case where the inter-cone gap is the same throughout the column. Where the upper and lower gaps are not equal, the surface area per unit volume is twice the average of the two.

The second definition of hydraulic radius takes account of unequal inter-cone spacings ($B \neq 0.5$) whereas the surface area per unit volume is unaffected by a change in the relative positions of the spinning and stationary cones.

The hydraulic radius of the annular inner throat area is included as an option, firstly because this flow area is one of the two being considered as characteristic flow areas, at which the characteristic vapour velocity is evaluated, and secondly because it, along with the inter-cone gap, basically defines the geometry of the inner throat region.

4.3.2.4.3 Evaluation of flood point correlations

From the two options for characteristic flow area and the three for packing factor/hydraulic radius, we shall evaluate and compare five distinct correlations of flooding, based on the results the small column trials. These five definitions of capacity parameter are given in table 4.11; also shown is the relationship between each term and t, the upper inter-cone gap, and the relationship between the resulting capacity parameter Y and t.

Table 4.11
Definitions of capacity parameter Y, types 1 to 5

TYPE	F_p	Variation of F_p with t	A_{char}	Variation of A_{char} with t	Variation of Y with t
1	a_p	FIXED	A_{min}	$\propto t$	$\propto t^{-2}$
2	a_p	FIXED	A_{throat}	FIXED	FIXED
3	$r_{h,min}^{-1}$	$\propto t^{-1}$	A_{min}	$\propto t$	$\propto t^{-3}$
4	$r_{h,min}^{-1}$	$\propto t^{-1}$	A_{throat}	FIXED	$\propto t^{-1}$
5	$r_{h,throat}^{-1}$	FIXED	A_{min}	$\propto t$	$\propto t^{-2}$

A_{char} = characteristic flow area
A_{throat} = inner throat (annular) area
a_p = wetted area per unit gas volume
$r_{h,min}$ = hydraulic radius of smallest flow section
$r_{h,throat}$ = hydraulic radius of the inner throat annular area
t = gap between spinning cone and stationary cone immediately above
F_p = packing factor
A_{min} = minimum flow area

Table 4.12
Numerical values of dimensional quantities used in definitions of capacity parameter for correlation of small column flooding data

	B = 0.40	B = 0.33	B = 0.30
A_{min} (m^2)	0.00110	0.00088	0.00079
A_{throat} (m^2)	0.00244	0.00244	0.00244
$r_{h,min}$ (mm)	2.6	2.2	2.0
$r_{h,throat}$ (mm)	6.9	6.9	6.9
a_p (m^2/m^3)	123	123	123

A capacity parameter based on the only other possible combination, the area and hydraulic radius of the inner throat annulus, can be discounted because it would be completely unaffected by changes in cone spacing (i.e. cone pitch, not spacing parameter).

4.3.2.4.4 Results

Figs 4.15 to 4.18 are plots of capacity parameter Y against flow parameter X for the five definitions of Y described above (table 4.11). Also shown in each of these figures is a curve which has been fitted to the data; the curve has the following form:

$$\log Y = a(\log X)^2 + b(\log X) + c \tag{4.6}$$

where a, b and c are regression constants.

One measure of how well a particular definition of Y correlates the flooding data is the r^2 value obtained from the curve-fitting procedure. Table 4.13 gives the regression constants a, b and c and the r^2 term for each of the five definitions of Y.

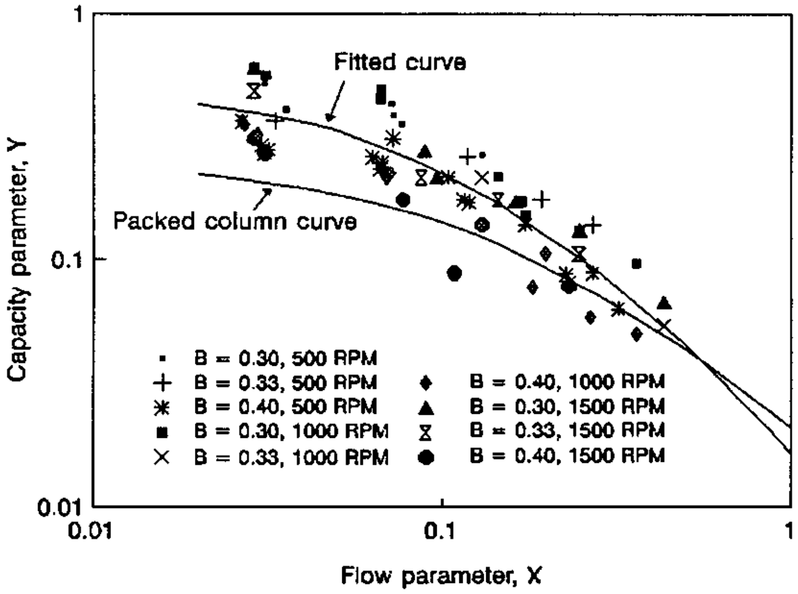

Figure 4.15
Type 1 flooding correlation: small column flooding data

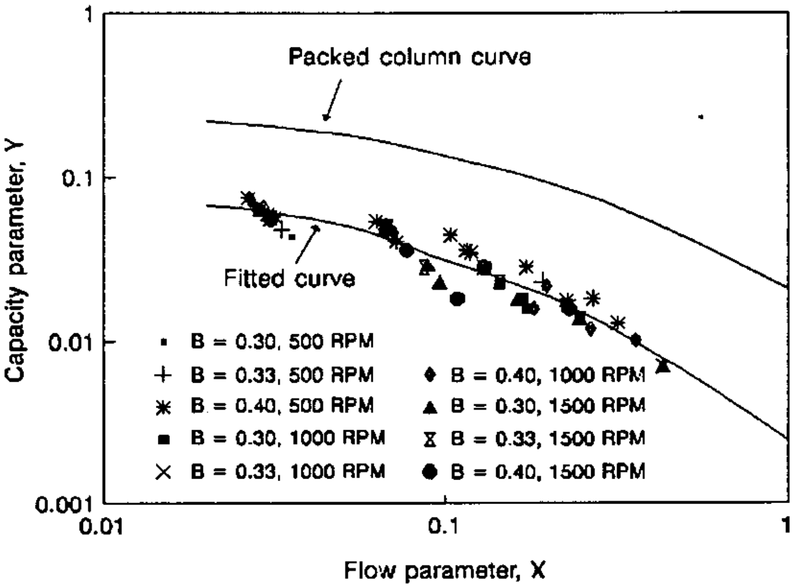

Figure 4.16
Type 2 flooding correlation: small column flooding data

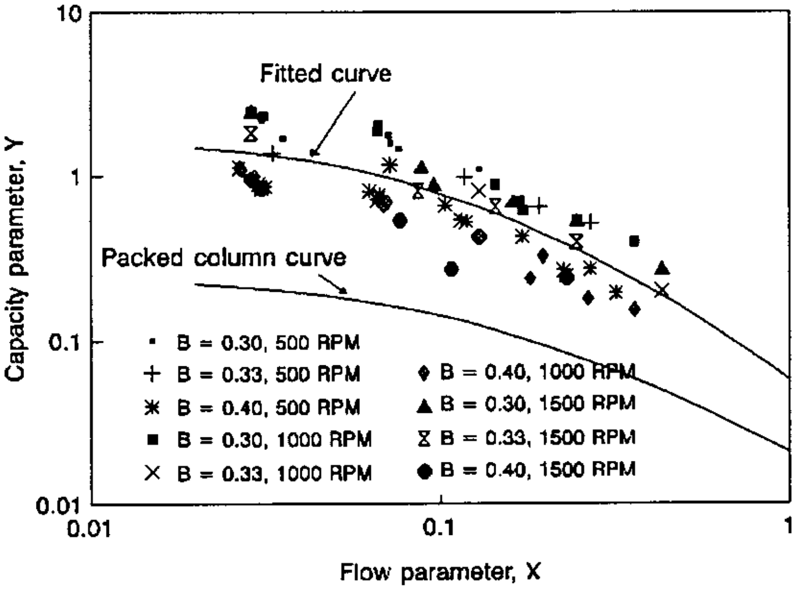

Figure 4.17
Type 3 flooding correlation: small column flooding data

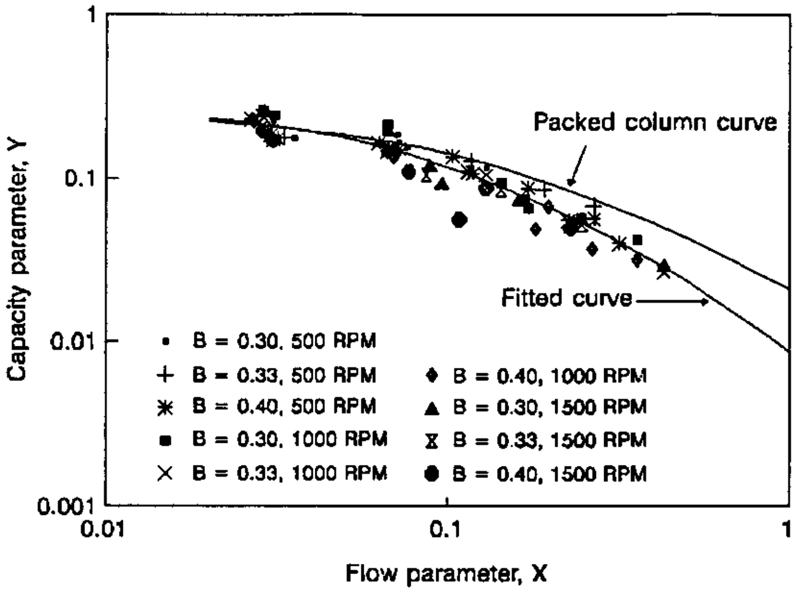

Figure 4.18
Type 4 flooding correlation: small column flooding data

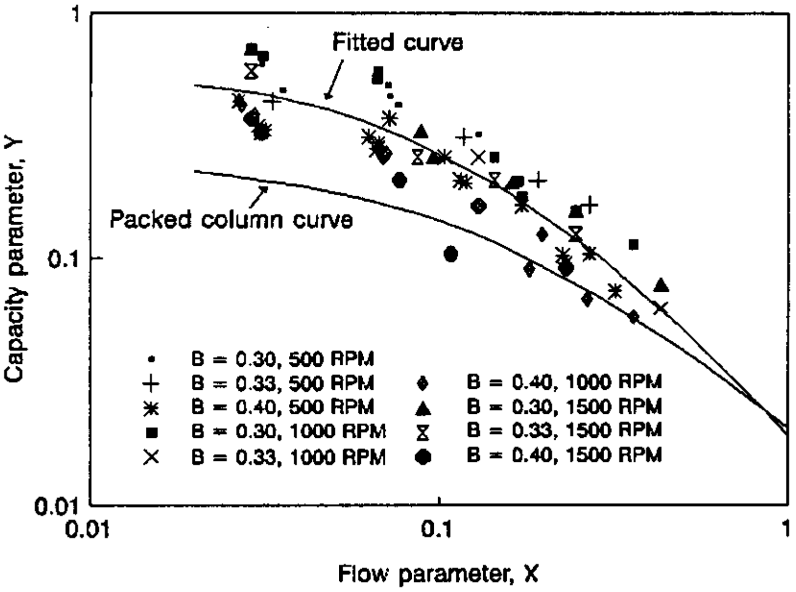

Figure 4.19
Type 5 flooding correlation: small column flooding data

Table 4.13
Regression data for small column flooding correlations (see eq. 4.6)

TYPE	*a*	*b*	*c*	r^2
1	-0.43	-1.56	-1.79	0.79
2	-0.41	-1.54	-2.61	0.93
3	-0.44	-1.58	-1.24	0.66
4	-0.42	-1.55	-2.06	0.92
5	-0.43	-1.56	-1.72	0.79

The highest values of r^2 were obtained from the type 2 (fig. 4.16) and type 4 (fig. 4.18) correlations; the spread of capacity parameters for a given flow parameter is least for these two. The type 3 correlation is the worst in this sense. Recall that for this correlation, the characteristic flow area was taken to be the minimum flow area, proportional to the inter-cone gap t, and the packing factor the inverse of the hydraulic radius of the smallest flow area, which is half the inter-cone gap t; the capacity parameter so defined is therefore proportional to t^3 and is thereby more sensitive to changes in spacing parameter than any of the others. That the type 3 correlation is the poorest representation of the flooding data is consistent with the results of the statistical analysis discussed section 4.3.2.3; although the influence of spacing parameter on gas rate at flooding was found to be significant at the 95% level, it was much weaker than that required to support the type 3 definition of capacity parameter.

That the type 2 and type 4 definitions of capacity parameter best correlate the small column flooding data suggests that the upper inter-cone gap t has at most a marginal influence on the flooding behaviour of the column.

Another check on the validity of the various correlations being evaluated here is provided by comparing them with the SLE packed column flooding curve, which is also shown in figures 4.15 to 4.19. All the curves fitted to the small column flooding data have a similar form to the SLE packed column curve. The numerical correspondence is closest in the cases of the type 1, type 4 and type 5 correlations. The close numerical correspondence of the type 1 correlation to the packed column curve is noteworthy, given that the definition of the type 1 capacity parameter most closely parallels the definition of the packed column capacity parameter: characteristic area = minimum flow area and packing factor = wetted area per unit gas volume. This numerical similarity between SCC and packed column flooding behaviour militates in favour of the type 1 capacity parameter even though it implies a dependence on t which is not supported by these data.

It is not possible fully to resolve questions concerning the choice of A_{char} and packing factor/hydraulic radius using these data. Recall that when the spacing parameter was set at 0.21, stable liquid flow through the column was not possible at any gas flow; consequently no meaningful flooding data could be obtained at this value of B; this result does, however, support the contention that spacing parameter must ultimately influence the achievable capacity limits even though no effect was observed within the range B = 0.30 to 0.40.

The type 1 and type 5 correlations are effectively the same, since in both the characteristic flow area is taken to be the minimum flow area and the packing factors (wetted area per unit volume for type 1, and the inverse of the hydraulic diameter of the inner throat annulus for type 5), though numerically different, do not vary with spacing parameter B. These two correlations fall between the type 3 and the types 2 and 4 with regard to their representation of the flooding data; the two definitions of capacity parameter on which they are based are less sensitive to shaft position than that of the type 3 correlation, but more sensitive than those of types 2 and 4.

4.3.2.5 Extension of the correlations to larger columns

Figs 4.20 to 4.24 are plots of capacity parameter against flow parameter as defined above, but in this case the flooding data were obtained on larger columns. The medium column flooding data were obtained on the CSIRO Mk III SCC using steam and water, at atmospheric pressure and under vacuum. The large column flooding data were obtained during the commissioning and testing of a commercial 10000 litre/hour SCC (see section 4.2.1 of this chapter for the dimensions of both these larger columns).

Table 4.14
Numerical values of dimensional quantities used in definitions of capacity parameter for correlation of medium and large column flooding data

	Medium column	Large column
A_{min} (m^2)	0.0023	0.0399
A_{throat} (m^2)	0.0059	0.0742
$r_{h,min}$ (mm)	3.4	22
$r_{h,throat}$ (mm)	12.5	58
a_p (m^2/m^3)	52.3	15.2

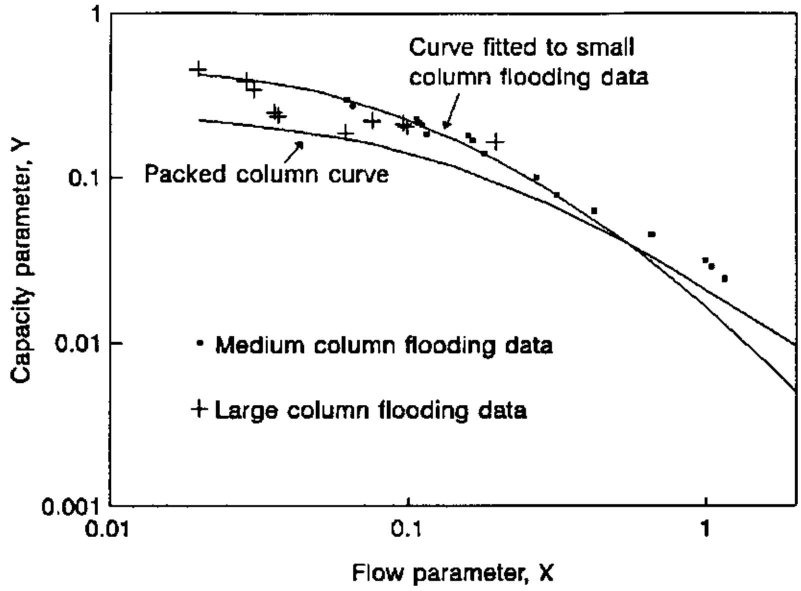

Figure 4.20
Type 1 flooding correlation: medium and large column flooding data

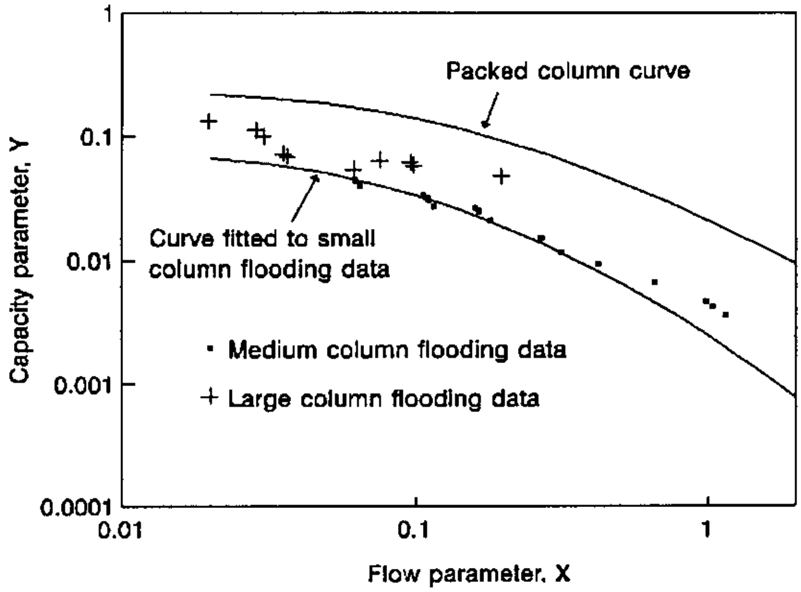

Figure 4.21
Type 2 flooding correlation: medium and large column flooding data

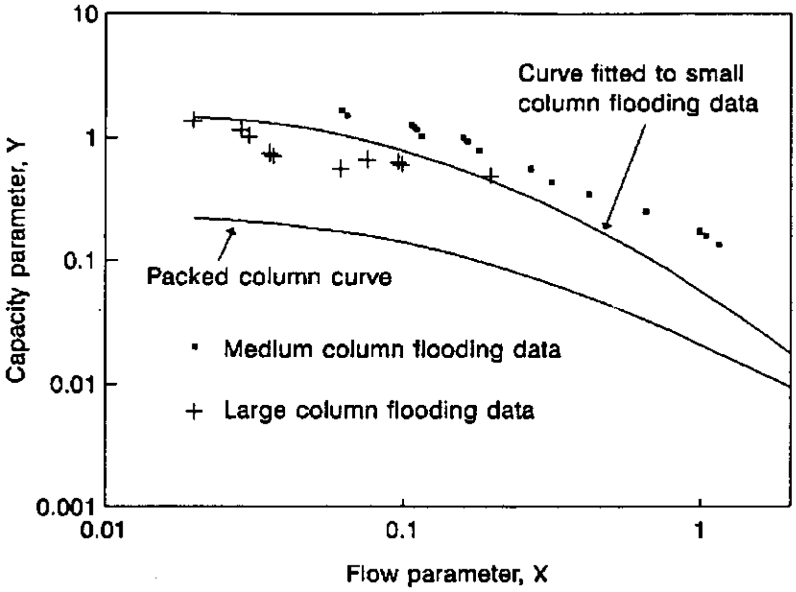

Figure 4.22
Type 3 flooding correlation: medium and large column flooding data

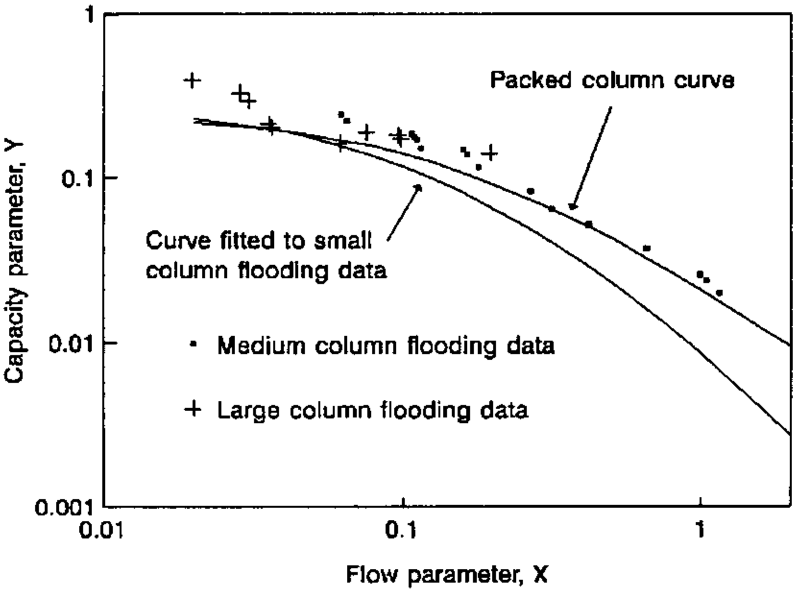

Figure 4.23
Type 4 flooding correlation: medium and large column flooding data

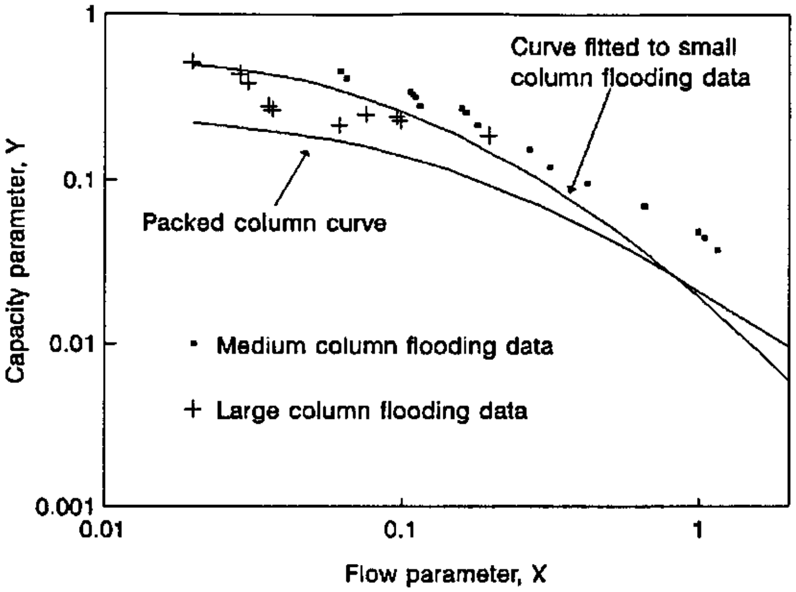

Figure 4.24
Type 5 flooding correlation: medium and large column flooding data

For all the correlations, types 1 to 5, the medium and large column flooding data exhibit the same pattern as, and are numerically similar to, the small column flooding data.

We can assess the agreement between the small column flooding data and those obtained on the larger columns by looking at the ratio of capacity parameters based on the medium and large column data to the corresponding capacity parameters obtained from the curves fitted to the small column data. Average values of these ratios, and their standard deviations, are given in table 4.15.

Table 4.15
Average values and standard deviations of ratio of capacity parameter *Y* based on observed medium and large column flood points to corresponding *Y* obtained from curves fitted to small column flooding data

Correlation type	Medium column flooding data		Large column flooding data	
	Average	Std. deviation	Average	Std. deviation
1	1.23	0.33	0.83	0.23
2	1.22	0.32	1.57	0.44
3	1.95	0.53	0.71	0.20
4	1.93	0.52	1.34	0.38
5	1.60	0.43	0.80	0.22

Comparing the different definitions of capacity parameter we see that the type 1 correlation performs best of all, in that the average values of the type 1 capacity parameters based on observed medium and large column flood points fall within 25% of the corresponding values on the small column curve. Whilst such agreement is not particularly close, it is of the same order as that generally claimed for packed column correlations (see section 2.3.4.2.1); furthermore, it is indicative of an underlying relationship, given that the dimensions used to calculate the capacity parameter vary by at least an order of magnitude from the small column to the large.

This is perhaps the most important result of the work discussed in this chapter: we have demonstrated that the flooding behaviour of three SCCs of widely varying sizes and internal geometries can be represented by a single relationship between an appropriately defined capacity parameter Y and flow parameter X. Moreover, this representation of flooding behaviour in the SCC corresponds closely, in both form and numerical magnitude, to the SLE correlation for flooding in packed columns.

On this basis it is proposed that the flood point in spinning cone columns be predicted using the type 1 correlation; a curve of the form of eq. (4.6) was fitted to the type 1 capacity parameters based on the full set of SCC flooding data. The resulting equation is

$$\log Y = -0.257(\log X)^2 - 1.172(\log X) - 1.596$$

This curve, along with type 1 capacity parameters based on the observed flood points, curves representing the upper and lower confidence limits for the mean value of Y, and the SLE curve for flooding in packed columns are shown in fig. 4.25.

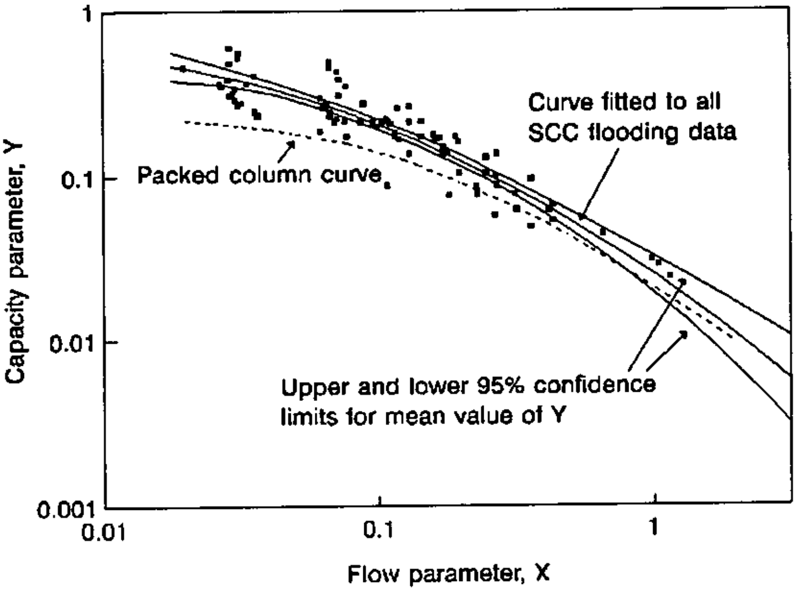

Figure 4.25
Type 1 flooding correlation based on full SCC flooding data set

4.3.3 Mechanisms of flooding in the SCC

In experiments conducted on the SCC flow visualization rig (described in Chapter 5 of this thesis) three distinct mechanisms of flooding have been observed:

(a) high rotor speed peripheral flooding

This type of flooding is a result of high liquid flow and high rotor speed; it can occur in the absence of gas flow.

Liquid leaves the lip of the spinning cone essentially as planar spray of fine droplets. At typical rotor speeds the velocity of the liquid leaving the lip of the spinning cone has a large tangential component; this results in the formation of a ring of liquid banked up against the wall of the column. This ring of liquid rotates at some fraction of the rate of rotation of the spinning cone. As the liquid in this rotating ring loses its angular momentum the centrifugal force holding it against the wall is reduced until gravity ultimately prevails and the liquid leaves the wall region and flows down the stationary cone.

As rotor speed rises so does the angular momentum of the liquid ring, resulting in an increase in the amount of liquid held up against the wall of the column. A rotor speed is reached at which this body of liquid fills the gap between the wall of the column and the lip of the spinning cone, at which point stability of liquid flow is lost and the cone set rapidly floods.

(b) low rotor-speed inner throat flooding

This type of flooding is a result of high liquid flow and low rotor speed; like the high rotor speed peripheral flooding mechanism, it can occur in the absence of gas flow.

Liquid falls from the lip of the stationary cone as a stream of droplets on to the base of the spinning cone. Once on the spinning cone, liquid adjacent to the rotating surface acquires angular momentum, which is transferred through the remainder of the liquid by viscous action. Each liquid particle experiences a centrifugal force which is proportional to its distance from the axis of rotation and to the square of its angular velocity. Once this force overcomes the gravitational force holding the liquid at the base of the spinning cone, the liquid begins to move upward and outward across the surface of the spinning cone. The net effect of these processes is the formation of a radially flowing film, the thickness of which decreases with distance from the axis of rotation.

For a given liquid flow the amount of liquid retained at the base of the spinning cone rises as rotor speed is reduced; at a given rotor speed the amount retained rises with liquid flow. Under conditions of high liquid flow and low rotor speed the surface of the liquid body held up at the base of the spinning cone can rise to meet the lip of the stationary cone, thereby disrupting the liquid flow pattern and blocking the gas flow path.

The flooding observed by Menzi, discussed in section 1.6.3, was most probably of this type.

(c) gas-induced flooding

Gas-induced flooding is that arising from interaction between the liquid stream and a high-velocity gas stream. It is a result of the gas stream exerting pressure on the liquid so that liquid hold-up is increased to the point where the area available for gas flow is significantly reduced and stable counterflow of the phases breaks down. This flooding mechanism is the most important from an operational point of view, and is directly comparable to flooding in packed columns.

The nature of the interaction between liquid and vapour in the region of the lip of the stationary cone is not easily deduced, not least because it is here that our assumptions of well-defined and geometrically simple flow patterns in both phases are the most problematical. Nevertheless, because the highest gas velocities are attained in this region, and because it is here than the largest volume of liquid is likely to accumulate, we expect gas-induced flooding in the spinning cone column, or at least the processes which initiate such flooding, to occur within it.

Observations of gas flow-induced flooding in the flow visualization rig indicate that the droplets leaving the lip of the stationary cone are deflected in the tangential direction by the gas stream. At low gas flows they fall vertically downwards; as gas flow is increased the droplets are increasingly deflected in the direction of rotation. A stage is reached at high gas flows where droplets are blown back onto the stationary cone and, ultimately, there is a pronounced build-up of liquid (an unstable rotating ring, much thicker than the stable, radially flowing gravity film) at the lip of the stationary cone; as gas flow is further increased this swirling body of liquid grows, backing up the stationary cone until it begins to disrupt the flow pattern in the outer throat region. Once it has backed up to this point the outer throat region very quickly floods with liquid, and the cone set is completely flooded.

4.4 Conclusions

The physical capacity of the spinning cone column can be predicted using an approach similar to the Sherwood-Leva-Eckert correlation for flooding in packed columns.

Flooding data obtained on three spinning cone columns, encompassing the full range of sizes currently in service, have been correlated using a capacity parameter of the same form as that in the SLE correlation, but having the following features:

(a) the critical flow area within the cone set, at which the vapour velocity is evaluated, is the minimum flow area.
(b) the packing factor equivalent is wetted area per unit gas volume.

The correlation so obtained takes account of variations in gas density; furthermore, its similarity to the SLE correlation leads us to suppose that it accounts for liquid properties such as density and viscosity in a comparable manner.

A mechanism of gas-induced flooding which is broadly consistent with this flooding correlation has been observed. It is unlikely, however, that flooding would occur in the same way under all conditions of liquid flow, gas flow and cone set geometry. More work is required in the following areas:

(a) determining the precise nature of the interactions between liquid and gas streams in the SCC cone set and how these are affected by physical and dimensional factors, especially where these are substantially different from existing systems.

(b) establishing the relationships between operational and configurational parameters and the flooding mechanisms which are not directly controlled by gas flow.

CHAPTER 5

FLOW OF A LIQUID FILM ON A ROTATING CONICAL SURFACE

5.1 Introduction

Methods for the prediction of liquid flow characteristics such as average and surface velocities and film thicknesses (i.e. the distribution of liquid inside the column) are required to estimate both physical capacity limits and mass transfer performance in the spinning cone column.

In this chapter the flow of a liquid film on a rotating conical surface is investigated. First, the main theoretical approaches are presented, after which the results of experiments conducted on a flow visualization rig are presented and compared with the theoretical predictions.

5.2 Theory of film flow

5.2.1 The Nusselt model

5.2.1.1 Gravity film flow on an inclined flat plate

The most general equations describing laminar flow of a viscous incompressible fluid having constant physical properties are the Navier-Stokes equations; expressed in rectangular coordinates x, y, z they can be written as:

$$
\begin{aligned}
u\frac{\partial u}{\partial x} + v\frac{\partial u}{\partial y} + w\frac{\partial u}{\partial z} + \frac{\partial u}{\partial t} &= -\frac{\partial \Omega}{\partial x} - \frac{1}{\rho}\frac{\partial p}{\partial x} + \nu\nabla^2 u \\
u\frac{\partial v}{\partial x} + v\frac{\partial v}{\partial y} + w\frac{\partial v}{\partial z} + \frac{\partial v}{\partial t} &= -\frac{\partial \Omega}{\partial y} - \frac{1}{\rho}\frac{\partial p}{\partial y} + \nu\nabla^2 v \qquad (5.1) \\
u\frac{\partial w}{\partial x} + v\frac{\partial w}{\partial y} + w\frac{\partial w}{\partial z} + \frac{\partial w}{\partial t} &= -\frac{\partial \Omega}{\partial z} - \frac{1}{\rho}\frac{\partial p}{\partial z} + \nu\nabla^2 w
\end{aligned}
$$

where u, v, w are the velocities in the x, y, z directions, t is the time, ρ and ν are the density and kinematic viscosity, p is the pressure, Ω is the force potential of the field in which flow occurs, and ∇^2 is the Laplacian operator.

Also, the continuity equation

$$\frac{\partial u}{\partial x} + \frac{\partial v}{\partial y} + \frac{\partial w}{\partial z} = 0 \qquad (5.2)$$

must be satisfied.

For steady, uniform two-dimensional flow (i.e. flow of a smooth film on an infinitely wide plate outside the acceleration zone) the Navier-Stokes equations reduce to the following equations, first proposed by Hopf and later by Nusselt (Fulford, 1965):

$$\frac{d^2u}{dy^2} + \frac{g}{\nu}\sin\theta = 0 \tag{5.3a}$$

$$\frac{dp}{dy} = \rho g\cos\theta \tag{5.3b}$$

$$\frac{dp}{dz} = 0 \tag{5.3c}$$

Here the x coordinate is directed along the plate surface in the direction of greatest slope, the y coordinate is perpendicular to the plate and the z coordinate is directed across the plate. The angle between the plate and the vertical is θ.

With the following boundary conditions

$$u = 0 \text{ at } y = 0 \text{ (no slip at wall)}$$

$$\frac{du}{dy} = 0 \text{ at } y = b \text{ (no drag at interface)}$$

the velocity distribution is given by the semi-parabolic equation

$$u = \frac{g}{\nu}\sin\theta\ (by - \frac{y^2}{2})$$

In particular, the average velocity across the film is

$$u_{av} = \frac{gb^2}{3\nu}\sin\theta \tag{5.4}$$

and the surface velocity is

$$u_s = \frac{gb^2}{2\nu}\sin\theta$$

whence

$$\frac{u_s}{u_{av}} = 1.5$$

5.2.1.2 Gravity film flow on a conical surface

The flat plate equations can be extended to deal with the case of gravity flow down a conical surface provided the radius of curvature of the surface is much greater than the film thickness. The average film velocity is found from eq. (5.4); the film thickness *b*, however, is no longer constant but instead varies with radius. We invoke the continuity condition to determine the relationship between film thickness and radius: i.e.

$$\frac{dQ}{dr} = \frac{d}{dr}(2\pi r u_{av} b) = 0$$

but from eq. (5.4)

$$u_{av} \propto b^2$$

whence

$$\frac{d}{dr}(b^3 r) = 0$$

Therefore

$$b = \left[\frac{c}{r}\right]^{\frac{1}{3}} \tag{5.5}$$

where c is a constant.

The value of c is obtained by conducting a material balance at arbitrary radius r; i.e.

$$Q = 2\pi r b u_{av}$$

Substituting equations (5.4) and (5.5) gives

$$c = \frac{3Q\nu}{2\pi g \sin\theta} \tag{5.6}$$

Finally, back-substituting this expression for c into equations (5.5) and (5.4) gives the following equations for film thickness b and average film velocity u_{av} for gravity flow down a conical surface:

$$b = \left[\frac{3Q\nu}{2\pi g\sin\theta r}\right]^{\frac{1}{3}} \tag{5.7a}$$

$$u_{av} = \left[\frac{g\sin\theta Q^2}{12\pi^2\nu r^2}\right]^{\frac{1}{3}} \tag{5.7b}$$

5.2.1.3 Centrifugal film flow on a conical surface

Similar equations describing the flow of a liquid film on a rotating conical surface can be derived by replacing the gravitational acceleration $g\sin\theta$ with the centrifugal acceleration $\omega^2 r\cos\theta$, where ω is the angular velocity of the conical surface and r is the radius; note that the acceleration now varies in proportion to distance from the axis of rotation rather than remaining constant as in the case of gravity flow. Making this substitution in eq. (5.4) gives

$$u_{av} = \frac{b^2\omega^2 r\cos\theta}{3\nu}$$

Since

$$u_{av} \propto b^2 r$$

the continuity condition becomes

$$\frac{d}{dr}(r^2 b^3) = 0$$

i.e. $$b = \left(\frac{c'}{r^2}\right)^{\frac{1}{3}}$$

where c' is a constant and is given by

$$c' = \frac{3Q\nu}{2\pi\omega^2\cos\theta}$$

Finally, back-substitution of this expression for c' gives the following equations for film thickness and average film velocity for a liquid film on a rotating conical surface:

$$b = \left[\frac{3Q\nu}{2\pi\omega^2\cos\theta\, r^2}\right]^{\frac{1}{3}} \tag{5.8a}$$

$$u_{av} = \left[\frac{\omega^2\cos\theta\, Q^2}{12\pi^2\nu r}\right]^{\frac{1}{3}} \tag{5.8b}$$

These equations are based on the following assumptions:

(a) The angular velocity of the liquid is everywhere equal to that of the conical surface.
(b) The film thickness b at r is much less than r.
(c) The flow is laminar.
(d) The component of centrifugal acceleration parallel to the cone surface $\omega^2 r\cos\theta$ is much greater than the corresponding component of gravitational acceleration $g\sin\theta$.
(e) The Coriolis acceleration can be neglected.
(f) Interfacial shear stress at the surface of the film is zero.

5.2.2 Film flow on rotating surfaces: the Bruin model

Bruin (1969) gave a more complete solution of the Navier-Stokes equations for flow of a liquid film over a rotating conical surface. Only three of the assumptions underlying the Nusselt model are required for Bruin's solution:

(a) Laminar flow
(b) Zero interfacial shear
(c) Film thickness much less than corresponding radius

Since the effects of gravity are included in this model, a fourth assumption is required, namely that gravity acts parallel to the axis of rotation.

Bruin's solution is derived from a simplified form of the Navier-Stokes equations, expressed in spherical coordinates (according to Bruin the simplifications follow from the assumptions that film thickness is much less than radius, and that the meridional velocity , v, is much less than the radial and tangential velocities, u and w); the velocities are expressed with respect to a reference frame rotating at an angular velocity ω so that the tangential velocity with respect to the rotating coordinate system w' is

$$w' = -w + \omega r \sin\theta \tag{5.9}$$

The simplified Navier-Stokes equations are

$$\begin{aligned} &u\frac{\partial u}{\partial r} + \frac{v}{r}\frac{\partial u}{\partial \theta} - \frac{(w')^2}{r} + 2w'\omega\sin\theta - \omega^2 r\sin\theta \\ &= -\frac{1}{\rho}\frac{\partial p}{\partial r} - g\cos\theta + \frac{\nu}{r^2}\frac{\partial^2 u}{\partial \theta^2} \end{aligned} \tag{5.10}$$

$$\begin{aligned} &-\frac{w^2\cot\theta}{r} + 2w\omega\cos\theta - \omega^2 r\sin\theta\cos\theta \\ &= -\frac{1}{\rho r}\frac{\partial p}{\partial \theta} + g\sin\theta + \frac{\nu}{r^2}\left[\frac{\partial^2 v}{\partial \theta^2} + 2\frac{\partial u}{\partial \theta}\right] \end{aligned} \tag{5.11}$$

$$u\frac{\partial w}{\partial r} + \frac{v}{r}\frac{\partial w}{\partial \theta} + \frac{uw}{r} - 2u\omega\sin\theta = \frac{\nu}{r^2}\frac{\partial^2 w}{\partial \theta^2} \tag{5.12}$$

and the continuity equation is

$$\frac{\partial u}{\partial r} + \frac{2}{r}u + \frac{1}{r}\frac{\partial v}{\partial \theta} = 0 \tag{5.13}$$

Bruin further simplifies these equations by neglecting the pressure term in (5.10) and the viscosity term in (5.11), "recognizing that [these terms] are one order smaller in magnitude than [other terms in the same equations]."

The trigonometrical functions of θ are replaced by corresponding functions of β, where 2β is the cone's angle of inclusion. This step follows from Bruin's first explicitly stated assumption: that the film thickness is much smaller than the radius, and therefore that θ is approximately equal to β for all θ.

A coordinate, s, perpendicular to the cone surface is now defined

$$-ds = rd\theta$$

The following dimensionless groups are introduced:

(a) Froude number, the ratio of centrifugal force to gravity at radius r

$$Fr = \frac{\omega^2 r\sin\beta}{g}$$

(b) Dimensionless flow

$$Q_0^+ = \frac{Q_0}{2\pi\sin^2\beta r^2\sqrt{\omega\nu}}$$

(c) Ratio of tangential velocity of cone to average radial velocity of liquid at r_0

$$\Omega = \frac{\omega\sin\beta r_0}{u_{av,r_0}}$$

(d) Dimensionless film thickness

$$\delta^+ = \left[\frac{\omega}{\nu}\right]^{\frac{1}{2}}\delta$$

(e) Dimensionless velocities

$$U = \frac{u}{\omega r\sin\beta}$$

$$V = \frac{v}{\sqrt{\omega\nu}}$$

$$W = \frac{w'}{\omega r\sin\beta}$$

(f) Dimensionless distance perpendicular to cone surface

$$\sigma = s\sqrt{\frac{\omega}{\nu}}$$

(g) Dimensionless radius

$$\eta = \frac{r}{r_0}$$

(h) Dimensionless pressure

$$P = \frac{p - p_0}{\rho\sqrt{\omega\nu}\ \omega r \sin\beta}$$

Substituting these dimensionless quantities into the equations of motion yields

$$U^2 + \eta U\frac{\partial U}{\partial \eta} - \frac{V}{\sin\beta}\frac{\partial U}{\partial \sigma} - W^2 - 1 + 2W = -\frac{\cot\beta}{Fr} + \frac{1}{\sin\beta}\frac{\partial^2 U}{\partial \sigma^2} \qquad (5.14)$$

$$-W^2 - 1 + 2W = \frac{\tan\beta}{Fr} + \frac{1}{\cos\beta}\frac{\partial P}{\partial \sigma} \qquad (5.15)$$

$$\eta U\frac{\partial U}{\partial \eta} + 2UW - \frac{V}{\sin\beta}\frac{\partial W}{\partial \sigma} - 2U = \frac{1}{\sin\beta}\frac{\partial^2 W}{\partial \sigma^2} \qquad (5.16)$$

$$\eta\frac{\partial U}{\partial \eta} + 3U - \frac{1}{\sin\beta}\frac{\partial V}{\partial \sigma} = 0 \qquad (5.17)$$

Note that the $\sin\beta$ term in the denominator of the final term in equations (5.14), (5.15) and (5.16) is (erroneously) omitted from Bruin's statement of these equations.

The dimensionless velocities are further transformed in the following way:

$$U_0 = \frac{u}{u_{av,r_0}} = \Omega\eta U \tag{5.18}$$

$$V_0 = \frac{v}{u_{av,r_0}} = \Omega\frac{\sqrt{\nu/\rho}}{r_0\sin\beta}V \tag{5.19}$$

$$W_0 = \frac{w}{u_{av,r_0}} = \Omega\eta W \tag{5.20}$$

These can be substituted into the dimensionless equations of motion derived above to give a new set of dimensionless equations:

$$\begin{aligned} U_0^2 + \eta^2 U_0\frac{\partial}{\partial\eta}\left[\frac{U_0}{\eta}\right] - \frac{\eta}{\Theta\sin\beta}V_0\frac{\partial U_0}{\partial\sigma} - W_0^2 - \Omega^2\eta^2 + 2\Omega\eta W_0 \\ = -\Omega^2\eta^2\frac{\cot\beta}{Fr} + \Omega\eta\frac{1}{\sin\beta}\frac{\partial^2 U_0}{\partial\sigma^2} \end{aligned} \tag{5.21}$$

$$2U_0W_0 + \eta^2 U_0\frac{\partial}{\partial\eta}\left(\frac{W_0}{\eta}\right) - \frac{\eta}{\Theta\sin\beta}V_0\frac{\partial W_0}{\partial\sigma} - 2\eta\Omega U_0 = \frac{\Omega\eta}{\sin\beta}\frac{\partial^2 W_0}{\partial\sigma^2} \tag{5.22}$$

$$-W_0^2 - \Omega^2\eta^2 + 2\Omega\eta W_0 = \Omega^2\eta^2\frac{\tan\beta}{Fr} + \frac{\Omega^2\eta^2}{\cos\beta}\frac{\partial P}{\partial\sigma} \tag{5.23}$$

$$\eta\frac{\partial}{\partial\eta}\left(\frac{U_0}{\eta}\right) + 3\frac{U_0}{\eta} - \frac{1}{\Theta\sin\beta}\frac{\partial V_0}{\partial\sigma} = 0 \tag{5.24}$$

where

$$\Theta = \frac{\sqrt{\nu/\omega}}{r_0 \sin\beta}$$

The boundary conditions are

$$U = V = W = 0 \quad \text{for} \quad \sigma = 0,\ \eta > 1$$

$$\frac{\partial U}{\partial \sigma} = \frac{\partial W}{\partial \sigma} = 0 \quad \text{for} \quad \sigma = b^{+},\ \eta > 1$$

$$P = 0 \quad \text{for} \quad \sigma = b^{+},\ \eta > 1$$

$$\int_0^{b^{+}} U d\sigma = Q_0^{+} \quad \text{for} \quad \eta > 1$$

Bruin proposes two solutions; one for $\Omega \gg 1$ and one for $\Omega > 1$.

5.2.2.1 Case 1: $\Omega \gg 1$

When $\Omega \gg 1$ (e.g. $\Omega > 10$), all terms on the left-hand sides of equations (5.21) to (5.24) other than those containing Ω^2 are discarded. Dividing eq. (5.21) by Ω^2 and re-arranging gives

$$\frac{1}{\Omega} \frac{\eta}{\sin\beta} \frac{\partial^2 U_0}{\partial \sigma^2} = -\eta^2 + \eta^2 \frac{\cot\beta}{Fr} + \frac{2\eta W_0}{\Omega} \tag{5.25}$$

Since $\Omega \gg 1$ the third term on the right-hand side of eq. (5.25) can also be discarded. Substituting eq. (5.18) for U_0 gives

$$-1 = -\frac{\cot\beta}{Fr} + \frac{1}{\sin\beta} \frac{\partial^2 U}{\partial \sigma^2} \tag{5.26}$$

Equation (5.22) becomes

$$-2\Omega^2\eta^2 U_0 = \Omega^2\eta^2 \frac{1}{\sin\beta}\frac{\partial^2 W_0}{\partial\sigma^2} \tag{5.27}$$

i.e.

$$\frac{\partial^2 W}{\partial\sigma^2} + 2\sin\beta U = 0 \tag{5.28}$$

Equation (5.23) becomes

$$-\Omega^2\eta^2 = \Omega^2\eta^2 \frac{\tan\beta}{Fr} + \Omega^2\eta^2 \frac{1}{\cos\beta}\frac{\partial P}{\partial\sigma} \tag{5.29}$$

i.e.

$$-1 = \frac{\tan\beta}{Fr} + \frac{1}{\cos\beta}\frac{\partial P}{\partial\sigma} \tag{5.30}$$

The continuity equation (5.17) is unchanged.

Equation (5.26) can be re-written as

$$\frac{\partial^2 U}{\partial\sigma^2} = \sin\beta\left[-1 + \frac{\cot\beta}{Fr}\right]$$

Integrating with respect to σ

$$\frac{\partial U}{\partial\sigma} = -\sin\beta\left[1 - \frac{\cot\beta}{Fr}\right]\sigma + C_1$$

$$= 0 \quad \text{for} \quad \sigma = b^+$$

from boundary condition (b) (the zero surface shear condition), so that

$$C_1 = \sin\beta\left[1 - \frac{\cot\beta}{Fr}\right] b^+$$

and

$$\frac{\partial U}{\partial \sigma} = -\sin\beta \left[1 - \frac{\cot\beta}{Fr}\right] (\sigma - b^{+})$$

Integrating again with respect to σ gives

$$U = -\sin\beta \left[1 - \frac{\cot\beta}{Fr}\right] (\frac{1}{2}\sigma^2 - b^{+}\sigma) + C_2$$

We now invoke boundary condition (a); i.e. $U = 0$ for $\sigma = 0$, to solve for C_2, which turns out to be zero.

An expression for the film thickness b^+ can be obtained by applying boundary condition (d) (continuity):

$$\int_0^{m^+} U d\sigma = Q_0^+ \quad \text{for} \quad \eta > 1$$

$$LHS = \int_0^{b^+} \sin\beta(1 - \frac{\cot\beta}{Fr})(b^{+}\sigma - \frac{1}{2}\sigma^2)d\sigma$$

$$= \frac{1}{3}\sin\beta(1 - \frac{\cot\beta}{Fr})b^{+3}$$

Therefore

$$b^{+} = \left[\frac{3Q_0^+}{\sin\beta(1 - \frac{\cot\beta}{Fr})}\right]^{\frac{1}{3}} \tag{5.31}$$

Equation (5.31) can be re-written to give an expression for the actual film thickness b:

$$b = \left[\frac{3Q_0\nu}{2\pi\sin^3\beta r^2\omega^2(1 - \frac{\cot\beta}{Fr})}\right]^{\frac{1}{3}} \tag{5.32}$$

Note that when the centrifugal acceleration is much greater than the gravitational acceleration, *Fr* becomes large and the value of film thickness obtained from eq. (5.32) approaches that given by eq. (5.8a), the simple modification of the Nusselt flat-plate equation for a liquid film flowing on a rotating conical surface. In fact, equation (5.32) can be obtained using the same approach as was used to derive eq. (5.8a) except that the total acceleration is the sum of the components of centrifugal and gravitational components parallel to the cone surface; in other words, equations (5.7a) and (5.8a) are limiting cases of eq. (5.32), eq. (5.7a) applying to pure gravity flow and (5.8a) to flow in which centrifugal force dominates.

5.2.2.2 Case 2: $\Omega > 1$

All terms on the left hand side of equations (5.21) to (5.24) containing Ω must now be considered. The differential equations become

$$-\Omega^2\eta^2 + 2\Omega\eta W_0 = -\Omega^2\eta^2\frac{\cot\beta}{Fr} + \Omega\eta\frac{1}{\sin\beta}\frac{\partial^2 U_0}{\partial\sigma^2} \tag{5.33}$$

i.e.

$$-1 + 2W = -\frac{\cot\beta}{Fr} + \frac{1}{\sin\beta}\frac{\partial^2 U}{\partial\sigma^2} \tag{5.34}$$

$$-2\Omega\eta U_0 = \Omega\eta\frac{1}{\sin\beta}\frac{\partial^2 W_0}{\partial\sigma^2} \tag{5.35}$$

i.e.

$$-2U = \frac{1}{\sin\beta}\frac{\partial^2 W}{\partial\sigma^2} \tag{5.36}$$

$$-\Omega^2\eta^2 + 2\Omega\eta W_0 = \Omega^2\eta^2\frac{\tan\beta}{Fr} + \Omega^2\eta^2\frac{1}{\cos\beta}\frac{\partial P}{\partial\sigma} \tag{5.37}$$

i.e.

$$-1 + 2W = \frac{\tan\beta}{Fr} + \frac{1}{\cos\beta}\frac{\partial P}{\partial \sigma} \qquad (5.38)$$

We can re-write equations (5.34) and (5.36) to get the following system of equations for U and W:

$$W = \frac{1}{2}\left[-\frac{\cot\beta}{Fr} + \frac{1}{\sin\beta}\frac{\partial^2 U}{\partial \sigma^2} + 1\right] \qquad (5.39)$$

$$U = -\frac{1}{2}\frac{1}{\sin\beta}\frac{\partial^2 W}{\partial \sigma^2} \qquad (5.40)$$

Equations (5.39) and (5.40) can be solved using the complex stream function ψ, where

$$\psi = U - iW$$

Substituting equations (5.39) and (5.40) for U and W gives

$$\begin{aligned}\psi &= -\frac{i}{2}\left[-\frac{\cot\beta}{Fr} + \frac{1}{\sin\beta}\frac{\partial^2 U}{\partial \sigma^2} + 1\right] - \frac{1}{2}\frac{1}{\sin\beta}\frac{\partial^2 W}{\partial \sigma^2} \\ &= \frac{i}{2}\left[\frac{\cot\beta}{Fr} - 1 - \frac{1}{\sin\beta}\left[\frac{\partial^2 U}{\partial \sigma^2} - i\frac{\partial^2 W}{\partial \sigma^2}\right]\right] \\ &= \frac{i}{2}\left[\frac{\cot\beta}{Fr} - 1 - \frac{1}{\sin\beta}\frac{\partial^2 \psi}{\partial \sigma^2}\right]\end{aligned}$$

i.e.

$$\frac{\partial^2\psi}{\partial\sigma^2} - 2i\sin\beta\psi - \sin\beta(\frac{\cot\beta}{Fr} - 1) = 0$$

The solution of this differential equation given by Bruin, corrected to include the $\sin\beta$ term omitted in his earlier manipulation, is

$$\psi = \frac{F(\eta)}{i2\sin\beta}\left[\tanh(b^{+}\sqrt{i2\sin\beta})\sinh(\sigma\sqrt{i2\sin\beta}) + 1 - \cosh(\sigma\sqrt{i2\sin\beta})\right] \qquad (5.41)$$

where

$$F(\eta) = \sin\beta(1 - \frac{\cot\beta}{Fr})$$

Expressions for U and W can be obtained by separating eq. (5.41) into its real and imaginary components:

$$U = \frac{1}{2}(1 - \frac{\cot\beta}{Fr})(-\sinh\sigma\sin\sigma + \xi_r) \qquad (5.42a)$$

$$W = -\frac{1}{2}(1 - \frac{\cot\beta}{Fr})(1 - \cosh\sigma\cos\sigma + \xi_i) \qquad (5.42b)$$

where

$$\xi_r = \frac{\sin(2Bb^{+})\sinh(B\sigma)\cos(B\sigma) + \sinh(2Bb^{+})\cosh(B\sigma)\sin(B\sigma)}{\cosh(2Bb^{+}) + \cos(2Bb^{+})}$$

$$\xi_i = \frac{\sinh(2Bb^{+})\sinh(B\sigma)\cos(B\sigma) - \sin(2Bb^{+})\cosh(B\sigma)\sin(B\sigma)}{\cosh(2Bb^{+}) + \cos(2Bb^{+})}$$

$$B = \sqrt{\sin\beta}$$

Finally, the dimensionless film thickness b^+ is found by invoking the continuity condition (i.e. integrating eq. (5.42a) across the film) to obtain the following implicit relationship between film thickness and radius:

$$4Q_0^+ = F(\eta) I_0(b^+) \tag{5.43}$$

where

$$I_0(b^+) = \frac{\sinh(2Bb^+) - \sin(2Bb^+)}{\cosh(2Bb^+) + \cos(2Bb^+)}$$

Eq. (5.43) does not always have a solution. The integral $I_0(b^+)$ attains a maximum value of 1.09 for $Bb^+ \approx 1.6$. Therefore, if the ratio $4Q_0^+/F(\eta) > 1.09$ there can be no solution.

5.3 Experimental measurement of film surface velocities

In this section a set of experiments is described in which surface velocities of a liquid film flowing on a rotating cone were measured.

5.3.1 Outline of experimental procedure

The procedure for determining liquid film surface velocities used in the experiments described here was similar in principle to that used by Wood and Watts (1973) in studies of film flow across a rotating disc. In our case, the flow of the liquid film on a rotating cone was recorded using a video camera capable of operating with short exposure times (0.005s). Tracers, small (ca 4 mm^2) pieces of coloured paper, were dropped onto the liquid surface while the video camera was recording. A number of such drops were made while the camera was running, all the while the flow visualization rig running at constant rotational speed and liquid flow. This procedure was followed for three liquid flows, 2, 5 and 10 kg/minute, and for three rotational speeds, 250, 500 and 1000 RPM.

5.3.2 Description of flow visualization rig

A schematic diagram of the flow visualization rig is shown in fig. 5.1. The rotating cone element was identical to those in the CSIRO Mk III spinning cone column (see table 4.1): the inner and outer diameters of the conical surface were 100 mm and 290 mm respectively; the cone angle was 45°. Immediately below the spinning cone was a conical perspex housing having the same dimensions as the stationary cones in the CSIRO Mk III SCC. Attached to the throat of the conical perspex housing was a stainless steel cylinder with an outlet pipe through which water drained from the rig.

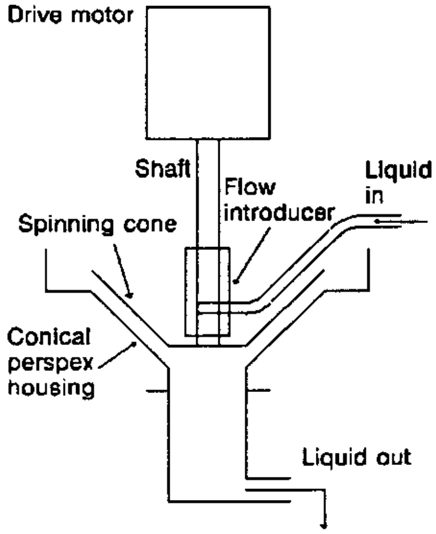

Figure 5.1
Schematic diagram of flow visualization rig

5.3.3 Determination of tracer trajectories and velocities from video recordings

The trajectories of the tracer particles were determined by analysis of successive individual frames of the video recordings. Like all conventional video cameras, the unit used in these experiments recorded video images at a (nominal) rate of 25 per second, implying a time interval of 0.04 seconds between successive frames.

The procedure followed was as follows:

(a) The recording of a particular drop was located on the video tape.

(b) Each frame in which tracer particles were visible recorded during this drop was printed on a video printer.

(c) The positions of the tracer particles were traced from the print onto transparent graph paper, along with designated fixed scaling points on the flow visualization rig.

(d) The actual positions of the tracer particles on the surface of the liquid film were estimated by transforming the relative positions of the tracers and the fixed scaling points obtained from the frame print. The basis of this transformation, and the assumptions on which it was based, are discussed in (5.3.3.1).

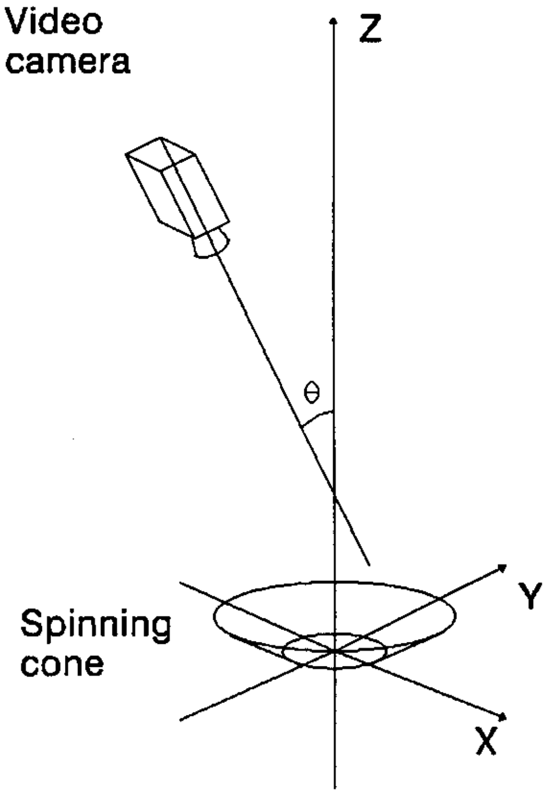

Figure 5.2
Geometrical definition of experimental set-up

5.3.3.1 Geometrical basis for transformation of video images to locations in 3-dimensional space

Fig. 5.2 is a diagrammatic representation of the geometrical layout of the experimental set-up. Consider a 3-dimensional rectangular coordinate system as shown in fig. 5.2. The origin is at the centre of base of the spinning cone; the x-axis, when viewed through the video camera, runs horizontally from left to right; the y-axis is also horizontal but when viewed through the video camera appears coincident with the vertical z-axis. This is because the video camera was positioned so that its optical axis lay in the y-z plane but tilted at an angle θ with respect to the z-axis.

The video camera was mounted about 1.5m above the spinning cone and its zoom lens adjusted so that the image of the spinning cone (nearly) filled the frame. The image appearing in the frame was printed and then traced onto transparent graph paper; each tracing yielded coordinates x' and y' of the particle on the traced image and an image of the rim of the spinning cone which was used to scale the coordinates. The scaling factor, G, was the ratio of the actual outer diameter of the spinning cone to the outer diameter of the traced image of the spinning cone, measured parallel to the x'-axis. The cosine of the tilt angle θ was the ratio of the outer diameter of the traced image of the spinning cone measured parallel to the y'-axis to that measured parallel to the x'-axis.

Because the optical axis of the camera was assumed to lie in the y-z plane, the actual x coordinate of the tracer particle was given directly from its position on the traced image; i.e $x = x' \times G$.

The y coordinate of the tracer particle was found in the following way: the particle was assumed to lie on the surface of the spinning cone (thereby neglecting film thickness) and also on a straight line parallel to the optical axis of the camera and passing through a point (Gx', Gy') on a plane surface perpendicular to the optical axis of the camera (this surface is a direct projection of the traced image; see fig. 5.3).

The equation of this straight line is

$$z = \frac{y}{\tan\theta} + \frac{Gy'}{\sin\theta}$$

The equation of the conical surface is

$$x^2 + y^2 = (z + R_i)^2$$

where R_i is the inner radius of the spinning cone.

The y coordinate of the tracer particle is found by substituting the expression for z (the equation of the straight line) into the equation of the conical surface and solving the resulting quadratic for y.

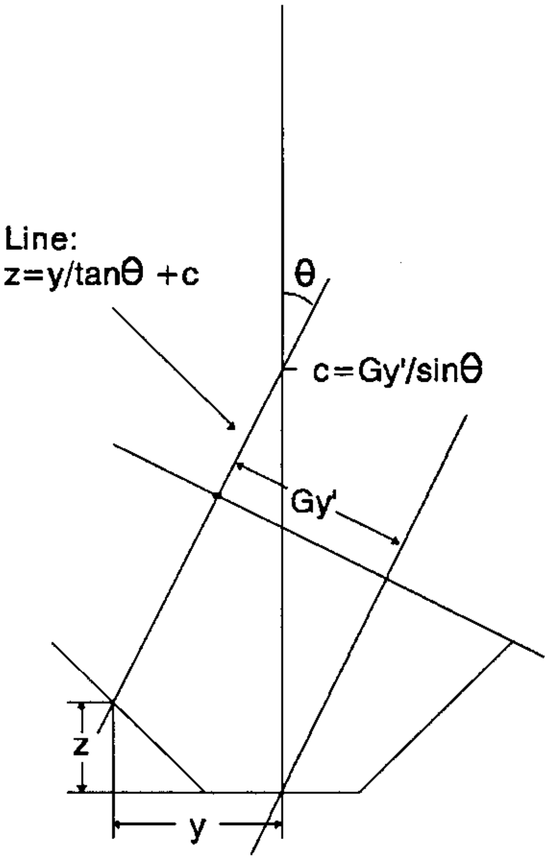

Figure 5.3
Plane section, parallel to *y*-*z* plane at $x = Gx'$, showing tracer particle on cone surface at (y,z)

5.4 Results and discussion

5.4.1 Method of analysis of experimental data

The results from these experiments were quantified in the following way: the average radial velocity of the tracer particles on the conical surface (i.e. for $0.05 \text{ m} < r < 0.145 \text{ m}$) was calculated from the observed trajectories (position vs time), these having been obtained from the video recordings in the manner described in 5.3.3.1. The mean value and 95% confidence limits of the observed average radial velocities, along with the surface radial velocities predicted by the Nusselt and Bruin models, are plotted in figures 5.4 to 5.12 for each of the nine sets of values of liquid flow and rotational speed.

5.4.2 Limits of experimental procedure

The fixed time interval of 0.04s between consecutive video frames imposes an upper limit on velocities which can be measured using this procedure. The length of the conical surface in the radial direction was 0.139 m. Therefore, if the particle's radial velocity was greater than a limiting value of 3.5 m/s it would have left the conical surface before 0.04 seconds had elapsed and so would not appear in the next frame. In fact it can be shown that, if we consider only particles moving at constant radial velocity, the probability of successfully measuring such a particle's velocity (i.e. observing the particle in two consecutive video frames) varies linearly from unity where the particle's velocity is half the limiting velocity, to zero where its velocity is equal to the limiting velocity. Under conditions where the true mean velocities were close to or within this range, we would expect the observed average radial velocities to be lower than the true values as a result of this characteristic of the experimental method.

5.4.3 Surface waves

Waves were observed on the surface of the film in all these trials. In the case of 2-dimensional laminar film flow the wave velocity is twice the surface velocity. It is possible that some of the tracer particles on the surface of the film were picked up and carried by these waves, and therefore moved at roughly twice the actual surface velocity.

5.4.4 Sensitivity/accuracy of experimental method

There is wide scatter in the values of observed average radial velocity (see tabulated values in the appendix to this chapter); factors contributing to this scatter may include the following:

- the film itself was by no means smooth or free of disturbances (making such an experimental rig operate without vibration would be virtually impossible, given its mechanical layout and the rotational speeds involved);
- there would be some error associated with the measurement of position of the tracer particles and this error would be compounded when the particle trajectories are converted to velocities, an operation equivalent to numerical differentiation.

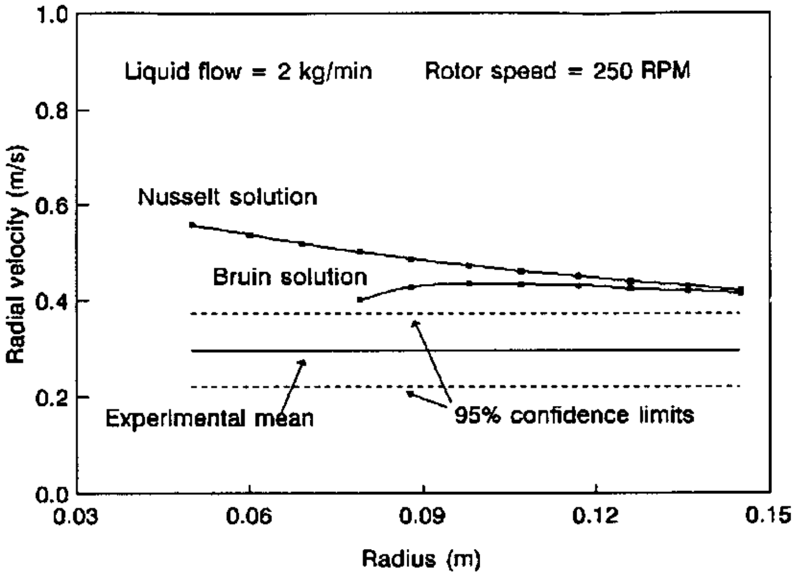

Figure 5.4
Average radial liquid velocity vs radius: 250 RPM, 2 kg/min.

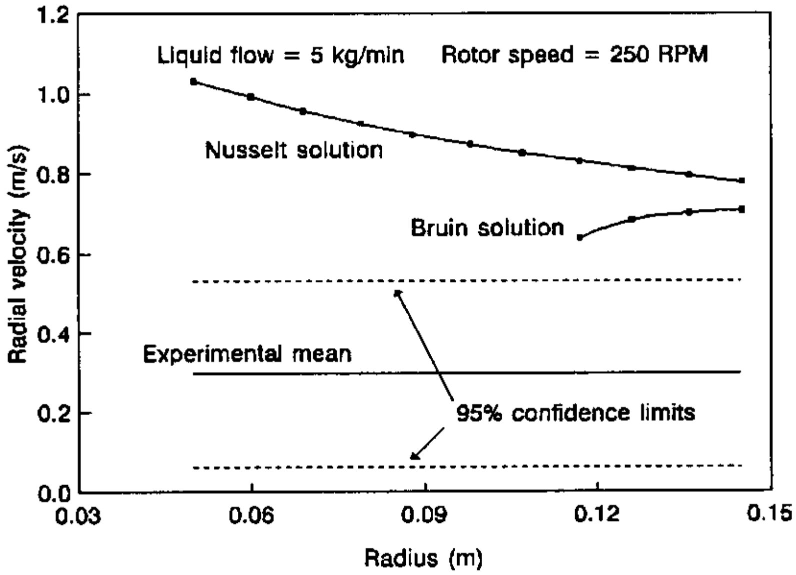

Figure 5.5
Average radial liquid velocity vs radius: 250 RPM, 5 kg/min.

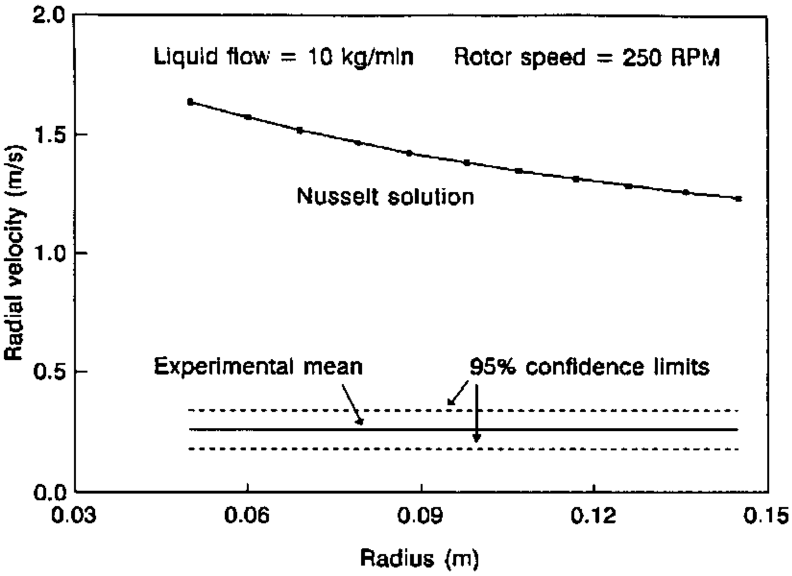

Figure 5.6
Average radial liquid velocity vs radius: 250 RPM, 10 kg/min.

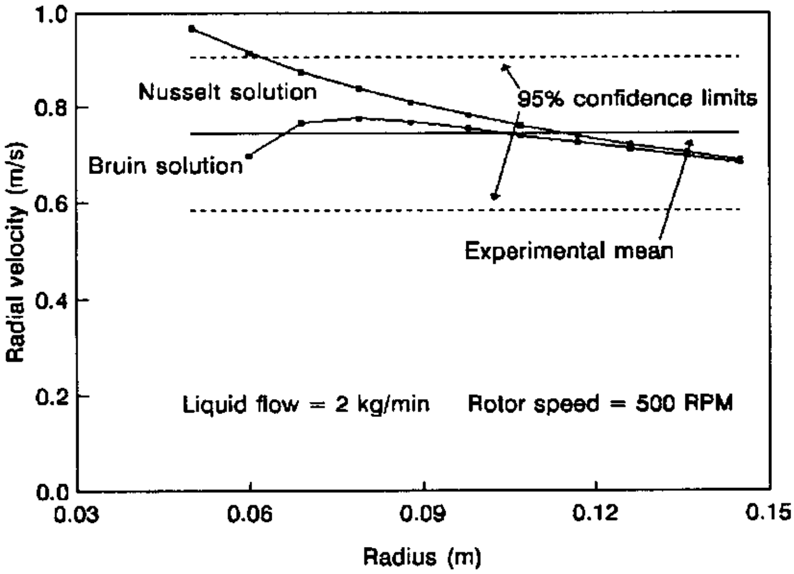

Figure 5.7
Average radial liquid velocity vs radius: 500 RPM, 2 kg/min.

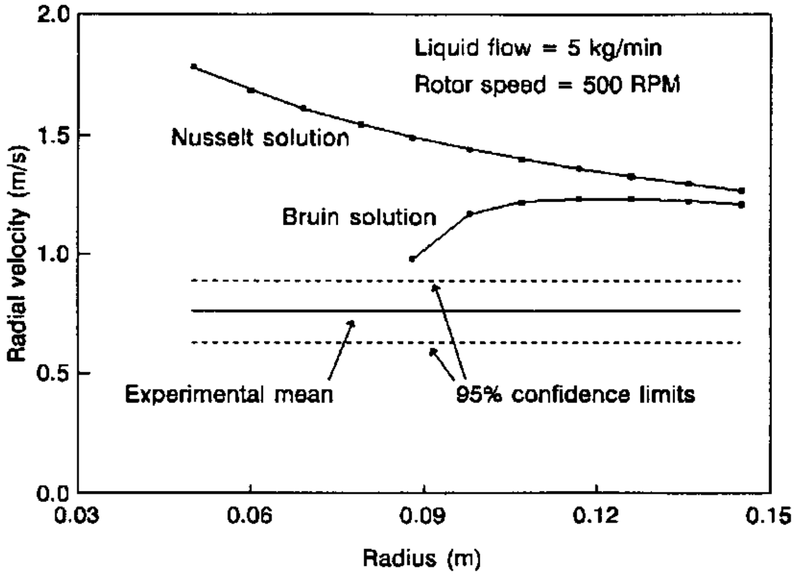

Figure 5.8
Average radial liquid velocity vs radius: 500 RPM, 5 kg/min.

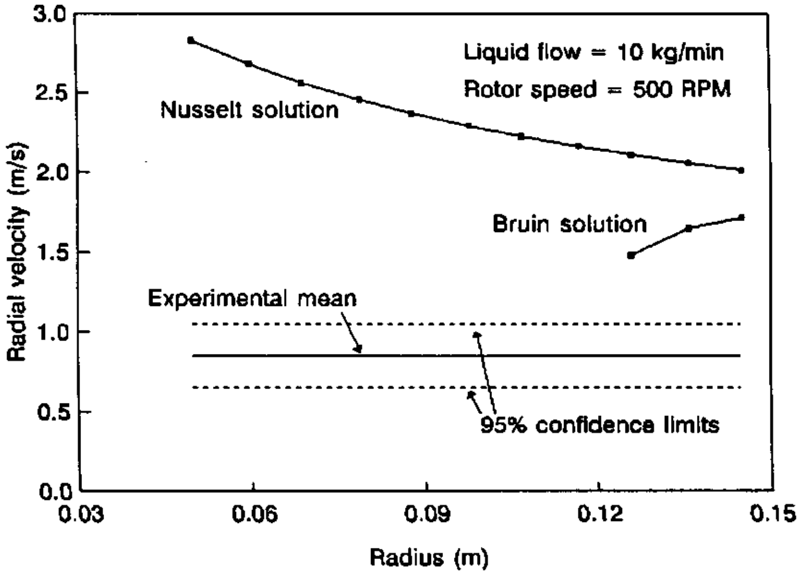

Figure 5.9
Average radial liquid velocity vs radius: 500 RPM, 10 kg/min.

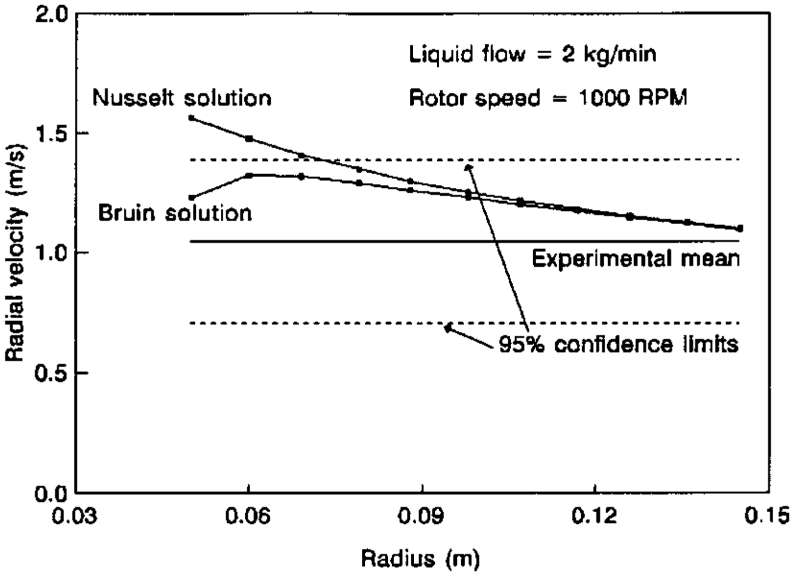

Figure 5.10
Average radial liquid velocity vs radius: 1000 RPM, 2 kg/min.

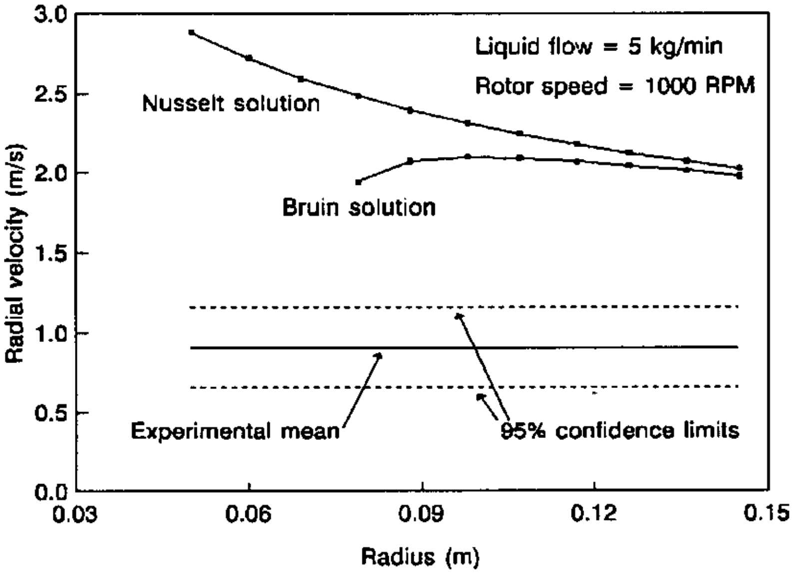

Figure 5.11
Average radial liquid velocity vs radius: 1000 RPM, 5 kg/min.

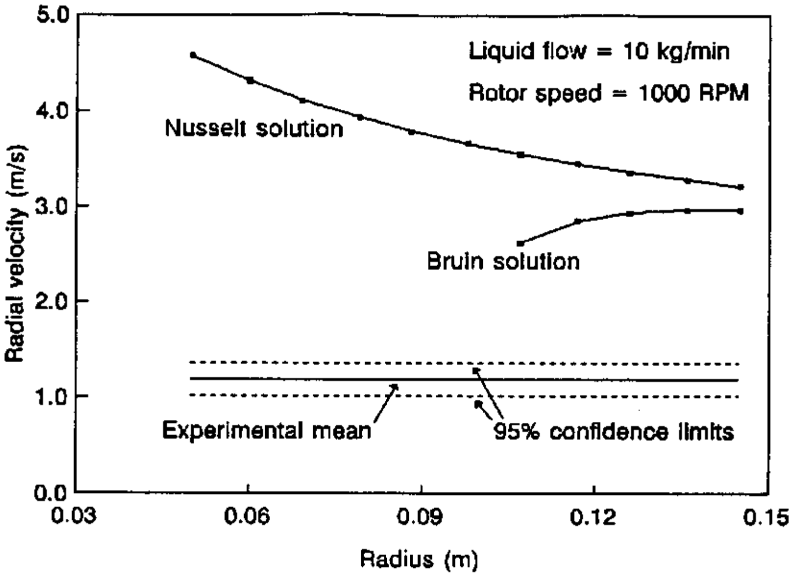

Figure 5.12
Average radial liquid velocity vs radius: 1000 RPM, 10 kg/min.

5.4.5 Results

The results obtained in the manner described in 5.4.1 are summarized in table 5.1.

Table 5.1
Average radial velocities parallel to cone surface (m/s)

		2 kg/min.	5 kg/min.	10 kg/min.
250 RPM	Experimental	0.30	0.30	0.26
	Bruin	0.45 (70%)	0.72 (30%)	No solution
	Modified Bruin	0.38	0.47	No solution
	Nusselt	0.48	0.87	1.41
500 RPM	Experimental	0.75	0.76	0.85
	Bruin	0.77 (90%)	1.24 (60%)	1.70 (20%)
	Modified Bruin	0.73	0.99	1.02
	Nusselt	0.80	1.48	2.34
1000 RPM	Experimental	1.05	0.91	1.19
	Bruin	1.28 (100%)	2.15 (70%)	3.03 (40%)
	Modified Bruin	1.28	1.83	2.12
	Nusselt	1.29	2.37	3.76

The percentage in parentheses after the average radial velocity obtained from the Bruin model indicates the fraction of the distance between the inner and outer radiuses of the cone for which the Bruin solution exists (see figures 5.4 to 5.12).

The modified Bruin average radial velocity was obtained by assuming that the average radial velocity on that part of the conical surface for which there is no solution in the Bruin model is half the average radial velocity over the portion of the conical surface for which a solution exists; i.e. we assume that the radial velocity in the no-solution zone varies linearly between zero and the average radial velocity over the portion of the conical surface for which the Bruin model has a solution (see fig. 5.13). This assumption is crude and somewhat arbitrary but is likely to give a more realistic prediction of average radial velocity over the whole conical surface than either the Nusselt model or the unmodified Bruin model.

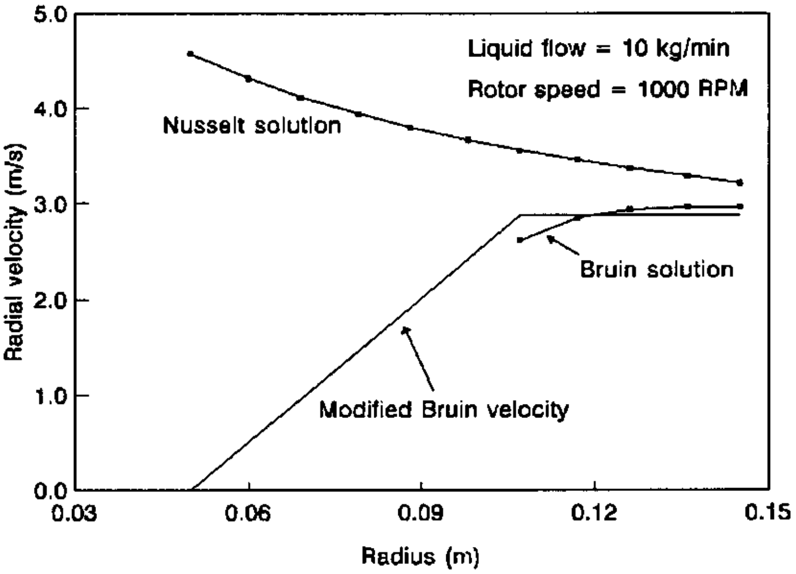

Figure 5.13
Radial velocity vs radius for 1000 RPM and 10 kg/min showing Nusselt, Bruin and modified Bruin velocities.

Fig. 5.14 is a graph of the mean observed average radial velocities plotted against the corresponding modified average radial velocity obtained from the Bruin solution, defined above. These data are also given in table 5.1.

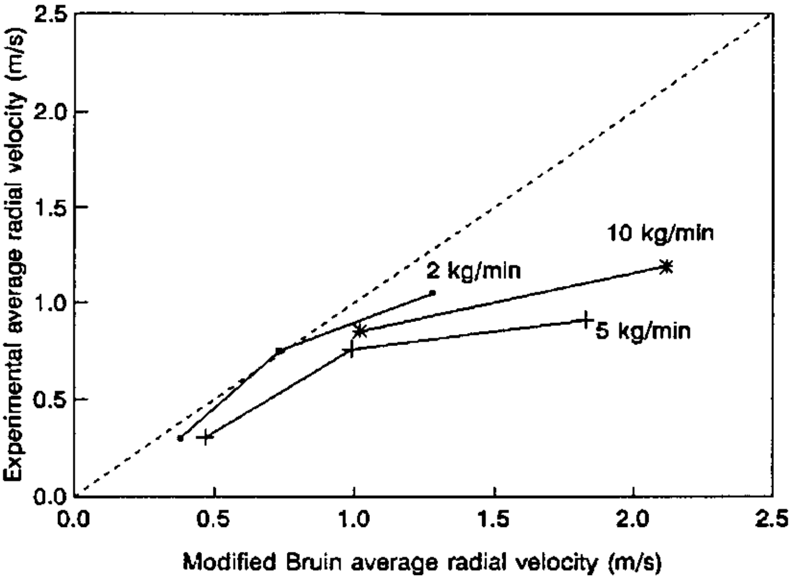

Figure 5.14
Mean experimental average radial velocities plotted against modified Bruin average radial velocities

5.4.6 General discussion

As foreshadowed in section 5.2 the Bruin solution breaks down (ceases to exist) when the ratio $4Q_0^+/F(\eta) > 1.09$. The radius at which this condition is met increases as liquid flow rises and rotational speed falls. The critical assumption on which the Bruin solution (and by implication the Nusselt solution) rests is that the film thickness is small compared to the corresponding radius. We expect film thickness to increase as liquid flow is increased and as rotational speed and radius fall. The limits of the Bruin solution can be interpreted as the combination of liquid flow, rotational speed and radius at which this assumption ceases to be valid. For example, the only set of operating conditions of the nine studied for which the Bruin model has a solution for the whole of the conical surface was for 1000 RPM and 2 kg/min., i.e the highest rotational speed and the lowest liquid flow; at the other extreme, 250 RPM and 10 kg/min, the Bruin model did not have a solution for any point on the conical surface (i.e. for $r < 0.145$m).

The observed average velocities are of the same order as those predicted by both the Bruin and Nusselt models. Indeed, given the aforementioned limitations of the experimental method, and the simplification implicit in the modified Bruin average radial velocity, the agreement between observed and predicted values is quite close (see fig. 5.14). At 2 kg/min. the observed average velocities are within 20% of the modified Bruin average for all rotational speeds. At 500 RPM the observed values are within 25% of the predicted values for all liquid flows.

The main area of divergence is at 1000 RPM where the observed values are substantially lower than those predicted, especially at 5 and 10 kg/min. It is under these conditions that we expect the highest film surface velocities; the low observed average radial velocities are consistent with the limitations on the experimental procedure discussed in 5.4.2.

These results broadly confirm the validity of the Bruin model. Neither the Bruin nor the Nusselt model, however, can be applied without modification to conditions which would typically obtain in a commercial SCC having the same cone dimensions as the experimental rig: typical operating conditions for such a column are 1000 kg/hour liquid flow at a rotational speed of 400 RPM. In table 5.1 we see that at a liquid flow of 10 kg/min. = 600 kg/hour, and a rotational speed of 500 RPM, the Bruin solution exists only for radiuses greater than 80% of the outer radius of the conical surface.

Prediction of flow characteristics, such as film thickness, and surface and average film velocities, for typical operating conditions in the SCC requires a more complete solution of the Navier-Stokes equations for this flow system than can be provided by the Bruin model; the Nusselt model is effectively a simplified form of the Bruin model. In particular, the limits of physical capacity of the SCC are associated with flow conditions at the inner throat, the region where the Nusselt and Bruin models are least likely to provide valid solutions since the assumption that film thickness is much smaller than radius does not apply.

Development of computer-based numerical solutions of the Navier-Stokes equations describing this flow, which are not subject to the limitations suffered by the Nusselt and Bruin models, is in progress (Langrish *et al.*, 1993).

CHAPTER 6

MASS TRANSFER IN THE SPINNING CONE COLUMN

6.1 Introduction

In this chapter the results of experimental studies of mass transfer in the SCC are presented. These results are compared to estimates derived from simple mass transfer correlations and the implications of the differences between the measured results and the estimates are discussed.

6.2 Experimental studies

6.2.1 Acetic acid/water trials on the CSIRO Mk II SCC

In this series of trials the CSIRO Mk II SCC was run under total reflux at atmospheric pressure with dilute acetic acid/water solutions. The independent variables were heat input to the reboiler, which determines the liquid and gas flows, and rotor speed.

By running the system under total reflux, allowing it to come to equilibrium, and then measuring the concentration of acetic acid in the liquid streams entering and leaving the column the mass transfer performance at the prevailing conditions of rotor speed and vapour and liquid flows could be calculated.

6.2.1.1 Experimental procedure

A schematic diagram of the system used in these trials is shown in fig. 6.1.

The experimental procedure was as follows:

(a) a fixed charge, about 15 kg, of liquid was placed in the reboiler. The concentration of acetic acid in the charge was varied between 5% and 20% by weight.
(b) the system was started up: steam was admitted to reboiler jacket, and the SCC drive motor and discharge pump started etc.
(c) once the system had attained thermal equilibrium, indicated by a steady flow of reflux from the condenser, steam input to the reboiler was adjusted to obtain the required reflux flow; also the rotor speed was adjusted to the required value.
(d) the system was allowed to run at steady conditions for about 30 minutes, after which samples of the discharge and reflux streams were withdrawn.
(e) the concentrations of acetic acid in the discharge and reflux samples were determined by titration with sodium hydroxide (0.1N).
(f) steps (c), (d) and (e) were repeated two or three times for each charge of liquid.

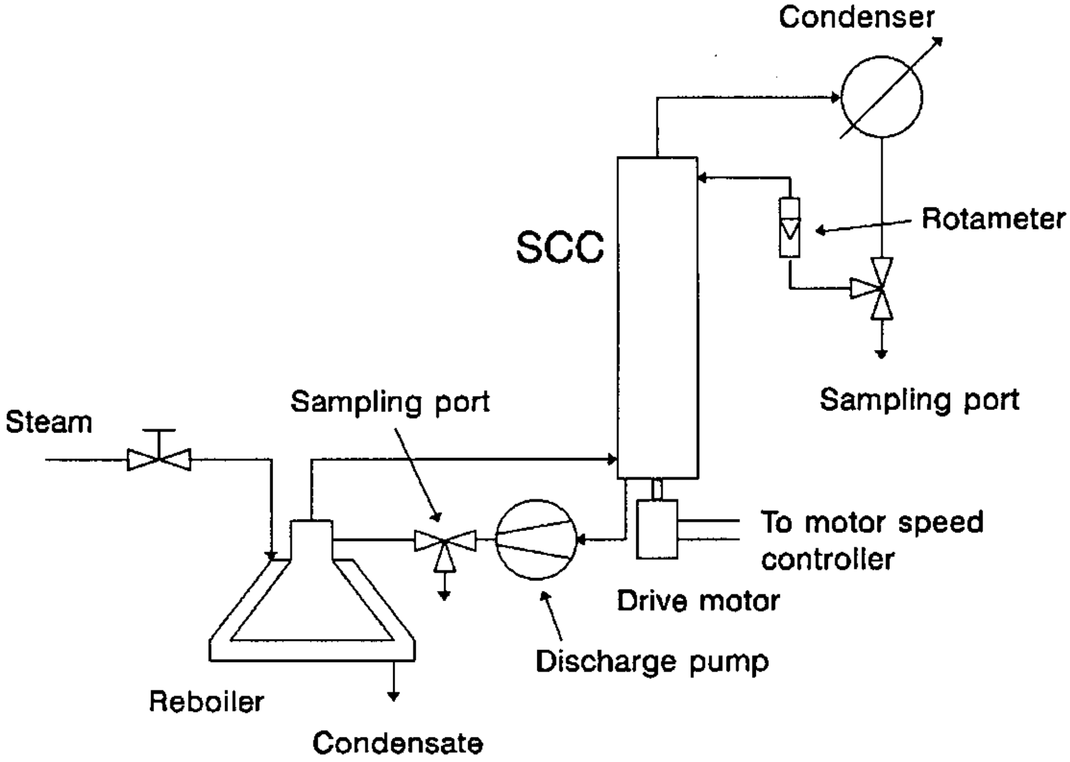

Figure 6.1
Schematic diagram of experimental set-up used in acetic acid/water total reflux trials

6.2.1.2 Analysis of experimental results

One measure of the separation efficiency of a distillation column is the number of theoretical stages (*NTS*) achieved under conditions of total reflux.

In the case where the relative volatility of the components is effectively constant, the value of *NTS* achieved under total reflux can be calculated using Fenske's equation (Treybal, 1981):

$$NTS = \frac{\log \frac{x_{AD}}{1-x_{AD}} \frac{1-x_{AW}}{x_{AW}}}{\log \alpha} \tag{6.1}$$

where x_{AD} is the mole fraction of the more volatile component in the liquid entering the column,

x_{AW} is the mole fraction of the more volatile component in the liquid leaving the column, and

α is the relative volatility.

We can also calculate overall mass transfer coefficients, K'_x and/or K'_y, using the same data.

Sample calculations, using the data of run 14 (see table A4.1 in Appendix 4), are set out in 6.2.1.2.1 and 6.2.1.2.2 to illustrate the procedure by which the experimental results were analysed.

6.2.1.2.1 Sample calculation of number of theoretical stages, *NTS*

Raw data from run 14 (see table A4.1):

Concentration of acetic acid in liquid entering	12.54% by weight
Concentration of acetic acid in liquid leaving	0.0986% by weight

Water is in fact the more volatile component in acetic acid/water solutions. We shall follow conventional practice and designate water as component A. Therefore the mole fraction of water leaving the column is

$$x_{AW} = \frac{\omega_{AW}/M_A}{\omega_{AW}/M_A + \omega_{BW}/M_B} \tag{6.2}$$

where ω_{AW} is the mass fraction of water in the liquid leaving the column,
ω_{BW} is the mass fraction of acetic acid in the liquid leaving the column,
M_A is the molecular weight of water (18.02), and
M_B is the molecular weight of acetic acid (120.1).

Note that the actual molecular weight of acetic acid is in fact 60.05 but its VLE behaviour (specifically its tendency to exist in dimer form) is such that the appropriate value to use in distillation calculations is double the actual value.

The value of relative volatility of water with respect to acetic acid, α, used in these calculations was determined from VLE data for acetic acid/water solutions given by Seader and Zdzislaw (1984). The mole fraction of the more volatile component, water, in the reflux and discharge streams varied in a narrow range: $0.94 < x_A < 1$. The VLE data indicate that the relative volatility in this range varies between 1.46 and 1.43. As the bulk of the measured concentrations were closer to the upper end of this range, α was assumed to take a constant value of 1.43.

From eq. (6.2), $x_{AW} = 0.9789$ and by similar arguments $x_{AD} = 0.99985$. Substituting these values, and $\alpha = 1.43$, into eq. (6.1) gives the number of theoretical stages, *NTS*, achieved in this separation (run 14) as 17.0.

6.2.1.2.2 Sample calculation of overall mass transfer coefficient, K'_x

The volume flow of liquid into the column was measured using a rotameter, and in the case of run 14 it was

$$Q_D = 221 \text{ ml/min} = 3.683 \times 10^{-6} \text{ m}^3\text{/s}$$

The density of liquid entering the column is taken to be

$$\rho = \omega_A \rho_{\text{water}} + \omega_B \rho_{\text{acetic acid}}$$

At 100°C the densities of water and acetic acid are respectively 957.9 kg/m^3 and 1002.0 kg/m^3 so that $\rho = 957.9$ kg/m^3.

The molar flow of water into the column is

$$\Phi_{AD} = \omega_{AD} \rho Q_D / M_A$$

$$= \frac{0.000986 \times 957.9 \times 3.683 \times 10^{-6}}{18.02}$$

$$= 1.956 \times 10^{-4} \text{ kmol/s}$$

Similarly, at the bottom of the column, the molar flow of water leaving the column is

$$\Phi_{AW} = 1.915 \times 10^{-4} \text{ kmol/s}$$

and the quantity of water transferred from liquid to vapour in the column is therefore

$$\Phi_{A,T} = \Phi_{AD} - \Phi_{AW}$$

$$= 4.10 \times 10^{-6} \text{ kmol/s}$$

The average interfacial molar flux is given by

$$N_A = \frac{\Phi_{A,T}}{A_i} \qquad (6.3)$$

where A_i is the interfacial area.

We assume that the interfacial area $A_i = 1.53\ \text{m}^2$, the area of the upper surfaces of the cones, and by implication, the wetted area in the column. Therefore the molar flux between gas and liquid in the column is $N_A = 2.673 \times 10^{-6}\ \text{kmol/m}^2\text{s}$.

The overall liquid mass transfer coefficient, K'_x, is defined in the following way:

$$N_A = K_x' \left(x_A - x_A * \right) \tag{6.4}$$

where x_A is the bulk concentration of A in the liquid at some particular point in the column, and

x_A* is the mole fraction of A in the liquid in equilibrium with y_A, the bulk concentration of A in the vapour at the same point in the column.

That is

$$x_A * = \frac{y_A}{\alpha + y_A(1 - \alpha)} \tag{6.5}$$

Under conditions of total reflux the mole fraction of A in the liquid is equal to the mole fraction of A in the vapour at the same point in the column: $x_A = y_A$. Therefore

$$x_A * = \frac{x_A}{\alpha + x_A(1 - \alpha)}$$

Finally, we define a logarithmic mean concentration difference

$$\left(x_A - x_A * \right)_{LM} = \frac{\left(x_{AD} - x_{AD} * \right) - \left(x_{AW} - x_{AW} * \right)}{\ln[\left(x_{AD} - x_{AD} * \right)/\left(x_{AW} - x_{AW} * \right)]} \tag{6.6}$$

$$= 0.00176$$

from which we obtain

$$K_x' = \frac{N_A}{\left(x_A - x_A * \right)_{LM}} \tag{6.7}$$

$$= 0.0015\ \text{kmol/m}^2\text{sMF}$$

6.2.1.3 Results

The results of the acetic acid/water trials, and the corresponding values of *NTS* and K'_x, are shown in table A4.1 in the appendix to this chapter.

6.2.1.4 Prediction of mass transfer performance

Before discussing these results in detail we shall employ simple mass transfer correlations to obtain estimates of the overall mass transfer coefficient, K'_x.

The approach taken is based on methods described by Treybal (1981). We shall use the data of run 14 (see table A4.1) to illustrate the means by which the estimates of mass transfer performance have been obtained.

6.2.1.4.1 Liquid phase mass transfer coefficient, k'_x

Table 6.1
Total reflux trials with acetic acid/water
Run 14: concentration data for liquid entering column

Component	Water (A)	Acetic acid (B)	
Pure density (kg/m^3)	957.9	1002.0	
Molecular weight, M	18.02	120.10	
Mass fraction, ω	0.999014	0.000986	
Density of solution (kg/m^3)			957.9
Mass concentration, ρ (kg/m^3)	957.0	0.9	
Molar concentration, c (kmol/m^3)	53.11	0.01	
Molar density of solution (kmol/m^3)			53.11
Mole fraction, x	0.99985	0.00015	
Mean molecular weight			18.04

Liquid viscosity, μ, will be taken as that of water at 100°C, 2.79×10^{-4} Pa s.

The liquid diffusivity, D_{AB}, is estimated using the following equation, the empirical correlation of Wilke and Chang, as recommended by Treybal (1981):

$$D_{AB} = \frac{117.3 \times 10^{-18} (\varphi M_B)^{0.5} T}{\mu v_A^{0.6}} \tag{6.8}$$

Table 6.2
Data for calculation of average film thickness and velocity

Liquid film calculations (velocity and thickness)						
Rotor speed	500 RPM					
Liquid flow	3.7×10^{-7} m^3/s					
Cone angle	50°					
			Gravity		Centrifugal	
	Radius (m)	Γ (kg/s m)	u_{av} (m/s)	b (mm)	u_{av} (m/s)	b (mm)
Inner radius	0.025	0.022	0.168	0.140	0.261	0.078
	0.029	0.019	0.152	0.133	0.249	0.070
	0.033	0.017	0.140	0.128	0.239	0.065
	0.037	0.015	0.130	0.123	0.230	0.060
	0.041	0.014	0.121	0.119	0.222	0.056
	0.045	0.013	0.114	0.115	0.216	0.053
	0.048	0.012	0.108	0.112	0.210	0.050
	0.052	0.011	0.103	0.109	0.204	0.047
	0.056	0.010	0.098	0.107	0.199	0.045
	0.060	0.009	0.094	0.104	0.195	0.043
Outer radius	0.064	0.009	0.090	0.102	0.191	0.041

The Reynolds number of a liquid film is conventionally defined as

$$\mathrm{Re} = \frac{4\Gamma}{\mu} \tag{6.10}$$

where Γ is the mass flow per unit circumference (kg/s m).

Average values of Γ and b were obtained by numerically integrating the appropriate values over the area of the conical surface; i.e.

$$\Gamma_{av} = \frac{1}{A_{cone}} \int_{A_{cone}} \Gamma \, dA \tag{6.11a}$$

$$b_{av} = \frac{1}{A_{cone}} \int_{A_{cone}} b \, dA \tag{6.11b}$$

giving Γ_{av} = 0.0126 kg/s m, and b_{av} = 0.109 mm for the gravity film and 0.050 mm for the centrifugal film.

The average Reynolds number is therefore

$$\mathrm{Re}_{av} = \frac{4 \times 0.0126}{2.79 \times 10^{-4}} = 181$$

The Schmidt number is

$$\mathrm{Sc} = \frac{\mu}{\rho D_{AB}} \tag{6.12}$$

$$= \frac{2.79 \times 10^{-4}}{957.9 \times 9.97 \times 10^{-9}} = 29.2$$

and from eq. (6.9)

$$\mathrm{Sh} = \left[\frac{3}{2\pi} \times \frac{0.000109}{0.051} \times 181 \times 29.21 \right]^{0.5} = 1.51$$

The Sherwood number, Sh, is defined as

$$\mathrm{Sh} = \frac{k_x' b}{c D_{AB}} \tag{6.13}$$

so that, in the case of the gravity film

$$k_x' = 1.514 \times \frac{53.11 \times 9.97 \times 10^{-9}}{0.000109} = 0.0074 \text{ kmol/m}^2\text{sMF}$$

Similarly, for the centrifugal film

$$k_x' = 1.514 \times \frac{53.11 \times 9.97 \times 10^{-9}}{0.000050} = 0.0160 \text{ kmol/m}^2\text{sMF}$$

6.2.1.4.2 Vapour phase mass transfer coefficient, k'_y

Table 6.3
Run 14: concentration data for vapour leaving column

Component	Water (A)	Acetic acid (B)	
Pure density (kg/m^3)	0.5977	0.5977	
Molecular weight, M	18.02	120.10	
Mass fraction, ω	0.999014	0.000986	
Density of solution (kg/m^3)			0.5977
Mass concentration, ρ (kg/m^3)	0.5971	0.0006	
Molar concentration, c (kmol/m^3)	0.03314	0.00000	
Molar density of solution (kmol/m^3)			0.03314
Mole fraction, x	0.99985	0.00015	
Mean molecular weight			18.04

Vapour viscosity, μ, will be taken as that of steam at 100°C, 1.20×10^{-5} Pa s.

The vapour diffusivity, D_{AB}, is estimated using the following equation (the Wilke-Lee modification of the Hirschfelder-Bird-Spotz method, as recommended by Treybal):

$$D_{AB} = \frac{10^{-4}(1.084 - 0.249\sqrt{1/M_A + 1/M_B})T^{3/2}\sqrt{1/M_A + 1/M_B}}{p_t(r_{AB})^2 f(\mathrm{k}T/\epsilon_{AB})} \qquad (6.14)$$

where T is the absolute temperature (K),
p_t is the absolute pressure (Pa),
r_{AB} is the molecular separation at collision (nm) = $(r_A + r_B)/2$,
ϵ_{AB} is the energy of molecular attraction = $\sqrt{(\epsilon_A \epsilon_B)}$,
k is Boltzmann's constant, and
$f(kT/\epsilon_{AB})$ is the collision function, presented in graphical form by Treybal.

The data used to calculate the vapour diffusivity are set out in table 6.4.

Table 6.4
Data for estimation of vapour diffusivity

	A: water	B: acetic acid	Solution
ϵ/k	809.1	473.3	618.8
kT/ϵ_{AB}			0.603
$f(kT/\epsilon_{AB})$			0.82
r	0.264	0.472	
r_{AB}			0.368
$\sqrt{(1/M_A + 1/M_B)}$			0.269
D_{AB} (m²/s)			1.75×10^{-5}

In order to estimate the vapour phase mass transfer coefficient, k'_y, we shall use the Sherwood-Gilliland correlation for turbulent flow in circular pipes:

$$\mathrm{Sh}_{av} = 0.023\,\mathrm{Re}^{0.83}\mathrm{Sc}^{1/3} \tag{6.15}$$

The Reynolds number for the vapour stream is

$$\mathrm{Re} = \frac{\rho u 2t}{\mu} \tag{6.16}$$

where u is the average vapour velocity at a particular flow section (m/s),
t is the perpendicular gap between adjacent cones, whence $2t$ is hydraulic diameter of the vapour flow passage (m),
ρ is the vapour density (kg/m³), and
μ is the vapour viscosity (Pa s).

The area of the vapour flow passage varies with radius and we therefore define an average vapour velocity for the whole cone surface similar to those used to evaluate the liquid film thickness and Reynolds number; i.e.

$$u_{av} = \frac{1}{A_{cone}} \int_{A_{cone}} u dA \qquad (6.17)$$

The data used to evaluate the average vapour velocity are set out in table 6.5.

Table 6.5
Data for calculation of average vapour velocity

Vapour flow (m^3/s)			0.0059
Cone pitch (m)			0.021
Inter-cone gap, *t* (m)			0.008
	Radius (m)	Flow area (m^2)	*u* (m/s)
Inner radius	0.025	0.0014	4.16
	0.029	0.0016	3.65
	0.033	0.0018	3.25
	0.037	0.0020	2.94
	0.041	0.0022	2.67
	0.045	0.0024	2.45
	0.048	0.0026	2.27
	0.052	0.0028	2.11
	0.056	0.0030	1.97
	0.060	0.0032	1.85
Outer radius	0.064	0.0034	1.74
u_{av} (m/s)			2.33

The average Reynolds number for the vapour stream is therefore

$$\mathrm{Re} = \frac{\rho u 2t}{\mu} = \frac{0.5977 \times 2.33 \times 2 \times 0.008}{0.000012} = 1857$$

The Schmidt number is

$$\mathrm{Sc} = \frac{\mu}{\rho D_{\mathrm{AB}}} = \frac{0.000012}{0.5977 \times 1.75 \times 10^{-5}} = 1.15$$

From eq. (6.15), the Sherwood number is

$$\begin{aligned} \mathrm{Sh}_{av} &= 0.023\,\mathrm{Re}^{0.83}\,\mathrm{Sc}^{1/3} \\ &= 0.023 \times 1857^{0.83} \times 1.15^{1/3} \\ &= 12.45 \end{aligned}$$

Finally, the vapour phase mass transfer coefficient is

$$k_y' = 12.45 \times \frac{0.03314 \times 1.75 \times 10^{-5}}{2 \times 0.008} = 0.00045 \text{ kmol/m}^2\text{sMF}$$

6.2.1.4.3 Overall liquid phase mass transfer coefficient, K'_x

The overall liquid phase mass transfer coefficient is

$$K_x' = (1/m'' k_y' + 1/k_x')^{-1} \tag{6.18}$$

where m'' is the slope of the chord DM to the VLE curve shown in fig. 6.2.

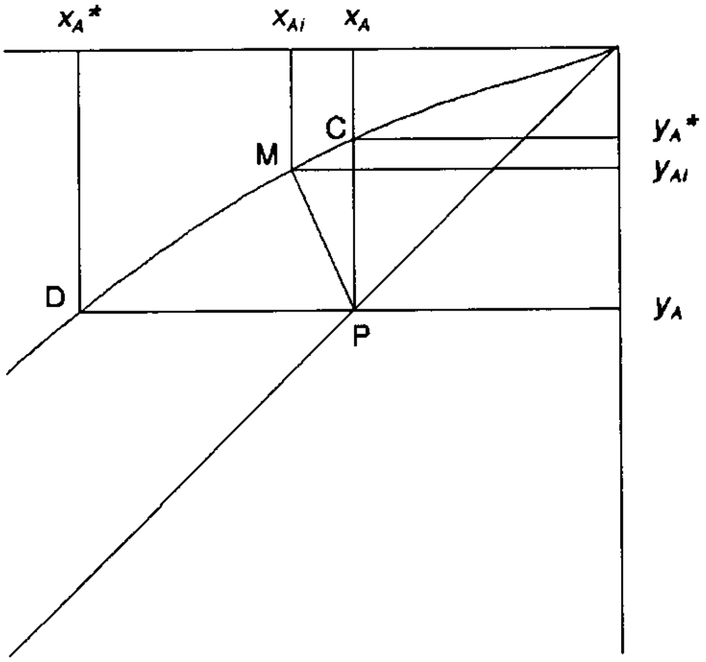

Figure 6.2
Definition sketch for calculation of overall mass transfer coefficients

The slope of the line segment *PM* is $-k'_x/k'_y$, and since in this case $k'_x \gg k'_y$ we assume that the slope of the chord *DM* is approximately equal to the slope of the chord *DC*; that is

$$m'' \approx \frac{y_A^* - y_A}{x_A - x_A^*} \tag{6.19}$$

Values of x_A* and y_A* are found using eq. (6.5):

$$x_A^* = \frac{y_A}{\alpha - y_A(\alpha - 1)}$$

$$y_A^* = \frac{\alpha x_A}{1 + x_A(\alpha - 1)}$$

Substituting $x_{AD} = y_{AD} = 0.99985$ and $\alpha = 1.43$ gives $x_{AD}^* = 0.99979$ and $y_{AD}^* = 0.99990$.

Substituting these values into eq. (6.19) gives $m'' = 0.833$, whence, at the top of the column

$$K_x' = \left[\frac{1}{0.833 \times 0.00045} + \frac{1}{0.0160}\right]^{-1} = 0.00037 \text{ kmol/m}^2\text{sMF}$$

Similarly, at the bottom of the column, where $x_{AW} = y_{AW} = 0.97893$, we obtain $x_{AW}^* = 0.97015$, $y_{AW}^* = 0.98517$, and $m'' = 0.712$, whence

$$K_x' = \left[\frac{1}{0.712 \times 0.00045} + \frac{1}{0.0160}\right]^{-1} = 0.00031 \text{ kmol/m}^2\text{sMF}$$

If we assume that $m'' = 0.7$ at both the top and bottom of the column, we obtain an estimate of $K_x' = 0.00031$ kmol/m²sMF for the whole column. Recall that the measured/observed value for these conditions was 0.0015 kmol/m²sMF; the calculated value of K_x' is about a fifth (21%) of the observed value.

6.2.1.5 Discussion

6.2.1.5.1 Experimental results

Figs 6.3 and 6.4 are graphs of *NTS* and K'_x plotted against gas mass velocity, *G*.

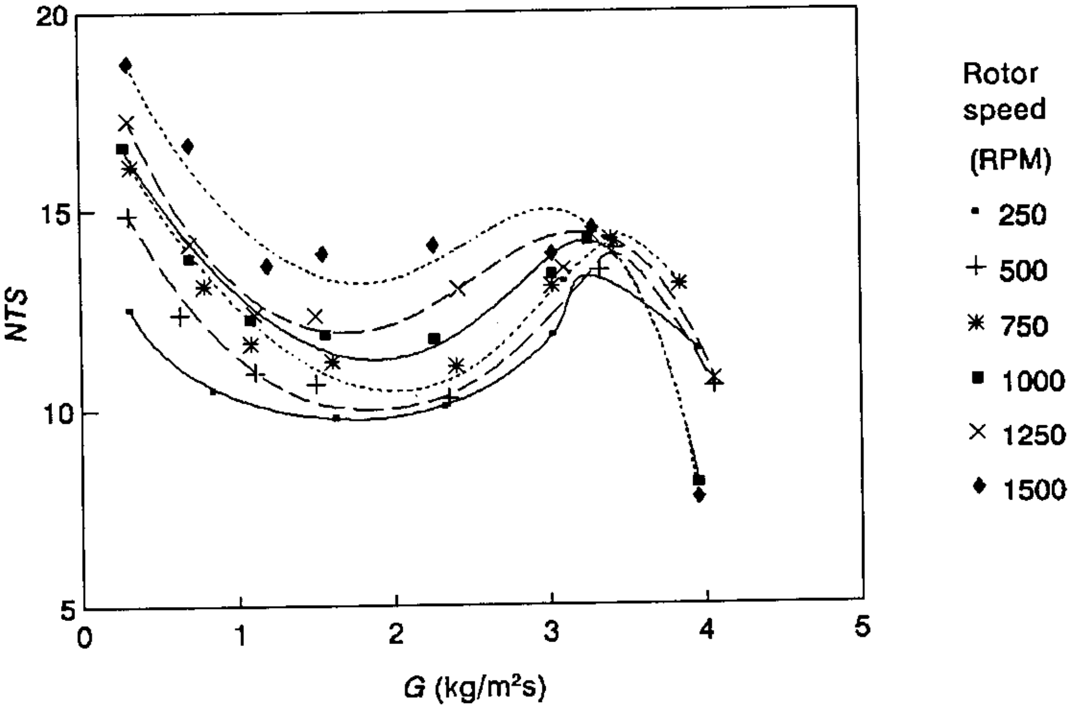

Figure 6.3
Variation of number of theoretical stages, *NTS*, with vapour mass velocity, *G*

Referring first to fig. 6.3, we see that at all rotational speeds the relationship between separation efficiency and vapour loading is more or less trough-shaped; at low vapour flows separation efficiency is relatively high but falls away sharply as flow rises. At values of G between about 1 and 2.5 kg/m^{2}s the separation efficiency is roughly constant for a given rotational speed. As G approaches 3.5 kg/m^{2}s the separations efficiencies at all rotational speeds rise and converge towards a value of about 15 theoretical stages. At values of G above 3.5 kg/m^{2}s the separation efficiency drops sharply, with no clear relationship to rotor speed being evident.

It should be noted that these latter vapour loadings are close to the expected flooding value under these conditions; the SLE-type flooding relationship derived in Chapter 4 predicts flooding to occur at a vapour mass velocity of 3.9 kg/m^{2}s under these conditions (total reflux, atmospheric pressure). The convergence of the NTS values as this vapour loading is approached implies that the influence of rotor speed on separation efficiency is reduced as the flood condition is approached and that once stable operation has ceased mass transfer performance in the column breaks down altogether.

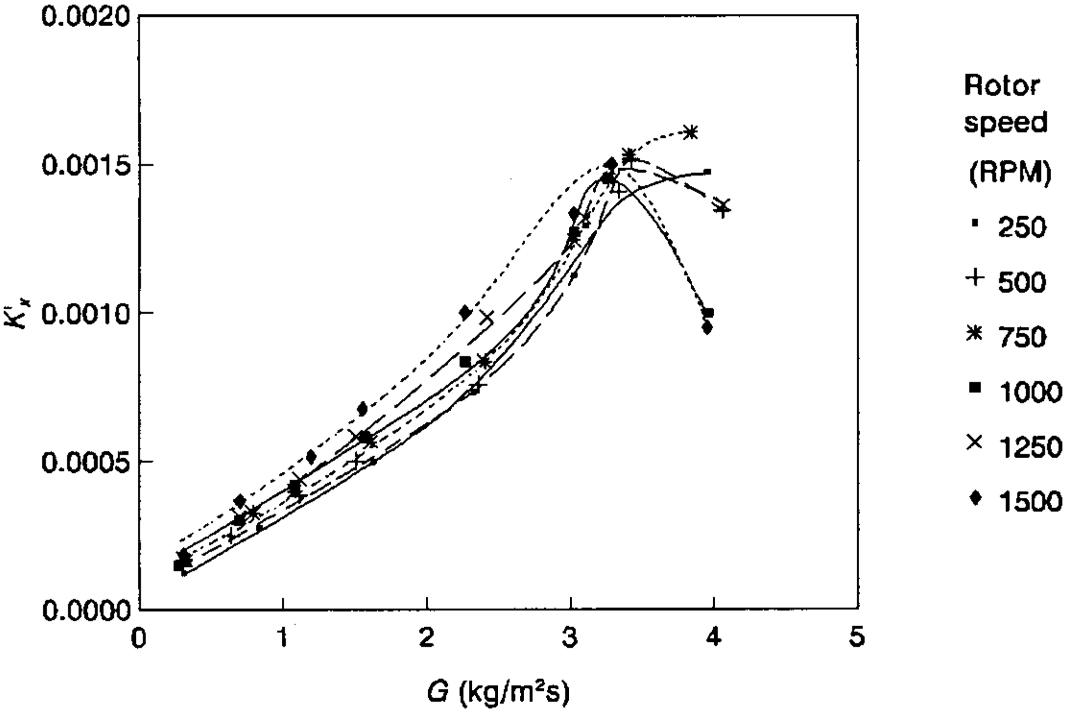

Figure 6.4
Variation of overall mass transfer coefficient, K'_x, with vapour mass velocity, G

The data depicted in fig. 6.4, overall mass transfer coefficients referred to the liquid phase K'_x, are simply a transformation of the data shown in fig. 6.3. They show a regular, approximately linear increase of K'_x with G. The mass transfer coefficient also increases with rotor speed but this effect is much smaller than that of vapour loading.

6.2.1.5.2 Discussion of difference between calculated and observed mass transfer coefficients

In section 6.2.1.4 we used the data of run 14 (see table A4.1(a)) and simple mass transfer correlations to estimate the overall mass transfer coefficient, K'_x. The value so obtained was 21% of that observed.

According to our calculations the bulk of the resistance to mass transfer is in the vapour phase; i.e. $1/k'_y \gg 1/k'_x$. This implies that the difference between calculated and observed values of K'_x is due either to low estimates of interfacial area or of vapour phase mass transfer coefficient k'_y, or both. (It should be noted that while gas phase mass transfer resistance generally controls in normal distillation, where $m = O(1)$, in flavour distillation, where m may be O(100) the liquid resistance may well control.)

Our simple model takes no account of mass transfer in the "off-cone" regions: the inner throat and the region between the lip of the spinning cone and the wall of the column. These regions could be considered liquid-dispersed.

The outer throat is the region between the lip of the spinning cone and the wall of the column, bounded by adjacent stationary cones. Liquid leaves the lip of the spinning cone essentially as a horizontal sheet which quickly breaks up into streams of droplets. Vapour passes through this stream of droplets as it turns through 180° and enters the flow passage above the liquid film on the spinning cone.

At the inner throat liquid drains from the lip of the stationary cone into the base of the spinning cone immediately below; this liquid stream may be composed of droplets, a continuous curtain, or some combination thereof depending on liquid and vapour flow rates and fluid properties. Vapour passes through this liquid as it turns, again through 180°, and enters the flow passage above the liquid film flowing downwards and inwards over the surface of the stationary cone.

In both these regions there is intimate mixing of the phases, and thereby, mass transfer between them over and above that allowed for in the estimate derived in section 6.2.1.4.

Also, the value of interfacial area used in the mass transfer calculation is simply the area of the wetted surfaces inside the column. The presence of waves on the surface of the liquid films throughout the column would tend to increase the actual interfacial area and reduce mass transfer resistance in both phases adjacent to the interface.

Some of the disparity between the predicted and observed mass transfer rates may be due to a low estimate of the vapour phase mass transfer coefficient, k'_y. Recall that k'_y was obtained using the Sherwood-Gilliland correlation for mass transfer in circular pipes. In evaluating the Reynolds number used in this correlation we took account only of the radial component of vapour flow. The motion of the rotor, particularly of the fins attached to the undersides of the spinning cones, introduces a degree of swirl and turbulence/mixing into the vapour flow which may significantly reduce the mass transfer resistance.

6.2.2 De-alcoholization of wine: mass transfer performance

Ethanol stripping is an important commercial application of the spinning cone column. In this section the results of one of a series of trials on the de-alcoholization of white wine are presented; these trials were run on a pilot-scale SCC. Our aims are

(a) to assess the mass transfer performance achieved in this commercial application, and

(b) to compare the observed mass transfer performance observed on this column and with this system (ethanol/water) to the results obtained on the smaller column discussed in the previous section.

The operating conditions were as follows:

Feed concentration:	9.2% ethanol by volume
Distillate concentration:	48.4 % ethanol by volume
Discharge concentration:	< 0.1% ethanol by volume
Feed rate:	100 litres/hour
Strip rate:	16.7%
System temperature:	38°C at top of column

Vapour was generated by reboiling discharge (rather than direct steam injection). Therefore, the vapour entering the column is assumed to be in equilibrium with the liquid leaving the reboiler.

6.2.2.1 Liquid phase mass transfer coefficient, k'_x

Table 6.6
Concentration data for liquid entering column

Component	Ethanol (A)	Water (B)	
Pure density (kg/m^3)	772	993.15	
Molecular weight, M	46.05	18.02	
Volume fraction	0.092	0.908	
Mass fraction, ω	0.073	0.927	
Density of solution (kg/m^3)			972.8
Mass concentration, ρ (kg/m^3)	71.02	901.78	
Molar concentration, c (kmol/m^3)	1.542	50.043	
Molar density of solution (kmol/m^3)			51.586
Mole fraction, x	0.030	0.970	
Mean molecular weight			18.86

The liquid diffusivity is found in this case from diffusivity data for the ethanol/water system taken from Treybal (1981), and shown in table 6.7:

Table 6.7
Liquid diffusivity data for ethanol/water

Temperature (°C)	Molar concentration of ethanol (kmol/m³)	Diffusivity (m²/s)
10	3.75	5.0×10^{-10}
10	0.05	8.3×10^{-10}
16	2	9.0×10^{-10}

In the case under consideration the molar concentration of ethanol is 1.542 kmol/m³. Linearly interpolating between the first two sets of values in the above table gives the diffusivity at 10°C as 7.0×10^{-10} m²/s. If we assume that the ratio $D_{AB}\mu/T$ is constant we have for $T = 37.2$°C

$$D_{AB} = \frac{7.0 \times 10^{-10} \times 0.000703}{273.15 + 10} \times \frac{273.15 + 37.2}{\mu_{10^\circ C}}$$

$$= 1.4 \times 10^{-9} \text{ m}^2/\text{s}$$

Table 6.8
Data for calculation of average film thickness and velocity

Liquid film calculations (velocity and thickness)						
Rotor speed	500 RPM					
Liquid flow	2.8×10^{-5} m³/s					
Cone angle	45°					
			Gravity		Centrifugal	
	Radius (m)	Γ (kg/s m)	u_{av} (m/s)	b (mm)	u_{av} (m/s)	b (mm)
Inner radius	0.050	0.086	0.292	0.30	0.627	0.13
	0.060	0.072	0.260	0.29	0.592	0.11
	0.069	0.062	0.236	0.27	0.564	0.10
	0.079	0.055	0.216	0.26	0.540	0.09
	0.088	0.049	0.201	0.25	0.520	0.09
	0.098	0.044	0.187	0.24	0.502	0.08
	0.107	0.040	0.176	0.23	0.487	0.08
	0.117	0.037	0.166	0.23	0.473	0.07
	0.126	0.034	0.158	0.22	0.461	0.07
	0.136	0.032	0.150	0.22	0.450	0.06
Outer radius	0.145	0.030	0.144	0.21	0.440	0.06

Average values of mass flow per unit width of film, Γ, and film thickness *b* were obtained in the same way as in the acetic acid/water case treated earlier (6.2.1.4.1.1):

$$\mathrm{Re}_{av} = 251$$

$$b_{av} = 0.230 \text{ mm (gravity film)}$$

$$b_{av} = 0.076 \text{ mm (centrifugal film)}$$

The Schmidt number is given by (eq. (6.12)):

$$\mathrm{Sc} = \frac{\mu}{\rho D_{\mathrm{AB}}} = \frac{7.03 \times 10^{-4}}{972.8 \times 1.41 \times 10^{-9}} = 512.2$$

We use the same mass transfer correlation as before, eq. (6.9) :

$$\begin{aligned} \mathrm{Sh} &= \left[\frac{3}{2\pi}\frac{b}{L}\,\mathrm{Re}\;\mathrm{Sc}\right]^{1/2} \\ &= 10.20 \text{ (gravity film)} \\ &= 5.88 \text{ (centrifugal film)} \end{aligned}$$

and the corresponding mass transfer coefficients are

$$\begin{aligned} k_x' &= 0.0057 \text{ kmol/m}^2\text{sMF (centrifugal film)} \\ &= 0.0033 \text{ kmol/m}^2\text{sMF (gravity film)} \end{aligned}$$

6.2.2.2 Vapour phase mass transfer coefficient, k'_y

Table 6.9
Concentration data for vapour leaving column

Component	Ethanol (A)	Water (B)	
Pure density (kg/m^3)	0.0713	0.0439	
Molecular weight, M	46.05	18.02	
Mass fraction, ω	0.4217	0.5783	
Density of solution (kg/m^3)			0.0524
Mass concentration, ρ (kg/m^3)	0.0221	0.0303	
Molar concentration, c (kmol/m^3)	0.00048	0.00168	
Molar density of solution (kmol/m^3)			0.00216
Mole fraction, x	0.222	0.778	
Mean molecular weight			24.24

The viscosity of ethanol vapour at this pressure is (approximately) 8.5 × 10^{-6} Pa s; likewise the viscosity of water vapour at this pressure is 9.63 × 10^{-6} Pa s. The viscosity of the vapour leaving the column is taken to be

$$\mu_G = \omega_A \mu_{\text{ethanol}} + \omega_B \mu_{\text{water}}$$

$$= 0.4217 \times 8.5 \times 10^{-6} + 0.5783 \times 9.63 \times 10^{-6}$$

$$= 9.15 \times 10^{-6} \text{ Pas}$$

The vapour diffusivity is estimated using eq. (6.14). The data used for this estimation are set out in table 6.10.

Table 6.10
Data for estimation of vapour diffusivity

	A: ethanol	B: water	Solution
ϵ/k	425	809.1	586.4
$\mathrm{k}T/\epsilon_{AB}$			0.522
$f(\mathrm{k}T/\epsilon_{AB})$			1
r	0.46	0.264	
r_{AB}			0.362
$\sqrt{(1/M_A + 1/M_B)}$			0.278
D_{AB} (m^2/s)			2.92 × 10^{-6}

The Reynolds number of the vapour stream is found using the same procedure as before. The data used to evaluate the average vapour velocity are set out in table 6.11.

The average Reynolds number for the vapour stream is therefore

$$\mathrm{Re} = \frac{\rho u 2t}{\mu} = \frac{0.0524 \times 5.97 \times 2 \times 0.021}{9.15 \times 10^{-6}} = 1450$$

The Schmidt number is

$$\mathrm{Sc} = \frac{\mu}{\rho D_{\mathrm{AB}}} = \frac{9.15 \times 10^{-6}}{0.05240 \times 2.92 \times 10^{-4}} = 0.598$$

Table 6.11
Data for calculation of average vapour velocity

Vapour flow (m^3/s)	0.0885		
Cone pitch (m)	0.060		
Inter-cone gap, *t* (m)	0.021		
	Radius (m)	Flow area (m^2)	*u* (m/s)
Inner radius	0.050	0.0077	11.55
	0.060	0.0089	9.91
	0.069	0.0102	8.68
	0.079	0.0115	7.72
	0.088	0.0127	6.96
	0.098	0.0140	6.33
	0.107	0.0153	5.80
	0.117	0.0165	5.36
	0.126	0.0178	4.98
	0.136	0.0191	4.65
Outer radius	0.145	0.0203	4.36
u_{av} (m/s)	5.97		

From eq. (6.15), the Sherwood number is

$$\begin{aligned}\mathrm{Sh}_{av} &= 0.023\,\mathrm{Re}^{0.83}\mathrm{Sc}^{1/3}\\ &= 0.023 \times 1450^{0.83} \times 0.598^{1/3}\\ &= 8.15\end{aligned}$$

Finally, the vapour phase mass transfer coefficient is

$$k_y' = 8.15 \times \frac{0.00216 \times 2.92 \times 10^{-4}}{2 \times 0.021} = 0.000121 \text{ kmol/m}^2\text{sMF}$$

The overall mass transfer coefficients are

$$K_y' = (1/k_y' + m'/k_x')^{-1} \tag{6.20a}$$

$$K_x' = (1/k_x' + 1/m'' k_y')^{-1} \tag{6.20b}$$

where m' and m'' are slopes of chords of the equilibrium curve.

In this case (i.e. at the top of the column) the actual values of m' and m'' are 5.54 and 6.30 respectively, hence

$$K_y' = 0.000112 \text{ kmol/m}^2\text{sMF}$$

$$K_x' = 0.000697 \text{ kmol/m}^2\text{sMF}$$

6.2.2.3 Stage-wise calculation of ethanol stripping performance

We can use the procedure described in sections 6.2.2.1.1 and 6.2.2.1.2 as the basis of a stage-wise calculation of ethanol stripping performance. This calculation yields a value of interfacial area (i.e. number of cone sets) required to effect the observed separation on the basis of the correlations assumed to apply to the mass transfer processes in the column. We can then compare this value to the actual number of cone sets in the column in which this separation was observed.

6.2.2.3.1 Basis of stage-wise calculation

In the stage-wise calculation we use the mass transfer coefficients k'_x and k'_y, calculated in the manner described in 6.2.2.1.1 and 6.2.2.1.2, along with the vapour-liquid equilibrium characteristics of the system to obtain a value of interfacial mass transfer within the stage. In this case we start at the top of the column and work downwards; the initial concentrations are those measured in the feed entering and vapour leaving the column. Using the calculated interfacial mass transfer and conducting a mass balance over the stage we obtain the concentrations in the vapour entering and liquid leaving the stage. These values are then used to repeat the procedure for the next stage, and so on for each succeeding stage until we obtain concentrations which are equal to those observed at the bottom of the column.

In this case we treat each cone as a single stage (i.e. 2 stages per cone set). This is the smallest element we can use which is consistent with the assumptions on which the estimates of the mass transfer coefficients were based.

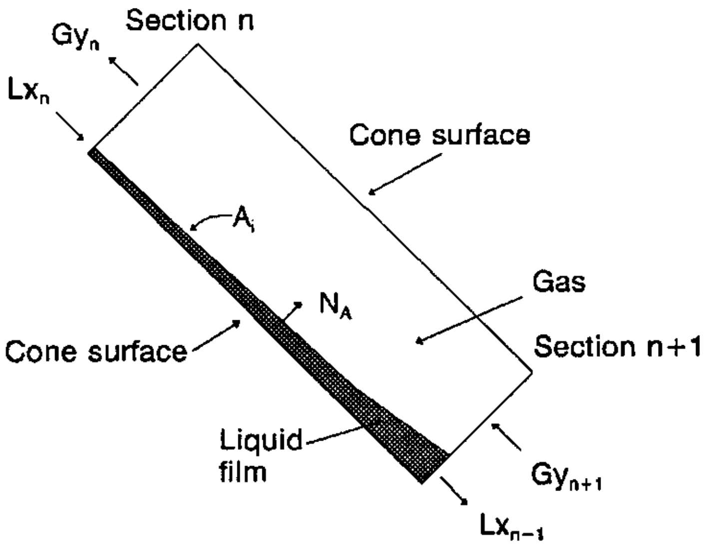

Figure 6.5
Definition sketch for stage-wise calculation

The interfacial mass flux is taken to be

$$N_A = k_x'(x_{A,n} - x_{Ai}) = k_y'(y_{Ai} - y_{A,n}) \tag{6.21}$$

where x_{Ai} and y_{Ai} are the interfacial concentrations. (A more refined estimate of N_A could be obtained by replacing the bulk concentrations $x_{A,n}$ and $y_{A,n}$ with averages of the bulk concentrations entering and leaving the stage. This would introduce an additional set of iterations into the procedure and would not substantially alter the results where the concentration changes over a stage are small. In other words, we are effectively assuming that the average bulk concentration $x_{A,av} \approx x_{A,n}$; in the more refined scheme we would put $x_{A,av} = (x_{A,n} + x_{A,n+1})/2$. A similar argument could be made concerning the estimates of the mass transfer coefficients, which are based on the bulk concentrations at section n, whereas a more refined scheme would use average concentrations based on the bulk and interfacial concentrations at sections n and $n+1$)

We obtain an expression for the interfacial concentration x_{Ai} by substituting the equilibrium condition

$$y_{Ai} = m x_{Ai} \tag{6.22}$$

where m is the equilibrium distribution coefficient, into eq. (6.21). Hence

$$x_{Ai} = \frac{y_{A,n} + \dfrac{k_x'}{k_y'} x_{A,n}}{m + \dfrac{k_x'}{k_y'}} \tag{6.23}$$

The value of the equilibrium distribution coefficient m in general varies with x_{Ai}, so we must use an iterative solution of eq. (6.23): first we guess a value of m and use eq. (6.23) to obtain the corresponding value of x_{Ai}; we use this x_{Ai} along with the vapour-liquid equilibrium data to obtain a new value of m, which is then used to calculate a new value of x_{Ai}, and so on until the results converge. A value of y_{Ai} can be obtained directly from the equilibrium condition and N_A found by substituting these values into eq. (6.21).

Finally, we conduct mass balances on the two phases to find the bulk concentrations in the vapour entering and liquid leaving the stage (see fig. 6.5):

$$x_{A,n+1} = x_{A,n} - \frac{N_A A_i}{L} \tag{6.24a}$$

$$y_{A,n+1} = y_{A,n} - \frac{N_A A_i}{G} \tag{6.24b}$$

where A_i is the interfacial area and L and G are the molar flows of liquid and gas respectively.

6.2.2.3.2 Results of stage-wise calculation

The results of these calculations are set out in tables A5.2 in the appendix to this chapter.

The most important result of this calculation is that it predicts that 110 stages, or 55 cone sets, are required to effect the observed separation; the actual number of cone sets in the column on which this trial was run is 21. That is, the specified mass transfer performance was achieved with 38% of the cone area predicted by the stage-wise calculation.

A simpler - but less precise - calculation would have been to use a logarithmic mean driving force to give an average driving force, hence obtain a mass transfer coefficient. With the highly curved equilibrium line one would have to break the stripping section into 2 or 3 parts.

6.2.2.4 Discussion

The results of the stage-wise calculation suggest that either the contact area is greater than the wetted cone area in the column, or the average mass transfer coefficient is greater than that obtained from the prediction, or both.

Whilst there is certainly additional contact area between the phases in the off-cone regions, it is unlikely to be more than double the wetted cone area. The implication of this is that the resistance to mass transfer in the vapour phase is substantially lower than that predicted by the Sherwood-Gilliland correlation, as it has been used here.

Recall that the predicted value of K'_x from the acetic acid/water trials was just over 20% of the observed value whereas in the ethanol/water case the predicted mass transfer rate was nearly 40% of that observed. This apparently large difference can be explained by considering typical values of the components of the overall mass transfer resistance.

Consider first the acetic acid/water case. The overall mass transfer resistance, referred to the liquid phase, is

$$\frac{1}{K_x'} = \frac{1}{k_x'} + \frac{1}{m'' k_y'}$$

Putting $m'' = 0.7$, $k'_x = 0.015$ kmol/m^{2}sMF, and $k'_y = 0.0005$ kmol/m^{2}sMF we obtain

$$\frac{1}{K'_x} = \frac{1}{0.015} + \frac{1}{0.7 \times 0.0005}$$

$$= 67 + 2860$$

That is, the resistance to mass transfer in the liquid phase represents only 2.3% of the total, and reducing the vapour phase resistance to a fifth of the predicted value reduces the overall resistance by a similar factor; 2927 to 639 m^{2}sMF/kmol (22%).

In the case of the ethanol/water system, typical values are $k'_x = 0.006$ kmol/m^{2}sMF, $k'_y = 0.0001$ kmol/m^{2}sMF, with m'' varying between 6.3 and 15.

Putting $m'' = 6.3$ we obtain

$$\frac{1}{K'_x} = \frac{1}{0.006} + \frac{1}{6.3 \times 0.0001}$$

$$= 167 + 1590$$

and when $m'' = 15$,

$$\frac{1}{K'_x} = \frac{1}{0.006} + \frac{1}{15 \times 0.0001}$$

$$= 167 + 667$$

Reducing the vapour phase mass transfer resistance terms to 20% of their predicted values reduces the overall resistance from 1767 to 485 m^{2}sMF/kmol where $m'' = 6.3$, and from 834 to 300 m^{2}sMF/kmol where $m'' = 15$. In other words the overall mass transfer resistance is reduced to between 27% and 36% of the predicted value.

This analysis suggests that the bulk of the difference between predicted and observed mass transfer rates in the SCC is due to the low estimates of vapour phase mass transfer resistance; reasons why the Sherwood-Gilliland correlation yields low estimates have already been discussed. A comparison of the acetic acid/water results to those obtained in wine de-alcoholization reveals an underlying consistency and leads us to suppose that a correlation of the same form as the Sherwood-Gilliland equation (perhaps simply eq. (6.15) with a multiplying constant of 0.115 rather than 0.023) might provide a satisfactory basis for predicting mass transfer in the design of spinning cone columns.

CHAPTER 7

THE OPERATING CHARACTERISTICS OF THE SPINNING CONE COLUMN: GENERAL CONCLUSIONS

7.1 Introduction

In this chapter the main conclusions of the material presented in the previous chapters are presented. Our purpose is to draw together the various elements of this thesis into a brief statement of the main results of the work, how those results might be used, and directions for future work arising from this.

7.2 Prediction of physical capacity of the spinning cone column

In Chapter 4, section 4.3.2, it was shown that the gas rate at which flooding occurs in an SCC can be predicted using a correlation of similar form and magnitude to the Sherwood-Leva-Eckert (SLE) correlation for flooding in packed columns. The definitions of the flow and capacity parameters are the same as those applying to the SLE correlation; the characteristic flow area, at which the vapour velocity is evaluated, is the minimum flow area within the cone set, and the packing factor equivalent is wetted area per unit gas volume.

The SCC flooding correlation was based on experimental data obtained on three SCCs which between them encompass the full range of sizes of all SCCs currently in service, and with vapour densities varying by more than an order of magnitude. The resulting method for predicting physical capacity takes account of:

(a) cone set dimensions and geometry (flow area and hydraulic radius)
(b) gas density

Furthermore, the similarity between the SCC flooding correlation and the SLE correlation for packed columns suggests that the definition of capacity parameter used also satisfactorily accounts for liquid properties such as density and viscosity.

The correlation of flooding in the SCC takes no account of rotor speed, although some evidence of an influence of rotor speed was found in the statistical analysis of the small column flooding data. The effect was marginal, however, and consequently had little bearing on the overall flooding behaviour. Rotor speed does have a significant effect on the flooding mechanisms which are not related to gas flow, discussed in Chapter 4, section 4.3.3.

7.3 Pressure drop

As is the case with packed columns, the effect of liquid flow on gas pressure drop in the SCC was not readily quantified (see Chapter 4, section 4.3.1). In broad terms wet-column pressure drop was found to be marginally higher than dry-column pressure drop at the same gas flow, until the onset of flooding.

An exception to this general conclusion was in the case where a combination of low rotor speed and small gap between the lip of the stationary cone and the spinning cone immediately below brought about a substantial increase in pressure drop in the presence of liquid flow, even at relatively low gas flows (see sections 4.3.1.3 and 4.3.1.4). This phenomenon, which we termed "pre-loading", appeared to arise from the build-up of liquid at the base of the spinning cone (due to low centrifugal forces) interfering with the passage of gas around the lip of the stationary cone.

The effect of vapour density on pressure drop was in accordance with our expectations and was accounted for by use of a density correction analogous to the F-factor formulation (see section 4.3.1.2).

Pressure drop in the SCC with rotor fixed and in the absence of liquid flow was found to vary with roughly the square of maximum gas velocity within the cone set (see Chapter 3, section 3.3). Comparison of experimental fixed-rotor dry-column pressure drop data with estimates of pressure drop obtained using published pressure loss coefficients for the flow of air in ducts indicated that by far the greatest part of the fixed-rotor pressure drop is due to the multiple reversals in flow direction experienced by the gas stream on its passage through the column.

Dry-column pressure drop with the rotor in motion was represented as a modification of fixed-rotor behaviour, using non-dimensional pressure and volume coefficients obtained by considering the SCC as a multi-stage centrifugal fan (see section 3.4). This non-dimensional representation of moving-rotor dry-column pressure drop took account of rotor speed, gas flow and cone set configuration. Similar values of these non-dimensional coefficients were obtained on small and large SCCs, suggesting that dry-column pressure drop might be predicted for new designs using this approach.

7.4 Liquid flow

The available theoretical descriptions of the flow of liquid films on rotating conical surfaces were presented in Chapter 5, section 5.2. These were the Nusselt model and the Bruin model, both solutions of the Navier-Stokes equations.

The predictions of these models were compared to the results of experiments conducted on a flow visualization rig, in which liquid velocities were measured for a range of liquid flows and rotational speeds typically encountered in operating (pilot-scale and commercial) SCCs (see section 5.3).

The experimentally observed average velocities were of the same order as those predicted by both the Bruin and Nusselt models. Indeed, given the limitations of the experimental method, and the simplification inherent in the modified Bruin average radial velocity, the agreement between observed and predicted values was close (see section 5.4.5). At a liquid flow of 2 kg/min. the observed average velocities were within 20% of the modified Bruin average for all rotational speeds. At 500 RPM the observed values were within 25% of the predicted values for all liquid flows.

The experimental results broadly confirmed the validity of the Bruin model. Neither the Bruin nor the Nusselt model, however, can be applied without modification to conditions which would typically obtain in a commercial SCC since the assumptions on which both models are based cease to be valid at radiuses and liquid flows well within the typical operating range.

Prediction of flow characteristics, such as film thickness, and surface and average film velocities, for typical operating conditions in the SCC requires a more complete solution of the governing equations for this flow system than can be provided by the Bruin model; the Nusselt model is effectively a simplified form of the Bruin model. In particular, the limits of physical capacity of the SCC are associated with flow conditions at the inner throat, the region where the Nusselt and Bruin models are least likely to provide valid solutions since the assumption that film thickness is much smaller than radius does not apply.

7.5 Mass transfer

The results of trials on two different SCCs with two different systems were compared; firstly, total reflux trials using acetic acid/water in the small SCC of Chapters 3 and 4; secondly, ethanol stripping trials in a medium-sized SCC, generally similar in layout and dimensions to the CSIRO Mk III SCC referred to in Chapter 4 (see Chapter 6, sections 6.2.1 and 6.2.2).

In the case of the small column mass transfer trials the controlling mass transfer resistance was in the vapour phase; we found also that the overall mass transfer resistance was about 20% of the predicted value, found by applying simple correlations of Sherwood number with Reynolds and Schmidt numbers to both the liquid and vapour phases.

In the ethanol stripping trials we found a similar pattern. The controlling resistance was again in the vapour phase and the overall mass transfer resistance was found to be about 38% of the predicted value, obtained from a stage-wise calculation which was based on the same correlations of Sherwood number with Reynolds and Schmidt numbers as were used in the acetic acid/water trials.

Comparison of predicted and observed mass transfer coefficients suggested that the resistance to mass transfer in the vapour phase is substantially lower than that predicted by the Sherwood-Gilliland correlation, from which estimates of the vapour mass transfer coefficients were obtained.

Reasons why the Sherwood-Gilliland correlation might yield low estimates of vapour mass transfer coefficient include:

(a) swirl-induced turbulence in the vapour phase due to rotor motion
(b) presence of waves on the liquid surface, which would increase interfacial area and reduce mass transfer resistance in both phases adjacent to the interface

A comparison of the acetic acid/water results to those obtained in wine de-alcoholization revealed an underlying consistency and leads us to suppose that a simple correlation of the same form as the Sherwood-Gilliland equation might provide a satisfactory basis for predicting mass transfer in the design of spinning cone columns.

REFERENCES

Anon., *Minitab Reference Manual Release 7*, Minitab Inc., State College, PA, USA (1989).

Bakowski, S. *Trans. Instn Chem. Engrs*, **32**, Supplement, 537 (1954).

Bakowski, S. *Br. Chem. Engng*, **17**, 789 (1972).

Bolles, W.L. and Fair, J.R. *I. Chem. E. Symp. Ser.*, **56**, 3.3/35 (1979).

Bravo, J.L., Rocha, J.A. and Fair, J.R. *Hydrocarb. Proc.*, **65**, 91 (1985).

Bruin, S. "Velocity distributions in a liquid film flowing over a rotating conical surface," *Chem. Eng. Sci.*, **24**, 1647 (1969)

Casimir, D.J. and Huntington, J.N. "A spinning cone distillation column for essence recovery," *Int. Fruchtsaftunion, Wiss.-Tech. Komm. Ber.*, **15**, 115 (1978).

Casimir, D.J. "Technological aspects of the production of concentrates of passionfruit," Dissertation, University of New South Wales (1974).

Coulson, J.M., Richardson, J.F., Backhurst, J.R. and Harker, J.H. *Chemical Engineering, Volume 2, Third edition (in SI units) Unit Operations*, Pergamon Press Ltd, Oxford (1978).

Croome, D.J. and Roberts, B.M. *Air conditioning and ventilation of buildings (Volume 1)*, 2nd ed. Pergamon Press, Oxford (1981).

Danckwerts, P.V. *Chem. Engng Sci.*, **2**, 1 (1953).

Draper, N.R. and Smith, H. *Applied regression analysis*, 2nd ed. John Wiley & Sons, Inc., New York (1981).

Eck, B. *Fans*, 1st English ed. translated/edited, Azad, R.S. and Scott, D.R. Pergamon Press, Oxford (1973).

Eckert, J.S. *Chem. Eng. Progr.*, **66**, 39 (1970).

Fair, J.R. and Bravo, J.L. "Distillation columns containing structured packing," *Chem. Eng. Progr.*, **86**, 19 (1990).

Fair, J.R., Steinmeyer, D.E., Penney, W.R. and Brink, J.A. "Liquid-gas systems," In *Chemical Engineers' Handbook*, Ed. Perry, R.H. and Chilton, C.H. McGraw-Hill Book Company, New York. 5th ed. (1973).

Fulford, G.D. "The flow of liquids in thin films," *Adv. Chem. Eng.*, **5**, 151 (1964).

Hickman, K.C.D. *Chem. Rev.*, **34**, 70 (1944).

Hinze, J.O. and Milborn, H. *J. Appl. Mech.*, **17**, 145 (1950).

Huffman, J.R. and Urey, H.C. "Separation of oxygen isotopes by a fractionating column," *Ind. Eng. Chem.*, **29**, 531 (1937).

Humphrey, J.L. and Seibert, A.F. "New horizons in distillation," *Chem. Eng.*, 86 (1992).

Kister, H.Z. and Gill, D.R. "Predict flood point and pressure drop for modern random packings," *Chem. Eng. Progr.*, **87**, 32 (1991).

Kister, H.Z. and Gill, D.R. "Flooding and pressure drop prediction for grid and structured packings," Presented at the AIChE Annual Meeting, Los Angeles, California. (November, 1991).

Langrish, T.A.G., Prince, R.G.H., Messner, S., Sykes, S.J. and Meldrum, A.L. "The flow of liquid in spinning cone columns," *Proc. CHEMECA '93*, **2**(13), EA Books, Sydney (1993).

Leva, M. *Chem. Eng. Progr. Symp. Ser.*, **50**(10), 51 (1954).

McNulty, K.J. and Hsieh, C.L. "Hydraulic performance and efficiency of Koch Flexipac structured packings," Presented at the AIChE Annual Meeting, Los Angeles, California. (November, 1982).

Mair, B.J. and Willingham, C.B. "Efficiency of a rotary distillation column," *J. Res. Natn. Bur. Stand.*, **22**, 519 (1939).

Menzi, H.R. "Eine Drehtellerkolonne zur schonenden Gewinnung von Aromastoffen aus Lebensmitteln," Dissertation ETH Nr. 8485, Zurich (1988).

Menzi, H.R. and Emch, F. "The spinning cone column - an efficient separator of aroma volatiles from a liquid," *Lebensm.-Wiss. u.-Technol.*, **22**, 324 (1989).

O'Connell, H.E. *Trans. AIChE*, **42**, 741 (1946).

Osborne, W.C. *Fans*, 2nd ed. Pergamon Press, Oxford (1977).

Pegram, G.B., Urey, H.C. and Huffman, J.R. *Phys. Rev.*, **49**, 883 (1936a).

Pegram, G.B., Urey, H.C. and Huffman, J.R. *J. Chem. Phys.*, **4**, 623 (1936b).

Seader, J.D. and Zdzislaw, M.K. "Distillation," In *Chemical Engineers' Handbook*, Ed. Perry, R.H. and Chilton, C.H. McGraw-Hill Book Company, New York. 6th ed. (1984).

Sherwood, T.K., Shipley, G.H. and Holloway, F.A.L. *Ind. Eng. Chem.*, **30**(7), 765 (1938).

Stichlmair, J., Bravo, J.L. and Fair, J.R. *Gas Sep. Purif.*, **3**, 19 (1989).

Treybal, R.E. *Mass-Transfer Operations*, McGraw-Hill International Book Company, Tokyo. 3rd ed. (1981).

Weisberg, S. *Applied linear regression*, 2nd ed. John Wiley & Sons, Inc., New York (1985).

Wood, R.M. and Watts, B.E. "The flow, heat and mass transfer characteristics of liquid films on rotating discs," *Trans. Instn Chem. Engrs*, **51**, 315 (1973).

Yang, L. and Chuang, K.T. "Efficiency considerations for choice between trays and packings," *Chem. Eng. Comm.*, **137**, 161 (1995).

York, J.L., Barberio, J.T., Samyn, M., Zenz, F.A. and Zenz, J.A. "Solve all column flows with one equation," *Chem. Eng. Progr.*, **88**, 93 (1992).

Ziolowski, Z., Filip, S. and Kawala, Z. "Rectification column with rotating cones," *Przem. chem.*, **42**(9), 512 (1963).

APPENDIX 1

PRESSURE DROP AND FLOODING DATA: SMALL COLUMN, SERIES 1

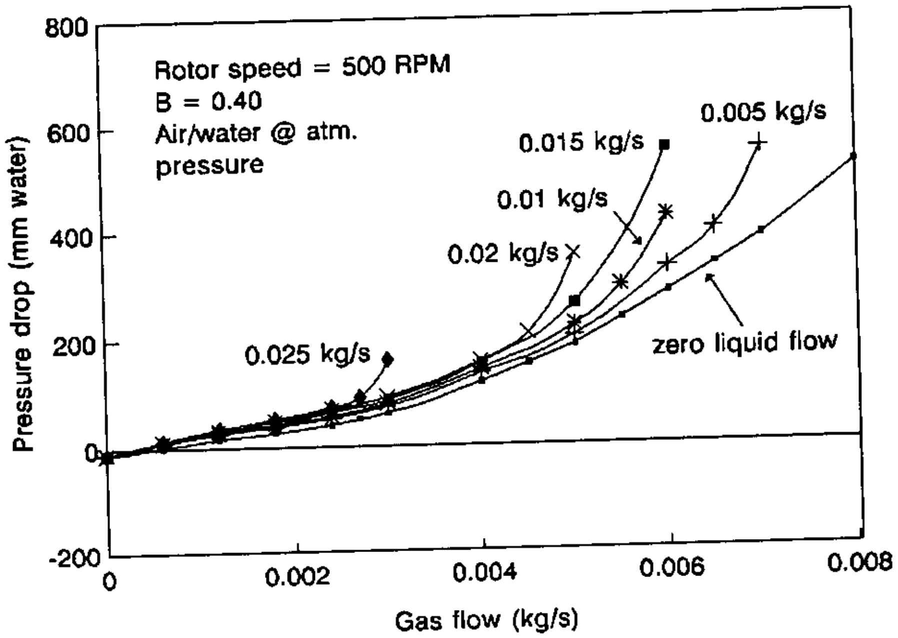

Figure A1.1
Pressure drop vs gas flow for various liquid flows: 500 RPM; $B = 0.40$; air/water at atmospheric pressure

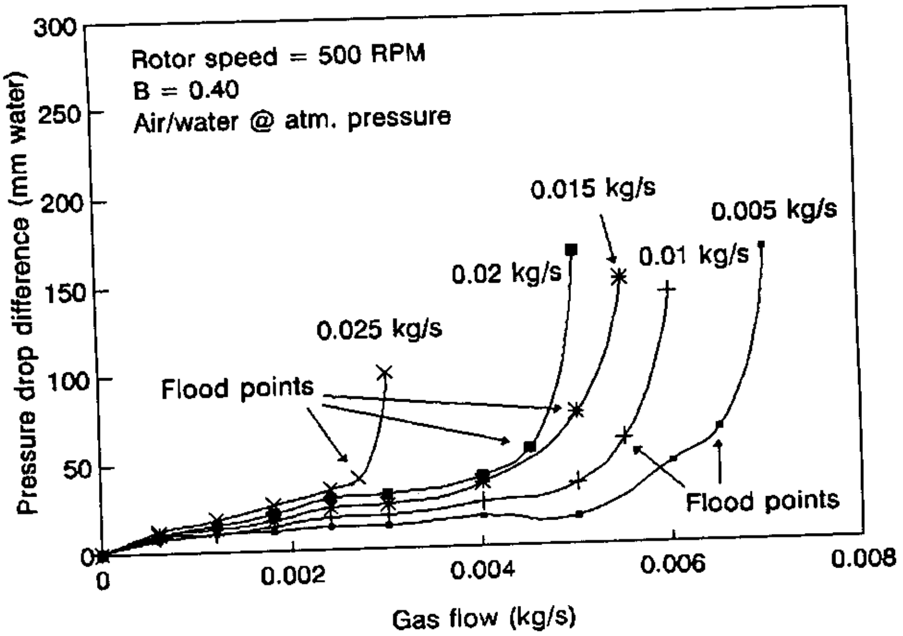

Figure A1.2
Pressure drop difference ΔP_L vs gas flow for various liquid flows: 500 RPM; $B = 0.40$; air/water at atmospheric pressure

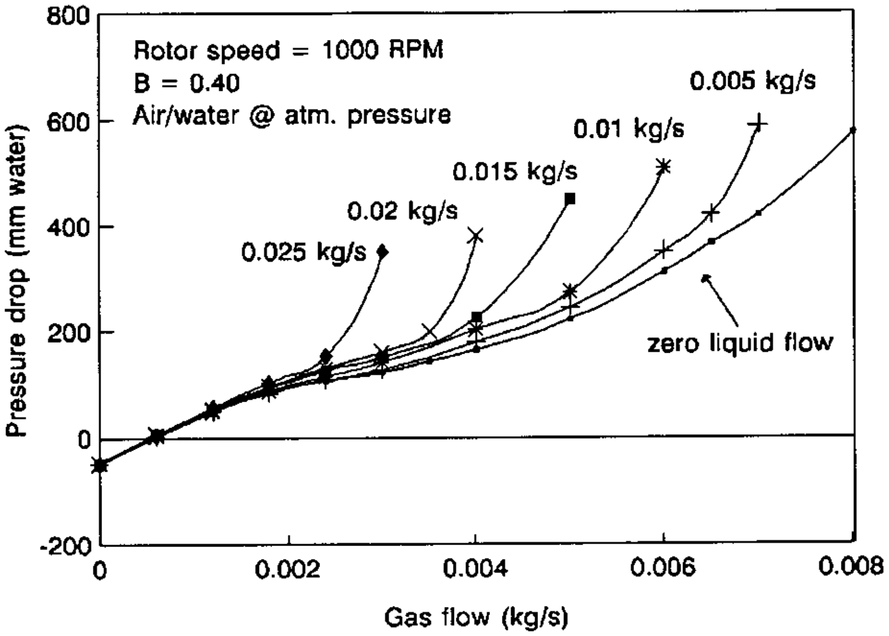

Figure A1.3
Pressure drop vs gas flow for various liquid flows: 1000 RPM; B = 0.40; air/water at atmospheric pressure

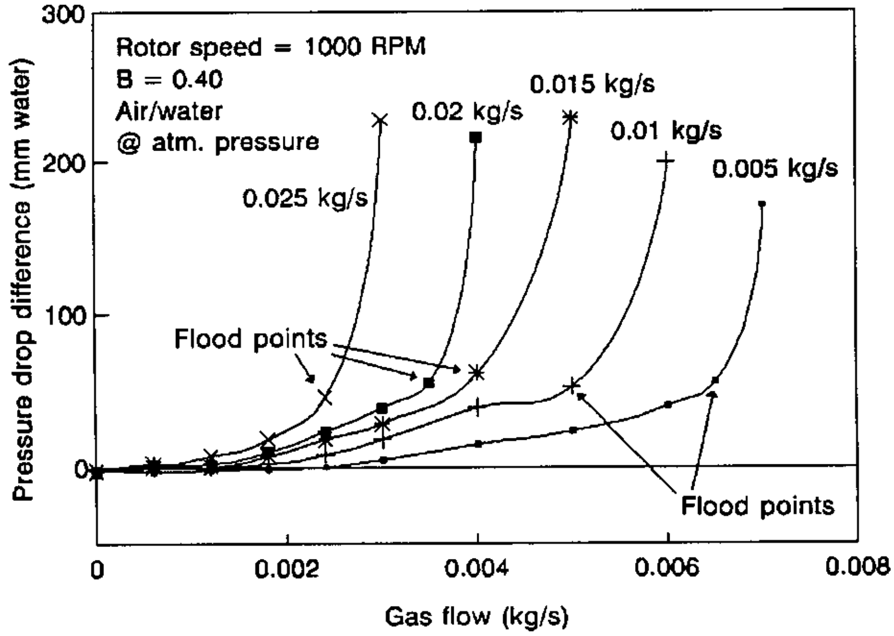

Figure A1.4
Pressure drop difference ΔP_L vs gas flow for various liquid flows: 1000 RPM; B = 0.40; air/water at atmospheric pressure

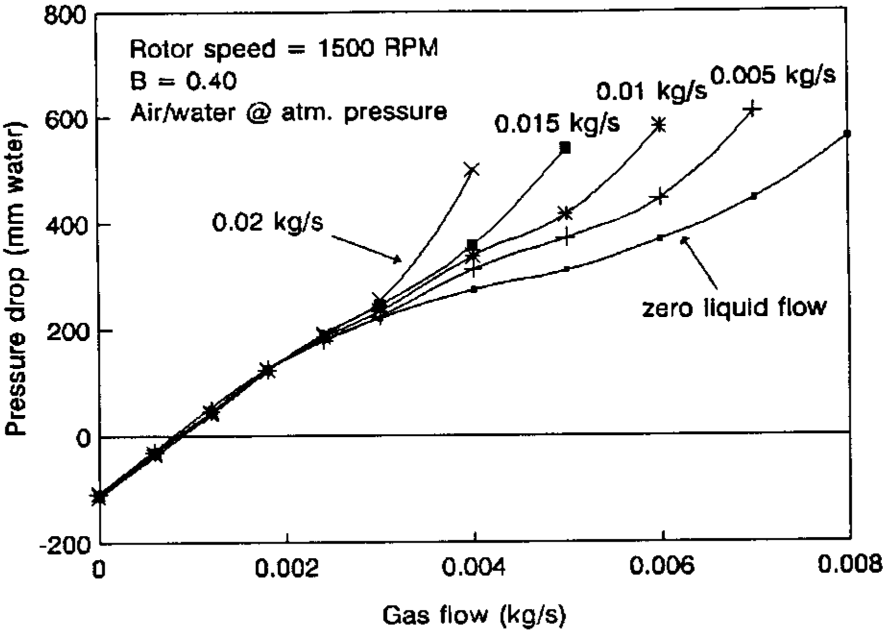

Figure A1.5
Pressure drop vs gas flow for various liquid flows: 1500 RPM; $B = 0.40$; air/water at atmospheric pressure

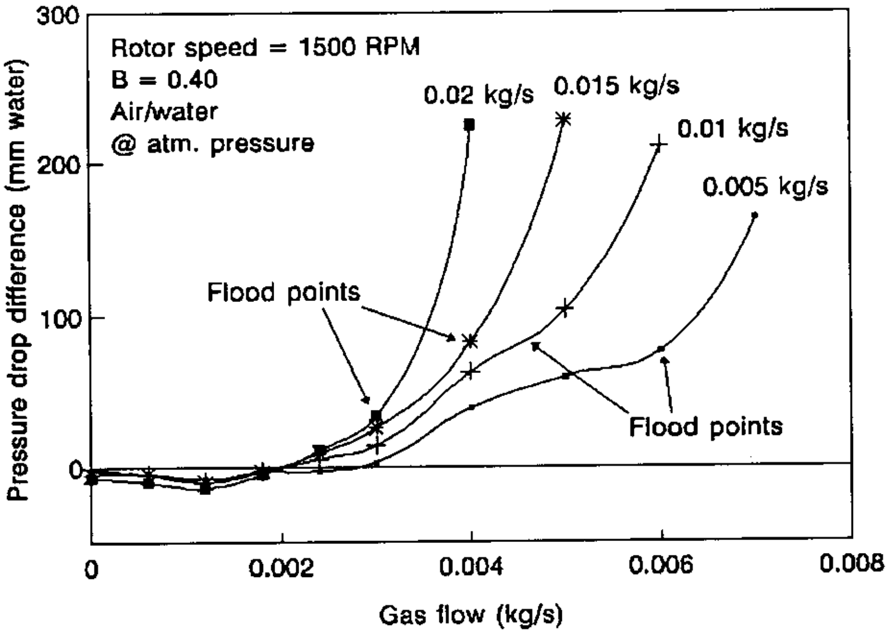

Figure A1.6
Pressure drop difference ΔP_L vs gas flow for various liquid flows: 1500 RPM; $B = 0.40$; air/water at atmospheric pressure

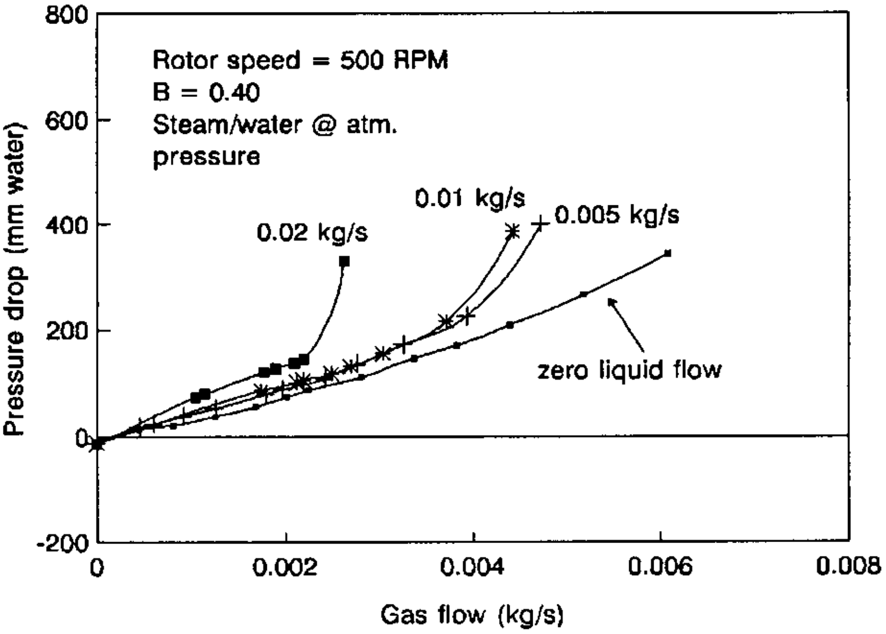

Figure A1.7
Pressure drop vs gas flow for various liquid flows: 500 RPM;
$B = 0.40$; steam/water at atmospheric pressure

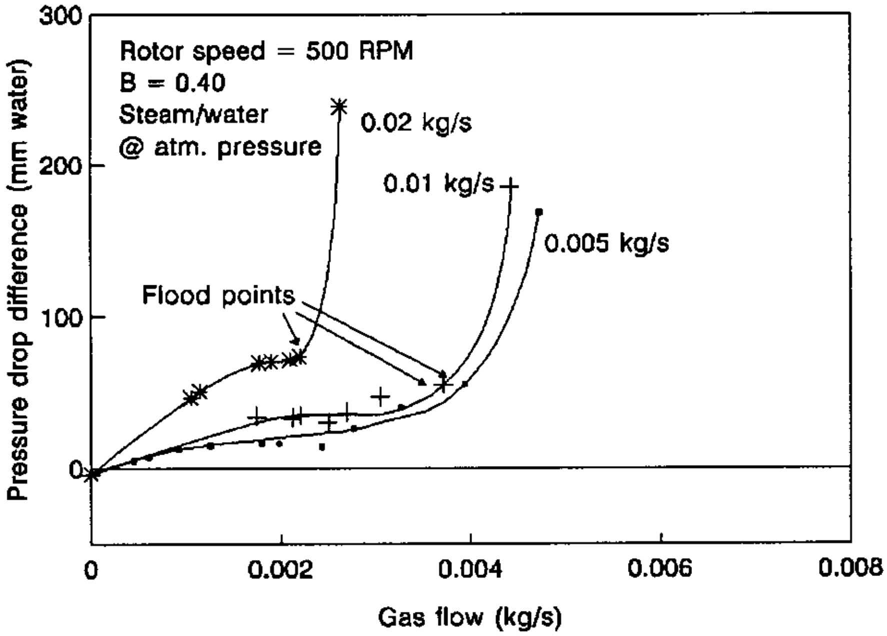

Figure A1.8
Pressure drop difference ΔP_L vs gas flow for various liquid flows: 500 RPM;
$B = 0.40$; steam/water at atmospheric pressure

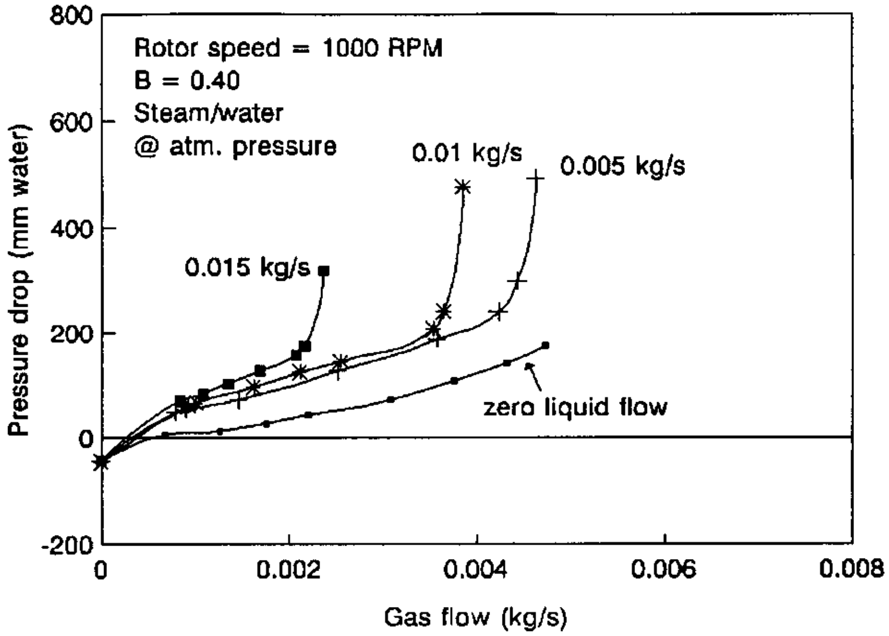

Figure A1.9
Pressure drop vs gas flow for various liquid flows: 1000 RPM; $B = 0.40$; steam/water at atmospheric pressure

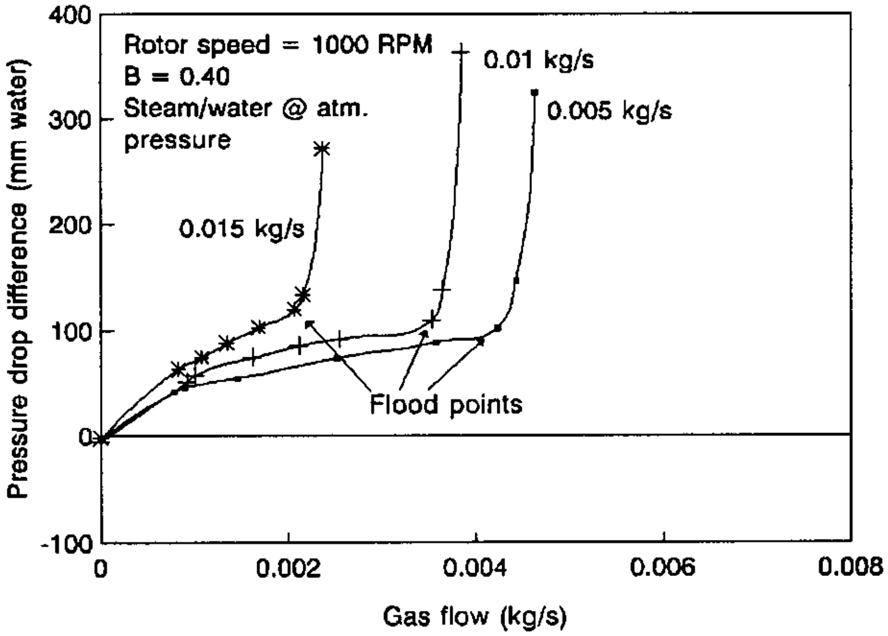

Figure A1.10
Pressure drop difference ΔP_L vs gas flow for various liquid flows: 1000 RPM; $B = 0.40$; steam/water at atmospheric pressure

SMALL COLUMN, SERIES 3

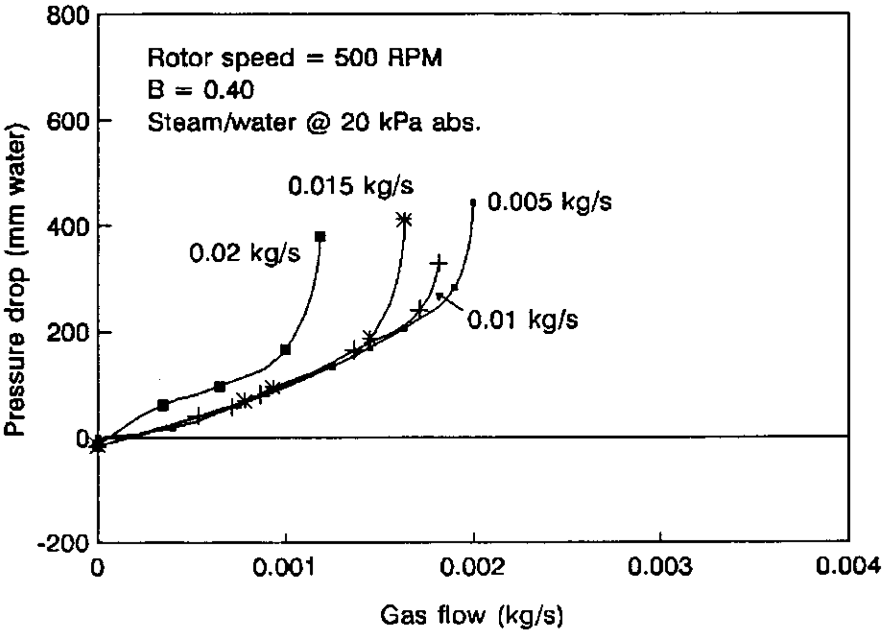

Figure A1.11
Pressure drop vs gas flow for various liquid flows: 500 RPM; $B = 0.40$; steam/water at 20 kPa abs.

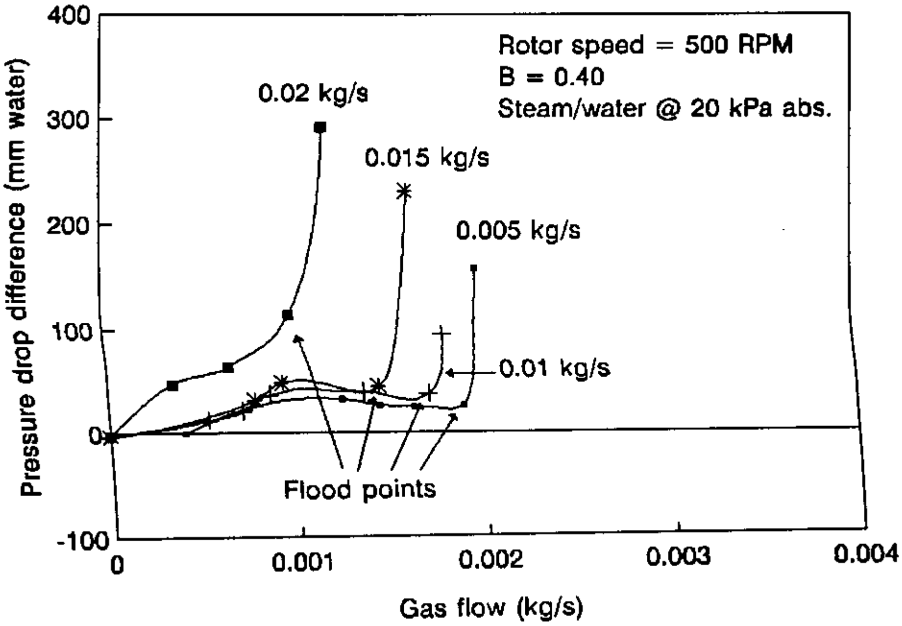

Figure A1.12
Pressure drop difference ΔP_L vs gas flow for various liquid flows: 500 RPM; $B = 0.40$; steam/water at 20 kPa abs.

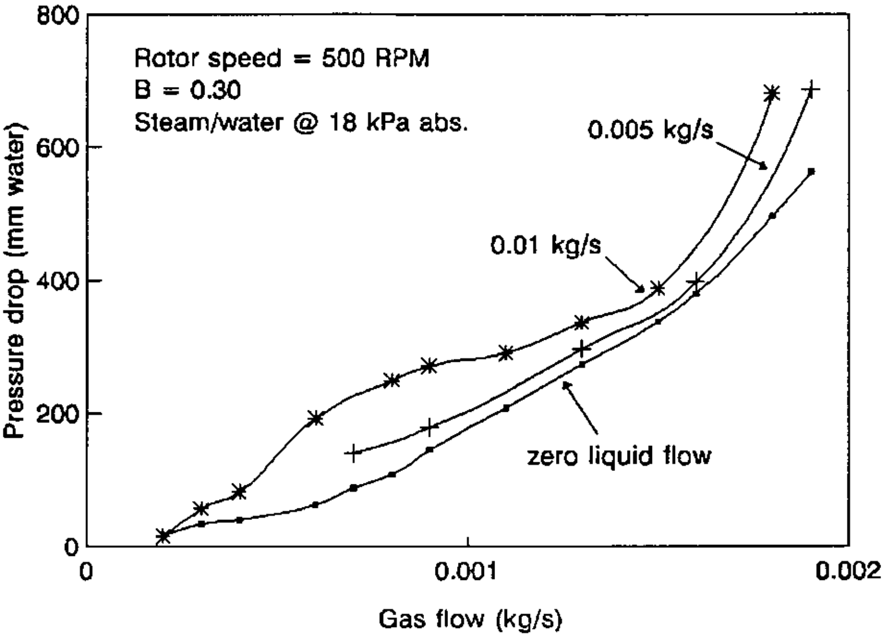

Figure A1.13
Pressure drop vs gas flow for various liquid flows: 500 RPM; $B = 0.30$; steam/water at 18 kPa abs.

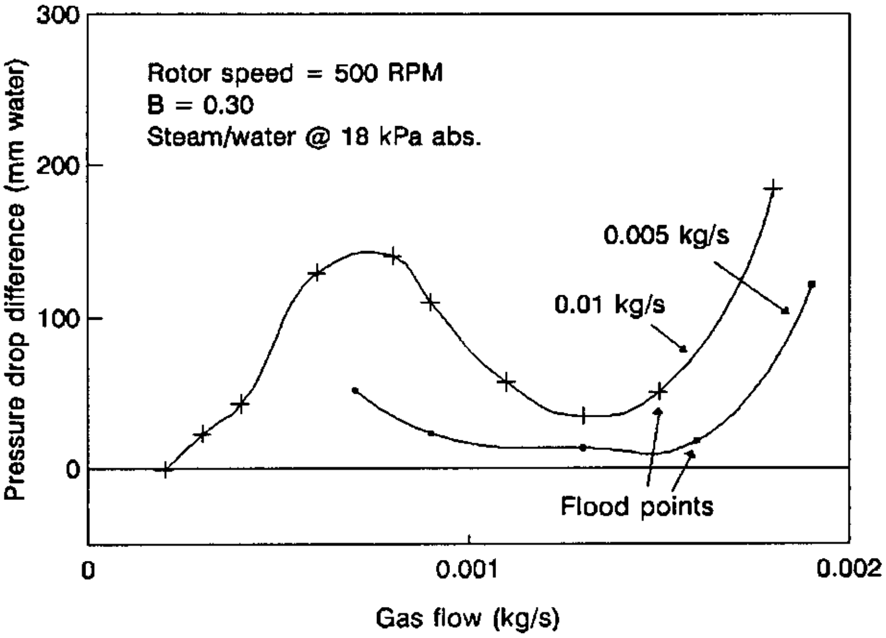

Figure A1.14
Pressure drop difference ΔP_L vs gas flow for various liquid flows: 500 RPM; $B = 0.30$; steam/water at 18 kPa abs.

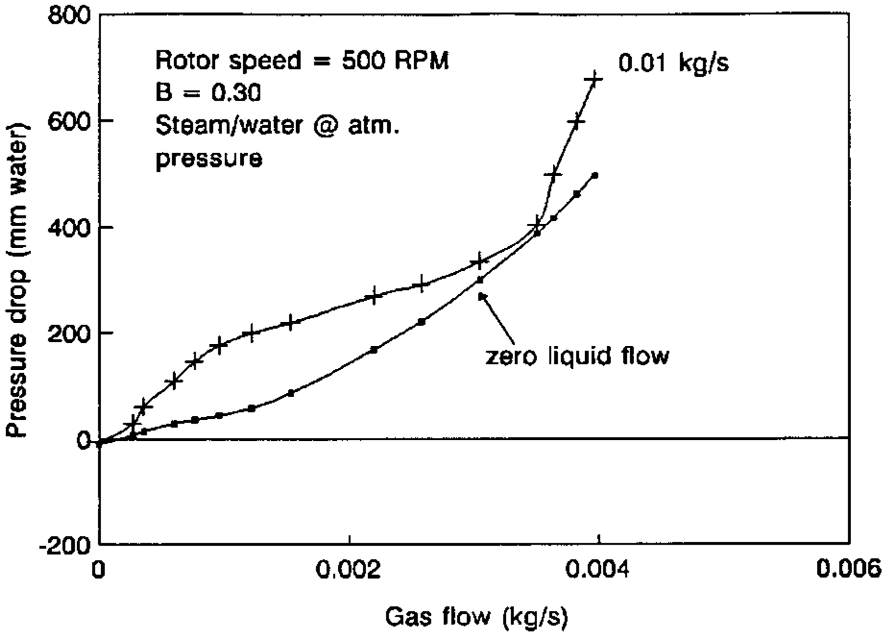

Figure A1.15
Pressure drop vs gas flow for various liquid flows: 500 RPM; B = 0.30; steam/water at atmospheric pressure

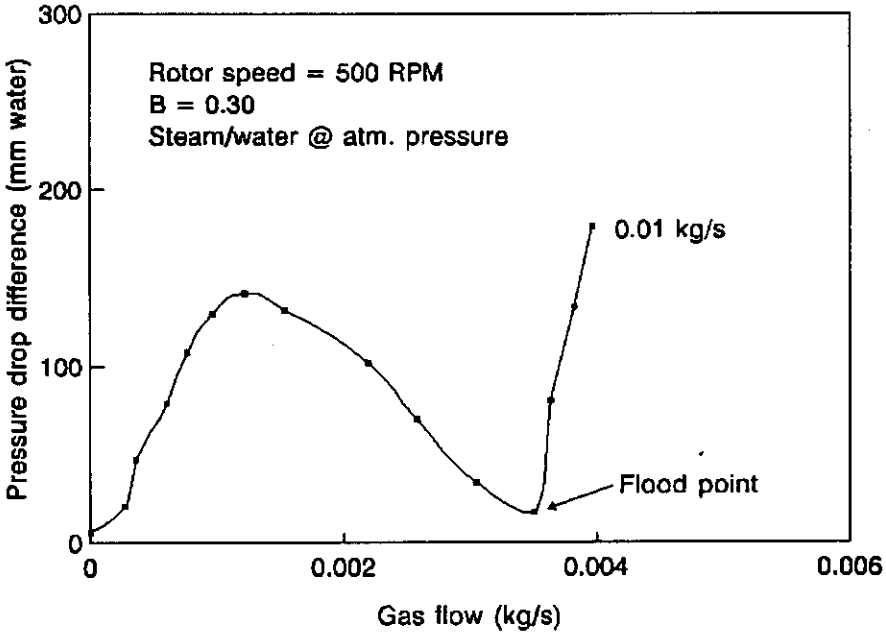

Figure A1.16
Pressure drop difference ΔP_L vs gas flow: 500 RPM; B = 0.30; steam/water at atmospheric pressure

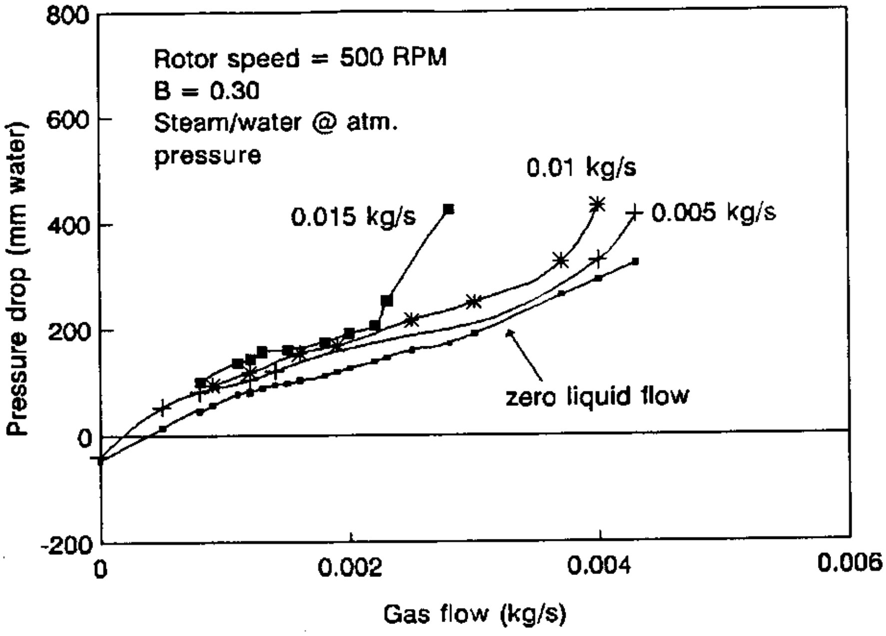

Figure A1.17
Pressure drop vs gas flow for various liquid flows: 500 RPM;
$B = 0.30$; steam/water at atmospheric pressure

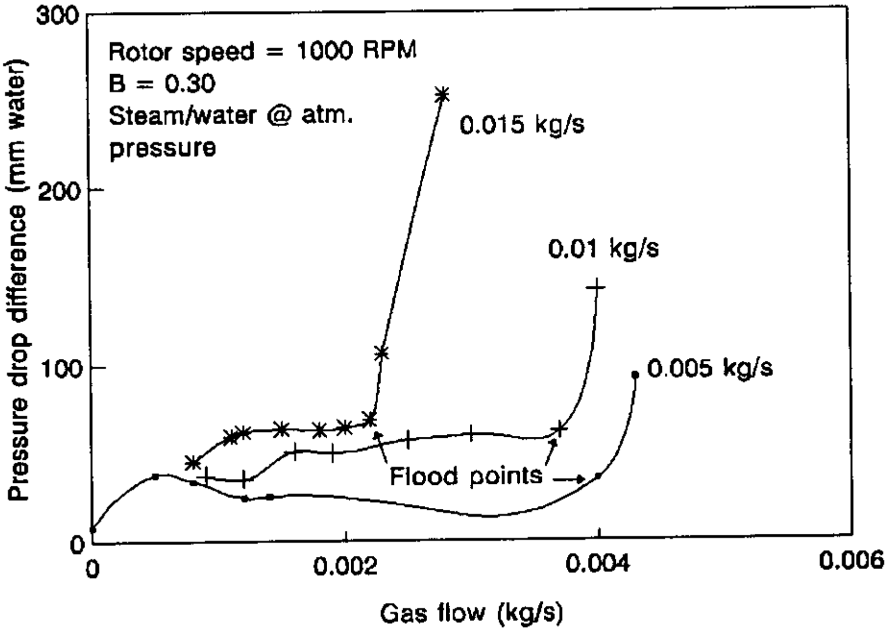

Figure A1.18
Pressure drop difference ΔP_L vs gas flow for various liquid flows: 500 RPM;
$B = 0.30$; steam/water at atmospheric pressure

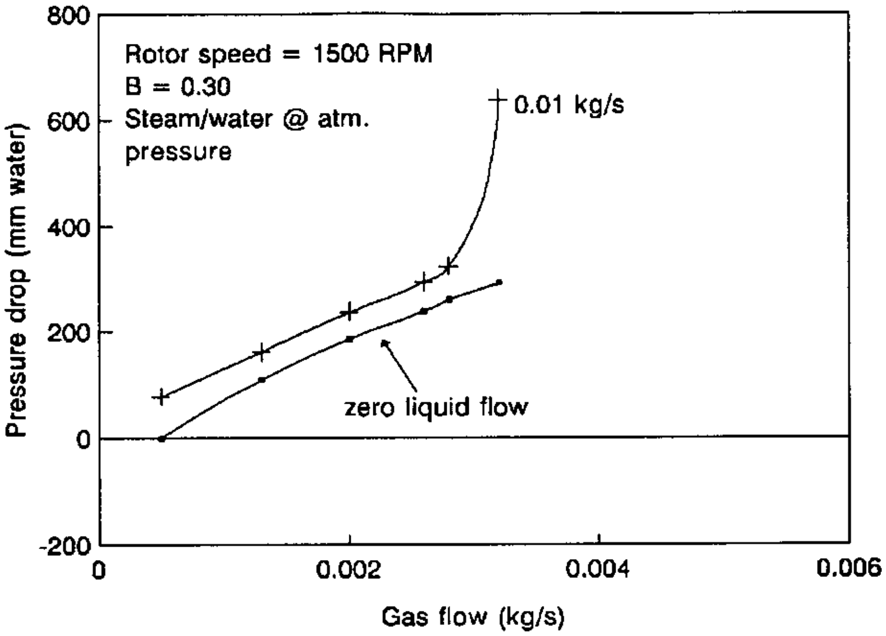

Figure A1.19
Pressure drop vs gas flow for various liquid flows: 500 RPM;
B = 0.30; steam/water at atmospheric pressure

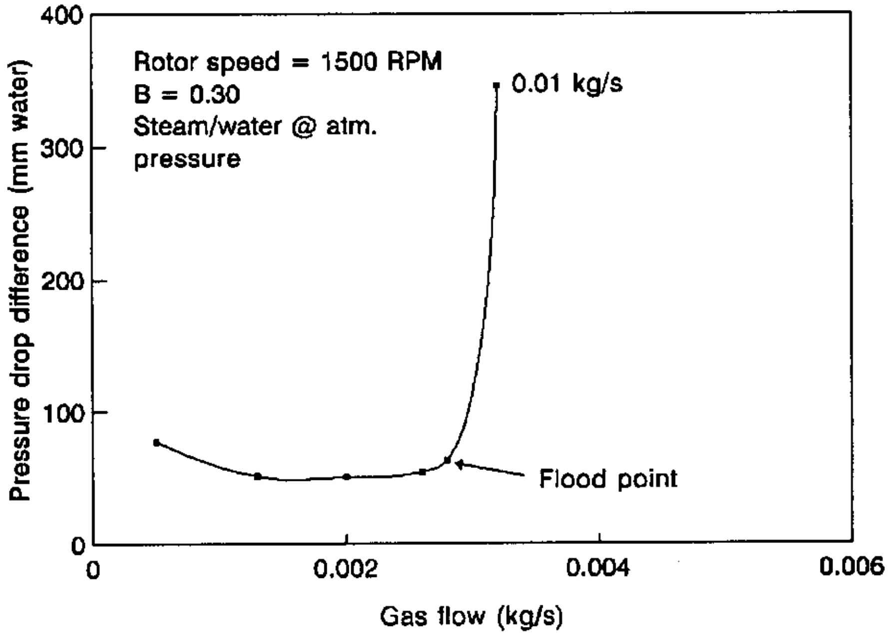

Figure A1.20
Pressure drop difference ΔP_L vs gas flow: 500 RPM;
B = 0.30; steam/water at atmospheric pressure

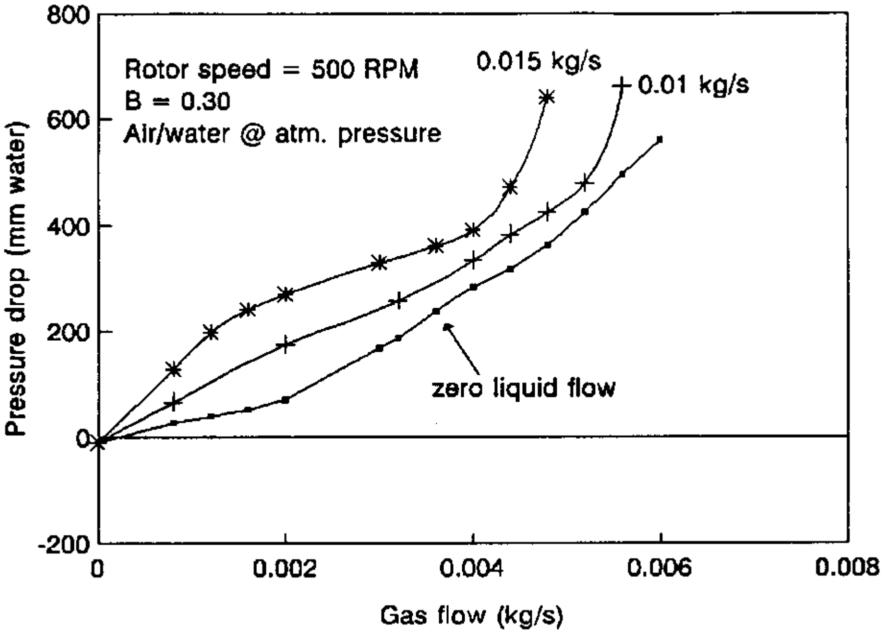

Figure A1.21
Pressure drop vs gas flow for various liquid flows: 500 RPM; B = 0.30; air/water at atmospheric pressure

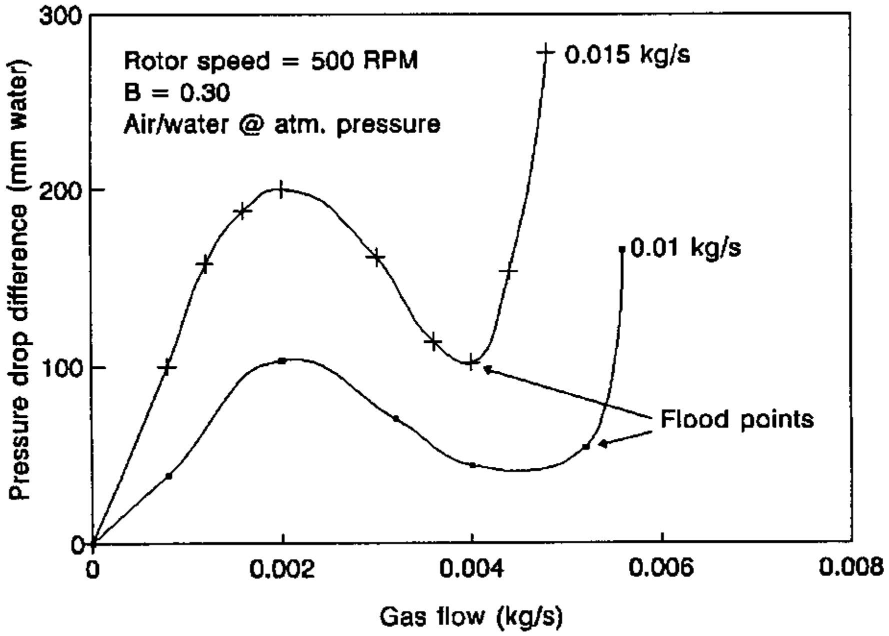

Figure A1.22
Pressure drop difference ΔP_L vs gas flow for various liquid flows: 500 RPM; B = 0.30; air/water at atmospheric pressure

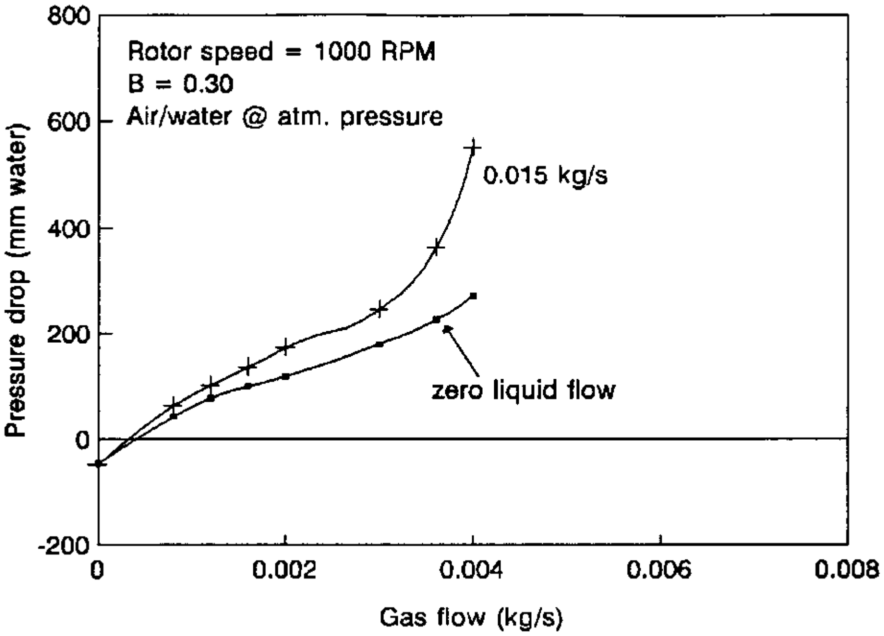

Figure A1.23
Pressure drop vs gas flow for various liquid flows: 500 RPM;
$B = 0.30$; air/water at atmospheric pressure

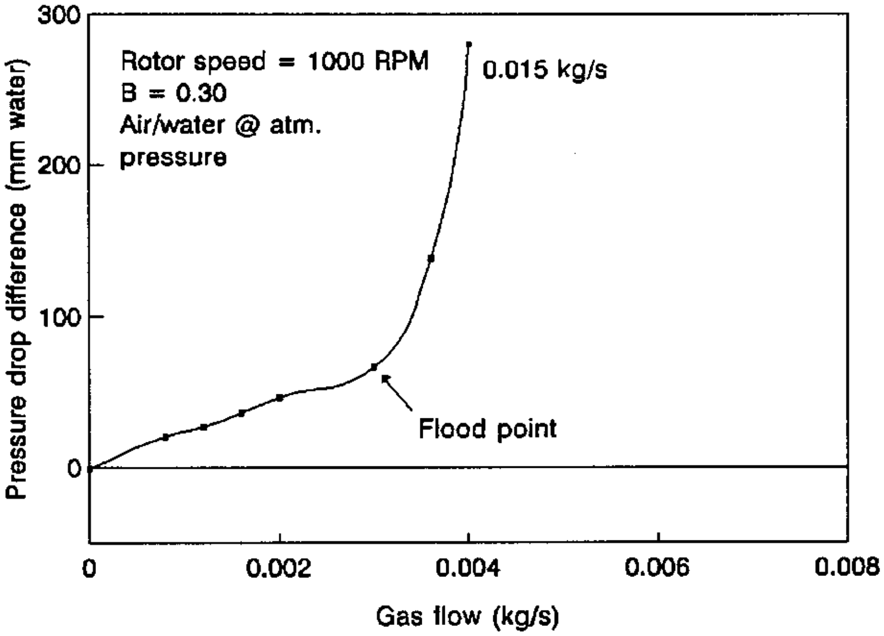

Figure A1.24
Pressure drop difference ΔP_L vs gas flow for various liquid flows: 500 RPM;
$B = 0.30$; air/water at atmospheric pressure

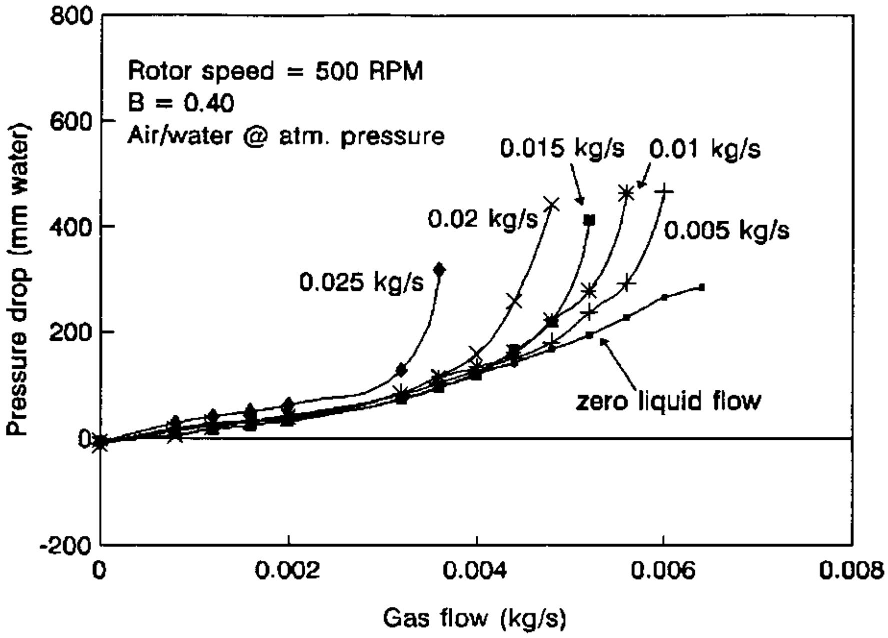

Figure A1.25
Pressure drop vs gas flow for various liquid flows: 500 RPM;
B = 0.40; air/water at atmospheric pressure

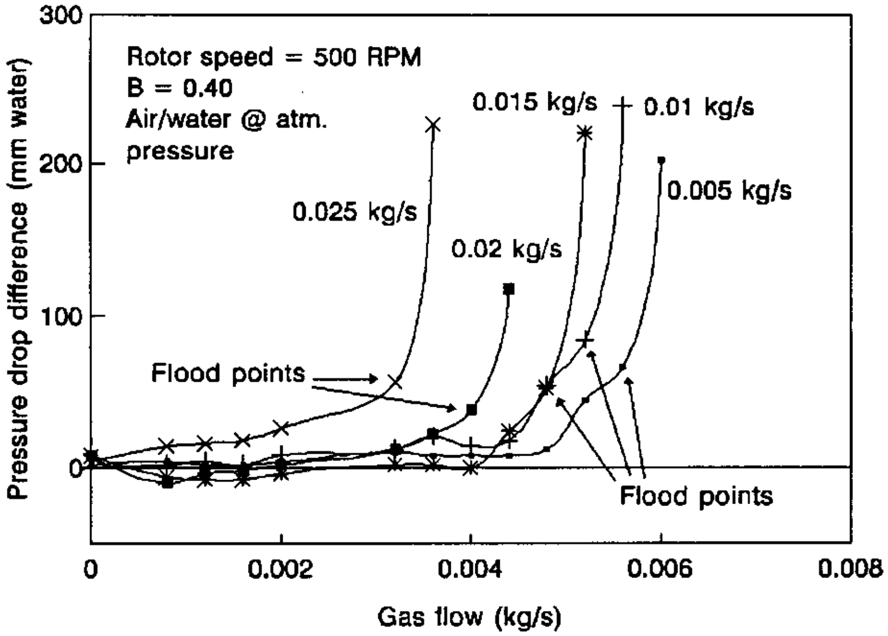

Figure A1.26
Pressure drop difference ΔP_L vs gas flow for various liquid flows: 500 RPM;
B = 0.40; air/water at atmospheric pressure

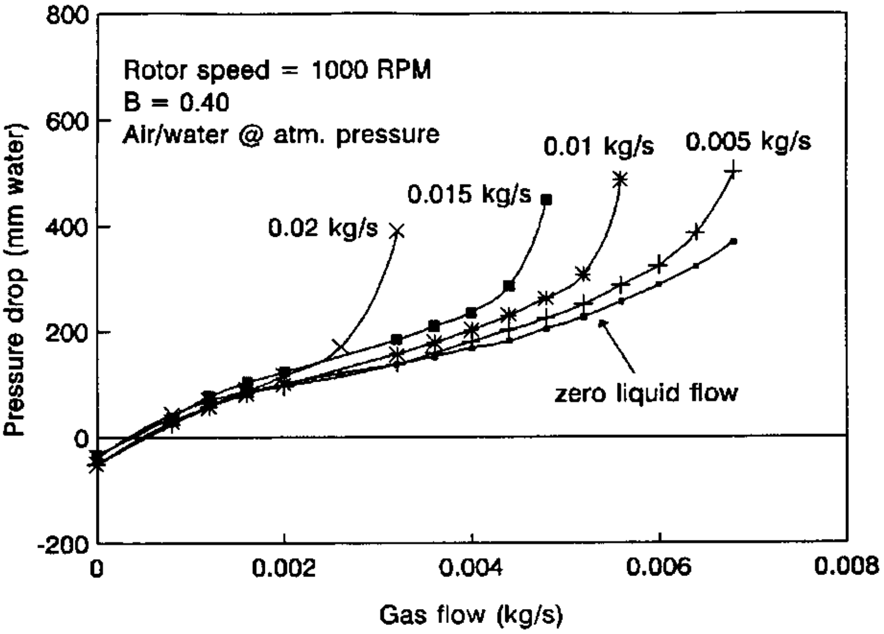

Figure A1.27
Pressure drop vs gas flow for various liquid flows: 1000 RPM;
$B = 0.40$; air/water at atmospheric pressure

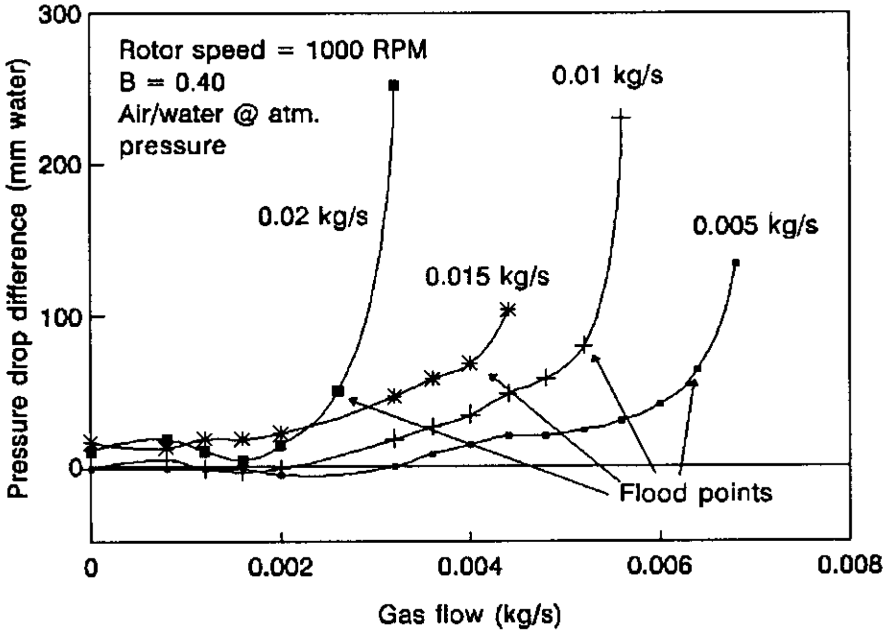

Figure A1.28
Pressure drop difference ΔP_L vs gas flow for various liquid flows: 1000 RPM;
$B = 0.40$; air/water at atmospheric pressure

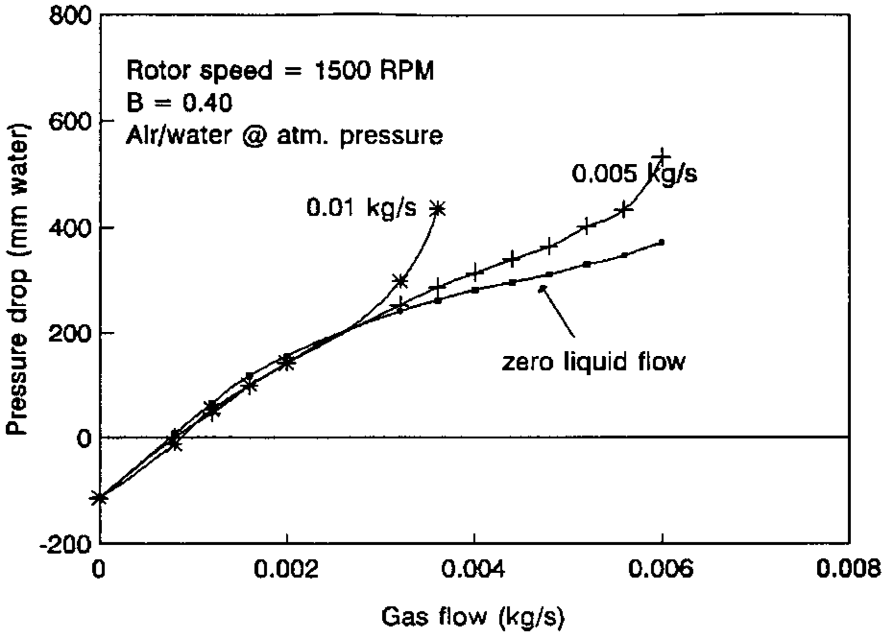

Figure A1.29
Pressure drop vs gas flow for various liquid flows: 1500 RPM; $B = 0.40$; air/water at atmospheric pressure

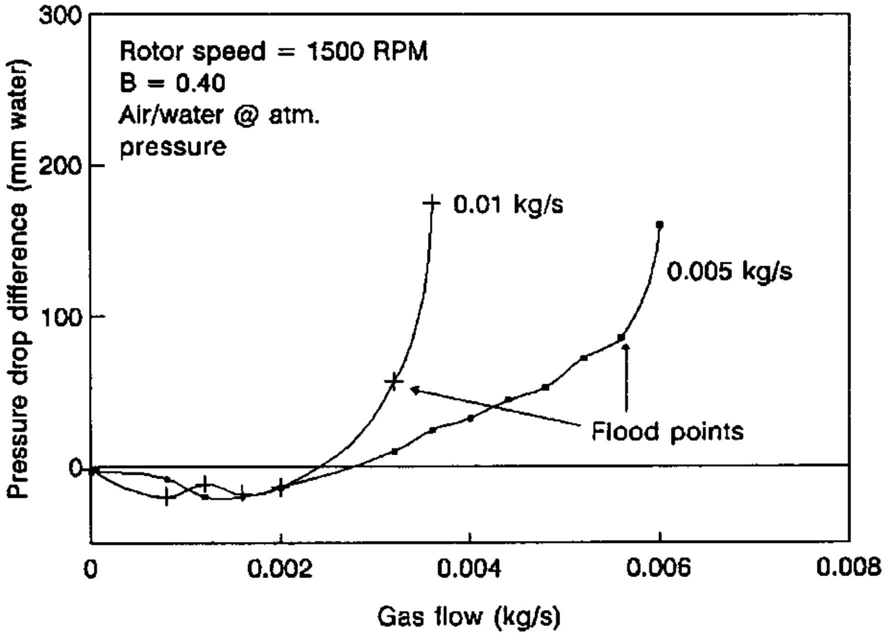

Figure A1.30
Pressure drop difference ΔP_L vs gas flow for various liquid flows: 500 RPM; $B = 0.40$; air/water at atmospheric pressure

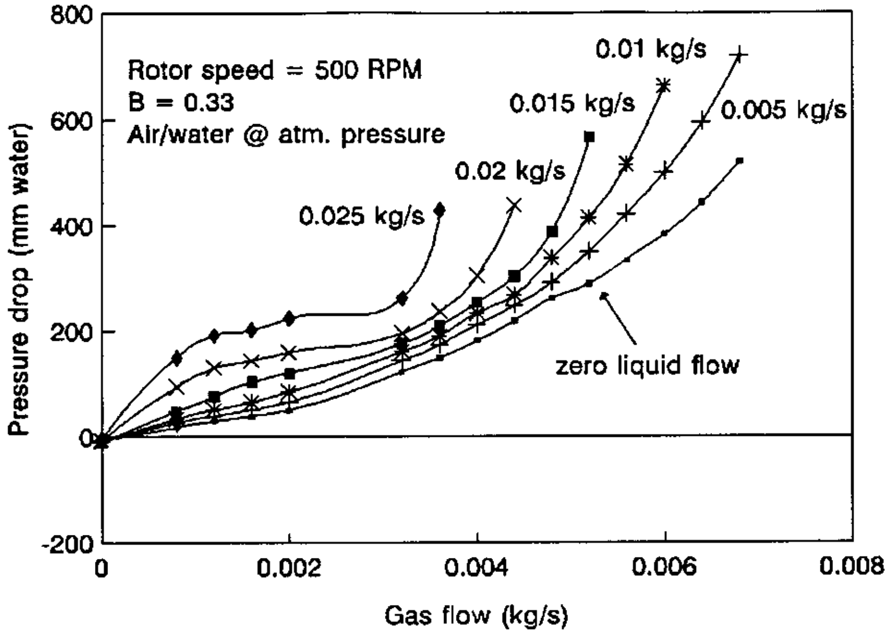

Figure A1.31
Pressure drop vs gas flow for various liquid flows: 500 RPM; $B = 0.33$; air/water at atmospheric pressure

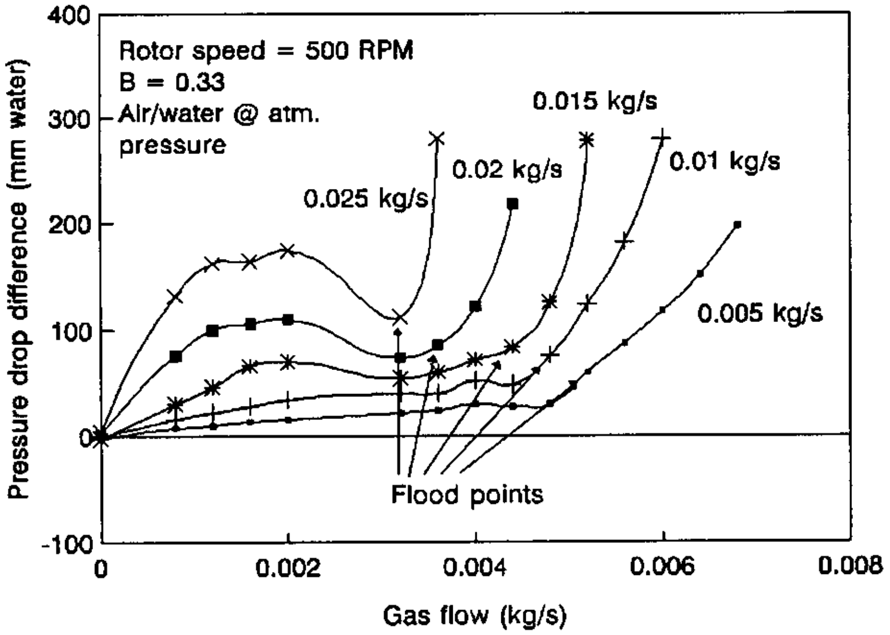

Figure A1.32
Pressure drop difference ΔP_L vs gas flow for various liquid flows: 500 RPM; $B = 0.33$; air/water at atmospheric pressure

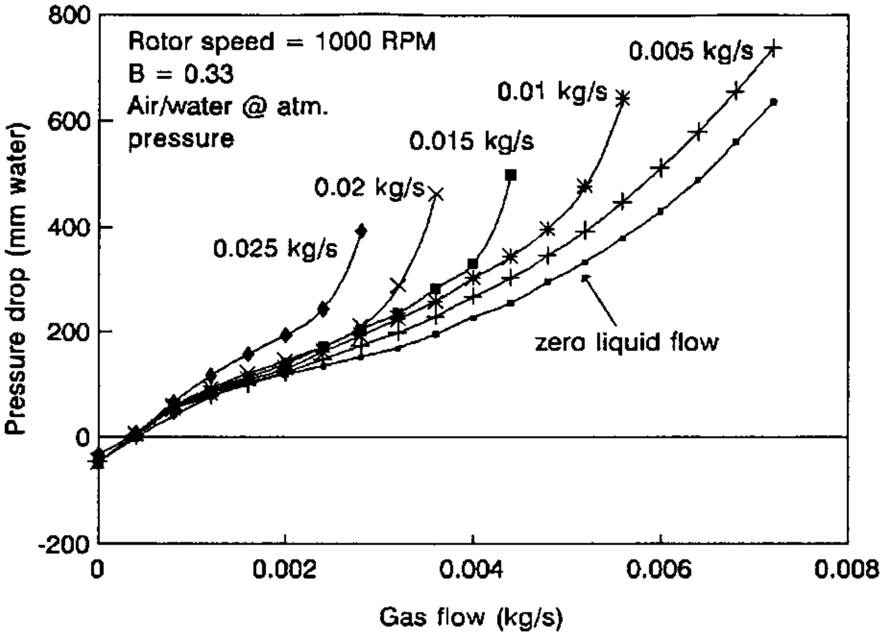

Figure A1.33
Pressure drop vs gas flow for various liquid flows: 1000 RPM;
$B = 0.33$; air/water at atmospheric pressure

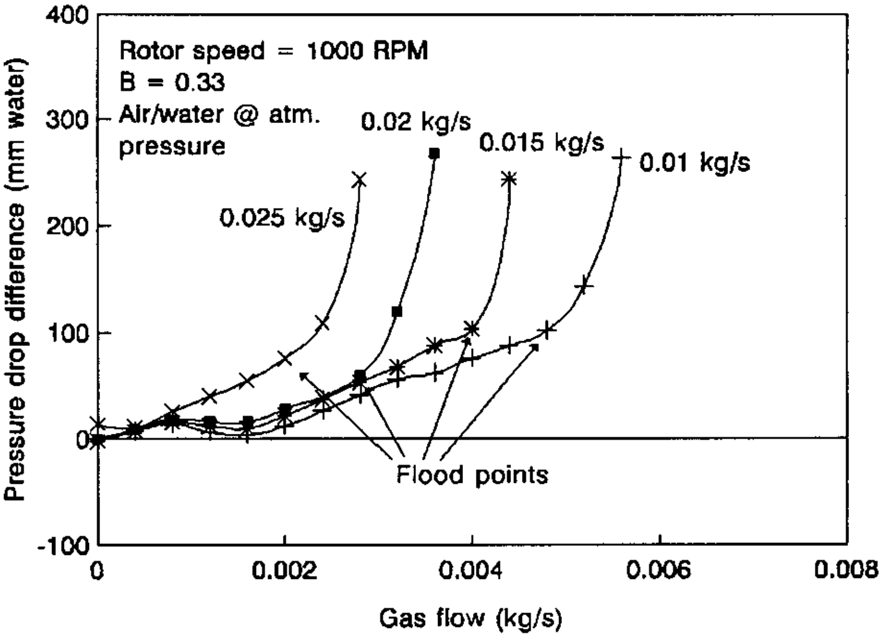

Figure A1.34
Pressure drop difference ΔP_L vs gas flow for various liquid flows: 1000 RPM;
$B = 0.33$; air/water at atmospheric pressure

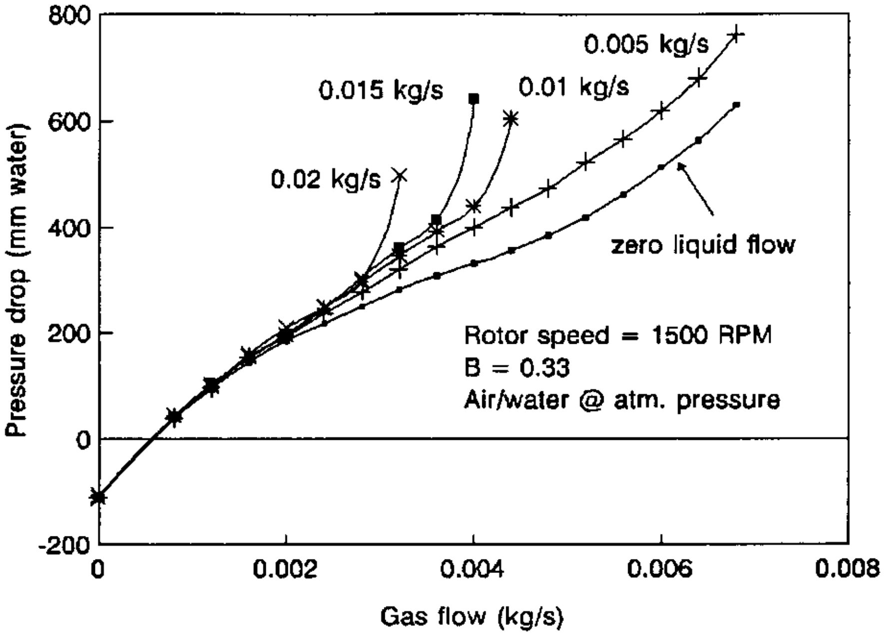

Figure A1.35
Pressure drop vs gas flow for various liquid flows: 1500 RPM; *B* = 0.33; air/water at atmospheric pressure

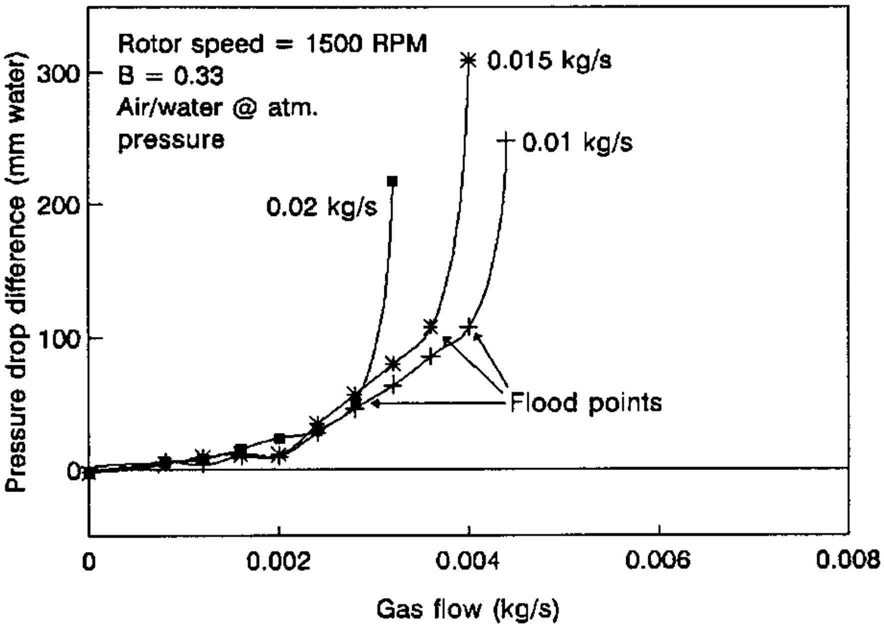

Figure A1.36
Pressure drop difference ΔP_L vs gas flow for various liquid flows: 1500 RPM; *B* = 0.33; air/water at atmospheric pressure

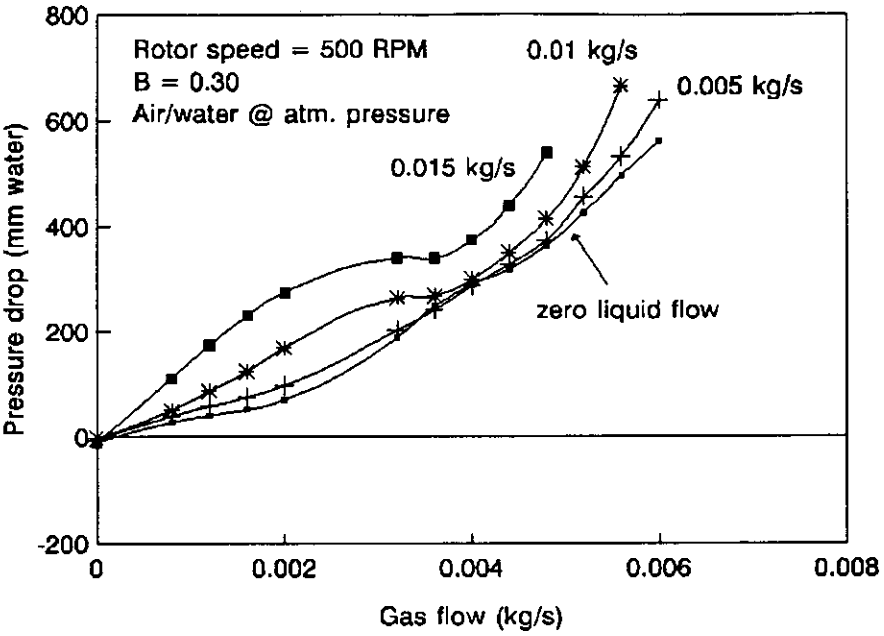

Figure A1.37
Pressure drop vs gas flow for various liquid flows: 500 RPM;
$B = 0.30$; air/water at atmospheric pressure

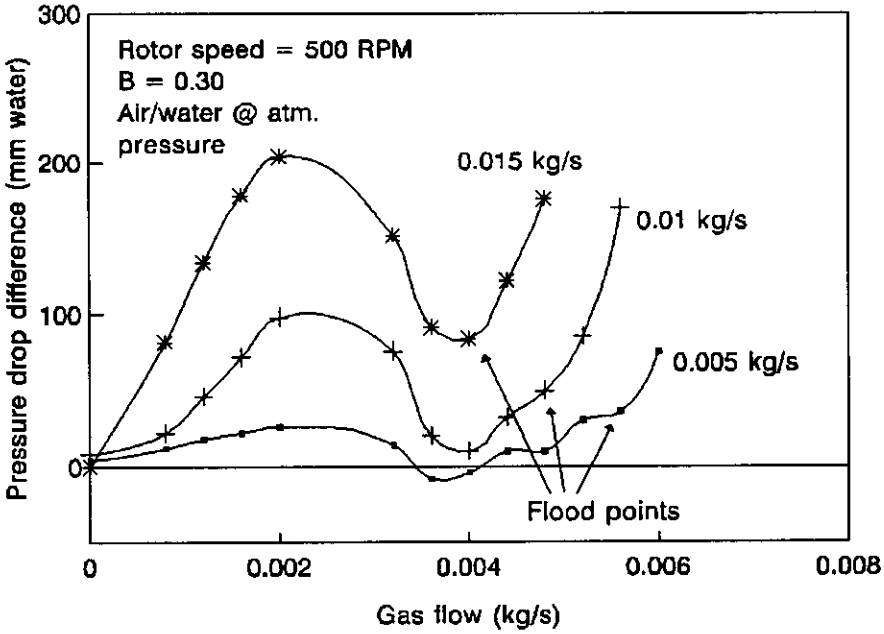

Figure A1.38
Pressure drop difference ΔP_L vs gas flow for various liquid flows: 500 RPM;
$B = 0.30$; air/water at atmospheric pressure

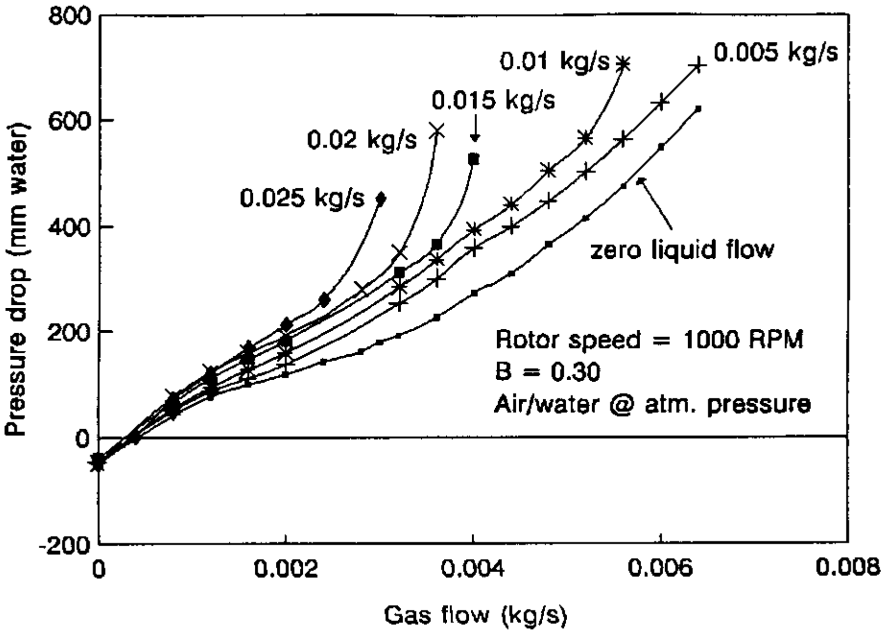

Figure A1.39
Pressure drop vs gas flow for various liquid flows: 1000 RPM; B = 0.30; air/water at atmospheric pressure

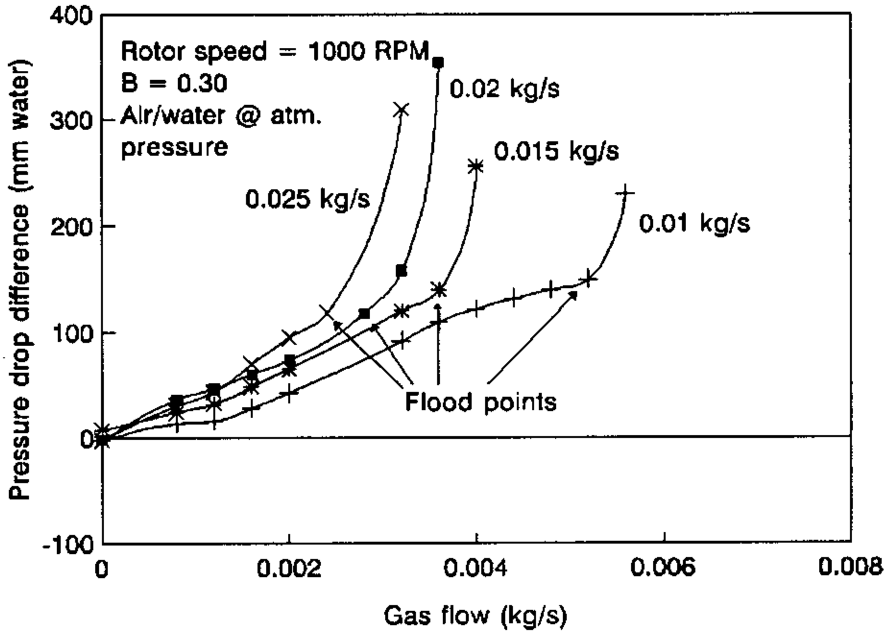

Figure A1.40
Pressure drop difference ΔP_L vs gas flow for various liquid flows: 1000 RPM; B = 0.30; air/water at atmospheric pressure

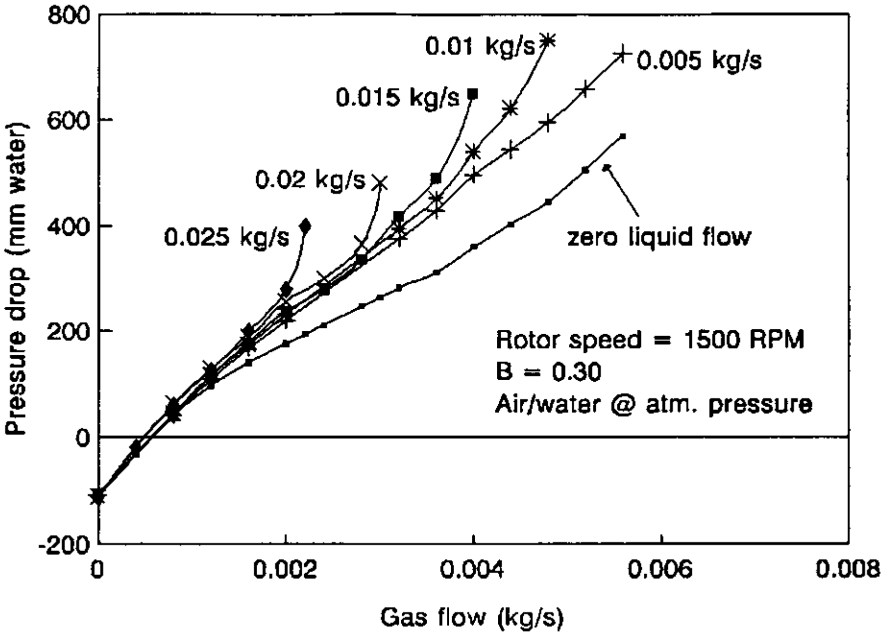

Figure A1.41
Pressure drop vs gas flow for various liquid flows: 1500 RPM;
$B = 0.30$; air/water at atmospheric pressure

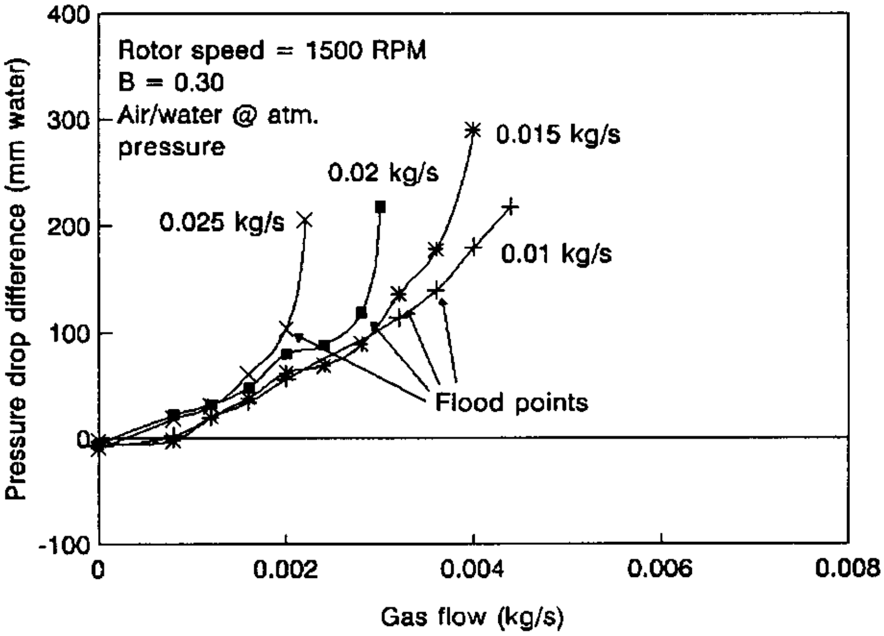

Figure A1.42
Pressure drop difference ΔP_L vs gas flow for various liquid flows: 1500 RPM;
$B = 0.30$; air/water at atmospheric pressure

APPENDIX 2: TABULATED FLOODING DATA

TABLE A2.1

Series	1							
Machine	CSIRO Mk II							
System	air/water							
System pressure	atmos.							
Shaft position parameter	0.4	0.4	0.4	0.4	0.4	0.4	0.4	0.4
Shaft speed (RPM)	500	500	500	500	500	1000	1000	1000
Minimum flow area (m^2)	0.0011	0.0011	0.0011	0.0011	0.0011	0.0011	0.0011	0.0011
Inner throat area (m^2)	0.0024	0.0024	0.0024	0.0024	0.0024	0.0024	0.0024	0.0024
a_p (m^2/m^3)	123	123	123	123	123	123	123	123
Hydraulic radius, min. flow area (m)	0.0026	0.0026	0.0026	0.0026	0.0026	0.0026	0.0026	0.0026
Hydraulic radius, inner throat (m)	0.0069	0.0069	0.0069	0.0069	0.0069	0.0069	0.0069	0.0069
Liquid density (kg/m^3)	998.2	998.2	998.2	998.2	998.2	998.2	998.2	998.2
Vapour density (kg/m^3)	1.204	1.204	1.204	1.204	1.204	1.204	1.204	1.204
Liquid flow at flooding (kg/min)	0.3	0.6	0.9	1.2	1.5	0.3	0.6	0.9
Vapour flow at flooding (l/min)	325	275	250	200	135	325	250	200
Flow parameter, X	0.027	0.063	0.104	0.173	0.321	0.027	0.069	0.130
TYPE 1 Capacity parameter, Y	0.367	0.263	0.217	0.139	0.063	0.367	0.217	0.139
TYPE 2 Capacity parameter, Y	0.075	0.053	0.044	0.028	0.013	0.075	0.044	0.028
TYPE 3 Capacity parameter, Y	1.130	0.809	0.668	0.428	0.195	1.130	0.668	0.428
TYPE 4 Capacity parameter, Y	0.230	0.164	0.136	0.087	0.040	0.230	0.136	0.087
TYPE 5 Capacity parameter, Y	0.431	0.309	0.255	0.163	0.074	0.431	0.255	0.163

APPENDIX 2: TABULATED FLOODING DATA

TABLE A2.2

Series	1					
Machine	CSIRO Mk II					
System	air/water					
System pressure	atmos.					
Shaft position parameter	0.4	0.4	0.4	0.4	0.4	0.4
Shaft speed (RPM)	1000	1000	1500	1500	1500	1500
Minimum flow area (m^2)	0.0011	0.0011	0.0011	0.0011	0.0011	0.0011
Inner throat area (m^2)	0.0024	0.0024	0.0024	0.0024	0.0024	0.0024
a_p (m^2/m^3)	123	123	123	123	123	123
Hydraulic radius, min. flow area (m)	0.0026	0.0026	0.0026	0.0026	0.0026	0.0026
Hydraulic radius, inner throat (m)	0.0069	0.0069	0.0069	0.0069	0.0069	0.0069
Liquid density (kg/m^3)	998.2	998.2	998.2	998.2	998.2	998.2
Vapour density (kg/m^3)	1.204	1.204	1.204	1.204	1.204	1.204
Liquid flow at flooding (kg/min)	1.2	1.5	0.3	0.6	0.9	1.2
Vapour flow at flooding (l/min)	175	120	300	225	200	150
Flow parameter, X	0.198	0.361	0.029	0.077	0.130	0.231
TYPE 1 Capacity parameter, Y	0.106	0.050	0.313	0.176	0.139	0.078
TYPE 2 Capacity parameter, Y	0.022	0.010	0.064	0.036	0.028	0.016
TYPE 3 Capacity parameter, Y	0.328	0.154	0.963	0.541	0.428	0.241
TYPE 4 Capacity parameter, Y	0.067	0.031	0.196	0.110	0.087	0.049
TYPE 5 Capacity parameter, Y	0.125	0.059	0.367	0.207	0.163	0.092

APPENDIX 2: TABULATED FLOODING DATA

TABLE A2.3

Series	2					
Machine	CSIRO Mk II					
System	steam/water					
System pressure	atmos.					
Shaft position parameter	0.4	0.4	0.4	0.4	0.4	0.4
Shaft speed (RPM)	500	500	500	1000	1000	1000
Minimum flow area (m^2)	0.0011	0.0011	0.0011	0.0011	0.0011	0.0011
Inner throat area (m^2)	0.0024	0.0024	0.0024	0.0024	0.0024	0.0024
a_p (m^2/m^3)	123	123	123	123	123	123
Hydraulic radius, min. flow area (m)	0.0026	0.0026	0.0026	0.0026	0.0026	0.0026
Hydraulic radius, inner throat (m)	0.0069	0.0069	0.0069	0.0069	0.0069	0.0069
Liquid density (kg/m^3)	957.9	957.9	957.9	957.9	957.9	957.9
Vapour density (kg/m^3)	0.5977	0.5977	0.5977	0.5977	0.5977	0.5977
Liquid flow at flooding (kg/min)	0.3	0.6	1.2	0.3	0.6	0.9
Vapour flow at flooding (kg/min)	0.236	0.223	0.132	0.254	0.212	0.124
Flow parameter, X	0.032	0.067	0.227	0.030	0.071	0.181
TYPE 1 Capacity parameter, Y	0.281	0.250	0.088	0.324	0.226	0.078
TYPE 2 Capacity parameter, Y	0.057	0.051	0.018	0.066	0.046	0.016
TYPE 3 Capacity parameter, Y	0.864	0.768	0.270	0.998	0.696	0.239
TYPE 4 Capacity parameter, Y	0.176	0.156	0.055	0.203	0.141	0.049
TYPE 5 Capacity parameter, Y	0.330	0.293	0.103	0.381	0.265	0.091

APPENDIX 2: TABULATED FLOODING DATA

TABLE A2.4

Series	3			
Machine	CSIRO Mk II			
System	steam/water			
System pressure	20 kPa abs.			
Shaft position parameter	0.4	0.4	0.4	0.4
Shaft speed (RPM)	500	500	500	500
Minimum flow area (m^2)	0.0011	0.0011	0.0011	0.0011
Inner throat area (m^2)	0.0024	0.0024	0.0024	0.0024
a_p (m^2/m^3)	123	123	123	123
Hydraulic radius, min. flow area (m)	0.0026	0.0026	0.0026	0.0026
Hydraulic radius, inner throat (m)	0.0069	0.0069	0.0069	0.0069
Liquid density (kg/m^3)	977.5	977.5	977.5	977.5
Vapour density (kg/m^3)	0.13	0.13	0.13	0.13
Liquid flow at flooding (kg/min)	0.3	0.6	0.9	1.2
Vapour flow at flooding (kg/min)	0.114	0.103	0.087	0.060
Flow parameter, X	0.030	0.067	0.119	0.231
TYPE 1 Capacity parameter, Y	0.294	0.240	0.172	0.082
TYPE 2 Capacity parameter, Y	0.060	0.049	0.035	0.017
TYPE 3 Capacity parameter, Y	0.907	0.740	0.528	0.251
TYPE 4 Capacity parameter, Y	0.184	0.150	0.107	0.051
TYPE 5 Capacity parameter, Y	0.346	0.282	0.201	0.096

TABLE A2.5

Series	4						
Machine	CSIRO Mk II						
System	steam/water	steam/water		steam/water			steam/wate
System pressure	atmos.	18 kPa abs.		atmos.			atmos
Spacing parameter	0.3	0.3	0.3	0.3	0.3	0.3	0.3
Shaft speed (RPM)	500	500	500	1000	1000	1000	1500
Minimum flow area (m^2)	0.00079	0.00079	0.00079	0.00079	0.00079	0.00079	0.00079
Inner throat area (m^2)	0.00244	0.00244	0.00244	0.00244	0.00244	0.00244	0.00244
a_p (m^2/m^3)	123	123	123	123	123	123	123
Hydraulic radius, min. flow area (m)	0.0020	0.0020	0.0020	0.0020	0.0020	0.0020	0.0020
Hydraulic radius, inner throat (m)	0.0069	0.0069	0.0069	0.0069	0.0069	0.0069	0.0069
Liquid density (kg/m^3)	957.9	984	984	957.9	957.9	957.9	957.9
Vapour density (kg/m^3)	0.5977	0.1247	0.1247	0.5977	0.5977	0.5977	0.5977
Liquid flow at flooding (kg/min)	0.6	0.3	0.6	0.3	0.6	0.9	0.6
Vapour flow at flooding (kg/min)	0.210	0.095	0.089	0.241	0.225	0.133	0.169
Flow parameter, X	0.071	0.036	0.076	0.031	0.067	0.169	0.089
TYPE 1 Capacity parameter, Y	0.432	0.411	0.357	0.566	0.493	0.173	0.279
TYPE 2 Capacity parameter, Y	0.045	0.043	0.037	0.059	0.052	0.018	0.029
TYPE 3 Capacity parameter, Y	1.772	1.687	1.465	2.325	2.025	0.712	1.144
TYPE 4 Capacity parameter, Y	0.186	0.177	0.154	0.244	0.212	0.075	0.120
TYPE 5 Capacity parameter, Y	0.507	0.483	0.419	0.665	0.579	0.204	0.327

APPENDIX 2: TABULATED FLOODING DATA

TABLE A2.6

Series	4		
Machine			
System	air/water		air/water
System pressure	atmos.		atmos
Spacing parameter	0.3	0.3	0.3
Shaft speed (RPM)	500	500	1000
Minimum flow area (m^2)	0.00079	0.00079	0.00079
Inner throat area (m^2)	0.00244	0.00244	0.00244
a_p (m^2/m^3)	123	123	123
Hydraulic radius, min. flow area (m)	0.0020	0.0020	0.0020
Hydraulic radius, inner throat (m)	0.0069	0.0069	0.0069
Liquid density (kg/m^3)	998.2	998.2	998.2
Vapour density (kg/m^3)	1.204	1.204	1.204
Liquid flow at flooding (kg/min)	0.6	0.9	0.9
Vapour flow at flooding (l/min)	260	200	150
Flow parameter, X	0.067	0.130	0.173
TYPE 1 Capacity parameter, Y	0.455	0.269	0.152
TYPE 2 Capacity parameter, Y	0.048	0.028	0.016
TYPE 3 Capacity parameter, Y	1.869	1.106	0.622
TYPE 4 Capacity parameter, Y	0.196	0.116	0.065
TYPE 5 Capacity parameter, Y	0.535	0.316	0.178

APPENDIX 2: TABULATED FLOODING DATA

TABLE A2.7

Series	5							
Machine	CSIRO Mk II							
System	air/water							
System pressure	atmos.							
Spacing parameter	0.3	0.3	0.3	0.3	0.3	0.3	0.3	0.3
Shaft speed (RPM)	500	1000	1500	500	1000	1500	500	1000
Minimum flow area (m^2)	0.00079	0.00079	0.00079	0.00079	0.00079	0.00079	0.00079	0.00079
Inner throat area (m^2)	0.00244	0.00244	0.00244	0.00244	0.00244	0.00244	0.00244	0.00244
a_p (m^2/m^3)	123	123	123	123	123	123	123	123
Hydraulic radius, min. flow area (m)	0.0020	0.0020	0.0020	0.0020	0.0020	0.0020	0.0020	0.0020
Hydraulic radius, inner throat (m)	0.0069	0.0069	0.0069	0.0069	0.0069	0.0069	0.0069	0.0069
Liquid density (kg/m^3)	998.2	998.2	998.2	998.2	998.2	998.2	998.2	998.2
Vapour density (kg/m^3)	1.204	1.204	1.204	1.204	1.204	1.204	1.204	1.204
Liquid flow at flooding (kg/min)	0.3	0.3	0.3	0.6	0.6	0.6	0.9	0.9
Vapour flow at flooding (l/min)	280	300	300	240	260	180	200	180
Flow parameter, X	0.031	0.029	0.029	0.072	0.067	0.096	0.130	0.144
TYPE 1 Capacity parameter, Y	0.528	0.606	0.606	0.388	0.455	0.218	0.269	0.218
TYPE 2 Capacity parameter, Y	0.055	0.064	0.064	0.041	0.048	0.023	0.028	0.023
TYPE 3 Capacity parameter, Y	2.168	2.488	2.488	1.593	1.869	0.896	1.106	0.896
TYPE 4 Capacity parameter, Y	0.227	0.261	0.261	0.167	0.196	0.094	0.116	0.094
TYPE 5 Capacity parameter, Y	0.620	0.712	0.712	0.456	0.535	0.256	0.316	0.256

APPENDIX 2: TABULATED FLOODING DATA

TABLE A2.8

Series	5							
Machine	CSIRO Mk II							
System	air/water							
System pressure	atmos.							
Spacing parameter	0.3	0.3	0.3	0.3	0.3	0.4	0.4	0.4
Shaft speed (RPM)	1500	1000	1500	1000	1500	500	1000	1500
Minimum flow area (m^2)	0.00079	0.00079	0.00079	0.00079	0.00079	0.0011	0.0011	0.0011
Inner throat area (m^2)	0.00244	0.00244	0.00244	0.00244	0.00244	0.00244	0.00244	0.00244
a_p (m^2/m^3)	123	123	123	123	123	123	123	123
Hydraulic radius, min. flow area (m)	0.0020	0.0020	0.0020	0.0020	0.0020	0.0026	0.0026	0.0026
Hydraulic radius, inner throat (m)	0.0069	0.0069	0.0069	0.0069	0.0069	0.0069	0.0069	0.0069
Liquid density (kg/m^3)	998.2	998.2	998.2	998.2	998.2	998.2	998.2	998.2
Vapour density (kg/m^3)	1.204	1.204	1.204	1.204	1.204	1.204	1.204	1.204
Liquid flow at flooding (kg/min)	0.9	1.2	1.2	1.5	1.5	0.3	0.3	0.3
Vapour flow at flooding (l/min)	160	140	140	120	100	280	320	280
Flow parameter, X	0.162	0.247	0.247	0.361	0.433	0.031	0.027	0.031
TYPE 1 Capacity parameter, Y	0.172	0.132	0.132	0.097	0.067	0.272	0.356	0.272
TYPE 2 Capacity parameter, Y	0.018	0.014	0.014	0.010	0.007	0.055	0.072	0.055
TYPE 3 Capacity parameter, Y	0.708	0.542	0.542	0.398	0.276	0.839	1.095	0.839
TYPE 4 Capacity parameter, Y	0.074	0.057	0.057	0.042	0.029	0.170	0.223	0.170
TYPE 5 Capacity parameter, Y	0.203	0.155	0.155	0.114	0.079	0.320	0.418	0.320

TABLE A2.9

Series	5							
Machine	CSIRO Mk II							
System	air/water							
System pressure	atmos.							
Spacing parameter	0.4	0.4	0.4	0.4	0.4	0.4	0.4	0.4
Shaft speed (RPM)	500	1000	1500	500	1000	500	1000	500
Minimum flow area (m^2)	0.0011	0.0011	0.0011	0.0011	0.0011	0.0011	0.0011	0.0011
Inner throat area (m^2)	0.00244	0.00244	0.00244	0.00244	0.00244	0.00244	0.00244	0.00244
a_p (m^2/m^3)	123	123	123	123	123	123	123	123
Hydraulic radius, min. flow area (m)	0.0026	0.0026	0.0026	0.0026	0.0026	0.0026	0.0026	0.0026
Hydraulic radius, inner throat (m)	0.0069	0.0069	0.0069	0.0069	0.0069	0.0069	0.0069	0.0069
Liquid density (kg/m^3)	998.2	998.2	998.2	998.2	998.2	998.2	998.2	998.2
Vapour density (kg/m^3)	1.204	1.204	1.204	1.204	1.204	1.204	1.204	1.204
Liquid flow at flooding (kg/min)	0.6	0.6	0.6	0.9	0.9	1.2	1.2	1.5
Vapour flow at flooding (l/min)	260	260	160	225	200	200	130	160
Flow parameter, X	0.067	0.067	0.108	0.115	0.130	0.173	0.266	0.270
TYPE 1 Capacity parameter, Y	0.235	0.235	0.089	0.176	0.139	0.139	0.059	0.089
TYPE 2 Capacity parameter, Y	0.048	0.048	0.018	0.036	0.028	0.028	0.012	0.018
TYPE 3 Capacity parameter, Y	0.723	0.723	0.274	0.541	0.428	0.428	0.181	0.274
TYPE 4 Capacity parameter, Y	0.147	0.147	0.056	0.110	0.087	0.087	0.037	0.056
TYPE 5 Capacity parameter, Y	0.276	0.276	0.104	0.207	0.163	0.163	0.069	0.104

APPENDIX 2: TABULATED FLOODING DATA

TABLE A2.10

Series	5							
Machine	CSIRO Mk II							
System	air/water							
System pressure	atmos.							
Spacing parameter	0.33	0.33	0.33	0.33	0.33	0.33	0.33	0.33
Shaft speed (RPM)	500	1000	1500	500	1000	1500	500	1000
Minimum flow area (m^2)	0.00088	0.00088	0.00088	0.00088	0.00088	0.00088	0.00088	0.00088
Inner throat area (m^2)	0.00244	0.00244	0.00244	0.00244	0.00244	0.00244	0.00244	0.00244
a_p (m^2/m^3)	123	123	123	123	123	123	123	123
Hydraulic radius, min. flow area (m)	0.0022	0.0022	0.0022	0.0022	0.0022	0.0022	0.0022	0.0022
Hydraulic radius, inner throat (m)	0.0069	0.0069	0.0069	0.0069	0.0069	0.0069	0.0069	0.0069
Liquid density (kg/m^3)	998.2	998.2	998.2	998.2	998.2	998.2	998.2	998.2
Vapour density (kg/m^3)	1.204	1.204	1.204	1.204	1.204	1.204	1.204	1.204
Liquid flow at flooding (kg/min)	0.3	0.3	0.3	0.6	0.6	0.6	0.9	0.9
Vapour flow at flooding (l/min)	260	300	300	240	240	200	220	200
Flow parameter, X	0.033	0.029	0.029	0.072	0.072	0.087	0.118	0.130
TYPE 1 Capacity parameter, Y	0.367	0.488	0.488	0.313	0.313	0.217	0.263	0.217
TYPE 2 Capacity parameter, Y	0.048	0.064	0.064	0.041	0.041	0.028	0.034	0.028
TYPE 3 Capacity parameter, Y	1.368	1.821	1.821	1.166	1.166	0.810	0.980	0.810
TYPE 4 Capacity parameter, Y	0.178	0.237	0.237	0.152	0.152	0.105	0.127	0.105
TYPE 5 Capacity parameter, Y	0.431	0.574	0.574	0.367	0.367	0.255	0.309	0.255

APPENDIX 2: TABULATED FLOODING DATA

TABLE A2.11

Series	5					
Machine	CSIRO Mk II					
System	air/water					
System pressure	atmos.					
Spacing parameter	0.33	0.33	0.33	0.33	0.33	0.33
Shaft speed (RPM)	1500	500	1000	1500	500	1000
Minimum flow area (m^2)	0.00088	0.00088	0.00088	0.00088	0.00088	0.00088
Inner throat area (m^2)	0.00244	0.00244	0.00244	0.00244	0.00244	0.00244
a_p (m^2/m^3)	123	123	123	123	123	123
Hydraulic radius, min. flow area (m)	0.0022	0.0022	0.0022	0.0022	0.0022	0.0022
Hydraulic radius, inner throat (m)	0.0069	0.0069	0.0069	0.0069	0.0069	0.0069
Liquid density (kg/m^3)	998.2	998.2	998.2	998.2	998.2	998.2
Vapour density (kg/m^3)	1.204	1.204	1.204	1.204	1.204	1.204
Liquid flow at flooding (kg/min)	0.9	1.2	1.2	1.2	1.5	1.5
Vapour flow at flooding (l/min)	180	180	140	140	160	100
Flow parameter, X	0.144	0.192	0.247	0.247	0.270	0.433
TYPE 1 Capacity parameter, Y	0.176	0.176	0.106	0.106	0.139	0.054
TYPE 2 Capacity parameter, Y	0.023	0.023	0.014	0.014	0.018	0.007
TYPE 3 Capacity parameter, Y	0.656	0.656	0.397	0.397	0.518	0.202
TYPE 4 Capacity parameter, Y	0.085	0.085	0.052	0.052	0.067	0.026
TYPE 5 Capacity parameter, Y	0.207	0.207	0.125	0.125	0.163	0.064

APPENDIX 2: TABULATED FLOODING DATA

TABLE A2.12

Series	6							
Machine	CSIRO Mk III							
System	steam/water							
System pressure	atmos.							
Spacing parameter	0.7	0.7	0.7	0.7	0.7	0.7	0.7	0.7
Shaft speed (RPM)	500	500	500	500	500	500	500	500
Minimum flow area (m^2)	0.0023	0.0023	0.0023	0.0023	0.0023	0.0023	0.0023	0.0023
Inner throat area (m^2)	0.0059	0.0059	0.0059	0.0059	0.0059	0.0059	0.0059	0.0059
a_p (m^2/m^3)	52.3	52.3	52.3	52.3	52.3	52.3	52.3	52.3
Hydraulic radius, min. flow area (m)	0.0034	0.0034	0.0034	0.0034	0.0034	0.0034	0.0034	0.0034
Hydraulic radius, inner throat (m)	0.0125	0.0125	0.0125	0.0125	0.0125	0.0125	0.0125	0.0125
Liquid density (kg/m^3)	957.9	957.9	957.9	957.9	957.9	957.9	957.9	957.9
Vapour density (kg/m^3)	0.5977	0.5977	0.5977	0.5977	0.5977	0.5977	0.5977	0.5977
Liquid flow at flooding (kg/min)	10.15	10.01	9.90	7.87	5.95	5.00	4.83	2.80
Vapour flow at flooding (kg/min)	0.220	0.240	0.250	0.300	0.354	0.396	0.449	0.608
Flow parameter, X	1.153	1.042	0.989	0.656	0.420	0.315	0.269	0.115
TYPE 1 Capacity parameter, Y	0.024	0.029	0.031	0.045	0.063	0.079	0.101	0.186
TYPE 2 Capacity parameter, Y	0.004	0.004	0.005	0.007	0.009	0.012	0.015	0.028
TYPE 3 Capacity parameter, Y	0.135	0.161	0.174	0.251	0.349	0.438	0.563	1.032
TYPE 4 Capacity parameter, Y	0.020	0.024	0.026	0.037	0.052	0.065	0.084	0.153
TYPE 5 Capacity parameter, Y	0.037	0.044	0.048	0.069	0.096	0.121	0.155	0.284

APPENDIX 2: TABULATED FLOODING DATA

TABLE A2.13

Series	7							
Machine	CSIRO Mk III							
System	steam/water							
System pressure	vacuum							
Spacing parameter	0.7	0.7	0.7	0.7	0.7	0.7	0.7	0.7
Shaft speed (RPM)	500	500	500	500	500	500	500	500
Minimum flow area (m^2)	0.0023	0.0023	0.0023	0.0023	0.0023	0.0023	0.0023	0.0023
Inner throat area (m^2)	0.0059	0.0059	0.0059	0.0059	0.0059	0.0059	0.0059	0.0059
a_p (m^2/m^3)	52.3	52.3	52.3	52.3	52.3	52.3	52.3	52.3
Hydraulic radius, min. flow area (m)	0.0034	0.0034	0.0034	0.0034	0.0034	0.0034	0.0034	0.0034
Hydraulic radius, inner throat (m)	0.0125	0.0125	0.0125	0.0125	0.0125	0.0125	0.0125	0.0125
Liquid density (kg/m^3)	977.5	981.8	987.6	987.6	983.3	976.2	969.6	978.3
Vapour density (kg/m^3)	0.1982	0.1441	0.0866	0.0866	0.1302	0.2321	0.3397	0.1871
Liquid flow at flooding (kg/min)	3.91	3.93	3.95	2.96	2.95	2.93	1.94	1.96
Vapour flow at flooding (kg/min)	0.310	0.299	0.225	0.250	0.312	0.424	0.560	0.437
Flow parameter, X	0.180	0.159	0.164	0.111	0.109	0.107	0.065	0.062
TYPE 1 Capacity parameter, Y	0.143	0.182	0.170	0.210	0.218	0.228	0.274	0.300
TYPE 2 Capacity parameter, Y	0.021	0.027	0.025	0.031	0.032	0.034	0.041	0.045
TYPE 3 Capacity parameter, Y	0.793	1.010	0.946	1.168	1.211	1.265	1.523	1.670
TYPE 4 Capacity parameter, Y	0.118	0.150	0.141	0.173	0.180	0.188	0.226	0.248
TYPE 5 Capacity parameter, Y	0.218	0.278	0.260	0.321	0.333	0.348	0.419	0.460

APPENDIX 2: TABULATED FLOODING DATA

TABLE A2.14

Series	8							
Machine	Model 10000							
System	steam/water							
System pressure	vacuum							
Spacing parameter	0.5	0.5	0.5	0.5	0.5	0.5	0.5	0.5
Shaft speed (RPM)	350	350	350	350	350	350	350	350
Minimum flow area (m^2)	0.0399	0.0399	0.0399	0.0399	0.0399	0.0399	0.0399	0.0399
Inner throat area (m^2)	0.0742	0.0742	0.0742	0.0742	0.0742	0.0742	0.0742	0.0742
a_p (m^2/m^3)	15.2	15.2	15.2	15.2	15.2	15.2	15.2	15.2
Hydraulic radius, min. flow area (m)	0.0220	0.0220	0.0220	0.0220	0.0220	0.0220	0.0220	0.0220
Hydraulic radius, inner throat (m)	0.0578	0.0578	0.0578	0.0578	0.0578	0.0578	0.0578	0.0578
Liquid density (kg/m^3)	975.2	975.2	975.2	979.4	975.2	975.2	975.2	975.2
Vapour density (kg/m^3)	0.1302	0.1302	0.1302	0.1302	0.1302	0.1302	0.1302	0.1302
Liquid flow at flooding (kg/hour)	1500	4000	4000	9000	2000	2000	3000	5000
Vapour flow at flooding (kg/hour)	880	612	610	528	762	633	564	600
Flow parameter, X	0.020	0.076	0.076	0.197	0.030	0.037	0.061	0.096
TYPE 1 Capacity parameter, Y	0.459	0.222	0.221	0.165	0.344	0.238	0.189	0.213
TYPE 2 Capacity parameter, Y	0.133	0.064	0.064	0.048	0.100	0.069	0.055	0.062
TYPE 3 Capacity parameter, Y	1.371	0.663	0.659	0.491	1.028	0.709	0.563	0.637
TYPE 4 Capacity parameter, Y	0.396	0.192	0.190	0.142	0.297	0.205	0.163	0.184
TYPE 5 Capacity parameter, Y	0.522	0.252	0.251	0.187	0.391	0.270	0.214	0.243

TABLE A2.15

Series	8			
Machine	Model 10000			
System	steam/water			
System pressure	vacuum			
Spacing parameter	0.5	0.5	0.5	0.5
Shaft speed (RPM)	350	350	350	350
Minimum flow area (m^2)	0.0399	0.0399	0.0399	0.0399
Inner throat area (m^2)	0.0742	0.0742	0.0742	0.0742
a_p (m^2/m^3)	15.2	15.2	15.2	15.2
Hydraulic radius, min. flow area (m)	0.0220	0.0220	0.0220	0.0220
Hydraulic radius, inner throat (m)	0.0578	0.0578	0.0578	0.0578
Liquid density (kg/m^3)	975.2	975.2	975.2	975.2
Vapour density (kg/m^3)	0.1302	0.1302	0.1302	0.1302
Liquid flow at flooding (kg/hour)	2000	5000	2000	4000
Vapour flow at flooding (kg/hour)	650	585	810	610
Flow parameter, X	0.036	0.099	0.029	0.076
TYPE 1 Capacity parameter, Y	0.251	0.203	0.389	0.221
TYPE 2 Capacity parameter, Y	0.072	0.059	0.113	0.064
TYPE 3 Capacity parameter, Y	0.748	0.606	1.162	0.659
TYPE 4 Capacity parameter, Y	0.216	0.175	0.336	0.190
TYPE 5 Capacity parameter, Y	0.285	0.231	0.442	0.251

APPENDIX 3

AVERAGE RADIAL VELOCITIES OF LIQUID FILM ON A ROTATING CONICAL SURFACE:

RESULTS OF EXPERIMENTS DESCRIBED IN CHAPTER 5

Table A3.1: 250 RPM

Rotational speed (RPM)	Liquid flow (kg/minute)	R_0 (m)	R_1 (m)	Average radial velocity (m/s)
250	2	0.072	0.139	0.279
250	2	0.082	0.125	0.358
250	2	0.050	0.133	0.231
250	2	0.056	0.135	0.282
250	2	0.058	0.143	0.425
250	2	0.058	0.143	0.425
250	2	0.059	0.141	0.256
250	2	0.061	0.108	0.131
250	5	0.082	0.135	0.221
250	5	0.083	0.128	0.375
250	10	0.099	0.144	0.225
250	10	0.099	0.144	0.225
250	10	0.106	0.145	0.244
250	10	0.080	0.137	0.407
250	10	0.080	0.137	0.407
250	10	0.086	0.125	0.163
250	10	0.091	0.129	0.119
250	10	0.094	0.146	0.289

Table A3.2a: 500 RPM

Rotational speed (RPM)	Liquid flow (kg/minute)	R_0	R_1	Average radial velocity (m/s)
500	2	0.064	0.146	0.684
500	2	0.069	0.132	0.225
500	2	0.047	0.138	0.455
500	2	0.047	0.118	0.592
500	2	0.048	0.136	1.467
500	2	0.049	0.129	0.500
500	2	0.049	0.075	0.650
500	2	0.049	0.115	0.825
500	2	0.052	0.126	0.529
500	2	0.055	0.142	0.870
500	2	0.056	0.129	0.608
500	2	0.057	0.084	0.675
500	2	0.059	0.134	0.417
500	2	0.059	0.108	0.817
500	2	0.060	0.143	1.383
500	2	0.063	0.122	0.738
500	2	0.075	0.129	0.675
500	2	0.079	0.105	1.300

Table A3.2b : 500 RPM

Rotational speed (RPM)	Liquid flow (kg/minute)	R_0 (m)	R_1 (m)	Average radial velocity (m/s)
500	5	0.040	0.097	1.440
500	5	0.041	0.085	0.364
500	5	0.044	0.071	0.231
500	5	0.044	0.114	0.440
500	5	0.045	0.107	0.512
500	5	0.045	0.095	0.621
500	5	0.045	0.095	0.631
500	5	0.046	0.076	0.212
500	5	0.047	0.105	0.365
500	5	0.047	0.091	0.368
500	5	0.047	0.105	0.576
500	5	0.048	0.113	0.409
500	5	0.048	0.102	0.467
500	5	0.048	0.113	0.814
500	5	0.049	0.119	0.295
500	5	0.049	0.118	0.434
500	5	0.049	0.119	0.500
500	5	0.049	0.142	0.779
500	5	0.050	0.120	0.497
500	5	0.050	0.120	0.497
500	5	0.051	0.107	0.308
500	5	0.051	0.079	0.355
500	5	0.053	0.104	0.257
500	5	0.053	0.107	0.272
500	5	0.054	0.111	0.475
500	5	0.054	0.099	1.122
500	5	0.055	0.084	0.245
500	5	0.055	0.120	0.546
500	5	0.057	0.083	0.333
500	5	0.057	0.102	0.375

Table A3.2c: 500 RPM

Rotational speed (RPM)	Liquid flow (kg/minute)	R_o (m)	R_1 (m)	Average radial velocity (m/s)
500	5	0.058	0.111	0.440
500	5	0.060	0.113	0.443
500	5	0.060	0.118	0.725
500	5	0.061	0.089	0.279
500	5	0.062	0.118	0.467
500	5	0.062	0.118	0.467
500	5	0.062	0.113	0.636
500	5	0.063	0.082	0.232
500	5	0.063	0.114	0.631
500	5	0.065	0.119	1.354
500	5	0.066	0.085	0.472
500	5	0.066	0.107	0.519
500	5	0.068	0.088	0.517
500	5	0.068	0.115	1.193
500	5	0.069	0.102	0.409
500	5	0.071	0.117	0.575
500	5	0.072	0.086	0.343
500	5	0.076	0.081	0.123
500	5	0.078	0.111	0.819
500	5	0.094	0.129	0.707
500	5	0.047	0.130	2.075
500	5	0.047	0.130	2.075
500	5	0.049	0.084	0.438
500	5	0.049	0.141	1.150
500	5	0.049	0.125	1.900
500	5	0.049	0.125	1.900
500	5	0.053	0.116	0.394
500	5	0.053	0.085	0.400
500	5	0.053	0.123	1.167
500	5	0.056	0.144	1.100

Table A3.2d: 500 RPM

Rotational speed (RPM)	Liquid flow (kg/minute)	R_0 (m)	R_1 (m)	Average radial velocity (m/s)
500	5	0.057	0.137	2.000
500	5	0.061	0.131	1.750
500	5	0.061	0.131	1.750
500	5	0.066	0.124	1.450
500	5	0.067	0.119	1.300
500	5	0.071	0.130	2.950
500	5	0.081	0.122	1.025
500	5	0.096	0.117	0.525
500	10	0.045	0.125	0.670
500	10	0.048	0.129	0.580
500	10	0.051	0.130	0.655
500	10	0.052	0.090	0.313
500	10	0.058	0.102	0.552
500	10	0.058	0.102	0.552
500	10	0.059	0.081	0.188
500	10	0.059	0.088	0.239
500	10	0.060	0.114	0.449
500	10	0.062	0.095	0.271
500	10	0.064	0.134	0.499
500	10	0.066	0.102	0.305
500	10	0.066	0.099	0.412
500	10	0.068	0.087	0.315
500	10	0.068	0.119	0.423
500	10	0.070	0.113	0.350
500	10	0.072	0.114	0.297
500	10	0.085	0.124	0.965
500	10	0.044	0.127	0.520
500	10	0.052	0.113	0.504
500	10	0.054	0.112	0.358
500	10	0.055	0.120	0.652

Table A3.2e: 500 RPM

Rotational speed (RPM)	Liquid flow (kg/minute)	R_0 (m)	R_1 (m)	Average radial velocity (m/s)
500	10	0.064	0.118	0.670
500	10	0.078	0.128	0.833
500	10	0.057	0.117	0.503
500	10	0.067	0.127	0.605
500	10	0.066	0.101	0.578
500	10	0.053	0.124	0.586
500	10	0.052	0.129	0.548
500	10	0.051	0.097	0.332
500	10	0.051	0.102	0.365
500	10	0.047	0.103	0.400
500	10	0.056	0.093	0.309
500	10	0.055	0.109	0.448
500	10	0.060	0.110	0.504
500	10	0.054	0.147	0.776
500	10	0.057	0.101	0.363
500	10	0.064	0.095	0.388
500	10	0.051	0.100	0.619
500	10	0.042	0.117	1.875
500	10	0.043	0.133	2.250
500	10	0.045	0.160	1.438
500	10	0.047	0.159	1.400
500	10	0.047	0.135	2.200
500	10	0.048	0.099	1.275
500	10	0.049	0.145	2.400
500	10	0.055	0.146	0.758
500	10	0.056	0.137	1.013
500	10	0.058	0.108	2.500
500	10	0.061	0.104	2.150
500	10	0.068	0.114	2.300
500	10	0.072	0.119	2.350

Table A3.3a: 1000 RPM

Rotational speed (RPM)	Liquid flow (kg/minute)	R_0 (m)	R_1 (m)	Average radial velocity (m/s)
1000	2	0.048	0.089	2.050
1000	2	0.049	0.117	0.850
1000	2	0.049	0.116	1.675
1000	2	0.049	0.084	1.750
1000	2	0.051	0.079	0.233
1000	2	0.051	0.111	1.500
1000	2	0.052	0.086	0.850
1000	2	0.052	0.137	0.850
1000	2	0.054	0.100	0.230
1000	2	0.055	0.134	1.317
1000	2	0.055	0.134	1.317
1000	2	0.055	0.122	3.350
1000	2	0.056	0.067	0.275
1000	2	0.059	0.093	0.567
1000	2	0.059	0.082	0.575
1000	2	0.059	0.101	0.700
1000	2	0.060	0.146	0.717
1000	2	0.061	0.096	1.750
1000	2	0.063	0.105	0.525
1000	2	0.064	0.099	0.438
1000	2	0.064	0.099	0.438
1000	5	0.046	0.109	1.575
1000	5	0.046	0.090	2.200
1000	5	0.046	0.146	2.500
1000	5	0.050	0.081	0.258
1000	5	0.050	0.118	1.133
1000	5	0.051	0.086	0.350
1000	5	0.052	0.073	0.525
1000	5	0.052	0.117	1.083

Table A3.3b: 1000 RPM

Rotational speed (RPM)	Liquid flow (kg/minute)	R_0 (m)	R_1 (m)	Average radial velocity (m/s)
1000	5	0.053	0.133	0.500
1000	5	0.055	0.126	0.710
1000	5	0.059	0.080	0.210
1000	5	0.059	0.085	0.433
1000	5	0.060	0.076	0.400
1000	5	0.060	0.147	0.483
1000	5	0.061	0.075	0.233
1000	5	0.061	0.084	0.288
1000	5	0.062	0.081	0.475
1000	5	0.063	0.103	0.667
1000	5	0.066	0.086	0.500
1000	5	0.066	0.086	0.500
1000	5	0.071	0.092	0.263
1000	5	0.079	0.130	1.275
1000	5	0.082	0.138	0.560
1000	5	0.043	0.120	1.283
1000	5	0.045	0.137	2.300
1000	5	0.047	0.119	1.800
1000	5	0.047	0.155	1.800
1000	5	0.066	0.115	0.817
1000	5	0.068	0.117	1.225
1000	10	0.046	0.080	0.567
1000	10	0.048	0.118	1.167
1000	10	0.048	0.140	1.533
1000	10	0.050	0.148	1.633
1000	10	0.052	0.147	1.583
1000	10	0.064	0.122	0.967
1000	10	0.067	0.123	0.933
1000	10	0.067	0.139	1.200
1000	10	0.088	0.132	1.100

Table A3.3c: 1000 RPM

Rotational speed (RPM)	Liquid flow (kg/minute)	R_0 (m)	R_1 (m)	Average radial velocity (m/s)
1000	10	0.088	0.133	1.125
1000	10	0.044	0.116	1.200
1000	10	0.045	0.130	1.417
1000	10	0.048	0.144	1.600
1000	10	0.049	0.130	1.013
1000	10	0.050	0.146	0.800
1000	10	0.061	0.101	0.667
1000	10	0.062	0.120	1.450
1000	10	0.064	0.103	1.950
1000	10	0.066	0.121	1.375
1000	10	0.076	0.109	0.550

APPENDIX 4
RESULTS OF ACETIC ACID/WATER TRIALS

Table A4.1a

Run	Speed (RPM)	Acetic acid conc. (% by weight)		Mole fraction water		NTS	Reflux flow (ml/min)	K'_x
		Bottom	Top	Bottom	Top			
1	250	4.95	0.060	0.99225	0.99991	12.5	20	0.00012
2	250	8.88	0.234	0.98559	0.99965	10.5	54	0.00028
3	250	8.18	0.274	0.98680	0.99959	9.8	105	0.00050
4	250	8.47	0.258	0.98630	0.99961	10.1	150	0.00073
5	250	10.00	0.164	0.98361	0.99975	11.9	195	0.00113
6	250	11.46	0.118	0.98095	0.99982	13.2	200	0.00129
7	250	28.75	0.674	0.94291	0.99898	11.5	255	0.00147
8	500	7.80	0.043	0.98746	0.99994	14.9	20	0.00014
9	500	8.80	0.118	0.98573	0.99982	12.4	41	0.00025
10	500	11.00	0.255	0.98179	0.99962	10.9	72	0.00038
11	500	7.38	0.182	0.98818	0.99973	10.6	97	0.00050
12	500	8.74	0.249	0.98583	0.99963	10.3	152	0.00076
13	500	9.19	0.085	0.98503	0.99987	13.5	215	0.00141
14	500	12.54	0.099	0.97893	0.99985	14.0	221	0.00152
15	500	10.45	0.276	0.98279	0.99959	10.5	262	0.00134
16	750	6.51	0.023	0.98966	0.99997	16.1	21	0.00016
17	750	7.64	0.079	0.98774	0.99988	13.1	51	0.00032
18	750	11.56	0.206	0.98077	0.99969	11.7	70	0.00040
19	750	8.59	0.176	0.98609	0.99974	11.2	104	0.00057
20	750	8.27	0.176	0.98665	0.99974	11.1	155	0.00083
21	750	10.19	0.109	0.98326	0.99984	13.1	195	0.00124
22	750	10.49	0.074	0.98272	0.99989	14.2	220	0.00153
23	750	18.54	0.216	0.96699	0.99968	13.1	248	0.00161
24	1000	8.82	0.027	0.98569	0.99996	16.6	18	0.00015
25	1000	7.11	0.057	0.98865	0.99991	13.8	45	0.00030
26	1000	12.57	0.182	0.97889	0.99973	12.3	70	0.00042
27	1000	8.26	0.131	0.98668	0.99980	11.9	101	0.00058
28	1000	8.00	0.133	0.98712	0.99980	11.8	146	0.00083
29	1000	10.67	0.103	0.98239	0.99985	13.4	195	0.00127
30	1000	8.16	0.057	0.98684	0.99991	14.2	210	0.00145

Table A4.1b

Run	Speed (RPM)	Acetic acid conc. (% by weight)		Mole fraction water		NTS	Reflux flow (ml/min)	K'_x
		Bottom	Top	Bottom	Top			
31	1000	16.00	1.069	0.97222	0.99838	8.1	255	0.00100
32	1250	7.15	0.017	0.98858	0.99997	17.2	20	0.00017
33	1250	10.20	0.074	0.98324	0.99989	14.2	45	0.00031
34	1250	13.00	0.182	0.97807	0.99973	12.4	72	0.00044
35	1250	7.79	0.104	0.98748	0.99984	12.4	97	0.00058
36	1250	7.10	0.075	0.98866	0.99989	13.0	156	0.00099
37	1250	11.14	0.103	0.98155	0.99985	13.5	200	0.00132
38	1250	8.39	0.057	0.98644	0.99992	14.3	212	0.00148
39	1250	8.82	0.214	0.98570	0.99968	10.7	262	0.00136
40	1500	4.42	0.006	0.99311	0.99999	18.7	20	0.00018
41	1500	9.46	0.028	0.98456	0.99996	16.6	45	0.00037
42	1500	13.91	0.127	0.97633	0.99981	13.6	77	0.00052
43	1500	8.42	0.066	0.98639	0.99990	13.9	100	0.00068
44	1500	8.06	0.059	0.98702	0.99991	14.1	146	0.00100
45	1500	15.14	0.128	0.97392	0.99981	13.9	195	0.00133
46	1500	9.36	0.060	0.98474	0.99991	14.5	212	0.00150
47	1500	11.89	0.870	0.98015	0.99869	7.7	255	0.00095

APPENDIX 5

RESULTS OF STAGE-WISE ETHANOL STRIPPING CALCULATION

Table A5.1a

Section	x_A	y_A	k'_x	k'_y	m	m'	m''	K'_x	K'_y
0	0.0299	0.2220							
1	0.0295	0.2191	0.00567	0.00013	9.56	5.54	6.30	0.00070	0.00011
2	0.0291	0.2163	0.00568	0.00013	9.61	5.61	6.37	0.00070	0.00011
3	0.0287	0.2133	0.00570	0.00013	9.67	5.67	6.45	0.00071	0.00011
4	0.0283	0.2104	0.00571	0.00013	9.73	5.73	6.54	0.00072	0.00011
5	0.0280	0.2074	0.00572	0.00013	9.78	5.79	6.63	0.00073	0.00011
6	0.0276	0.2044	0.00573	0.00013	9.84	5.86	6.72	0.00073	0.00011
7	0.0271	0.2014	0.00574	0.00013	9.90	5.92	6.81	0.00074	0.00011
8	0.0267	0.1983	0.00575	0.00013	9.96	5.99	6.91	0.00075	0.00011
9	0.0263	0.1953	0.00576	0.00012	10.03	6.05	7.00	0.00076	0.00011
10	0.0259	0.1922	0.00578	0.00012	10.09	6.12	7.10	0.00077	0.00011
11	0.0255	0.1890	0.00579	0.00012	10.15	6.18	7.21	0.00078	0.00011
12	0.0251	0.1859	0.0058	0.00012	10.22	6.25	7.31	0.00079	0.00011
13	0.0247	0.1827	0.00581	0.00012	10.29	6.32	7.42	0.0008	0.00011
14	0.0242	0.1795	0.00582	0.00012	10.36	6.39	7.52	0.00081	0.00011
15	0.0238	0.1763	0.00584	0.00012	10.43	6.45	7.63	0.00081	0.00011
16	0.0234	0.1731	0.00585	0.00012	10.51	6.52	7.75	0.00082	0.00011
17	0.0229	0.1699	0.00586	0.00012	10.58	6.59	7.86	0.00083	0.00011
18	0.0225	0.1667	0.00587	0.00012	10.66	6.66	7.98	0.00084	0.00011
19	0.0221	0.1634	0.00589	0.00012	10.74	6.73	8.10	0.00085	0.00011
20	0.0216	0.1602	0.00590	0.00012	10.82	6.80	8.22	0.00086	0.00011
21	0.0212	0.1569	0.00591	0.00012	10.90	6.87	8.35	0.00087	0.00011
22	0.0208	0.1536	0.00592	0.00012	10.98	6.97	8.47	0.00089	0.00011
23	0.0203	0.1504	0.00594	0.00012	11.06	7.21	8.57	0.00089	0.00011
24	0.0199	0.1471	0.00595	0.00012	11.13	7.47	8.67	0.0009	0.00011
25	0.0195	0.1439	0.00596	0.00012	11.21	7.70	8.77	0.00091	0.00011

Table A5.1b

Section	x_A	y_A	k'_x	k'_y	m	m'	m''	K'_x	K'_y
26	0.0190	0.1406	0.00598	0.00012	11.29	7.81	8.87	0.00092	0.00011
27	0.0186	0.1374	0.00599	0.00012	11.37	7.92	8.97	0.00092	0.00010
28	0.0182	0.1342	0.00600	0.00012	11.44	8.03	9.06	0.00093	0.00010
29	0.0177	0.1310	0.00601	0.00012	11.52	8.14	9.16	0.00094	0.00010
30	0.0173	0.1278	0.00603	0.00012	11.60	8.25	9.26	0.00095	0.00010
31	0.0169	0.1247	0.00604	0.00012	11.68	8.36	9.39	0.00096	0.00010
32	0.0165	0.1216	0.00605	0.00012	11.76	8.46	9.52	0.00097	0.00010
33	0.0161	0.1185	0.00606	0.00012	11.85	8.57	9.65	0.00098	0.00010
34	0.0157	0.1154	0.00608	0.00012	11.93	8.67	9.79	0.00099	0.00010
35	0.0153	0.1124	0.00609	0.00012	12.01	8.78	9.93	0.00100	0.00010
36	0.0149	0.1094	0.0061	0.00012	12.10	8.88	10.07	0.00101	0.00010
37	0.0145	0.1064	0.00611	0.00012	12.18	8.98	10.22	0.00102	0.00010
38	0.0141	0.1034	0.00613	0.00012	12.27	9.08	10.36	0.00103	0.00010
39	0.0137	0.1005	0.00614	0.00012	12.36	9.18	10.51	0.00104	0.00010
40	0.0133	0.0976	0.00615	0.00012	12.44	9.28	10.67	0.00105	0.00010
41	0.0129	0.0948	0.00616	0.00012	12.53	9.38	10.82	0.00107	0.00010
42	0.0125	0.0920	0.00617	0.00012	12.62	9.47	10.98	0.00108	0.00010
43	0.0122	0.0892	0.00618	0.00012	12.72	9.57	11.14	0.00109	0.00010
44	0.0118	0.0865	0.0062	0.00012	12.81	9.66	11.31	0.00110	0.00010
45	0.0114	0.0838	0.00621	0.00012	12.91	9.75	11.48	0.00111	0.00010
46	0.0111	0.0812	0.00622	0.00012	13.00	9.84	11.66	0.00113	0.00010
47	0.0107	0.0786	0.00623	0.00012	13.10	9.93	11.84	0.00114	0.00010
48	0.0104	0.0760	0.00624	0.00012	13.19	10.22	11.98	0.00115	0.00010
49	0.0101	0.0735	0.00625	0.00012	13.25	10.63	12.09	0.00116	0.00010
50	0.0097	0.0710	0.00626	0.00012	13.32	11.07	12.20	0.00116	0.00010

Table A5.1c

Section	x_A	y_A	k'_x	k'_y	m	m'	m''	K'_x	K'_y
51	0.0094	0.0687	0.00627	0.00012	13.39	11.28	12.30	0.00117	0.00010
52	0.0091	0.0663	0.00628	0.00012	13.45	11.41	12.41	0.00118	0.00010
53	0.0088	0.064	0.00629	0.00012	13.52	11.54	12.51	0.00118	0.00010
54	0.0085	0.0618	0.00630	0.00012	13.58	11.67	12.61	0.00119	0.00010
55	0.0082	0.0597	0.00631	0.00012	13.64	11.79	12.70	0.00120	0.00010
56	0.0079	0.0575	0.00632	0.00012	13.70	11.91	12.80	0.00120	0.00010
57	0.0077	0.0555	0.00633	0.00012	13.75	12.03	12.89	0.00121	0.00010
58	0.0074	0.0535	0.00634	0.00012	13.81	12.14	12.98	0.00121	0.00009
59	0.0071	0.0515	0.00634	0.00012	13.86	12.26	13.06	0.00122	0.00009
60	0.0069	0.0496	0.00635	0.00012	13.91	12.36	13.14	0.00123	0.00009
61	0.0066	0.0478	0.00636	0.00012	13.96	12.48	13.22	0.00123	0.00009
62	0.0064	0.0460	0.00637	0.00012	14.01	12.58	13.30	0.00123	0.00009
63	0.0062	0.0443	0.00638	0.00012	14.06	12.68	13.37	0.00124	0.00009
64	0.0059	0.0426	0.00638	0.00011	14.10	12.77	13.45	0.00124	0.00009
65	0.0057	0.0410	0.00639	0.00011	14.15	12.87	13.52	0.00125	0.00009
66	0.0055	0.0394	0.00640	0.00011	14.19	12.96	13.59	0.00125	0.00009
67	0.0053	0.0379	0.0064	0.00011	14.23	13.04	13.65	0.00126	0.00009
68	0.0051	0.0364	0.00641	0.00011	14.27	13.13	13.72	0.00126	0.00009
69	0.0049	0.0349	0.00642	0.00011	14.31	13.21	13.78	0.00126	0.00009
70	0.0047	0.0335	0.00642	0.00011	14.35	13.29	13.84	0.00127	0.00009
71	0.0046	0.0322	0.00643	0.00011	14.39	13.37	13.90	0.00127	0.00009
72	0.0044	0.0309	0.00643	0.00011	14.42	13.44	13.95	0.00127	0.00009
73	0.0042	0.0296	0.00644	0.00011	14.46	13.51	14.01	0.00128	0.00009
74	0.004	0.0284	0.00644	0.00011	14.49	13.58	14.06	0.00128	0.00009
75	0.0039	0.0272	0.00645	0.00011	14.52	13.65	14.11	0.00128	0.00009

Table A5.1d

Section	x_A	y_A	k'_x	k'_y	m	m'	m''	K'_x	K'_y
76	0.0037	0.0261	0.00645	0.00011	14.55	13.71	14.16	0.00129	0.00009
77	0.0036	0.0250	0.00646	0.00011	14.58	13.78	14.21	0.00129	0.00009
78	0.0034	0.0239	0.00646	0.00011	14.61	13.84	14.25	0.00129	0.00009
79	0.0033	0.0229	0.00647	0.00011	14.64	13.90	14.29	0.00129	0.00009
80	0.0032	0.0219	0.00647	0.00011	14.67	13.95	14.34	0.00129	0.00009
81	0.0030	0.0209	0.00648	0.00011	14.69	14.01	14.38	0.00130	0.00009
82	0.0029	0.0200	0.00648	0.00011	14.72	14.06	14.42	0.00130	0.00009
83	0.0028	0.0191	0.00649	0.00011	14.74	14.11	14.45	0.00130	0.00009
84	0.0027	0.0183	0.00649	0.00011	14.77	14.16	14.49	0.00130	0.00009
85	0.0026	0.0174	0.00649	0.00011	14.79	14.21	14.53	0.00131	0.00009
86	0.0025	0.0166	0.00650	0.00011	14.81	14.25	14.56	0.00131	0.00009
87	0.0024	0.0159	0.00650	0.00011	14.83	14.30	14.59	0.00131	0.00009
88	0.0023	0.0151	0.00650	0.00011	14.85	14.34	14.62	0.00131	0.00009
89	0.0022	0.0144	0.00651	0.00011	14.87	14.38	14.65	0.00131	0.00009
90	0.0021	0.0137	0.00651	0.00011	14.89	14.42	14.68	0.00131	0.00009
91	0.0020	0.0130	0.00651	0.00011	14.91	14.46	14.71	0.00132	0.00009
92	0.0019	0.0124	0.00652	0.00011	14.93	14.49	14.74	0.00132	0.00009
93	0.0018	0.0118	0.00652	0.00011	14.94	14.53	14.77	0.00132	0.00009
94	0.0017	0.0112	0.00652	0.00011	14.96	14.56	14.79	0.00132	0.00009
95	0.0017	0.0106	0.00652	0.00011	14.98	14.60	14.81	0.00132	0.00009
96	0.0016	0.0101	0.00653	0.00011	14.99	14.63	14.84	0.00132	0.00009
97	0.0015	0.0095	0.00653	0.00011	15.00	14.66	14.86	0.00132	0.00009
98	0.0015	0.0090	0.00653	0.00011	15.02	14.69	14.88	0.00132	0.00009
99	0.0014	0.0085	0.00653	0.00011	15.03	14.72	14.90	0.00133	0.00009
100	0.0013	0.0081	0.00654	0.00011	15.04	14.74	14.92	0.00133	0.00009

Table A5.1e

Section	x_A	y_A	k'_x	k'_y	m	m'	m''	K'_x	K'_y
101	0.0013	0.0076	0.00654	0.00011	15.06	14.77	14.94	0.00133	0.00009
102	0.0012	0.0072	0.00654	0.00011	15.07	14.79	14.96	0.00133	0.00009
103	0.0012	0.0067	0.00654	0.00011	15.08	14.82	14.98	0.00133	0.00009
104	0.0011	0.0063	0.00654	0.00011	15.09	14.84	14.99	0.00133	0.00009
105	0.0010	0.0059	0.00654	0.00011	15.10	14.86	15.01	0.00133	0.00009
106	0.0010	0.0056	0.00655	0.00011	15.11	14.88	15.03	0.00133	0.00009
107	0.0009	0.0052	0.00655	0.00011	15.12	14.91	15.04	0.00133	0.00009
108	0.0009	0.0049	0.00655	0.00011	15.13	14.93	15.06	0.00133	0.00009
109	0.0009	0.0045	0.00655	0.00011	15.14	14.94	15.07	0.00133	0.00009
110	0.0008	0.0042	0.00655	0.00011	15.15	14.96	15.08	0.00133	0.00009

Calculation of ethanol concentration at bottom of column

The liquid feed rate Q_L = 100 litres/hour = 2.78×10^{-5} m^3/s .

The vapour flow at the top of the column, Q_G = 16.7 kg/hour = 0.08853 m^3/s.

The molar inflow of A at the top of the column (*TOC*) is

$$\Phi_{AF} = Q_L \times c_{AL0}$$

$$= 2.78 \times 10^{-5} \times 1.542$$

$$= 4.28 \times 10^{-5} \text{ kmol/s}$$

Similarly, the molar inflow of B at the top of the column (*TOC*) is

$$\Phi_{BF} = Q_L \times c_{BL0}$$

$$= 2.78 \times 10^{-5} \times 50.043$$

$$= 139.12 \times 10^{-5} \text{ kmol/s}$$

The molar outflow of *A* at the top of the column (*TOC*) is

$$\Phi_{AD} = Q_G \times c_{AG0}$$

$$= 0.08853 \times 0.00048$$

$$= 4.25 \times 10^{-5} \text{ kmol/s}$$

and the molar outflow of *B* at the top of the column (*TOC*) is

$$\Phi_{BD} = Q_G \times c_{BG0}$$

$$= 0.08853 \times 0.00168$$

$$= 14.87 \times 10^{-5} \text{ kmol/s}$$

A mass balance over the whole column and reboiler requires that the molar outflows of both components from the reboiler equal the difference between the molar inflows and outflows at the top of the column. That is:

$$\Phi_{AW} = \Phi_{AF} - \Phi_{AD} = 0.036 \times 10^{-5} \text{ kmol/s}$$

$$\Phi_{BW} = \Phi_{BF} - \Phi_{BD} = 124.1 \times 10^{-5} \text{ kmol/s}$$

The mole fraction of ethanol in the discharge stream is then

$$x_{AW} = \frac{\Phi_{AW}}{\Phi_{AW} + \Phi_{BW}} = 0.00029$$

The mole fraction of *A* in the vapour leaving the reboiler and entering the column is

$$y_{AI} = y_{AW}* = mx_{AW} = 0.0045$$

from the VLE relationship for ethanol and water at the prevailing pressure.

The slope of the operating line is

$$\frac{L}{G} = \frac{\Phi_{AF} + \Phi_{BF}}{\Phi_{AD} + \Phi_{BD}} = 7.49$$

and, since the operating line intersects the 45° line at $x = x_W = 0.00029$, the equation of the operating line becomes

$$y_A = 7.49x_A - 0.0019$$

We find the mole fraction of ethanol in the liquid leaving the column and entering the reboiler by substituting $y_A = y_{AI}$ into the equation of the operating line and solving for x_A:

$$x_{AI} = \frac{y_{AI} + 0.0019}{7.49} = 0.00085$$

The stage-wise calculation presented here starts at the top of the column, where $x_{A0} = 0.030$ and $y_{A0} = 0.222$, and proceeds downwards until we obtain $x_A = x_{AI} = 0.00085$ and $y_A = y_{AI} = 0.00445$. From table A6.2(e) we see that these concentrations are attained with 110 stages.